Théorie de la spectroscopie électronique : au-delà de l'état de l'art

Jianqiang Zhou

▶ **To cite this version:**

Jianqiang Zhou. Théorie de la spectroscopie électronique : au-delà de l'état de l'art. Physique [physics]. Université Paris Saclay (COmUE), 2016. Français. NNT : 2016SACLX017 . tel-01457420

HAL Id: tel-01457420
https://pastel.hal.science/tel-01457420

Submitted on 6 Feb 2017

THÈSE DE DOCTORAT

DE L'UNIVERSITÉ PARIS-SACLAY
préparée À l'ÉCOLE POLYTECHNIQUE

Ecole Doctorale N° 572 ONDES ET MATIÈRE

Spécialité : PHYSIQUE

par

Jianqiang Sky Zhou

Theory of electron spectroscopy beyond the state-of-the-art

An improved description of fermion-plasmon coupling in Green's function calculations

Thèse présentée et soutenue à Palaiseau, le 23 mai 2016:

Prof.	Mark Oliver GOERBIG	Président
Prof.	Ferdi ARYASETIAWAN	Rapporteur
Dr.	Matteo CALANDRA	Rapporteur
Dr.	Vladimir STROCOV	Examinateur
Dr.	Pina ROMANIELLO	Examinateur
Dr.	Hong JIANG	Examinateur
Dr.	Lucia REINING	Directrice de thèse
Prof.	John J. REHR	Invité

Theory of electron spectroscopy beyond the state-of-the-art

An improved description of fermion-plasmon coupling in Green's function calculations

Jianqiang Sky Zhou

July 26, 2016

Abstract

The topic of this thesis is situated in the framework of theoretical spectroscopy. In particular, I propose a new *ab-initio* derivation to find approximations for the one-body Green's function (GF) [1–3]. This approach leads to an improved description of fermion-plasmon coupling in the framework of many-body perturbation theory (MBPT) [1–3], which can be used to study direct and inverse photoemission spectroscopy. Although the observed phenomena have been well known before, my formulation yields a better description than previous state-of-the-art approaches. It answers several open questions, cures some fundamental shortcomings and suggests a way for systematic improvement.

In photoemission spectroscopy [4], the sample is irradiated by photons and electrons are emitted and captured by the energy analyzer. From the energy difference of the incoming photon and outgoing electron, a great deal of information on the properties of the sample can be studied, e.g. the band structures or lifetimes of excitations *etc.*. In an independent-particle picture, this energy difference corresponds to the one-particle energy level that the emitted electron was occupying before the measurement. This leads to a sharp peak in the spectrum with weight normalized to one, representing one particle. In reality, photoemission is not just photons in and independent electrons out, because the sample is an interacting many-body system. The long range Coulomb interaction and anti-symmetric nature of fermions give rise to the so-called `exchange-correlation` effects, which makes the problem fundamentally difficult to solve. The description, understanding and prediction of the effects of the Coulomb interaction on the properties of materials has been one of the big challenges of theoretical condensed matter physics for ages [2]. In the framework of this thesis one can imagine that first, the photoemission creates a hole (i.e. a missing electron) in the sample, which causes all remaining electrons to relax. Due to the attractive interaction between positively charged holes and negatively charged electrons, the electrons move towards to the holes and dress them to create "*quasi-particles*". The effective interaction between quasi-particles is the dynamically screened Coulomb interaction W. It is in general weaker than the bare Coulomb interaction v_c. Consequently, the observed band structure is a quasi-particle band structure, which differs from the result of an independent-particles

band structure calculation. Second, when the hole propagates in the sample the remaining electrons get excited. They can show collective oscillations that is the density response to the perturbation. These are neutral excitations with approximately bosonic nature, because they are constituted by pairs of fermions. The coupling of the hole to the neutral excitations leads to additional structures in the photoemission spectrum which are called *satellites* [1–3]. This reduces the quasi-particle weight that is now fractional. Most often, the dominant satellites are due to plasmons, i.e. collective long-range oscillations, but one can also observe interband transitions or excitons, or other satellites that are due to more complicated couplings.

This overview shows that in order to have a good description of photoemission spectroscopy, we should study the propagation of particles, as well as the interaction between particles and plasmons or other excitations. The Green's function gives the probability amplitude of particles propagating from one point to another. Its imaginary part yields the spectral function that has a direct link to the spectrum measured in a photoemission experiment. The state-of-the-art method in this framework is the `GW` approximation (GWA) that was proposed by L. Hedin in 1965 [5]. In the GW approximation the one-particle Green's function is determined by the Dyson equation $G = G_0 + G_0\Sigma G$, where G_0 is the non-interacting Green's function, and Σ is the non-local and frequency dependent `self-energy` that is approximated to be the product of the one-particle Green's function G and the dynamical screened Coulomb interaction W leading to $\Sigma = iGW$. The GW approximation has become one of the most widely used methods [6,7] for the quasi-particle band structure calculations thanks to its success to the solution of the *band-gap problem* encountered in density-functional theory (DFT) [8]. However, as discussed above, the quasi-particles are only a part of the measured spectrum. The most interesting part, when it comes to explore correlation effects, is contained in the satellites that directly exhibit the effects of coupling between excitations. In principle one should expect that at least plasmon satellites are well described by the GW approximation, since plasmons are the dominant structures that are seen in the inverse dielectric function $\epsilon^{-1}(\omega)$ and hence in the screened Coulomb interaction $W = \epsilon^{-1}v_c$. Satellites due to plasmons are indeed found in the GW approximation, but they are often too far from the quasi-particle energy, and sometimes much too sharp, and

in other cases much too weak as compared to the experiment [9–12]. The main reason for the bad description of the plasmon satellites from the GWA is the so called `plasmaron effect` [9, 11–15] , which will be discussed in this thesis.

Alternatively, approaches based on a picture of electron-boson coupling such as the cumulant expansion approximation (CEA) are promising for a good description of plasmon satellites. The cumulant expansion approximation, inspired by the exact Green's function of the core-level quasi-boson model Hamiltonian [16], has an exponential expression of the Green's function, the expansion of which yields a series of plasmon satellites in the spectral function. The CEA has a very good agreement with the spectrum observed in the photoemission experiment [9–11]. In particular, my thesis project is a continuation of the thesis work of Dr. Matteo Guzzo [17] as well as previous work from Dr. Giovanna Lani [18]. Thanks to the excellent derivations done by them, I had the opportunity to go a bit further in the direction of understanding photoemission spectroscopy in a deeper way. The derivations and approximations proposed in this thesis give a new way to calculate the Green's function, which improves the description of photoemission spectroscopy. Moreover, they give access to other quantities that can be obtained from the one-body Green's function, in particular total energies.

In the present thesis manuscript, we discuss how one can obtain a better description of the one-body Green's function, in particular for the description of fermion-plasmon coupling in photoemission spectroscopy. To this purpose, in Chapter 1, a brief introduction of photoemission spectroscopy is given, together with some important physical concepts and the physical picture for describing photoemission spectroscopy in theory. The purpose of this chapter is to establish the link between the photoemission experiment and theory, such that one can have a clear picture about the physical phenomena I am going to study. The Green's function theory is also introduced and some important exact constraints are summarized such that one can use these constraints to examine the approximations that I will study in this thesis.

After the introduction, I will show a brief overview of state-of-the-art methods in electron spectroscopy in Chapter 2, including the Kohn-Sham density functional theory (KS-DFT), the GW approximation (GWA) and the cumulant expansion approximations (CEAs) (i.e.

the TOC96 in Ref. [9] and the retarded cumulant (RC) in Ref. [19]). Some calculated photoemission spectra are provided and discussed, such that one can understand the advantages and disadvantages of each present theory. I will also show some of my own calculations on bulk sodium to illustrate these methods. In particular, in section 2.2, I will discuss the importance of self-consistency in GW calculations using my original calculations on sodium valence and core states, which have been published in the Journal of Chemical Physics [20]. The GWA cannot describe the plasmon satellites in bulk sodium, the TOC96 on the other hand, is able to give a reasonably good photoemission spectrum. The retarded cumulant is designed for improving the sodium valence photoemission spectrum.

In Chapter 3, a unified derivation of the GWA, the TOC11 [11] and the retarded cumulant (RC) is shown, which is different from previous derivations and more compact. In particular, I will show two different ways of deriving the GWA starting from the functional differential equation of the one-body Green's function. The cumulant expansion approximation can be also obtained from this unified derivation: the decoupling approximation plus a GW quasi-particle correction yields the TOC11 and a clever *ansatz* Green's function leads to the retarded cumulant. An further study of this unified derivation which aims at exploring increasingly good approximations will be shown in Appendix C.

After the *ab-initio* derivations, two simplified hole-plasmon coupling Hamiltonians are studied in detail and the exact Green's functions are calculated in Chapter 4. The exact Green's functions of the model Hamiltonians can be used to examine the performance of the GWA and different CEAs. All the sophisticated formulas become fully analytical expression in these hole-plasmon coupling Hamiltonians such that one can see clearly the link between different approximations, as well as their physical meanings. Moreover all the exact constraints of the Green's function can be studied under different approximations. From this study, we will understand why the present CEAs are insufficient in the description of valence photoemission for different reasons.

Based on the understanding of the hole-plasmon coupling model Hamiltonians and our unified derivation of the CEA, as well as the study of the disadvantages of different approximations in the two-level hole-plasmon coupling Hamiltonian, I will propose a new cumulant Green's function that will be refereed to as the constrained retarded cumulant

(CRC) in Chapter 5. A detailed formulation of this method is provided, together with an implementation for real system calculations.

Chapter 6 aims at illustrating the cumulant expansion approximations in bulk sodium valence and core using the dynamically screened Coulomb interaction W in the random phase approximation (RPA W). The calculated spectra are compared to the experimental ones. All the results provided there are from my original calculations. The traditional time-ordered cumulants (the TOC96 and TOC11) are performed in the sodium core and valence, yielding reasonably good photoemission spectra compared to the experimental ones, however the performance of the time-ordered cumulant becomes worse when going from core to valence: the plasmon satellite energy and weight ratio between the QP and satellites are overestimated. These discrepancies are expected to be corrected by the newly derived constrained retarded cumulant. Therefore, the comparison of the calculated sodium valence spectra using the time-ordered cumulant and constrained retarded cumulant is provided, again using the RPA W. The constrained retarded cumulant does enhance the weights of satellites, but unfortunately the overestimation of the plasmon satellite energy is still present. In order to find out the origin of this overestimation with respect to the experimental spectrum, a study using more advanced calculations of the screened Coulomb interaction W is provided.

Besides the spectral functions, the Green's function is also able to provide the total energies. The total energies will be studied in Chapter 7, where a new total energy formula will be derived according to the hole-plasmon coupling model Hamiltonian. This new formula will be refereed to as the hole-plasmon coupling total energy (HPCtot) formula. The HPCtot formula that is different from the most widely used Galitskii-Migdal total energy formula, works better with the Green's function calculated from the GWA or the CEA. This phenomena reflects the importance on the consistency of approximations: the performance of the total energies does not only depend on the performance of the approximate Green's function, but also the total energy formula that is used. If the approximate total energy formula keeps consistency with the approximate Green's function, the total energy can be better than using the exact total energy formula with the same approximate Green's function. The philosophy is quite similar to the use of the cumulant expansion approxi-

mation with the GW self-energy versus the use of the Dyson equation with the same GW self-energy. The Dyson equation is the exact equation to determine the exact Green's function, however the GW self-energy is an approximation to the exact self-energy, such that the Green's function calculated using the cumulant expansion approximation works better than the solution of the exact Dyson equation (i.e. the GWA). The total energy study provided in Chapter 7 shows that the constrained retarded cumulant Green's function together with the newly derived hole-plasmon coupling total energy formula yields the best total energy compared to the exact total energy of the hole-plasmon coupling Hamiltonian. This suggests to go a step further to implement this formula in real system calculations. A suggestion for the final implementation is provided and will be used in the future to study the homogeneous electron gas.

Finally I will summarize and provide some outlooks from this work.

Résumé

Le sujet de cette thèse se place dans le cadre de la spectroscopie théorique. En particulier, je propose une nouvelle dérivation ab-initio pour trouver des approximations pour la fonction de Green (GF) à un corps. Cette approche conduit à une meilleure description du couplage fermion-plasmon dans le cadre de la théorie des perturbations à plusieurs corps (MBPT), qui peut tre utilisée pour étudier la spectroscopie de photoémission directe et inverse. Bien que les phénomènes observés étaient bien connus avant, ma formulation donne une meilleure description que les approches précédentes de l'état de l'art. Cela répond à plusieurs questions ouvertes, guérit certaines lacunes fondamentales et suggère un moyen d'amélioration systématique. En spectroscopie de photoémission, un échantillon est irradié par des photons et des électrons sont émis. A partir de la différence d'énergie du photon incident et des d'électrons sortant, un grand nombre d'informations sur les propriétés de l'échantillon peut tre obtenu, par exemple les structures de bandes ou la durée de vie des excitations. Dans une cadre de particules indépendantes, cette différence d'énergie correspond au niveau d'énergie d'une particule que l'électron émis occupait avant la mesure. Cela conduit à un pic très intense dans le spectre, avec un poids normalisé à un. En réalité, la photoémission n'est pas juste des photons entrants et des électrons indépendants sortants, car l'échantillon est un système à plusieurs corps en interaction. L'interaction de Coulomb et la nature anti-symétrique des fermions donnent lieu aux effets d'échange-corrélation, ce qui rend le problème fondamentalement difficile à résoudre. La description, la compréhension et la prédiction des effets de l'interaction de Coulomb sur les propriétés des matériaux a été, pendant des années, l'un des grands défis de la physique théorique de la matière condensée. Dans le cadre de cette thèse, on peut imaginer que, premièrement, la photoémission crée un trou (à savoir, un électron manquant) dans l'échantillon, ce qui provoque la relaxation de tous les électrons restants. En raison de l'interaction attractive entre les trous chargés positivement et les électrons chargés négativement, les électrons se déplacent vers les trous et créent des "quasi-particules". L'interaction effective entre les quasi-particules est l'interaction de Coulomb écrantée dynamiquement. Elle est en général plus faible que l'interaction de Coulomb nue. Par conséquent, la structure de bandes observée est celle

de quasi-particules, qui diffère du résultat en particules indépendantes. Deuxièmement, lorsque le trou se propage dans l'échantillon les électrons restants peuvent présenter des oscillations collectives: réponse de la densité à la perturbation. Ce sont des excitations neutres avec une nature approximativement bosonique, parce qu'elles sont constituées par des paires de fermions. Le couplage du trou avec les excitations neutres conduit à des structures supplémentaires dans le spectre de photoémission, appelées satellites. Cela réduit le poids des quasi-particules qui est maintenant fractionnée. Le plus souvent, les satellites dominants sont dus à des plasmons, des oscillations collectives à longue portée, mais on peut aussi observer des transitions ou excitons interbandes ou d'autres satellites qui sont dus à des couplages plus complexes. Cela montre que pour avoir une bonne description de la spectroscopie de photoémission, nous devrions étudier la propagation de particules, ainsi que l'interaction entre les particules et les plasmons ou d'autres excitations. La fonction de Green donne l'amplitude de probabilité de particules se propageant d'un point à un autre. Sa partie imaginaire donne la funtion spectrale qui a un lien direct vers le spectre mesuré dans une expérience de photoémission. Les dérivations et approximations proposées dans cette thèse donnent une nouvelle façon de calculer la fonction de Green, ce qui améliore la description de la spectroscopie de photoémission. En outre, cela permet d'accéder à d'autres grandeurs qui peuvent tre obtenues à partir de la fonction de Green à un corps, en particulier les énergies totales.

Acknowledgements

Firstly, I would like to express my special appreciation and sincere gratitude to my these supervisor Dr. Lucia Reining, you have been a tremendous mentor for me. Thank you very much for your continuous encouragement and patience such that I can grow as a qualified researcher. Your advice on both research as well as on family have been priceless and they will become the guide of my life forever. There were too many moments between us that might be too small for you to remember, but to me they are precious. Your attitude towards life has been my motto that will lead the rest of my life.

Besides my supervisor, I would like to express my sincere thanks to other researchers in the ETSF Palaiseau group who have given me incredible help during my thesis: Dr. Matteo Gatti who lead me on the *ab-initio* calculations. Thank you for proposing me the bulk sodium as a benchmark system in my thesis, which gave me many hopes ☺ at the beginning, but finally becomes my nightmare at the end ☹. Dr. Francesco Sottile, who is always available for the discussions on computer codes. Most importantly, your optimistic attitude makes you the best person to talk with when I have troubles, no matter the problem is work-related or family-related, you will always give me best suggestion I can find. To be honest, you have been my example of being a good researcher and father at the same time. Our computer engineer Mr. Andrea Cucca who has taught me a lot of computer science. I am sorry I have chosen MacBook that bring so many troubles for us, but since you are an expert on all systems, you can always solve my problems without any delay. My sincere thanks also go to Dr. Matteo Guzzo, Dr. Claudia Rödl, Dr. Igor Reshetnyak, Dr. Nicolas Tancogne-Dejean and all my fellow lab-mates for the stimulating discussions and support. Thanks all the people in my group, the atmosphere there has been always family-like. I will be always proud of having been part of this family.

I also would like to thank my collaborators from the University of Washington: Professor John J. Rehr and Dr. Joshua J. Kas for their insightful comments, for the sleepless nights we were working together before the deadline of our co-publication, but also for the hard question which incited me to widen my research from various perspectives.

Last but not the least, I would like to thank my family: my parents, my wife and my son who are always supporting me spiritually throughout writing this thesis. Words cannot express how grateful I am to my wife for all of the sacrifices that you have made on my behalf. Your accompany for me was what sustained me thus far.

To my wife, my son and my parents.

Contents

Notations and units

I provide here a list of abbreviations and symbols used, with the reference to the pages where they are defined.

Abbreviation	Definition	Pag.
(AR)PES	(Angular-resolved) Photoemission spectroscopy/spectrum	5
CEA	Cumulant expansion approximation	26
CRC	Constrained retarded cumulant	132
DFT	Density-functional theory	26
EOM	Equation of motion	35
$EscGW_0$	Eigenvalue (Energy) self-consistent GW_0 approximation	43
(E)HPC	(Electron-) Hole-plasmon coupling	90
FDE	Full functional differential (Kadanoff-Baym) equation	66
GW(A)	GW approximation	42
G_0W_0	Perturbative ("one-shot") GW scheme	43
GMtot	Galitskii-Migdal total energy (formula)	178
HEG	Homogeneous electron gas (jellium)	51
HPC-1	One-level hole-plasmon coupling Hamiltonian	92
HPC-2	Two-level hole-plasmon coupling Hamiltonian	99
HPCtot	hole-plasmon coupling total energy (formula)	179
(I)PES	(Inverse) Photoemission spectroscopy/spectrum	5
KS	Kohn-Sham	30
LDA	Local-density approximation	31
LDE	Linearized differential equation	69
MBPT	Many-body perturbation theory	34
RPA	Random-phase approximation	44
RC	Retarded cumulant	13
scGW	self-consistent GW approximation	43
TOC	Time-ordered cumulant	61
TCTC	Test-charge test-charge	41
TCTE	Test-charge test-electron	41
TDLDA	Time-dependent local-density approximation	160
QP	Quasi-particle	33

Symbol	Definition	Pag.
Z	QP renormalization factor 9
g	The fermion-plasmon coupling strength 11
ω_p	The plasmon energy 11
$c^{(\dagger)}$	Fermion annihilation (creation) operator 11
$a^{(\dagger)}$	Boson annihilation (creation) operator 11
1	Shorthand notation for $x_1, t_1 \equiv \boldsymbol{r}_1, \sigma_1, t_1$ 18
Ψ_0^N	Many-body ground state wavefunction 18
$\hat{\psi}$	Field operator of fermion 18
μ	Chemical potential 22
φ	The single-particle basis function 23
$	N\rangle$ or $\Psi(\boldsymbol{r}_1, \ldots, \boldsymbol{r}_N)$	Many-body wavefunction 27
v_c	Coulomb interaction 27
ψ	Kohn-Sham or quasi-particle orbital 30
$\mathcal{E}_i$	Kohn-Sham eigenvalue 30
V_H	The Hartree potential 30
V_{xc}	The exchange-correlation potential 30
V_{ks}	The Kohn-Sham potential 30
$\hat{h}_0(\boldsymbol{r})$	Non-interacting part of the many-body Hamiltonian 34
Σ	The self-energy 34
ϕ	The external perturbation 35
Σ_{xc}	The exchange-correlation self-energy 36
ϵ	The dielectric functions 37
W	The dynamically screened Coulomb interaction 38
ε_i	quasi-particle energy 45
$\hat{\phi}$	Field operator of boson 188

Units

If not otherwise specified, atomic units are adopted: $\hbar = m_e = e^2 = 4\pi\epsilon_0 = 1$.

Chapter 1

Introduction

In this thesis, I will show a development of a theory to describe the observables that can be measured by a photoemission spectroscopy (PES) experiment, as indicated by the title of my thesis. Before going to the details about the complicated theory, I will start with a brief introduction about the physical picture of photoemission spectroscopy. Thus this chapter will be organized in the following way:

- In section 1.1, a brief introduction to the photoemission process is given together with the terminologies used in the theoretical description. The aim is to understand what happens during photoemission, what kind of quantities can be measured or calculated, what kind of properties we can get from these measured quantities, as well as to see how one can theoretically model photoemission, such that the link between experiment and theory is built up.

- In section 1.2, I will introduce the one-body Green's function whose imaginary part yields the spectral function that has a direct link to the spectrum measured in experiment. The one-body Green's function will be the main target to calculate in this thesis.

- Finally I will summarize in section 1.3, and give some important exact constraints for the one-particle Green's function which will be studied in this thesis.

We have to keep in mind that the aim of theoretical spectroscopy is not to reproduce the experimental results, but to understand deeper and sometimes even predict the properties

of materials. On the other hand, whenever a new theoretical approach is developed, the experimental result can be a good tool for testing its performance. This is the case in the present thesis when I show the comparison between results from theory and experiment.

1.1 Photoemission spectroscopy

The photoemission spectroscopy originates from the discovery of the photoelectric effect by Hertz [21], which was later explained by Einstein [22], who obtained the Nobel prize in 1921. After its discovery photoemission spectroscopy has become more and more used to understand the electronic properties of materials [4]. In a general spectroscopy experiment, one perturbs an electronic system by transferring some external energy (perturbation), and measures the response of the system after excitation. This allows one to access a great deal of information about the electronic properties of the system. Photoemission spectroscopy can be divided into two complementary processes, namely direct and inverse photoemission spectroscopy ((I)PES). In the direct photoemission the sample absorbs photons and the electrons in the sample are excited and emitted. Knowing the photon energy and by measuring the kinetic energy of the photoelectrons, one can infer information about the energy distribution of electronic states (the occupied states in an independent-particle picture) of the sample. The inverse photoemission (IPES) can be considered as the time-reversal of PES, where the electrons are absorbed and photons are emitted and measured in the detector. Consequently one can access the information of the possible empty (unoccupied) states (in an independent-particle picture) of the sample.

1.1.1 What happens during photoemission spectroscopy?

A schematic view of the PES and IPES processes are shown in Fig. 1.1, where E_{kin} and $h\nu$ are the energies of electron and photon, respectively. In an (I)PES experiment, these two energies can be measured such that the energy difference of the sample before and after the measurement can be determined by energy conservation. The most complete information is angle-resolved photoemission spectroscopy (ARPES) [23–25] whose schematic view is shown in Fig. 1.2. In ARPES, besides the energy the angle of the photoelectrons can be measured,

such that the energy-momentum relations of electrons inside the sample can be deduced. As a result we can obtain the `angle-resolved spectrum` from ARPES, which corresponds to the spectra of each k-point in the Brillouin zone of a solid (`k-resolved spectrum`) (see Fig. 1.3).
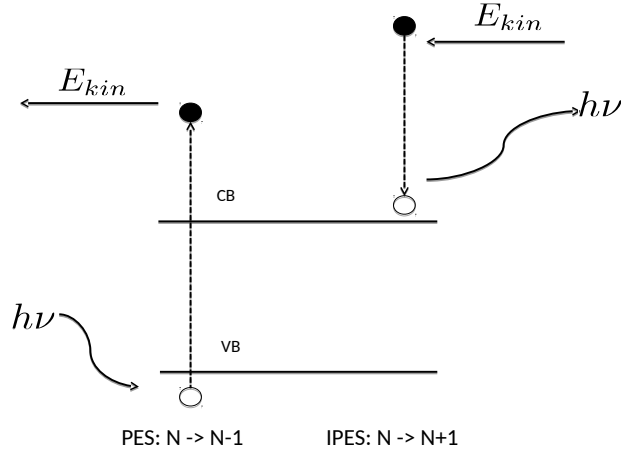
Figure 1.1: Schematic view of direct (on the left) and inverse (one the right) photoemission spectroscopy. The Fermi energy is between the valence (VB) and conduction (CB) band. In PES an electron is emitted with energy E_{kin} duo to the excitation induced by the photon of energy $h\nu$. The IPES is the inverse process of PES where one electron is added to the system and one photon is emitted as Bremsstrahlung. In both processes we can measure E_{kin} and $h\nu$ from which we can access the energy levels of the system using the energy conservation rule. The total number of electrons in the sample has been changed (from N to $N \pm 1$) in both processes. This is the reason why the excitations in (I)PES are called charged excitations, as opposed to the neutral excitations (e.g., excitons and plasmons) where the number of electrons is conserved during the excitation.

The quasi-particle excitation

In an `independent-particle` picture[1], the energy difference between the incoming photons and outgoing photoelectrons in (AR)PES gives directly the energy of the one-particle level that the one electron was occupying before being emitted from the system. Therefore under the independent-particle assumption, we will observe a series of δ-peaks corresponding to

---

[1]The independent-particle picture does not really neglect the interaction between particles. Instead it approximates the interaction between particles as an averaged effective potential that acts on all the particles of the system. As a consequence, there is no direct interaction between particles but particles are affected by this effective potential. Examples are the Hartree or Hartree-Fock mean fields, or the Kohn-Sham potential in density functional theory (see section 2.1).
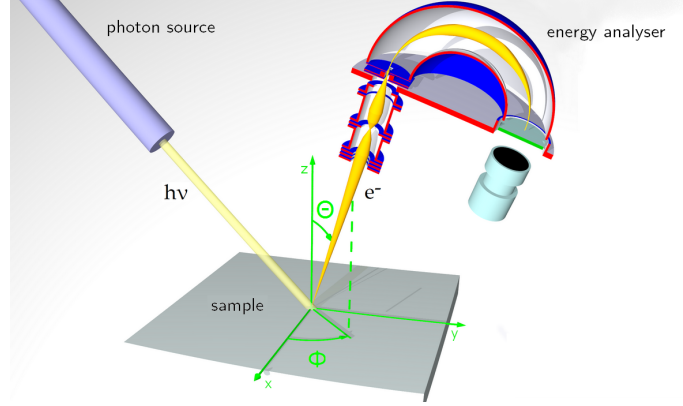
Figure 1.2: A schematic representation of an angle-resolved photoemission spectroscopy (ARPES) experiment taken from [26]. Besides the energy of the photoelectron, its angle is also measured in ARPES.

different independent-particle states in the sample as shown in the left panel of Fig. 1.3. Since there is no interaction between particles, each δ-peak has a normalized weight of $\mathbf{Z} = 1$ representing one particle. Moreover, there is no relaxation of remaining electrons in the independent-particle picture such that the excitation has an infinite lifetime (the excitation energy is real-valued as opposed to a complexed-valued energy from the GW approximations that will be discussed later) and the occupation number of each state is either 1 (for states below the Fermi level) or 0 (for states above the Fermi level).
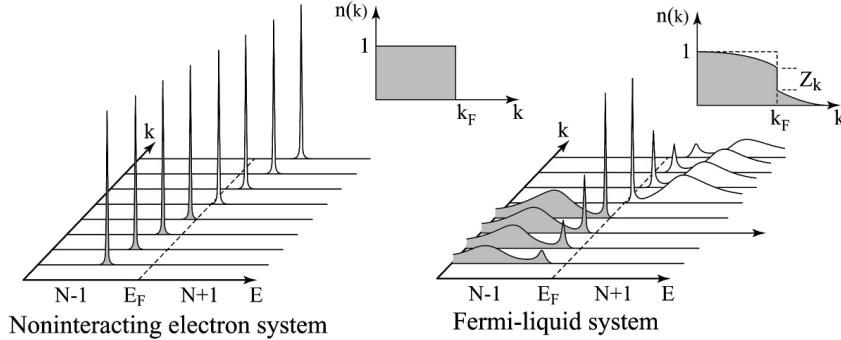
Figure 1.3: A schematic illustration of an ARPES spectrum. The figure is modified from Ref. [24]. The left figure shows an independent-particle spectrum of δ-functions with occupation 1 or 0. The right figure exemplifies a spectrum for interaction electrons with quasi-particle peaks (i.e., peaks in the spectrum due to one-particle excitations) with fractional weight $\mathbf{Z} < 1$ and satellites due to additional excitations in the system induced by the photoemission. In this figure $n(k)$ represents the momentum distribution.

However, the spectrum one actually obtains from an (AR)PES experiment is most of the time different from the simple independent-particle picture. In fact, the emitted electron leaves a hole in the electronic system corresponding to a positive charge. The remaining electrons in the system can react to that hole, which screens the hole. Alternatively speaking, the hole left behind attracts the surrounding electrons due to the attractive interaction between positive and negative charges. The screened particles are called quasi-particles (QPs). The interaction between QPs is weaker than the interaction between bare electrons: instead of the bare Coulomb interaction, the effective interaction in the system is the dynamically screened Coulomb interaction W (see Fig. 1.4). Since the dynamical screening corresponds to excitations into which the QP can decay, the latter corresponds to an excited state of the system with a finite lifetime. As a consequence, in an ARPES experiment we observe a broadened peak with finite width, which gives a measure of the interactions due to the presence of a hole. The broadened QP peaks, which replace the sharp δ-peaks of the independent-particle picture, are shown in the right panel of Fig. 1.3.
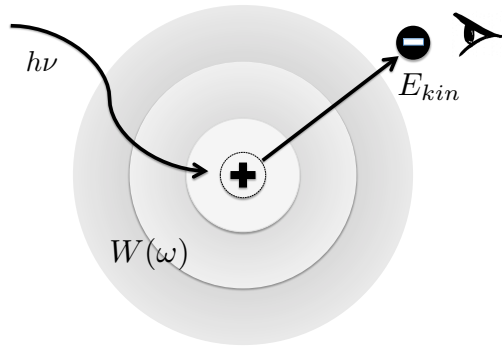
Figure 1.4: Schematic illustration of electron removal and the resulting reaction of the remaining electrons. The hole induced by the removal of one electron is dressed by the wave-like oscillation of all other electrons. This is a screening effect described by the dynamically screened Coulomb interaction W.

Coupling to neutral excitations

Moreover, besides the broadening the observed QP weight is reduced compared to the independent-particle picture. This is because the hole induced by the photoemission ex-

cites all remaining electrons, which often leads to collective wave-like oscillations in the system. This collective oscillation is a neutral excitation as opposed to the charged excitation, because after the photoemission, the remaining electrons move inside the system and the total number of electrons is conserved. The neutral excitations are of bosonic nature because they are constituted by pairs of fermions (e.g., excitons and plasmons)[2]. Therefore besides the QPs, the photon energy has been used also to excite the additional excitations (e.g., the plasmon excitation will be discussed intensively throughout this thesis) yielding new structures in the spectrum. The renormalized QP weight is reduced by giving some weight to these additional structures, leading to a fractional renormalization factor $\mathbf{Z} < 1$. In simple systems like simple metals or semiconductors, the weight of the plasmon excitations are smaller than the QP weight. The peaks due to the plasmon excitations are called `satellites`[3] in the photoemission spectrum. As a collective oscillation, the plasmon excitation should be able to propagate as all other waves in nature (e.g., waves of water), the longer it propagates, the smaller its weight (possibility of excitation) indicating that we should be able to observe not only one plasmon satellite but its replica with decreasing weights (see e.g., the left panel of Fig. 1.5).

Due to the screening and collective oscillation of electrons, the possibilities of excitations in a many-body system are infinite, leading to a continuous spectrum with broadening (finite lifetime) and extra structures (e.g., plasmon satellites). Moreover, the occupation numbers of the states close to the Fermi level become fractional instead of 0 or 1 as shown in the right panel of Fig. 1.3 due to the many-body interaction. To illustrate our analysis, the photoemission spectrum and the momentum distribution function of bulk sodium in the valence band region are shown in Fig. 1.5. The left panel is the photoemission spectrum of the sodium valence band taken from Ref. [20]. The experimental spectrum shows a strong QP peak centered around -0.9 eV together with two satellites centered around -6.9 and -12.9 eV with decreasing weights. The energy difference between the peaks is ≈ 6 eV

---

[2]The interaction between electrons and plasmons is the focus of this thesis and will be discussed in detail in the following chapters.

[3]There is another definition of satellites that is the poles in the Green's function induced only by the interactions. Therefore we would not observe any satellite in a non-interacting system. This definition is helpful to distinguish satellites from quasi-particles in a theoretical calculation because in any calculation, we could put the interaction to zero to see the spectrum such that we will only observe the QP excitations without interaction.
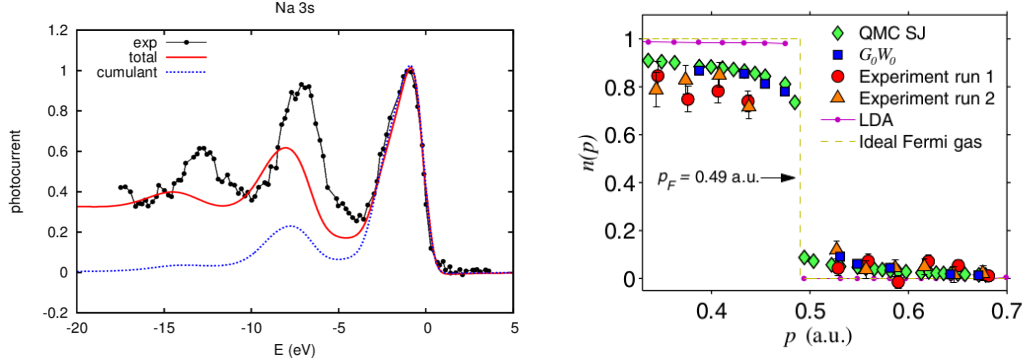
Figure 1.5: Bulk sodium valence band spectrum and momentum distribution. Left: the photoemission spectrum of sodium valence band taken from Ref. [20] (the calculations are my own results). The zero of energy axis is the Fermi energy from experiment. Blue dashed curve is the intrinsic spectral function calculated in a cumulant expansion approximation. The red curve is the cumulant intrinsic+extrinsic+interference calculation provided by my co-author J. Kas in Ref. [20]. The black curve is the experimental spectrum reproduced from Ref. [28]. Right: The momentum distribution of sodium determined by experiment, quantum Monte-Carlo, G_0W_0 and LDA calculations. The step function is the free-electron gas result. The figure is taken from Ref. [27].

which is the plasmon energy of bulk sodium, indicating that the satellites in this spectrum are indeed induced by the plasmon excitations. The other two spectra are calculated in the cumulant expansion approximations (CEA); they will be discussed in section 6.1. The right panel of Fig. 1.5 shows the momentum distribution function of bulk sodium (taken from Ref. [27]). The ideal Fermi gas and LDA results are very close to the non-interacting electron result as shown in the left panel of Fig. 1.3, where the momentum distribution is a step function. Whenever the interaction between particles is taken into account, as it is the case in all other calculations in Fig. 1.5, the momentum distribution function will give a fractional number at each momentum. The two experimental datasets confirm the fractional occupations in bulk sodium.

The quasi-boson model

The above description of the PES process suggests to introduce the so-called `quasi-boson model Hamiltonian`, which was proposed by B.I. Lundqvist to study the `GW` approximation [14], and was later solved exactly by D.C. Langreth [16] for the case of a core electron coupled to the plasmons, building upon the work of Nozières and De Dominicis [29]. The

Hamiltonian reads

$$\hat{H} = \varepsilon_0 c^\dagger c + cc^\dagger \sum_q g_q(a_q + a_q^\dagger) + \sum_q \omega_q a_q^\dagger a_q \,, \tag{1.1}$$

where $c^{(\dagger)}$ is the annihilation (creation) operator of a core electron with energy ε_0, $a^{(\dagger)}$ annihilates (creates) one plasmon with energy ω_q and g_q is the coupling strength between the core hole and plasmon. The plasmon dispersion ω as a function of momentum q can be taken into account with different functions ω_q[4]. This Hamiltonian describes right what I have discussed above, for the case of photoemission of a core electron:

- In the initial state (ground state), there is one core electron with energy ε_0 in the system[5]. Since there is no excitation yet, the number of plasmons is zero which leads to a ground state energy of ε_0.

- The incoming photon excites the system by removing the one core electron, as a consequence all other electrons in the system starts to oscillate, which creates the plasmons. The core hole can couple to these plasmons with coupling strength g_q.

The exact electron removal Green's function (G^h) of this Hamiltonian has been obtained by Langreth [16] from `linked-cluster theorem`[6], which has an exponential expression reading as

$$G^h(\tau) = G_0^h(\tau)e^{C^h(\tau)} \,, \tag{1.2}$$

where $\tau = t_1 - t_2$ with $t_1 < t_2$ and $G_0^h(\tau) = i\theta(-\tau)e^{-i\varepsilon_0\tau}$ is the non-interacting electron removal Green's function which is calculated in the limit of $g_q = 0$ of the quasi-boson Hamiltonian. The function $C^h(\tau)$ will be recognized as the `cumulant function` in section

---

[4]A study of the quasi-boson Hamiltonian with different plasmon dispersion function ω_q can be found in Ref. [30]. In the present thesis, I will mainly study the quasi-boson model Hamiltonian with Einstein boson, i.e. the dispersionless plasmon. Thus the different plasmon dispersion functions ω_q will not be studied.

[5]This energy ε_0 has taken into account the presence of all the electrons in the system, reflecting the fact that the system described by this quasi-boson Hamiltonian contains more than one electron and the effect of all other electrons is to induce an effective potential to determine the orbital energy ε_0. Different values of ε_0 correspond to model the core levels of different systems, and in different approximations.

[6]In the same paper [16], Langreth first obtained the exact Green's function of this quasi-boson Hamiltonian from an exact analytical diagonalization of the Hamiltonian and later proofed that the linked-cluster theorem yields the same result.

2.3. It reads

$$C^h(\tau) = -\sum_q g_q^2 \int \mathrm{d}\omega \frac{W_q(\omega)\left(1 + i\omega\tau - e^{i\omega\tau}\right)}{\omega^2}. \tag{1.3}$$

Here W_q is the exact plasmon propagator of the quasi-boson Hamiltonian which is nothing else than the exact screened interaction of the quasi-boson Hamiltonian, which reads

$$iW_q(t_1 - t_2) = \langle\psi_0|\mathbb{T}\hat{\phi}_q(t_1)\hat{\phi}_q^\dagger(t_2)|\psi_0\rangle = \theta(t_1 - t_2)e^{-i\omega_q(t_1-t_2)} + \theta(t_2 - t_1)e^{i\omega_q(t_1-t_2)}, \tag{1.4}$$

where $\hat{\phi}_q = a_q + a_q^\dagger$ is the boson field operator. The exact Green's function in equation (1.2) leads to a spectral function. Neglecting the plasmon dispersion (i.e., with $\omega_q \equiv \omega_p =$ constant) it reads

$$A(\omega) = \sum_{n=0}^{\infty} \frac{e^{-\beta}\beta^n}{n!}\delta(\omega - \varepsilon_0 - \omega_p\beta + n\omega_p), \tag{1.5}$$

where $\beta = \sum_q \dfrac{g_q^2}{\omega_p^2}$, and ω_p is the plasmon energy. This spectral function Eq. (1.5) is shown in Fig. 1.6. It shows a strong QP peak at energy $\varepsilon_0 + \beta\omega_p$ with normalized weight $\mathbf{Z} = e^{-\beta}$ as well as a series of plasmon satellites at $\varepsilon_0 + \beta\omega_p - n\omega_p$ with weight decreasing as a Poisson distribution. Thus the total spectral weight is conserved, i.e. $\int A(\omega)\mathrm{d}\omega = 1$. The blue arrow labeled ε_0 represents the δ-peak that we would obtain in the non-interacting limit $g_q = 0$. Therefore the coupling induces a shift of the QP peak together with a series of plasmon satellites. The exact spectral function in Fig. 1.6 is consistent with our analysis of the PES process, except for the fractional occupation numbers, since this Hamiltonian is built for studying core photoemission, where the occupation number is either 0 or 1. The validity of using this picture also for the valence states will be discussed in the following chapters.

Despite its simplicity, the quasi-boson Hamiltonian has drawn a lot of attention for the understanding of photoemission and plasmon excitations in a many-body system. It simplifies the PES process dramatically but keeps much important physics. It has brought
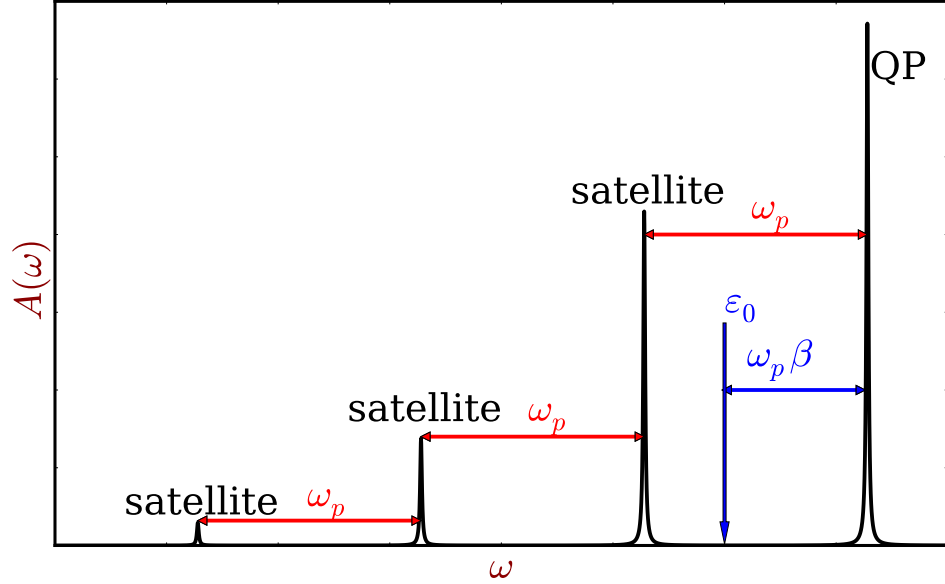
Figure 1.6: The spectral function Eq. (1.5) of the quasi-boson model Hamiltonian. The strong peak labeled QP represents the QP peak of energy $\varepsilon_0 + \omega_p \beta$ and renormalized weight $\mathbf{Z} = e^{-\beta}$. All the other peaks are the plasmon satellites and the energy difference between peaks is the plasmon energy ω_p. The blue arrow labeled ε_0 represents the position of the δ-peak that we would obtain in the case of $g_q = 0$, i.e. the non-interacting limit.

us a great deal of insight to improve our understanding. The correct description of fermion-plasmon coupling by the spectral function of this Hamiltonian was later acknowledged and summarized by several works e.g., Refs. [31–34]. In particular, the exponential expression of the exact Green's function (see Eq. (1.2)) from this Hamiltonian is the motivation of the `cumulant expansion approximation` (CEA) that is the central approximation I am going to discuss in this thesis.

Since the idea of this thesis can also be traced back to this Hamiltonian, detailed calculations can be found in section 4.1.1 together with a generalized two-level hole-plasmon coupling model Hamiltonian which is supposed to be able to model both core and valence photoemission processes. Several related works, namely the TOC96 [9], TOC11 [11] and the retarded cumulant (RC) [19] will be studied in the following chapters. In particular the most popular CEA by Aryasetiawan, Hedin and Karlsson (i.e. TOC96 [9]) and a version

developed in our group (i.e. TOC11 [11]) will be discussed in detail in section 2.3.1 and section 3.3, respectively.

1.1.2 Theoretical approach to photoemission spectroscopy

Up to now, we have seen what happens in the photoemission process and which results are expected to be given by a PES experiment. To describe this process theoretically is not so easy, because the observed results of a photoemission measurement contain more than just one incoming photon and one outgoing electron. In principle, there is a complicated process of excitation of two particles with their mutual interaction and interaction with all system particles, the electron traveling through the system and the surface until captured by the detector, coupling to phonons, a secondary electron background, *etc.* (see e.g., Ref. [24] for some discussion). It is desirable to treat the main effects at least approximately, which suggests to interpret the PES as a *three-step* process as proposed by Berglund and Spicer [35]:

1. First an electron is excited by the incoming photon and leaves its original position such that a hole is left behind that can propagate in the system. If the photoelectron is measured right after this step, (i.e. we neglect entirely the propagation of the photoelectron from its original position to the detector and take into account only the propagation of the hole and the interactions in the $N-1$ electron system) we will get the so-called `intrinsic` spectrum $A(\omega)$.

2. After excitation, the photoelectron can travel in the system, interact with the hole left behind, which leads to the so called `interference effect`. Moreover, the photoelectron can interact with all remaining $N-1$ electrons in the system until it arrives at the surface. The energy loss of the photoelectron in this process is called `extrinsic loss`.

3. The final step is the photoelectron leaves the surface of the system and travels to the energy analyzer when the electron kinetic energy is measured. The energy loss in this process also contributes to the `extrinsic loss`.

As a result, the photoemission intensity is the product of the possibilities of these three steps including the extrinsic and interference effect (see Ref. [36] for a more detailed discussion). In order to concentrate on the most important effect in PES, which we usually call the `intrinsic` electronic properties, one can isolate the first step by assuming that the photoelectron once excited by the photon, does not interact with the hole nor lose its energy on the way to the energy analyzer. This assumption is the so-called `sudden approximation` [37].

In a PES experiment, what is measured is actually the electric current induced by the photoelectron passing through the analyzer, which is called the `photocurrent`. The measured photocurrent $J_{\boldsymbol{k}}(\omega)$ is given by the probability of emitting an electron with momentum $\boldsymbol{k}$ per unit time when the sample is irradiated with the photon energy ω. The exact expression of $J_{\boldsymbol{k}}(\omega)$ in `Fermi's golden rule` [33] reads

$$J_{\boldsymbol{k}}(\omega) = \sum_{s} \left| \langle N-1, s; \boldsymbol{k} | \hat{\Delta} | N \rangle \right|^2 \delta(E_{\boldsymbol{k}} - E_s - \omega), \qquad (1.6)$$

where $|N\rangle$ and $|N-1, s; \boldsymbol{k}\rangle$ are the initial and final states of the system, respectively, s labels the possible excitations of the system and $\hat{\Delta}$ is the dipole transition operator that represents the coupling of the sample to the photon field. Due to the perturbation of the photon field, the system of N electrons in an initial state $|N\rangle$ goes to a final state $|N-1, s; \boldsymbol{k}\rangle$ composed of $N-1$ electrons in an excited state s and one photoelectron with momentum $\boldsymbol{k}$[7]. $E_{\boldsymbol{k}}$ is the kinetic energy of the photoelectron and $E_s = E_0^N - E_s^{N-1}$ is the energy difference of the sample before and after photoemission (see the definition of E_s^h in Eq. (1.20)). The total energy is conserved by the δ-function because the photon energy must equal the sum of the kinetic energy of the photoelectron and the excitations in the sample leading to $\omega = E_{\boldsymbol{k}} - E_0^N + E_s^{N-1}$. Therefore by measuring the energies of incoming photon and outgoing photoelectron, one can access information about excitations in the sample.

---

[7]In this picture, there are N electrons for both initial and final states but keep in mind that the reason why the final state contains N electrons is because we are taking into account the one photoelectron. In the sudden approximation this photoelectron can be considered as an electron outside of the sample (see Eq. (1.8)). Therefore there are $N-1$ electrons in the sample with all possible excitations $|N-1, s\rangle$.

The dipole transition operator in `second quantization` reads

$$\hat{\Delta} = \sum_{i,j} \hat{\Delta}_{ij} c_i^{\dagger} c_j \, , \tag{1.7}$$

where $c^{(\dagger)}$ is the fermion annihilation (creation) operator. In the sudden approximation, the photoelectron is considered completely decoupled from the sample after excitation, such that the final state can be simplified as a product

$$|N - 1, s; \boldsymbol{k}\rangle = c_{\boldsymbol{k}}^{\dagger} |N - 1, s\rangle \, . \tag{1.8}$$

If we further assume that there is no contribution of the photoelectron at the ground state, i.e., $c_{\boldsymbol{k}} |N\rangle \equiv 0$, we can write

$$\langle N - 1, s | c_{\boldsymbol{k}} \sum_{i,j} \hat{\Delta}_{ij} c_i^{\dagger} c_j | N \rangle = \sum_j \hat{\Delta}_{\boldsymbol{k}j} \langle N - 1, s | c_j | N \rangle \, . \tag{1.9}$$

Finally the photocurrent reads

$$J_{\boldsymbol{k}}(\omega) = \sum_s \left| \sum_j \hat{\Delta}_{\boldsymbol{k}j} \langle N - 1, s | c_j | N \rangle \right|^2 \delta(E_{\boldsymbol{k}} - E_s - \omega) \, . \tag{1.10}$$

It is now convenient to introduce matrix elements of the spectral function $A_{ij}(\omega)$, which will be discussed in detail in section 1.2 (see Eq. (1.29)). For the electron removal, they read

$$A_{ij}(\omega) = \sum_s \langle N | c_j^{\dagger} | N - 1, s \rangle \, \langle N - 1, s | c_i | N \rangle \, \delta(\omega - E_s) \, . \tag{1.11}$$

This leads to the expression of the photocurrent in terms of the spectral function

$$J_{\boldsymbol{k}}(\omega) = \sum_{i,j} \hat{\Delta}_{\boldsymbol{k}i} A_{ij}(E_{\boldsymbol{k}} - \omega) \hat{\Delta}_{j\boldsymbol{k}} \, . \tag{1.12}$$

If we suppose to work in a basis where the spectral function is diagonal, i.e. $A_{ij}(\omega) \equiv A_{ij}(\omega)\delta_{ij}$, we have

$$J_{\boldsymbol{k}}(\omega) = \sum_i \left|\hat{\Delta}_{\boldsymbol{k}i}\right|^2 A_{ii}(E_{\boldsymbol{k}} - \omega) \,. \tag{1.13}$$

Often one supposes the dipole matrix element to be constant when estimating the photocurrent. In that case, the intensity of the spectrum is the product of the trace of the spectral function and the dipole matrix element, which depends on the energy, momentum and polarization of the incoming photon. Therefore there is a direct link between the photocurrent measured in the experiment and the intrinsic spectral function. An example of the intrinsic spectral function from the cumulant expansion approximation is shown in the left panel of Fig. 1.5 where the blue dashed curve labeled as *cumulant* corresponds to $\sum_i \hat{\Delta}_{\boldsymbol{k}i} A_{ii}(\omega)$ in Eq. (1.13) where $E_{\boldsymbol{k}}$ has been taken as the experimental value. The red curve in that figure labeled as *total* represents the spectrum beyond the sudden approximation where the extrinsic and interference effect are calculated approximately (this plot is provided by my co-author J. Kas in Ref. [20]). The comparison between the intrinsic (blue dashed) and the total (red) spectrum confirms our assumption that the intrinsic spectrum $A(\omega)$ is the dominant part of the photocurrent measured from the experiment in the sense that the extrinsic and interference effects change only the intensities of the spectrum, not its main structures. In this thesis the intrinsic spectral function $A(\omega)$ will be a main target to be calculated. The calculation of the extrinsic and interference effects can be performed as a post process in order to bring the theoretical results close to a realistic description of an experimental spectrum.

1.2   Green's function theory

In this section, I am going to introduce the Green's function theory that is built for describing the propagation of particles (electrons or holes). In particular, the imaginary part of the one-body Green's function gives the intrinsic spectral function $A(\omega)$, which as we have seen above, has a direct link to the photoemission spectrum measured in the experiment.

1.2.1 Definition of the one-body Green's function

In order to describe photoemission spectroscopy, we need a good description of the propagation of electrons or holes. This job can be done by the one-body Green's function. At zero temperature and in equilibrium, the time-ordered one-body Green's function is defined as [1, 2]

$$G(1,2) \equiv -i \left\langle \Psi_0^N \left| \mathbb{T}\left[\hat{\psi}_H(1)\hat{\psi}_H^\dagger(2)\right] \right| \Psi_0^N \right\rangle. \tag{1.14}$$

Here and throughout the thesis, we always use atomic units ($\hbar = e^2 = m_e = 1$). In this definition, index (1), for the sake of compactness, includes the space, spin, and time variables: $(1) = (x_1, t_1) = (\boldsymbol{r}_1, \sigma_1, t_1)$[8]. The N-particle ground state wavefunction of the system is denoted by $\left|\Psi_0^N\right\rangle$[9]. The field operator in the `Heisenberg picture`[10] that annihilates (creates[11]) one particle at space, time and spin (1) is given by $\hat{\psi}_H(1)$ ($\hat{\psi}_H^\dagger(1)$). $\mathbb{T}$ is the time-ordering operator, which places the field operators with earlier time on the right.

If we write out the time-ordering operator using the Heaviside step function, we can express the time-ordered one-body Green's function as:

$$G(1,2) = -i\theta(t_1 - t_2)\left\langle \Psi_0^N \left| \hat{\psi}_H(1)\hat{\psi}_H^\dagger(2) \right| \Psi_0^N \right\rangle + i\theta(t_2 - t_1)\left\langle \Psi_0^N \left| \hat{\psi}_H^\dagger(2)\hat{\psi}_H(1) \right| \Psi_0^N \right\rangle$$

$$\equiv \theta(t_1 - t_2)G^> + \theta(t_2 - t_1)G^< \equiv G^e(12) + G^h(12), \tag{1.15}$$

---

[8]The spin will not be treated explicitly because we do not treat a spin-polarized system in this thesis. Nevertheless, the spin is not neglected since it is always present in the derivations.

[9]This notation has the same meaning as $|N\rangle$ to represent the N-electron ground state. I change the notation in this section for the sake of compactness because I will use $\left|\Psi_s^{N\pm1}\right\rangle$ to represent the excited state of the $N \pm 1$ electron system, instead of $|N \pm 1, s\rangle$.

[10]There are three pictures, namely the Heisenberg $\hat{\psi}_H(x,t)$, Schrödinger $\hat{\psi}(x)$ and interaction (Dirac) $\hat{\psi}_D(x,t)$ pictures, which can be transformed between each other. For simplicity I do not write the subindex S for the field operator in the Schrödinger picture since the quantities in that picture do not depend on time, hence it is easy to distinguish.

[11]For historical reason, I use the name "creation" for the operators who actually add a particle to the system. In general, one cannot create particles thus there is argument of changing it into "addition".

in which $G^e(1,2)$ and $G^h(1,2)$ are the so-called `electron` and `hole` Green's functions, $G^>$ and $G^<$ are the `greater` and `lesser` components defined as

$$G^>(1,2) = -i \left\langle \Psi_0^N \middle| \hat{\psi}_H(1)\hat{\psi}_H^\dagger(2) \middle| \Psi_0^N \right\rangle ; \qquad (1.16a)$$

$$G^<(1,2) = i \left\langle \Psi_0^N \middle| \hat{\psi}_H^\dagger(2)\hat{\psi}_H(1) \middle| \Psi_0^N \right\rangle ; \qquad (1.16b)$$

and $\theta(t)$ is the Heaviside step function defined as

$$\theta(t) = \begin{cases} 1 & \text{for } t > 0 ; \\ 0 & \text{for } t < 0 . \end{cases}$$

The one-body Green's function expresses the probability amplitude for one electron (hole) which at time t_2 (t_1) is added to the system (in its ground state) in space r_2 (r_1) with spin σ_2 (σ_1) to be found at r_1 (r_2) with spin $\sigma_1(\sigma_2)$ at a time $t_1 > t_2$ $(t_2 > t_1)$. For this reason, the Green's function of $t_1 > t_2$ is often called the `electron` Green's function G^e and its time-reversal counterpart $(t_2 > t_1)$ is called the hole Green's function G^h. The one-body Green's function carries all the information when one particle propagates in a given system. Therefore we can calculate the ground state expectation value of any single-particle operator of such system, e.g. the ground state density $\rho(1) = -iG^<(1,1^+)$ where 1^+ stands for $(x_1, t_1 + \eta)$[12]. Moreover, we can calculate the ground state energy of the system using the *Galitskii-Migdal formula* [38] although the Hamiltonian is not a single-particle operator. The discussion about total energies can be found in Chapter 7. Besides the ground state properties, the one-body Green's function can provide us with the single particle excitation spectra, which will be shown from its Lehmann representation later in this section.

1.2.2   The Lehmann representation and the intrinsic spectral function

The direct link between the one-body Green's function and the (I)PES experiments cannot be seen yet from the definition Eq. (1.14). Here we are going to write the one-body Green's

---

[12]The ground state density $\rho(1) \equiv -i \left\langle \Psi_0^N \middle| \hat{\psi}_H^\dagger(1)\hat{\psi}_H(1) \middle| \Psi_0^N \right\rangle$, which is nothing else than the diagonal lesser component of the one-body Green's function. Here (1^+) stands for $(x_1, t_1 + \eta)$ where $\eta \to 0^+$ is an infinitesimal positive number.

function in its *Lehmann representation*, from which we will see how we can get the (I)PES intrinsic spectra from the one-body Green's function.

The Lehmann representation of the one-body Green's function

In order to derive the Lehmann representation, we first have to transform the field operator from Heisenberg to Schrödinger picture using the following identity:

$$\hat{\psi}_H^{(\dagger)}(x,t) = e^{i\hat{H}t}\hat{\psi}^{(\dagger)}(x)e^{-i\hat{H}t} \,, \tag{1.17}$$

where $\hat{H}$ is the many-body time-independent Hamiltonian we are going to treat and $\hat{\psi}^{(\dagger)}(x)$ are the field operators in Schrödinger picture. Plugging Eq. (1.17) into the definition of the Green's function in equation (1.14), we get

$$iG(1,2) = \theta(t_1 - t_2)e^{iE_0^N(t_1-t_2)}\langle\Psi_0^N|\hat{\psi}(x_1)e^{-i\hat{H}(t_1-t_2)}\hat{\psi}^\dagger(x_2)|\Psi_0^N\rangle$$
$$- \theta(t_2 - t_1)e^{iE_0^N(t_2-t_1)}\langle\Psi_0^N|\hat{\psi}^\dagger(x_2)e^{-i\hat{H}(t_2-t_1)}\hat{\psi}(x_1)|\Psi_0^N\rangle \,. \tag{1.18}$$

We have used the identity $e^{i\hat{H}t}\left|\Psi_0^N\right\rangle = e^{iE_0^Nt}\left|\Psi_0^N\right\rangle$ in the above equation where E_0^N is the N-particle ground state energy. Now it becomes obvious that the one-body Green's function will only depend on the time difference $\tau = t_1 - t_2$, if the Hamiltonian is time-independent (i.e., an equilibrium Hamiltonian without time-dependent external potential) that is the main interest of this thesis. Now we introduce the completeness relation in *Fock space*

$$1 = |0\rangle\langle0| + \sum_s \left|\Psi_s^1\right\rangle\left\langle\Psi_s^1\right| + \cdots + \sum_s \left|\Psi_s^N\right\rangle\left\langle\Psi_s^N\right| + \cdots \tag{1.19}$$

where $\sum_s |\Psi_s^N\rangle$ represents the eigenfunctions of a N-particle system and s labels different states[13]. When one inserts the above equation into the Green's function in Schrödinger picture (1.18), for $t_1 > t_2$ the only term that is nonzero is $\sum_s \left|\Psi_s^{N+1}\right\rangle\left\langle\Psi_s^{N+1}\right|$ while for

---

[13]Note that when $s = 0$, it represents the N particle ground state. The increase of s follows the increase of the corresponding eigenvalues E_s^N.

$t_1 < t_2$ the nonzero term is $\sum_s |\Psi_s^{N-1}\rangle \langle \Psi_s^{N-1}|$. Thus we have

$$iG(x_1, x_2, \tau) = \theta(\tau) \sum_s e^{-iE_s^e \tau} \langle \Psi_0^N | \hat{\psi}(x_1) | \Psi_s^{N+1} \rangle \langle \Psi_s^{N+1} | \hat{\psi}^\dagger(x_2) | \Psi_0^N \rangle$$
$$- \theta(-\tau) \sum_s e^{-iE_s^h \tau} \langle \Psi_0^N | \hat{\psi}^\dagger(x_2) | \Psi_s^{N-1} \rangle \langle \Psi_s^{N-1} | \hat{\psi}(x_1) | \Psi_0^N \rangle , \qquad (1.20)$$

where we have defined $\tau \equiv t_1 - t_2$, the electron addition energy $E_s^e = E_s^{N+1} - E_0^N$ and electron removal energy $E_s^h = E_0^N - E_s^{N-1}$. After a Fourier transform (the equations for the Fourier transform can be found in Appendix Eq. (A.1)) of the above equation and using the differential representation of the Heaviside step function (see Appendix Eq. (A.2)), we arrive at the final Lehmann representation of the one-body time-ordered Green's function in frequency space, which reads

$$G(x_1, x_2, \omega) = \sum_s \frac{f_s(x_1) f_s^*(x_2)}{\omega - E_s^e + i\eta} + \sum_s \frac{g_s(x_1) g_s^*(x_2)}{\omega - E_s^h - i\eta} . \qquad (1.21)$$

Here and throughout the thesis $\eta \to 0^+$ which comes from the differential representation of the Heaviside step function. Its sign distinguishes between the hole propagation $(-i\eta)$ and electron propagation $(+i\eta)$. I have introduced the Lehmann amplitudes defined as

$$f_s(x) = \langle \Psi_0^N | \hat{\psi}(x) | \Psi_s^{N+1} \rangle ; \qquad (1.22a)$$

$$g_s(x) = \langle \Psi_s^{N-1} | \hat{\psi}(x) | \Psi_0^N \rangle , \qquad (1.22b)$$

to simplify the nominator. Now we analyze the physical meaning of the poles of the Green's function in equation (1.21):

$$E_s^e = \left(E_s^{N+1} - E_0^{N+1} \right) + \left(E_0^{N+1} - E_0^N \right) = E(N+1, s) + \mathcal{A} ; \qquad (1.23a)$$

$$E_s^h = -\left(E_s^{N-1} - E_0^{N-1} \right) + \left(E_0^N - E_0^{N-1} \right) = -\mathcal{I} - E(N-1, s) , \qquad (1.23b)$$

where $E(N \pm 1, s) \equiv E_s^{N\pm 1} - E_0^{N\pm 1}$ is the energy difference between the s-th excited state and the ground state of a $N\pm 1$ electron system[14]. I have used the definition of the `electron`

---

[14]Note that, all the energies appearing in the Green's function are real valued quantities.

affinity $\mathcal{A} \equiv E_0^{N+1} - E_0^N$ and `ionization energy` $\mathcal{I} \equiv E_0^{N-1} - E_0^N$, which represent the ground state energy difference between $N \pm 1$ and N electron systems, respectively. We further introduce the `chemical potential` μ^{15} that stays between the ionization energy and electron affinity. The poles of the one-body Green's function are exactly the excitation energies of electron removal and electron addition as shown schematically in Fig. 1.7.
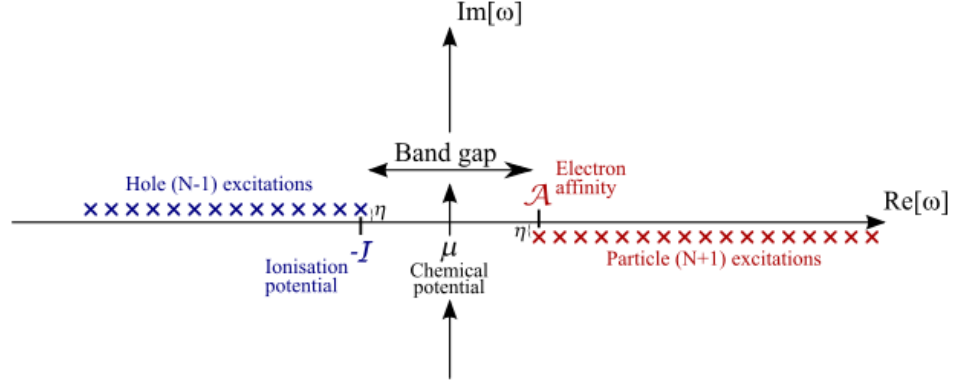
Figure 1.7: Schematical representation of the position of the poles of the time-ordered one-body Green's function. The figure is taken from `http://www.abinit.org/doc/helpfiles/for-v7.10/tutorial/theory_mbt.html`.

The spectral function of the one-body Green's function

The spectral function or density of states (DOS) $A(\omega)$ is proportional to the imaginary part of one-body Green's function. Thus from equation (1.21) using the *Cauchy principle value* identity (or *Kramers-Kronig* relation shown in Appendix (A.3)):

$$\frac{1}{\omega - \varepsilon \pm i\eta} \equiv \mathcal{P}\frac{1}{\omega - \varepsilon} \mp i\pi\delta(\omega - \varepsilon)\,, \tag{1.24}$$

where $\mathcal{P}$ represents the principle value, we have

$$A(x_1, x_2, \omega) \equiv -\frac{1}{\pi} \operatorname{Im} G(x_1, x_2, \omega) \operatorname{sgn}(\omega - \mu)$$
$$= \sum_s f_s(x_1)f_s^*(x_2)\delta(\omega - E_s^e) + \sum_s g_s(x_1)g_s^*(x_2)\delta\left(\omega - E_s^h\right)\,. \tag{1.25}$$

---

[15]At zero temperature that is of our interest, the chemical potential μ is equivalent to the Fermi energy.

One can show that the spectral function follows some important *sum rules*, in particular:

$$\int_{-\infty}^{\infty} d\omega \, A(x_1, x_2, \omega) = \delta(x_1, x_2) \, ; \tag{1.26a}$$

$$\int_{-\infty}^{\mu} d\omega \, A(x, x, \omega) = \rho(x) \, . \tag{1.26b}$$

We will name the first sum rule in Eq. (1.26a) as the `conservation of spectral weight` throughout this thesis. The second one in Eq. (1.26b) yields the `conservation of particle number` because the integration of the ground state density $\rho(x)$ over x yields the total particle number N (i.e. $\int \rho(x) dx = N$) in a given system.

Green's function and spectral function in a discrete basis

We have been talking about the Green's function in real space before, but in practice we always work on some discrete basis (e.g., site basis or orbital basis *etc.*). The field operator can be written in some arbitrary basis defined by the basis functions φ_i as

$$\hat{\psi}(x) = \sum_i c_i \varphi_i(x) \, ; \tag{1.27a}$$

$$\hat{\psi}^\dagger(x) = \sum_j c_j^\dagger \varphi_j^*(x) \, . \tag{1.27b}$$

The Green's function in such a basis is a matrix for which the matrix elements can be written as

$$G_{ij}(\omega) \equiv \langle i | G(\omega) | j \rangle = \int dx_1 x_2 \varphi_i^*(x_1) G(x_1, x_2, \omega) \varphi_j(x_2)$$

$$= \sum_s \frac{\langle \Psi_0^N | c_i | \Psi_s^{N+1} \rangle \langle \Psi_s^{N+1} | c_j^\dagger | \Psi_0^N \rangle}{\omega - E_s^e + i\eta} + \sum_s \frac{\langle \Psi_0^N | c_j^\dagger | \Psi_s^{N-1} \rangle \langle \Psi_s^{N-1} | c_i | \Psi_0^N \rangle}{\omega - E_s^h - i\eta} \, . \tag{1.28}$$

This Lehmann representation of the Green's function in a certain basis will be used in section 4.1 to calculate the exact Green's function of the hole-plasmon coupling Hamiltonian. The above formula tells us what is in principle needed to calculate a Green's function.

Suppose we want to calculate the electron removal Green's function G^h: we fist have to find a complete basis of Slater determinants ϕ_α for N and $N-1$ electron systems built with the single particle orbital ϕ_i, then we have to diagonalize the Hamiltonian in such a basis (i.e., diagonalize the matrix $\langle \phi_\alpha | \hat{H} | \phi_\beta \rangle$) and find the eigenvalues (E_0^N and E_s^{N-1}) and eigenfunctions ($|\Psi_0^N\rangle$ and $|\Psi_s^{N-1}\rangle$) of these two matrices. In particular, the lowest eigenvalue E_0^N and eigenfunction $|\Psi_0^N\rangle$ are the ground state energy and wavefunction of the N electron system.

The spectral function in such a basis becomes

$$A_{ij}(\omega) = \sum_s \langle \Psi_0^N | c_i | \Psi_s^{N+1} \rangle \langle \Psi_s^{N+1} | c_j^\dagger | \Psi_0^N \rangle \delta(\omega - E_s^e)$$
$$+ \sum_s \langle \Psi_0^N | c_j^\dagger | \Psi_s^{N-1} \rangle \langle \Psi_s^{N-1} | c_i | \Psi_0^N \rangle \delta(\omega - E_s^h). \qquad (1.29)$$

Note that the second line of the above equation is identical to the spectral function in equation (1.11). An important property of the spectral function that can be seen from the above equation: the excitation energy E_s is independent of the matrix index, i.e. all the matrix elements of the spectral function should have the poles at the same position. This important property is referred to as the `constraint of poles` throughout this thesis.

1.3 Summary

In this chapter, I have introduced photoemission spectroscopy and its physical picture, and in particular, the physical concepts of the quasi-particles and plasmons. In order to describe photoemission spectroscopy from theory, the one-body Green's function has been introduced. Its imaginary part is the spectral function, which has a direct link to the spectrum measured in photoemission spectroscopy. In this way, a fundamental relation between experiment and theory of PES has been established. We understand that the central quantity we need to obtain is the one-body Green's function. Moreover, I have emphasized some important phenomena that should appear in photoemission spectroscopy, as well as some exact constraints of the one-body Green's function or analogously its spectral function. These are the following:

1. **The quasi-particle excitation:** The main excitation in a photoemission spectrum usually is a quasi-particle excitation, which in principle should have a fractional renormalization factor **Z**, because the QP loses weight towards other excitations. In addition, the QP excitation should have a finite lifetime leading to a broadening of the QP peak in the spectrum.

2. **The satellite replica:** Besides the QP excitations, neutral excitations such as plasmons can be seen in photoemission spectroscopy. They appear as satellites in the spectrum. Due to the bosonic nature of neutral excitations, the satellites should have replica at a distance of the energy of the neutral excitation.

3. **Partial occupation number close the Fermi level:** Due to the many-body interactions, in a system with a small band gap, the states close to the top valence can be partially occupied.

4. **Conservation of particle number:** The spectral function should conserve the particle number, i.e. $\sum_{k} \int_{-\infty}^{\mu} \mathrm{d}\omega A_k(\omega) = N$ where k labels the states in the basis function where the spectral function A is diagonal, and N is the total particle number of the system.

5. **Conservation of spectral weight:** The integration of the spectral function should be normalized to unity, i.e. $\int_{-\infty}^{\infty} \mathrm{d}\omega A_k(\omega) = 1$.

6. **Constraint of poles:** The pole position of the one-particle Green's function is independent of the matrix elements, due to equation (1.29).

The properties (3-6) are in principle exact such that we should be able to observe all of them in the calculated spectra. However, whenever approximations (e.g., the GWA or CEA) are involved, some of the above properties might be violated. Thus the aim of this thesis is to look for an improved description of photoemission spectroscopy using a Green's function approach that fulfills the important constraints.

Chapter 2

State-of-the-art theories in electron spectroscopy

In this chapter, I will review the state-of-the-art methods in electron spectroscopy starting from the well developed density functional theory (DFT). I mainly focus on the Kohn-Sham formalism of DFT (KS-DFT) as the starting point, in particular the local-density approximation (LDA) from which we can get the ingredients for calculating the one-particle Green's function with good approximations e.g., the `GW` approximation (GWA) and cumulant expansion approximation (CEA). The derivations of the GW approximation and one of the cumulant expansion approximations will be shown in this chapter, together with the corresponding spectral functions to illustrate the performance of these approximations. The target of this chapter is to understand the following issues:

- What quantities can be given by different theories?

- How can we link the quantities calculated from different approximations? What is the general process for a realistic calculation using the approximations that are studied in this thesis?

- The advantages and disadvantages of different approximations.

2.1 Density functional theory

In chapter 1, we have seen that the one-particle Green's function (GF) has a direct link with PES or IPES experiments such that it is the central quantity we are going to calculate in this thesis. In this section, I will show how we treat the ground state problem with the Kohn-Sham formalism of density functional theory (KS-DFT). On one side, this allows us to calculate ground state properties such as lattice constants. Most importantly in this thesis, we can get the ingredients for the calculation of Green's functions in the GW approximation and the cumulant expansion approximation from KS-DFT.

2.1.1 The many-body problem

All the information of a many-body system that is described by the many-body Hamiltonian

$$\hat{H} = \sum_i^N \left(-\frac{\nabla_i^2}{2} + V_{ext}(\boldsymbol{r}_i) \right) + \frac{1}{2} \sum_{i \neq j}^N v_c(\boldsymbol{r}_i, \boldsymbol{r}_j) \,, \tag{2.1}$$

is contained in the many-body wavefunction Ψ, which can be found by solving the time-independent Schrödinger equation:[1]

$$\hat{H}\Psi = E\Psi \,. \tag{2.2}$$

This is an eigenvalue problem where the many-body wavefunctions Ψ and energies E are unknown. $V_{ext}(\boldsymbol{r})$ is the external local potential induced by e.g., the presence of nuclei[2]. $v_c(\boldsymbol{r}_i, \boldsymbol{r}_j)$ is the two-particle Coulomb interaction that reads

$$v_c(\boldsymbol{r}_i, \boldsymbol{r}_j) = \frac{1}{|\boldsymbol{r}_i - \boldsymbol{r}_j|} \,, \tag{2.3}$$

where $\boldsymbol{r}_i$ is the position of the i-th electron. To deal with the Hamiltonian Eq. (2.1) has been a major problem in molecular and condensed matter physics. If we could solve the Schrödinger equation (2.2) for such a many-body system, we could in principle get

---

[1]Throughout this thesis, if not otherwise specified, the relativistic effects have been neglected.

[2]All the theories in this thesis are supposing the Born-Oppenheimer approximation [39] in which the motion of nuclei and electrons are decoupled, yielding the fixed ionic positions.

all the properties of the system. However, there are two main problems which make the Hamiltonian (2.1) unsolvable, namely

1. The many-body wavefunction Ψ is a function with $3N$ arguments (each $\boldsymbol{r}$ has three coordinates in 3-dimensions), where N can be of the order of 10^{23}, i.e. Avogadro's number. In practice, the information contained in Ψ is too large to store in any computer, such that we are obliged to look for approximations or different ways to obtain the information of interest from a many-body Hamiltonian like Eq. (2.1).

2. Moreover, the two-body Coulomb interaction term in Eq. (2.1) is a strong interaction at short distance between two electrons and decays slowly with distance (long range interaction), which makes the Schrödinger equation (2.2) extremely difficult to solve. We have to find good approximations to represent the effects of the many-body Coulomb interaction as well as possible.

For these reasons, the Schrödinger equation (2.2) is at the same time exactly known and too complicated to be solvable. It is one of the big challenges of theoretical condensed matter physics to find alternative ways to deal with a many-body Hamiltonian like (2.1). One of the successfully alternative ways is density functional theory (DFT) where the fundamental quantity of interest is the density $\rho(\boldsymbol{r})$ of the many-body system instead of the wavefunction Ψ, which simplifies the computations dramatically.

Density functional theory is based on the Hohenberg-Kohn theorem [8] which states:

• There exists a universal functional $F[\rho_s]^3$ that enables the one-to-one mapping between a ground state observable and the total electronic density ρ_s of the system such that the only quantity we need to know is the density instead of the many-body wavefunction if we knew this functional.

• The ground state density ρ (when $s = 0$) minimizes the total energy.

With the first statement of Hohenberg-Kohn theorem, we can write the ground state expectation value of any operator as a functional of the density. In particular, the energy

---

[3]I use the symbol ρ_s to represent the density of a general system for either ground state density (when $s = 0$) $\rho_{s=0} \equiv \rho$, or the excite state density where $s \neq 0$.

functional can be written as

$$E[\rho_s] = \langle \Psi_0[\rho_s] | \hat{H} | \Psi_0[\rho_s] \rangle = F[\rho_s] + \int d\boldsymbol{r} \rho_s(\boldsymbol{r}) V_{ext}(\boldsymbol{r}), \tag{2.4}$$

where $\hat{H}$ is the many-body Hamiltonian in Eq. (2.1) and $F[\rho_s]$ is the universal functional of the density in the sense that it does not depend on the external potential V_{ext}[4]. The second statement of the Kohenberg-Kohn theorem tells that the ground state density ρ (when $s = 0$) minimizes the total energy such that we have

$$E[\rho] = F[\rho] + \int d\boldsymbol{r} \rho(\boldsymbol{r}) V_{ext}(\boldsymbol{r}) < E[\rho_s], \tag{2.5}$$

with $\rho(\boldsymbol{r}) \neq \rho_s(\boldsymbol{r})$. In DFT, all the unknown is still contained in the universal density functional $F[\rho_s]$, thus although it provides us a way to deal with the many-body Hamiltonian, it does not provide us any practical way to determine this universal functional. This suggests to the introduce of the Kohn-Sham formalism of DFT[5].

2.1.2 Kohn-Sham DFT

The big advantage of DFT compared with the wavefunction based methods is its emphasis of the electronic density, which is a much simpler quantity (with only 3 arguments) than the many-body wavefunction that has $3N$ arguments. However, the functional $F[\rho_s]$ is not known. The only known part is the classical electrostatic contribution, the Hartree potential energy $E_H[\rho_s] = \frac{1}{2} \int d\boldsymbol{r}\boldsymbol{r}' \frac{\rho_s(\boldsymbol{r})\rho_s(\boldsymbol{r}')}{|\boldsymbol{r} - \boldsymbol{r}'|}$. A large contribution to the unknown remainder is given by the kinetic energy $T[\rho_s]$. The idea of Kohn and Sham [44] was to describe exactly the non-interacting kinetic energy $T_{IP}[\rho_s]$. They stated that it is possible to define an independent-particle system described by a Hamiltonian $\hat{H}^{ks}$ with an effective potential (the Kohn-Sham potential $V_{ks}(\boldsymbol{r})$) that has exactly the same density as the system with

---

[4]If $F[\rho_s]$ depended on V_{ext}, it would become a system-dependent functional instead of a universal functional.

[5]Many books (e.g. [40]) and reviews (e.g. [41] and [42]) have been written on DFT and it has been well developed as a ground state theory in many *ab-initio* computational codes (e.g., ABINIT code [43]). Since in my thesis, DFT only serves as a starting point for calculating the electronic excitation properties, I will not spend too much time on it. If the reader is interested more in DFT, I suggest to read for example Refs. [40–42].

full interactions. In this non-interacting system, the kinetic energy can be expressed in terms of one electron orbitals. This finally provides us with a practical way to apply the Hohenberg-Kohn theorem in real systems. In the Kohn-Sham (KS) system, the ground state density is defined as

$$\rho(\boldsymbol{r}) = \sum_i^N |\psi_i(\boldsymbol{r})|^2 \,. \tag{2.6}$$

Here $\psi_i(\boldsymbol{r})$ is the independent-particle wavefunction that is also called Kohn-Sham orbital. It can be calculated from the Kohn-Sham equation

$$\hat{H}^{ks}(\boldsymbol{r}) = -\frac{\nabla_i^2}{2} + V_{ks}(\boldsymbol{r}) \,; \tag{2.7a}$$

$$\left(-\frac{\nabla_i^2}{2} + V_{ks}(\boldsymbol{r})\right)\psi_i(\boldsymbol{r}) = \mathcal{E}_i\psi_i(\boldsymbol{r}) \,, \tag{2.7b}$$

where $\mathcal{E}_i$ is the Kohn-Sham eigenenergy[6]. The Kohn-Sham potential V_{ks} contains three parts:

$$V_{ks}(\boldsymbol{r}) = V_{ext}(\boldsymbol{r}) + V_H(\boldsymbol{r}) + V_{xc}(\boldsymbol{r}) \,, \tag{2.8}$$

where the Hartree potential $V_H(\boldsymbol{r}) = \int d\boldsymbol{r}' \frac{\rho(\boldsymbol{r}')}{|\boldsymbol{r} - \boldsymbol{r}'|}$ is an average potential induced by all the electrons in the system. The last term of the above equation, V_{xc}, known as the exchange-correlation potential, contains all the remaining interactions[7] and it is defined as

$$V_{xc}(\boldsymbol{r}, [\rho_s]) = \frac{\delta E_{xc}[\rho_s]}{\delta \rho_s(\boldsymbol{r})}\bigg|_{\rho_s(\boldsymbol{r})=\rho(\boldsymbol{r})} \,. \tag{2.9}$$

Here $E_{xc}[\rho_s]$ is the exchange-correlation energy functional where all the unknown contributions are hidden, since by definition

$$E[\rho_s] = T_{ks}[\rho] + V_H[\rho] + E_{xc}[\rho_s] + \int d\boldsymbol{r} V_{ext}(\boldsymbol{r})\rho(\boldsymbol{r}) \,, \tag{2.10}$$

---

[6]Note that, the Kohn-Sham eigenvalues do not have a physical meaning except the highest occupied eigenvalue $\mathcal{E}_N$ that is equal to the ionization energy ($\mathcal{I}$) of the system [45]. Therefore strictly speaking, the Kohn-Sham eigenvalues are not the excitation energies.

[7]There is no universal definition of correlation, but a general agreement is that exchange-correlation is everything beyond the Hartree approximation.

where $T_{ks}[\rho]$ is the kinetic energy of the Kohn-Sham system. Compared to the Hohenberg-Kohn expression in equation (2.4), the advantage of the Kohn-Sham formalism is that it has removed the non-interacting kinetic energy and Hartree energy from the functional $F[\rho_s]$ and left the smaller part $E_{xc}[\rho_s]$ as unknown. Until this point, all the complicated many-body interactions are hidden in $E_{xc}[\rho_s]$ and there is no known expression for it. To find good approximations of $E_{xc}[\rho_s]$ has been a major task in the field of DFT and over last half century, many different approximations of $E_{xc}[\rho_s]$ have been developed [40], among which the first and still one of the most popular approximations is called the local-density approximation (LDA) [44]. As we will see later, LDA is often a good approximation as a starting point for the excited state calculations (e.g., the GWA and CEA).

The local density approximation

The exchange-correlation energy functional $E_{xc}[\rho_s]$ is non-local because it depends on the density $\rho_s(\boldsymbol{r}')$ at all points $\boldsymbol{r}'$ in the system. The local density approximation neglects the non-local dependence of the exchange-correlation energy functional on the density and replaces it by an functional E_{xc}^{LDA} that reads

$$E_{xc}^{LDA}[\rho] = \int \mathrm{d}\boldsymbol{r}\, \mathcal{E}_{xc}^{HEG}[\rho(\boldsymbol{r})]\rho(\boldsymbol{r})\,, \tag{2.11}$$

where $\mathcal{E}_{xc}^{HEG}[\rho]$ is the exchange-correlation energy density of a Homogeneous Electron Gas (HEG) that can be calculated numerically using quantum Monte Carlo for different densities [46]. LDA yields an exchange-correlation potential whose value at point $\boldsymbol{r}$ depends only on the density at the same point.

In order to illustrate the theory, a band structure of bulk sodium from a KS-LDA calculation using the ABINIT code [43] is shown in the left panel of Fig. 2.1[8]. The two core states of sodium ($2s$ and $2p$) are very flat, almost without dispersion, reflecting the fact that the interaction between core states and valence states is negligible, which explains why the quasi-boson Hamiltonian in equation (1.1) is designed for core electron photoemission. As a consequence the occupation number of these two core states is either 1 (before photoe-

---

[8]This is my own numerical calculation. The computational details can be found in section 6.4. They are the same, if not otherwise specified, for all the original numerical calculations in this thesis.

mission) or 0 (after photoemission) for each spin. LDA gives a binding energy of ≈ -52.5 eV and ≈ -25 eV for these two states, respectively, which is much smaller (absolute value) than the experimental results: $2s$ of -63.7 eV and $2p$ of -30.5 eV reported in Ref. [47]. Different from the core, the valence ($3s$) has a strong dispersion and part of this band crosses the Fermi level leading to some partially occupied states. The bandwidth of sodium from my LDA calculation is ≈ 3.18 eV which is $\approx 16\%$ wider than the experimental value reported in Ref. [48] as shown in Fig. 2.2, where the red dashed curve also shows the LDA calculation of Ref. [49]. Both LDA calculations overestimate the bandwidth of sodium by more than 15%.
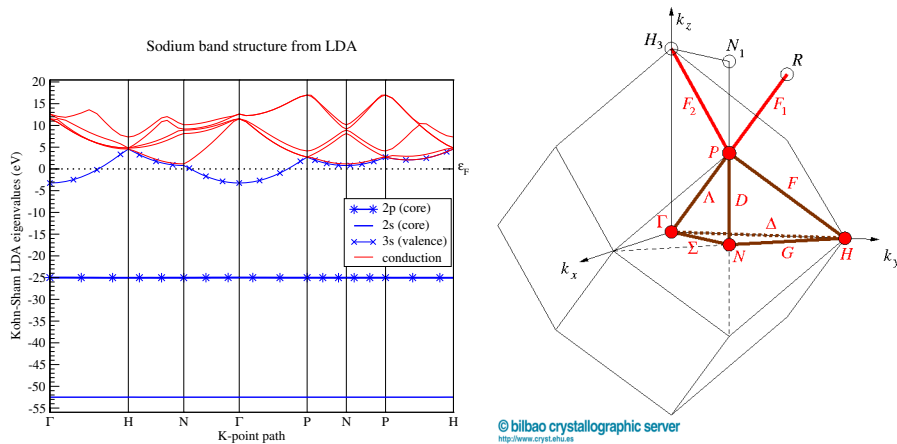
Figure 2.1: The band structure of bulk sodium calculated from KS-LDA using the ABINIT code is shown in the left panel. The right panel is the first Brillouin zone (BZ) of bulk sodium (which is body-centered cubic in real space) where all the high symmetry points are indicated. This figure of the Brillouin zone is taken from Refs. [50,51]. In the left panel, the chemical potential (ε_F) has been shifted to zero. The bands represented by the red curves are conduction bands. The two core bands contained in my calculation are shown in thick blue ($2s$) and thick blue with stars ($2p$), respectively. The valence band ($3s$) is shown in thin blue curve with crosses.

2.2 Hedin's equations and the GW approximation

The Kohn-Sham eigenvalues ($\mathcal{E}$) are not the total energy differences of the system between N and $N \pm 1$ particles, besides the highest occupied state in a finite system or metal [45,52]. Thus they cannot be interpreted as electron addition ($E_s^{N+1} - E_0^N$) or removal ($E_0^N - E_s^{N-1}$) energies as the one that appear in the photocurrent Eq. (1.6). The band structure in
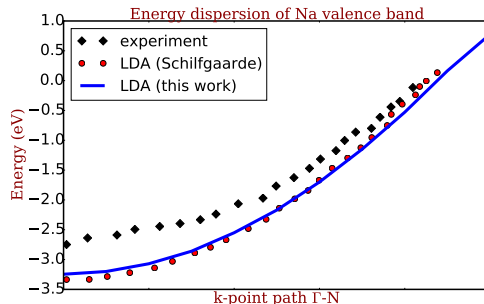
Figure 2.2: Dispersion of the sodium valence band along Γ-N k-point path. The black diamonds are experimental data reproduced from Ref. [49]. The red circles are the LDA result reproduced from the same article. The blue solid curve is the result from my own calculation.

Fig. 2.1 given by the Kohn-Sham eigenvalues is therefore different from the one that is measured in experiment where the energies correspond to the quasi-particle (QP) energies. In particular the Kohn-Sham band gap is in general substantially smaller than the measured photoemission band gap (see e.g. Ref. [6, 49]). This is sometimes called the Kohn-Sham *band-gap problem*. In a metal like sodium, this fact as well as the quality of the approximate functional influence the bandwidth.

In order to go beyond the ground state and describe phenomena such as electron addition and removal, it is more appropriate to change the framework and work with Green's functions [1, 3] instead of the density. In particular, the imaginary part of the one-particle Green's function yields the intrinsic spectral function that can be directly linked to the spectrum measured from a PES or IPES experiment as discussed in Chapter 1. In an independent-particle picture like the Kohn-Sham formalism, the spectral functions consist of peaks that are δ-functions at the independent-particle energies such as the KS eigenvalues $\mathcal{E}_i^{ks}$. Instead in an interacting system, the peaks of spectral function are shifted and broadened: these are the quasi-particle peaks with an finite lifetime. Moreover, they lose weight towards additional structures and incoherent background that appear in the spectra, because all excitations are coupled, and the initial excitation decays by exciting electron-hole pairs, or collective excitations such as plasmons. The GW approximation is designed for describing photoemission spectroscopy in such a picture.

2.2.1 The GW approximation in theory

A route to approximate the one-body Green's function is traced by many-body perturbation theory (MBPT) [1,3] in which the one-body Green's function is determined from the Dyson equation[9]

$$G(1, 2) = G_0(1, 2) + \int \mathrm{d}13 G_0(1, 3) \Sigma(3, 4) G(4, 2) , \tag{2.12}$$

where G_0 is the non-interacting Green's function which is supposed to be known since it is calculated from the non-interacting part of the many-body Hamiltonian (see Eq. (2.1)) $\hat{h}_0 \equiv -\nabla^2/2 + V_{ext}$. $\Sigma(1, 2)$ is the non-local and frequency-dependent self-energy where the Hartree potential as well as all the unknown exchange-correlation contributions are stored. Compared to the Kohn-Sham formalism where the unknown is hidden in the local and energy-independent exchange-correlation potential $V_{xc}(\boldsymbol{r})$, in MBPT the unknown becomes an nonlocal and energy-dependent self-energy $\Sigma(\boldsymbol{r}, \boldsymbol{r}'; \omega)$. In fact, the non-locality of the self-energy is responsible for the opening of the band gap with respect to a Kohn-Sham calculation. The frequency dependence makes the self-energy fundamentally different from any independent-particle potential. It causes the " **Z**-factor " to be smaller than one. This factor gives the fraction of spectral weight that remains in the QP peak since the rest of the spectral weight has been transferred to the satellites and the background. The **Z**-factor is a measure of correlation since in any independent-particle system, the **Z**-factor must be equal to one. Satellites can only appear when the **Z**-factor is smaller than one, and they are always due to interactions; the stronger the interaction, the smaller the **Z**-factor.

Up to now, we have discussed the physical meaning of the self-energy Σ, but not yet given any practical way to calculate this complex quantity. Most modern *ab-initio* calculations of Σ can be traced back to 1965 when Lars Hedin formulated his closed set of equations to determine Σ and proposed the famous `GW approximation` (GWA) [5]. In the GWA, the self-energy is approximated as a simple product of the one-body Green's function and the dynamically screened interaction, leading to $\Sigma = iGW$. Here I am going to derive these equations in a slightly different way than what can be found in Hedin's paper in Ref. [5],

---

[9]Throughout this thesis, the short notation $\int \mathrm{d}12 \equiv \int_{-\infty}^{\infty} \mathrm{d}1\, \mathrm{d}2$ is adopted.

and closer to the derivations in Ref. [53]. To do so, we have to start from the equation of motion (EOM) of the one-body Green's function that can be found in Appendix B.1. In particular, equation (B.17) gives the definition of Σ because

$$G_0^{-1}(1,4) = G^{-1}(1,4) - i \int \mathrm{d}23 v_c(1,3^+) G_2(1,3^+;2,3^{++}) G^{-1}(2,4) , \qquad (2.13)$$

where G_2 is the two-body Green's function. Compared with the Dyson equation (2.12), the self-energy is defined as

$$\Sigma(1,4) = -i \int \mathrm{d}23 v_c(1,3^+) G_2(1,3^+;2,3^{++}) G^{-1}(2,4) . \qquad (2.14)$$

With the above definition of the self-energy, the EOM in Eq. (B.14) becomes

$$\left(i\frac{\partial}{\partial t_1} - \hat{h}_0(\boldsymbol{r}_1) \right) G(1,2) - \int \mathrm{d}3 \Sigma(1,3) G(3,2) = \delta(1,2) . \qquad (2.15)$$

However, this definition dose not tell us how to calculate Σ because it contains a more complicated quantity that is the two-body Green's function G_2 whose EOM yields the three-body Green's function G_3 and so on. In order to overcome this problem following Schwinger [54], we can introduce a fictitious external time-dependent perturbation $\phi(x,t)$ to rewrite the EOM in presence of $\phi(x,t)$ as shown in Appendix B.2. The trick is that the two-body Green's function can be expressed in terms of a variation of the one-body Green's function. Thus we need the EOM in non-equilibrium as shown in equation (B.44):

$$\begin{aligned}
G(1,2;\phi) = G_0(1,2) &+ \int \mathrm{d}3 G_0(1,3) \phi(3) G(3,2;\phi) \\
&+ \int \mathrm{d}3 G_0(1,3) V_H(3;\phi) G(3,2;\phi) \\
&+ i \int \mathrm{d}34 G_0(1,3) v_c(3,4^+) \frac{\delta G(3,2;\phi)}{\delta \phi(4)} ,
\end{aligned} \qquad (2.16)$$

where $V_H(3;\phi) = -i \int d4 v_c(3, 4^+) G(4, 4^{++}; \phi)$ is the Hartree potential in presence of the external potential ϕ. The self-energy in presence of ϕ reads

$$\Sigma(1, 2; \phi) = V_H(1; \phi)\delta(1, 2) + i \int d34 v_c(1, 3^+) \frac{\delta G(1, 4; \phi)}{\delta \phi(3)} G^{-1}(4, 2; \phi) \,. \qquad (2.17)$$

The first term in the self-energy is the Hartree term which is supposed to be known. Since there is no functional derivative with respective to ϕ in the Hartree term, $\phi \to 0$ can be taken whenever it is necessary such that $V_H(1; \phi) \to V_H^{(0)}(1) = -i \int d2 v_c(1, 2^+) G(2, 2^+)$ (see Eq. (3.4)) in equilibrium. The second term in the above equation is sometimes refereed to as the `mass operator` M where all the unknown exchange-correlation effects are hidden. We call it the `exchange-correlation` self-energy Σ_{xc}. It reads

$$\Sigma_{xc}(1, 2; \phi) = i \int d34 v_c(1, 3^+) \frac{\delta G(1, 4; \phi)}{\delta \phi(3)} G^{-1}(4, 2; \phi) \,. \qquad (2.18)$$

At this moment $\phi = 0$ cannot be taken yet since there is still the functional derivative of G with respect to ϕ in Σ_{xc}[10]. To get rid of this functional derivative, we can further introduce the `total classical potential` defined as:

$$V_{cl}(1; \phi) = V_H(1; \phi) + \phi(1) \,, \qquad (2.19)$$

to rewrite Σ_{xc} as[11]

$$\Sigma_{xc}(1, 2; \phi) = -i \int d345 v_c(1, 3^+) G(1, 4; \phi) \frac{\delta G^{-1}(4, 2; \phi)}{\delta V_{cl}(5; \phi)} \frac{\delta V_{cl}(5; \phi)}{\delta \phi(3)} \,. \qquad (2.20)$$

---

[10]The reason why we have to get rid of the functional derivative with respect to the external perturbation ϕ is that, we want to study the property of materials in equilibrium where $\phi = 0$. The calculation of Green's function in equilibrium is the main interest of this thesis.

[11]We have used the following identity of the Green's function:

$$\frac{\delta [GG^{-1}]}{\delta \phi} = \frac{\delta G}{\delta \phi} G^{-1} + \frac{\delta G^{-1}}{\delta \phi} G \,; \quad \frac{\delta G}{\delta \phi} G^{-1} = -\frac{\delta G^{-1}}{\delta \phi} G \,,$$

as well as the *chain-rule*

$$\frac{\delta G^{-1}}{\delta \phi} = \frac{\delta G^{-1}}{\delta V_{cl}} \frac{\delta V_{cl}}{\delta \phi} \,.$$

The first derivative of the above equation suggests to introduce a *irreducible*[12] `vertex function` $\tilde{\Gamma}$ defined as

$$\tilde{\Gamma}(4, 2, 5; \phi) = -\frac{\delta G^{-1}(4, 2; \phi)}{\delta V_{cl}(5; \phi)} = \delta(4, 5)\delta(2, 5) + \frac{\delta \Sigma_{xc}(4, 2; \phi)}{\delta V_{cl}(5; \phi)}, \qquad (2.21)$$

where the inverse of the Dyson equation (2.12) $G^{-1} = G_0^{-1} - V_{cl} - \Sigma_{xc}$ has been used to derive the above equation. Again using the identity

$$\frac{\delta G}{\delta \phi} = -G\frac{\delta G^{-1}}{\delta \phi}G, \qquad (2.22)$$

the `vertex function` can be written in a closed form

$$\begin{aligned}
\tilde{\Gamma}(4, 2, 5; \phi) &\equiv \delta(4, 5)\delta(2, 5) + \int d67 \frac{\delta \Sigma_{xc}(4, 2; \phi)}{\delta G(6, 7)} \frac{\delta G(6, 7; \phi)}{\delta V_{cl}(5; \phi)} \\
&= \delta(4, 5)\delta(2, 5) + \int d6789 \frac{\delta \Sigma_{xc}(4, 2; \phi)}{\delta G(6, 7; \phi)} G(6, 8; \phi) \frac{\delta G^{-1}(8, 9; \phi)}{\delta V_{cl}(5; \phi)} G(9, 7; \phi) \\
&= \delta(4, 5)\delta(2, 5) + \int d6789 \frac{\delta \Sigma_{xc}(4, 2; \phi)}{\delta G(6, 7; \phi)} G(6, 8; \phi)\tilde{\Gamma}(8, 9, 5; \phi)G(9, 7; \phi). \quad (2.23)
\end{aligned}$$

In equilibrium, we have

$$\tilde{\Gamma}(4, 2, 5) = \delta(4, 5)\delta(2, 5) + \int d6789 \frac{\delta \Sigma_{xc}(4, 2)}{\delta G(6, 7)} G(6, 8)\tilde{\Gamma}(8, 9, 5)G(9, 7). \qquad (2.24)$$

In equation (2.20), the derivative of the total potential with respect to the external potential gives the definition of the `inverse dielectric function` ϵ^{-1}:

$$\epsilon^{-1}(1, 2; \phi) = \frac{\delta V_{cl}(1)}{\delta \phi(2)} = \delta(1, 2) + \int d3 v_c(1, 3^+)\frac{\delta \rho(3; \phi)}{\delta \phi(2)}. \qquad (2.25)$$

We have used the definition of the ground state density $\rho(1) \equiv -iG(1, 1^+)$ in the above equation. The functional derivative of the density with respect to the external potential is

---

[12] All the quantities that are defined as a functional derivative with respect to the classical total potential V_{cl} are refereed to be the *irreducible* one, which distinguishes from the *reducible* one that is the functional derivative with respect to the external potential ϕ.

a measure of the `polarizability` of a system:

$$\chi(1,2;\phi) \equiv \frac{\delta\rho(1;\phi)}{\delta\phi(2)}\,. \tag{2.26}$$

To connect the `polarizability` χ with the Green's function it is more appropriate to write it in its *irreducible* form $\tilde{\chi}$, which has a direct link to the *irreducible* `vertex function` $\tilde{\Gamma}$ since

$$\tilde{\chi}(1,2;\phi) \equiv \frac{\delta\rho(1;\phi)}{\delta V_{cl}(2;\phi)} = -i\frac{\delta G(1,1^+;\phi)}{\delta V_{cl}(2;\phi)} = i\int d34 G(1,3;\phi)\frac{\delta G^{-1}(3,4;\phi)}{\delta V_{cl}(2;\phi)}G(4,1^+;\phi)$$
$$= -i\int d34 G(1,3;\phi)\tilde{\Gamma}(3,4,2;\phi)G(4,1^+;\phi)\,. \tag{2.27}$$

The link between χ and $\tilde{\chi}$ is obvious with the help of the *chain rule* and equation (2.25):

$$\chi(1,2;\phi) = \int d3\frac{\delta\rho(1;\phi)}{\delta V_{cl}(3;\phi)}\frac{\delta V_{cl}(3;\phi)}{\delta\phi(2)} = \int d3\tilde{\chi}(1,3;\phi)\left(\delta(3,2;\phi) + \int d4 v_c(3,4^+)\frac{\delta\rho(4;\phi)}{\delta\phi(2)}\right)$$
$$= \tilde{\chi}(1,2;\phi) + \int d34\tilde{\chi}(1,3;\phi)v_c(3,4^+)\chi(4,2;\phi)\,. \tag{2.28}$$

At this point, all the functional derivatives with respect to ϕ have been carried out and all the quantities are linked to each other so that we are ready to put $\phi \to 0$ in equation (2.20) to calculate Σ_{xc} in equilibrium (see Eqs. (2.21) and (2.25)).

$$\Sigma_{xc}(1,2) = i\int d345 v_c(1,3^+)G(1,4)\tilde{\Gamma}(4,2,5)\epsilon^{-1}(5,3)\,. \tag{2.29}$$

It is convenient to further introduce the `dynamically screened interaction` W defined as

$$W(1,2) \equiv \int d3\epsilon^{-1}(1,3)v_c(3,2^+) = \int d3\left(\delta(1,3) + \int d4 v_c(1,4^+)\chi(4,3)\right)v_c(3,2^+)$$
$$= v_c(1,2^+) + \int d34 v_c(1,4^+)\chi(4,3)v_c(3,2^+)\,. \tag{2.30}$$

We can also express W in terms of the *irreducible* `polarizability` $\tilde{\chi}$, since

$$\epsilon(1,2) \equiv \frac{\delta\phi(1)}{\delta V_{cl}(2)} = \delta(1,2) - \int d3 v_c(1,3^+)\tilde{\chi}(3,2)\,, \tag{2.31}$$

which yields

$$\epsilon^{-1}(1,2) = \delta(1,2) + \int d34 v_c(1,3^+)\tilde{\chi}(3,4)\epsilon^{-1}(4,2)\,. \tag{2.32}$$

Therefore W in terms of $\tilde{\chi}$ reads

$$W(1,2) \equiv \int d3 \epsilon^{-1}(1,3)v_c(3,2^+) = v_c(1,2^+) + \int d34 v_c(1,4^+)\tilde{\chi}(4,3)W(3,2^+) \tag{2.33}$$

Now collecting all the equations that have been derived above, we can write them in a closed form in equilibrium, which is often called *Hedin's equations*:

$$G(1,2) = G_0(1,2) + \int d34 G_0(1,3)\Sigma(3,4)G(4,2)\,; \tag{2.34a}$$

$$\Sigma_{xc}(1,2) = i\int d34 W(1,3)G(1,4)\tilde{\Gamma}(4,2,3)\,; \tag{2.34b}$$

$$W(1,2) = v_c(1,2^+) + \int d34 v_c(1,4^+)\tilde{\chi}(4,3)W(3,2)\,; \tag{2.34c}$$

$$\tilde{\chi}(1,2) = -i\int d34 G(1,3)\tilde{\Gamma}(3,4,2)G(4,1^+)\,; \tag{2.34d}$$

$$\tilde{\Gamma}(1,2,3) = \delta(1,3)\delta(2,3) + \int d4567 \frac{\delta\Sigma_{xc}(1,2)}{\delta G(4,5)}G(4,6)\tilde{\Gamma}(6,7,3)G(7,5)\,. \tag{2.34e}$$

There are five unknown quantities i.e. $G, \Sigma, W, \tilde{\chi}$ and $\tilde{\Gamma}$ and five equations to link them together as shown by the pentagon in Fig. 2.3. Up to now all quantities in the above equations are still exact. This way of formulating the many-body problem is appealing, since it highlights the important physical ingredients [55]:

- The `irreducible polarizability` $\tilde{\chi}$ in equation (2.34d) contains the response of the system to the `total classical potential` according to its definition in equation (2.27). As a consequence, pairs of particles are created leading to two one-particle Green's functions. Note that the particles are interacting with each other represented by the vertex function $\tilde{\Gamma}$. Moreover, depending on the time ordering of the two Green's functions, the particle pairs can be either *electron-hole* or *electron-electron*
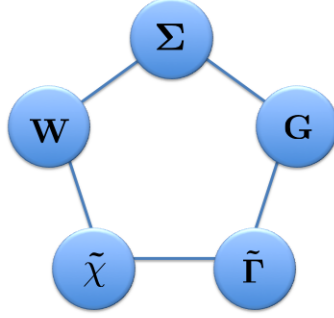
Figure 2.3: Hedin's pentagon which represents the five closed set of integro-differential equations as shown in (2.34). In principle, one can start from some guess of the self-energy and run clockwise this pentagon until the desired level of approximation for the various quantities is reached.

or *hole-hole*. In particular in the GW approximation (that will be discussed later) where $\tilde{\Gamma} = 1$, the pairs become electron and hole ($\tilde{\chi} = -iG(1,2)G(2,1)$) leading to the `random phase approximation` [56] (RPA)[13] of the polarizability where the interaction between electron and hole is neglected.

- The dielectric function $\epsilon = \epsilon_1 + i\epsilon_2$ in Eq. (2.25) is a complex valued quantity whose real and imaginary parts are ϵ_1 and ϵ_2, respectively. It contains the neutral excitations of the system. In particular, the frequency that fulfills the condition of $\epsilon_1(\omega) = 0$ is defined as the plasmon frequency of a many-body system [58]. In a solid, plasmons are the dominant structures that are seen in $\epsilon^{-1}(\omega)$, which are identified as the maximum of the imaginary part of $\epsilon^{-1}(\omega)$ in practice since, $-\operatorname{Im}\epsilon^{-1} = \dfrac{\epsilon_2}{\epsilon_1^2 + \epsilon_2^2}$ thus $-\operatorname{Im}\epsilon^{-1}$ has a sharp peak when $\epsilon_1 = 0$ and ϵ_2 is very small. This property is transferred to the dynamically screened interaction $W = \epsilon^{-1}v_c$ (see Eq. (2.30)) hence the self-energy $\Sigma_{xc} = iGW\tilde{\Gamma}$ if the vertex $\tilde{\Gamma}$ is close to 1.

---

[13]The name random phase approximation (RPA) was first introduced by Pines and Bohm [56] for the HEG where it leads to the Lindhard dielectric function [57]. Strictly speaking, the RPA response function corresponds to the product of two independent-particle Green's functions (e.g., the KS Green's functions) instead of the full interacting Green's function.

- The effective classical interaction between two particles in the system is not the bare Coulomb interaction v_c, but its screened counterpart W as shown in equation (2.34c). The Dyson equation for W reflects the self-consistent response of the system to the total classical potential $V_{cl} = \phi + V_H$ because $\tilde{\chi}$ is the response to the total classical potential as expressed by equation (2.27). In particular, the definition of $W = v_c \epsilon^{-1}$ in equation (2.30) reflects the fact that the bare Coulomb interaction is screened by the induced Hartree potential due to the definition of inverse dielectric function ϵ^{-1} in equation (2.25). For this reason, W in Eq. (2.34c) is the potential that is created and seen by the external classical charges[14] and the dielectric function ϵ in Eq. (2.25) is thus called the *test-charge test-charge* (TCTC) dielectric function.

- An electron in the system is not an external classical charge, but a fermion that is indistinguishable from the other electrons in the system. Therefore besides the total classical potential $V_{cl} = \phi + V_H$, an electron should feel the `exchange-correlation` potential Σ_{xc}, leading to the total potential $V_{tot} = \phi + V_H + \Sigma_{xc}$. However the latter cannot be given by W because it appears in the vertex function $\tilde{\Gamma}$ Eq. (2.34e). Due to the vertex, the effective interaction becomes $W\tilde{\Gamma}$ in equation (2.34b), instead of W in the GW approximation. Note that the relation of the effective interaction to the exchange-correlation potential $W\tilde{\Gamma} = \dfrac{\delta \Sigma_{xc}}{\delta G}$ is quite similar to the relation of the bare Coulomb interaction to the Hartree potential $v_c = \dfrac{\delta V_H}{\delta \rho}$. One may call the total effective interaction $W\tilde{\Gamma}$ a generalized *test-charge test-electron* (TCTE) screened interaction[15].

In principle, one can start from an approximated self-energy Σ_{xc} and iterate Hedin's equations as illustrated in the pentagon 2.3 clockwise until convergence is achieved. The self-consistent solution should be in principle, the exact solution of the many-body problem. However, due to the complicated three point `vertex function` $\tilde{\Gamma}$ where a functional derivative is involved, it is impossible to achieve this for a many-electron system. Moreover, even for a small system as simple as the Hydrogen molecule H_2, there can be problems

---

[14]The classical charge does not have the anti-symmetry property of fermions such that it differs from the fermion in the exchange-correlation part.

[15]A calculation of bulk sodium photoemission spectrum using the test-charge test-electron dielectric function will be shown in section 6.2.

such as multiple solutions. A straightforward expansion for the self-energy in powers of the screened interaction W may yield unphysical results such as negative spectral functions when truncated at some order [59]. Recently it has been suggested to correct this by adding some higher order terms [60]. In fact, there are many ways of expanding Σ with respect to different quantities but there is even no unique answer to the question *"which quantity is the best parameter to expand, the bare Coulomb interaction v_c, the screened interaction W, or other?"* Different expansions can be good to describe some physical phenomena (e.g. transport) but not necessarily also good for others (e.g. spectra). An important point that I would like to address here is the fact that different approximations might cause the breakdown of different exact constraints that should in principle hold for the one-particle Green's function. This can induce unphysical phenomena in certain applications. There seems to be no approximate solution of Hedin's equations that fulfills all exact constraints, except the exact one (at least so far no one has found it). The good point is that, not all the exact constraints are important for all applications, e.g if we are only interested in the quasi-particle energies so as to get a good band structure, we do not need to worry about the negative spectral functions, which will appear at higher binding energy. In the framework of this thesis, the important constraints for our purpose have been summarized in section 1.3.

The problems posed by perturbation theory, Hedin's equations (e.g. non-physical solutions) and proper ways to expand the self-energy [60] have been studied for decades and countless approximations have been proposed. These discussions go beyond the scope of this thesis. Here I will focus on the most popular approximation, i.e. the GW approximation (GWA) [5] and work in a system where GW can give good quasi-particle energies and reasonable spectral functions. The GW approximation corresponds to solving Hedin's equations without vertex corrections, i.e., the irreducible vertex $\tilde{\Gamma}$ in the GW approximation has been approximated as

$$\tilde{\Gamma}(1,2,3) = \delta(1,3)\delta(2,3) \equiv \tilde{\Gamma}^{GW}(1,2,3)\,. \tag{2.35}$$

The vertex function appears in $\tilde{\chi}$ Eq. (2.34d) and Σ_{xc} Eq. (2.34b). The GW approximation of $\tilde{\Gamma}^{GW}$ in the polarizability $\tilde{\chi}$ yields the random phase approximation (RPA) (see Eq. (2.34d)), which further yields the the random phase approximation for W. On the other hand, $\tilde{\Gamma}^{GW}$ in the self-energy Σ_{xc} yields the GW self-energy that reads $\Sigma^{GW}(1,2) \equiv iG(12)W(12)$. The GW approximation can be further separated into two main different frameworks. One of them is called the one-shot GW (G_0W_0). It starts from some independent-particle Green's function and runs one single shot of Hedin's pentagon with $\tilde{\Gamma}^{GW} = 1$ as shown in figure 2.4. The starting independent-particle Green's function can be fore example a Hartree-Fock or Kohn-Sham Green's function. A G_0W_0 calculation in bulk sodium starting from a KS-LDA Green's function will be discussed later in this section. The other framework is called the self-consistent GW (scGW) where instead of running a single shot of Hedin's pentagon keeping $\tilde{\Gamma}^{GW} = 1$, some quantities (eigenvalues, eigenfunctions or the full Green's function) will be updated during the iteration. Depending on which quantity is updated, there are different methods of doing scGW, e.g. the eigenvalue self-consistent GW_0 (EscGW$_0$) updates only the eigenenergies appearing in the Green's function when we evaluate Σ in equation (2.34b) but W is kept to be fixed during iteration, i.e. the RPA W. Again, I will take bulk sodium as an example to show the importance of self-consistency for sodium core states, where in particular the EscGW$_0$ is needed.

2.2.2   The GW approximation in practice

In practical calculation, we start from the Kohn-Sham local-density approximation (LDA) to calculate the starting independent-particle Green's function. Hence $G_0 \to G_{ks}^{LDA}$ that is calculated from the KS-LDA eigenvalues ($\mathcal{E}_i$) and eigenfunctions (ψ_i) by solving the KS equation (2.7b), and $\Sigma_{xc} \to (\Sigma_{xc} - V_{xc}^{LDA})$. Therefore GW starting from a KS-LDA Green's function corresponds to solving the following equations either in one run yielding G_0W_0 or
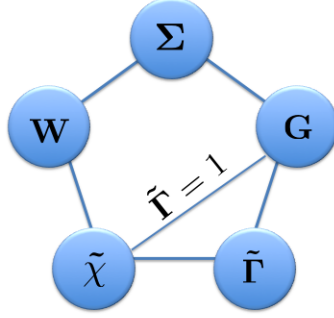
Figure 2.4: Schematic representation of the GW approximation. If one only runs a single shot of these equations starting from $G = G_0$, one ends up with the G_0W_0 approximation. If we iterate these equations until self-consistency is reached we end up with a scGW approximation.

self-consistently yielding scGW:

$$\tilde{\chi}_0(1,2) = -iG_{ks}^{LDA}(1,2)G_{ks}^{LDA}(2,1)\,; \tag{2.36a}$$

$$W_0(1,2) = v_c(1,2^+) + \int \mathrm{d}34 v_c(1,4)\tilde{\chi}_0(4,3)W_0(32)\,; \tag{2.36b}$$

$$\Sigma^{GW}(1,2) = iG_{ks}^{LDA}(1,2)W_0(1,2)\,; \tag{2.36c}$$

$$G(1,2) = G_{ks}^{LDA}(1,2) + \int \mathrm{d}34 G_{ks}^{LDA}(1,3)\big(\Sigma^{GW}(3,4) - V_{xc}^{LDA}(3,4)\delta(3,4)\big)G(4,2)\,. \tag{2.36d}$$

In G_0W_0, the above equations are calculated in one run, which yields the random phase approximation (RPA) of the dynamically screened Coulomb interaction W_0 due to the random phase approximation of the irreducible polarizability [61, 62] that is a product of two KS-LDA Green's function ($\tilde{\chi} = -iG_{ks}G_{ks}$) representing two independent particles (one electron and one hole) propagating without interaction. In EscGW$_0$, the eigenenergies appearing in G_{ks}^{LDA} (Eq. (2.36c)) are updated during the iteration until self-consistency is achieved. The screened interaction W_0 is kept fixed during iteration so that EscGW$_0$

also uses the RPA W[16]. Therefore the difference between EscGW$_0$ and G$_0$W$_0$ is that the former has updated eigenenergies $\mathcal{E}_i \to \varepsilon_i$ in the Green's function when calculating Σ^{GW} such that the EscGW$_0$ self-energy has a shift in its poles compared to the G$_0$W$_0$ one. Note that an energy shift in the denominator of Σ^{GW} will induce not only a shift in the final Green's function when solving the Dyson equation (2.36d) compared to a G$_0$W$_0$ calculation, but it changes the structure of the spectral function which can be seen in Fig. 2.8. This energy self-consistent process is important when the KS-LDA eigenenergies are far from the quasi-particle energies, e.g. for the sodium core states ($2s$ and $2p$).

The RPA W contains one bare Coulomb interaction term v_c that is time-independent and another time-dependent term $W_c = v_c \tilde{\chi} W$ where W_c is called the correlation part of the screened interaction. This separation yields the separation of the self-energy into its `exchange` and `correlation` parts $\Sigma^{GW} = \Sigma_x + \Sigma_c$:

$$\Sigma_x(x_1, x_2, t_1 - t_2) = iG(x_1, x_2, t_1 - t_2)v_c(x_1 - x_2)\delta(t_1 - t_2);$$

$$\Sigma_c(1, 2) = iG(1, 2)W_c(1, 2).$$

In practice, Σ_x and Σ_c are calculated separately[17]. Assuming that $\Sigma^{GW} - V_{xc}^{LDA}$ is diagonal in the Kohn-Sham orbitals, the spectral function of a certain state labeled i (see Eq. (2.36)) can be written as

$$
\begin{aligned}
A_i(\omega) &= \frac{1}{\pi} \left| \operatorname{Im} G_i(\omega) \right|, \\
&= \frac{1}{\pi} \left| \operatorname{Im} \frac{1}{\omega - \mathcal{E}_i + V_{xc,i}^{LDA} - \Sigma_i^{GW}(\omega)} \right|, \\
&= \frac{1}{\pi} \frac{\left| \operatorname{Im} \Sigma_i^{GW}(\omega) \right|}{\left[\omega - \mathcal{E}_i + V_{xc,i}^{LDA} - \operatorname{Re} \Sigma_i^{GW}(\omega) \right]^2 + \left[\operatorname{Im} \Sigma_i^{GW}(\omega) \right]^2},
\end{aligned}
\tag{2.37}
$$

---

[16]As discussed above, the plasmons are described by the maximum of $- \operatorname{Im} \epsilon^{-1}$, hence of $\operatorname{Im} W = -v_c \operatorname{Im} \epsilon^{-1}$. In particular, plasmons calculated using the RPA often compare well to experimental spectra such as electron energy loss spectra or inelastic x-ray scattering (see e.g. Refs. [63–67]). Therefore, in principle one expects that at least plasmon satellites are well described by the GWA. Plasmon satellites are indeed found in the GWA as can be seen in the following discussions, but they are often too far from the quasi-particle energy, and sometimes much too sharp, and in other cases much too weak, as compared to experiment.

[17]The exchange part Σ_x corresponds to the Fock operator $\Sigma_x = iGv_c$ evaluated with the interacting density matrix $-iG(xx', tt^+)$.

where Σ^{GW} can be the one from G_0W_0 or $EscGW_0$. An illustration of the GW spectral function using the quasi-boson Hamiltonian[18] in equation (1.1) is shown in Fig. 2.5. For vanishing GW self-energy $\Sigma^{GW} = 0$, $A_i(\omega)$ shows a δ-peak at energy $\mathcal{E}_i - V_{xc,i}^{LDA} \equiv \varepsilon_i^H$ where ε_i^H is the Hartree eigenvalue[19] as represented by the green arrow labeled ε_H in Fig. 2.5.
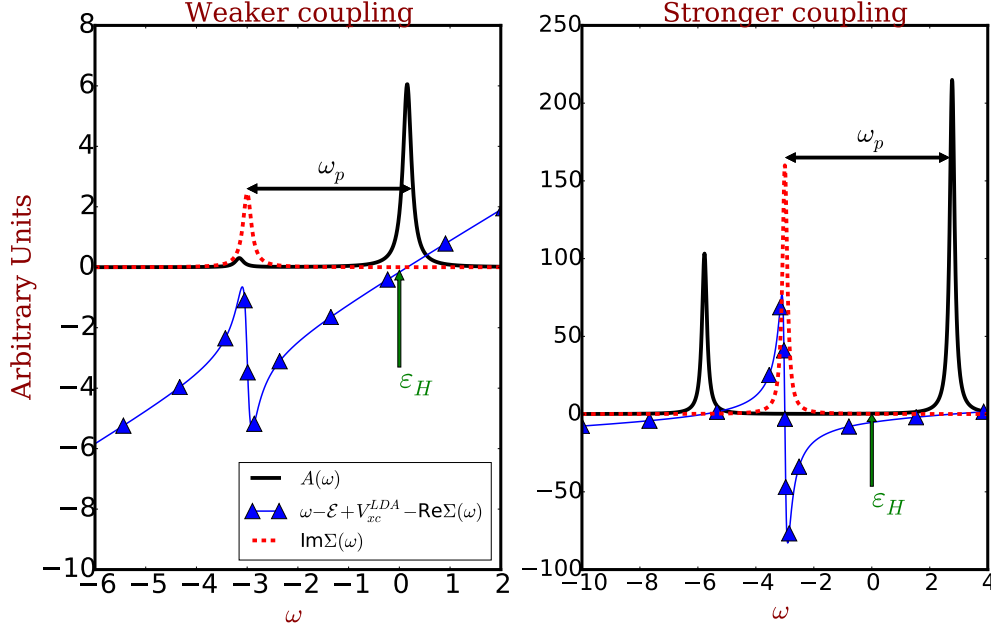
Figure 2.5: An illustration of the GW spectral function in equation (2.37) using the quasi-boson Hamiltonian in equation (1.1). Left and right panels are cases of weaker and stronger coupling strength g_q, respectively. The black solid curve represents the spectral function $A(\omega)$ shown in Eq. (2.37). The red dashed and blue curve with up-triangles are the imaginary $\text{Im}\,\Sigma$ and shifted real part $\omega - \mathcal{E} + V_{xc}^{LDA} - \text{Re}\,\Sigma$ of the GW self-energies, respectively. The green arrow labeled ε_H is the Hartree eigenenergy which corresponds to $\Sigma^{GW} = 0$.

The real part of the GW self-energy shifts the Hartree eigenenergy to the GW QP energy ε, as can be see from the denominator of A_i. The QP peak is still very sharp if $\text{Im}\,\Sigma^{GW}(\omega = \varepsilon)$ is small. In that case, the zero of the shifted real part of the GW self-energy gives the QP energy, i.e.

$$\varepsilon_i = \mathcal{E}_i - V_{xc,i}^{LDA} + \text{Re}\,\Sigma_i^{GW}(\omega = \varepsilon_i),\qquad(2.38)$$

---

[18]Note that the exchange part of the self-energy Σ_x is contained in the orbital energy ε_0 of the quasi-boson model. Therefore, we only need to calculate the correlation part. This will be clear in section 4.2.

[19]The Hartree eigenvalues are obtained from the diagonalization of the Hartree Hamiltonian that reads $\hat{h}_H = \hat{h}_0 + V_H$. Thus compared to the KS Hamiltonian, the Hartree approximation corresponds to a vanishing exchange-correlation potential $V_{xc} = 0$.

as illustrated in the left panel of Fig. 2.5. In principle, the width of this QP peak is determined by $\mathrm{Im}\,\Sigma_i^{GW}(\omega = \varepsilon_i)$[20] as can be seen in the denominator of Eq. (2.37). The neutral excitations induced by electron removal lead to a distinct structure in $\mathrm{Im}\,\Sigma^{GW}$ as shown in the red dashed curve of the same figure. As discussed before, the peak in $\mathrm{Im}\,\Sigma^{GW}$ stems from the peak in $\mathrm{Im}\,\epsilon^{-1}$ such that it links to the neutral excitations of the system. This explains why the distance between the QP peak and the the peak in $\mathrm{Im}\,\Sigma^{GW}$ is the plasmon energy[21]. The peaks in the spectral function induced by these structures are satellites. In a weaker coupling system, the GW satellite is very close to the peak of $\mathrm{Im}\,\Sigma^{GW}$, but with a small weight. This explains why the GWA can give good satellites for example for vanadium dioxide (VO_2) in Ref. [68][22]. However, when the coupling becomes stronger, the shifted real part of the GW self-energy has a second crossing of zero (blue curve with up-triangles in the right panel of Fig. 2.5), leading to a strong satellite at an energy too far from the energy where $\mathrm{Im}\,\Sigma^{GW}$ has a peak. This satellite is called a `plasmaron` [13, 14] satellite. It has been shown to be an artifact of the GW approximation when the vertex correction is neglected [11, 15, 69] and it completely masks the very week satellite close to the peak in $\mathrm{Im}\,\Sigma$.

Eq. (2.37) shows how the intrinsic spectral function is obtained from the GWA, but the quasi-particle energy is not calculated explicitly yet. In practice, often one wants only the quasi-particle energies from the GWA, e.g. the band corrections to a Kohn-Sham calculation (see e.g. Refs. [70, 71]). In that case one can avoid the calculation of the Green's function in (2.36d). This suggests to introduce the so-called *quasi-particle equation*.

The quasi-particle equation

It would be more convenient to have an effective Schrödinger equation like the Kohn-Sham equation (2.7b) from which the eigenvalues and eigenfunctions of the corresponding effective

---

[20]However, in the study of the quasi-boson model, all the energies are real. Thus in Fig. 2.5 the Lorentzian broadening of the QP peaks are put by hand.

[21]Note that the plasmon dispersion has been neglected in the quasi-boson model when plotting the Fig. 2.5. In practical calculation of real materials, both the QP peak and the imaginary part of Σ are broadened, such that the distance between the maximum of these two peaks can be different for different orbitals or k-points in the Brillouin zone. The calculation in bulk sodium will be shown in Chapter 6.

[22]In the case of VO_2, the satellites in the spectrum are due to *d-d* transitions which corresponds to a weaker coupling g_q in the quasi-boson model. Therefore, the left panel of Fig. 2.5 could be an illustration of a *d-d* transition satellite in the GWA.

Hamiltonian similar to $\hat{H}^{ks}$, can be calculated. Such an equation is the quasi-particle equation. To derive the quasi-particle equation, we first have to Fourier transform the EOM (2.15) to frequency space, which yields

$$\left(\omega - \hat{h}_H(x_1)\right)G(x_1, x_2, \omega) - \int \mathrm{d}x_3 \, \Sigma_{xc}(x_1, x_3, \omega)G(x_3, x_2, \omega) = \delta(x_1, x_2)\,. \qquad (2.39)$$

The so-called *quasi-particle approximation* [3] assumes that the dominant energies of the above equation are the complex quasi-particle energies $\omega = \mathcal{E}_i^{QP}$. The real part of the quasi-particle energy ε_i gives the quasi-particle excitation energy and the imaginary part gives the damping of the quasi-particle excitation that is proportional to the inverse life-time of that excitation. Expanding the Green's function around the quasi-particle energies and introducing a set of independent-particle wavefunctions ψ_i^{QP} called the quasi-particle wavefunctions, we arrive at the quasi-particle equation that reads

$$\hat{h}_H(x_1)\psi_i^{QP}(x_1) + \int \mathrm{d}x_2 \, \Sigma_{xc}(x_1, x_2, \mathcal{E}_i^{QP})\psi_i^{QP}(x_2) = \mathcal{E}_i^{QP}\psi_i^{QP}(x_1)\,. \qquad (2.40)$$

Compared to the KS equation (2.7b) which reads

$$\left(\hat{h}_H(\boldsymbol{r}) + V_{xc}(\boldsymbol{r})\right)\psi_i(\boldsymbol{r}) = \mathcal{E}_i\psi_i(\boldsymbol{r})\,, \qquad (2.41)$$

the quasi-particle equation replaces the local and energy-independent Kohn-Sham exchange-correlation potential V_{xc} by a nonlocal and energy dependent exchange-correlation self-energy Σ_{xc}. Note that Σ_{xc} could still be the exact exchange-correlation self-energy, instead of the GW self-energy at this moment. Under the assumption that the Kohn-Sham wavefunctions ψ_i are nearly identical with the quasi-particle wavefunctions ψ_i^{QP}, we can calculate the quasi-particle energies from first-order perturbation theory assuming the starting Hamiltonian as $\hat{H}^{ks}$ (see Eq. (2.7a)) with LDA V_{xc}^{LDA} and $\langle\psi_i|\psi_i^{QP}\rangle \approx 1$, which means that we can replace the quasi-particle wavefunctions in the quasi-particle equation (2.40) by the KS wavefunctions.

Quasi-particle energies from the GWA

We now use for Σ_{xc} the GW self-energy Σ^{GW}, and obtain

$$\mathcal{E}_i^{QP} = \mathcal{E}_i + \langle\psi_i|\Sigma^{GW}(\mathcal{E}_i^{QP}) - V_{xc}^{LDA}|\psi_i\rangle = \mathcal{E}_i + \Sigma_i^{GW}(\mathcal{E}_i^{QP}) - V_{xc,i}^{LDA}\,. \tag{2.42}$$

Since all Kohn-Sham ingredients $\mathcal{E}$ and V_{xc} are real, the imaginary part of the quasi-particle energy is determined by the imaginary part of the self-energy, i.e. $\mathrm{Im}\,\mathcal{E}^{QP} = \mathrm{Im}\,\Sigma^{GW}(\mathcal{E}^{QP})$. From the spectral function Eq. (2.37), we can see that when $\mathrm{Im}\,\Sigma$ is small, the real part of the quasi-particle energy ε_i corresponds indeed to a peak in the spectra function because it fulfills the condition that

$$\varepsilon_i - \mathcal{E}_i + V_{xc,i}^{LDA} - \mathrm{Re}\,\Sigma_i^{GW}(\varepsilon_i) = 0\,, \tag{2.43}$$

In order to calculate the real part of the quasi-particle energy ε_i from equation (2.42), we can expand $\Sigma^{GW}(\omega)$ around the KS-LDA eigenvalue $\mathcal{E}_i$ and keep the linear order term:

$$\begin{aligned}
\varepsilon_i - \mathcal{E}_i &\approx \left\langle\psi_i\left|\Sigma^{GW}(\mathcal{E}_i) + (\varepsilon_i - \mathcal{E}_i)\left.\frac{\partial\Sigma_i^{GW}(\omega)}{\partial\omega}\right|_{\omega=\mathcal{E}_i} - V_{xc,i}^{LDA}\right|\psi_i\right\rangle \\
&= \mathbf{Z}_i^{GW}\left(\Sigma_i^{GW}(\mathcal{E}_i) - V_{xc,i}^{LDA}\right),
\end{aligned} \tag{2.44}$$

where the quasi-particle weight from the GWA is given by the **Z**-factor that reads

$$\mathbf{Z}_i^{GW} = \left(1 - \left\langle\psi_i\left|\left.\frac{\partial\Sigma_i^{GW}(\omega)}{\partial\omega}\right|_{\omega=\mathcal{E}_i}\right|\psi_i\right\rangle\right)^{-1}. \tag{2.45}$$

One can see from the following paragraphs, the G_0W_0 self-energy is good enough for getting the QP energies of the sodium valence state ($3s$) because the Kohn-Sham eigenvalues of valence states are close to the GW quasi-particle energy. But for the sodium core states ($2s$ and $2p$), the Kohn-Sham eigenvalues are far from the GW quasi-particle energies such that eigenvalue self-consistency is crucial.

The intrinsic spectral function of sodium valence band

Here I am going to show some of my own GW calculations on bulk sodium. The aim is to illustrate the performance of the GWA in different situations, i.e. valence and core. The comparison of G_0W_0 and $EscGW_0$ spectral functions for the sodium valence state $(3s)$ at the Γ point (i.e., k=0,0,0) of the Brillouin zone is shown in Fig. 2.6. We first study the QP energies from different calculations. There are four different kinds of QP energies appearing in the lower panel of Fig. 2.6 which are:
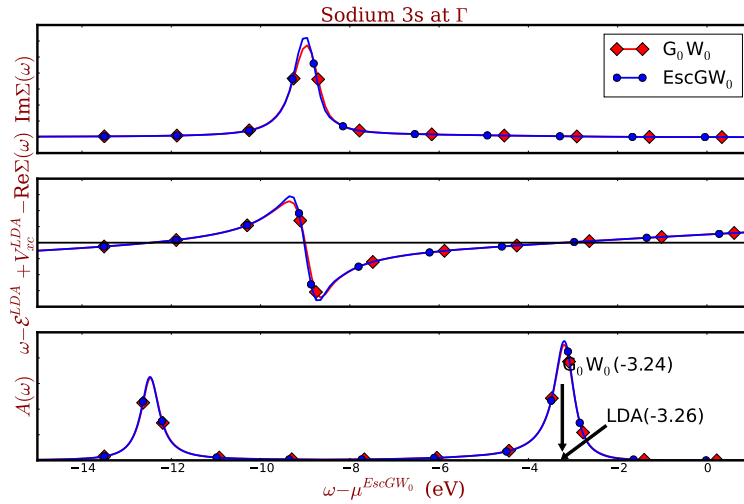
Figure 2.6: Intrinsic spectral functions of the sodium $3s$ band at the Γ point (lower panel). Red curves with diamonds are G_0W_0 results, blue curves with circles are $EscGW_0$ results. The position of the LDA band at Γ is given by the black arrow labeled LDA. The arrow labeled G_0W_0 indicates the quasi-particle energy that one would obtain by the usual first-order approximation based on a linearization of the self-energy as discussed in equation (2.44). The upper two panels show the imaginary and shifted real parts of the GW self-energy. The zero of the energy axis is set to be the $EsGW_0$ Fermi energy.

- The black arrow labeled as LDA is the KS-LDA eigenvalue $\mathcal{E}$.

- The black arrow labeled as G_0W_0 is the quasi-particle energy from G_0W_0 with linearization thus it is calculated from equation (2.44) using a G_0W_0 self-energy instead of the $EscGW_0$ one.

- The first peak in the red diamond curve shows the quasi-particle energy from G_0W_0 by solving the quasi-particle equation (2.42) with the G_0W_0 self-energy instead of the $EscGW_0$ one.

- The first peak in the blue circle curve shows the quasi-particle energy from $EscGW_0$ by solving the quasi-particle equation (2.42) with the $EscGW_0$ self-energy.

To understand the origin of the features in the spectrum, we also show the imaginary part of the GW self-energy (upper panel) as well as the shifted real part (middle panel). Note that $(\omega - \mathcal{E}^{LDA} + V_{xc}^{LDA} - \operatorname{Re}\Sigma^{GW}(\omega))$ is plotted to avoid double counting. As discussed in equations (2.37) and (2.42), when the shifted $\operatorname{Re}\Sigma^{GW}$ crosses zero, we have the quasi-particle peak in the spectral function. Red curve with diamonds are G_0W_0 results and blue curve with circles are $EscGW_0$ (i.e., updated energies in G). The imaginary part of Σ^{GW} shows one pronounced peak at about 6 eV below the quasi-particle energy, corresponding to the plasmon energy of bulk sodium. In correspondence, the real part is strongly dispersing around that energy. It crosses zero at the quasi-particle energy, giving rise to the quasi-particle peak of the bottom valence band. It is close to the band energy found in the KS-LDA indicated by the black arrow, there is just a slight band narrowing, as is also found in the homogeneous electron gas (HEG) [72]. The arrow labeled G_0W_0 indicates the quasi-particle energy that one would obtain by the usual first-order approximation based on a linearization of the self-energy as discussed in equation (2.44), which is nearly the same as the real quasi-particle energy by finding the zero crossing of shifted $\operatorname{Re}\Sigma^{GW}$ (quasi-particle peak of G_0W_0). However, there is also a second crossing, around 12 eV binding energy. This causes a second pronounced peak in the spectral function. This is the so-called `plasmaron` satellite I have mentioned before, which is a spurious peak induced by the GW approximation. It is further away from the quasi-particle peak than the plasmon energy (the distance between the QP and plasmaron satellite is $\approx$ 9.2 eV), which explains the bad agreement between G_0W_0 and experiment found also in the earlier work [9]. Energy self-consistency does not change the results significantly. The total intrinsic GW spectral functions of sodium valence state (sum over all the k-points in the Brillouin zone) in Fig. 2.7 show that the G_0W_0 and $EscGW_0$ results are almost identical.
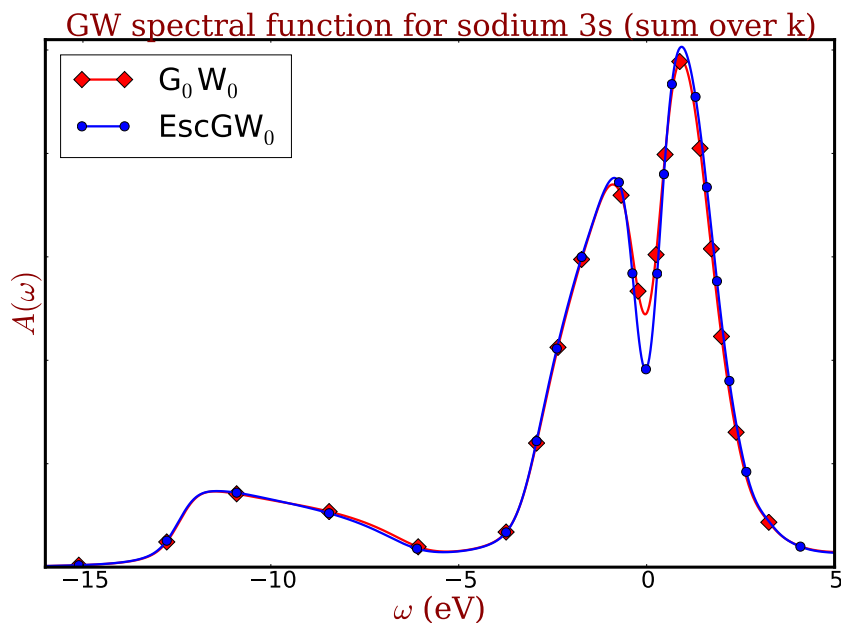
Figure 2.7: Intrinsic spectral function of the sodium $3s$ band where the spectral function of each k-point in the BZ has been summed. Red curve with diamonds are G_0W_0 results, blue curve with circles are $EscGW_0$ results. The zero of the energy axis is set to be the $EsGW_0$ Fermi energy. A Gaussian broadening of 0.3 eV has been used when plotting these two spectral functions.

The core states of sodium: the importance of self-consistency

We have seen that the G_0W_0 is sufficient to give good QP energies in the valence band region of sodium. How about the core? The results for the core levels at Γ are shown in Fig. 2.8: left and right panels are 2s and 2p results, respectively (they are analogous to Fig. 2.7). Again the G_0W_0 and $EscGW_0$ results show satellites that are of plasmaronic origin and therefore too sharp and too far away from the quasi-particle energy as compared to the plasmon frequency[23]. Two things should be noted in the core level spectra. First, G_0W_0 and $EscGW_0$ give very different results. This is due to the fact that GW shifts the core level significantly with respect to the KS-LDA as shown in table 2.1. Energy self-consistency is therefore mandatory for the core. Second, in the non-self-consistent calculation the commonly made assumption that one could calculate quasi-particle levels

---

[23]The sodium experimental photoemission spectra will be shown in Chapter 6. In particular Fig. 6.2 shows the spectra of the sodium core states and Fig. 6.5 shows the experimental spectrum of the sodium valence.
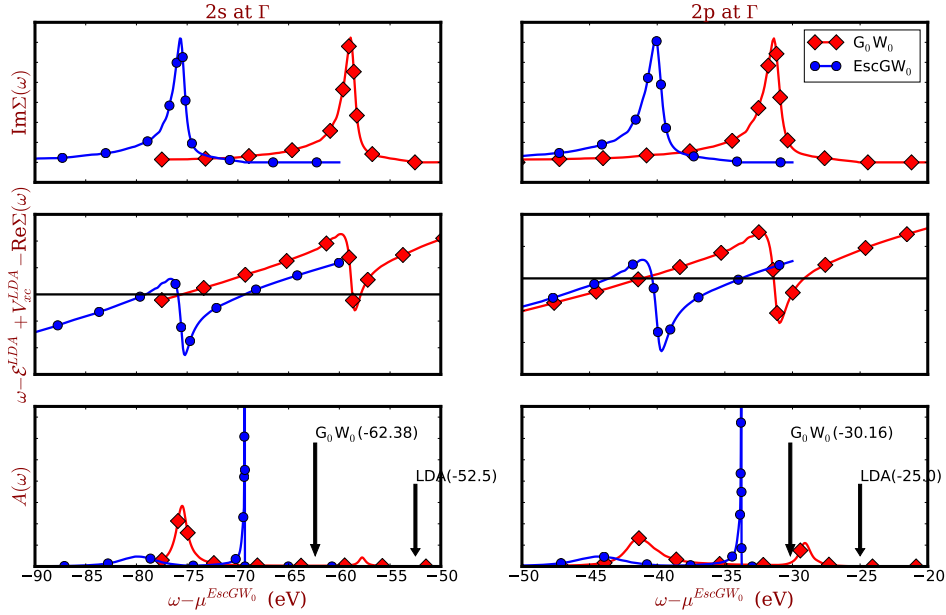
Figure 2.8: Intrinsic spectral function of the sodium $2s$ state at the Γ point (lower panel). Red curves with diamonds are G_0W_0 results, blue curves with circles are $EscGW_0$ results. The position of the LDA band at Γ is given by the black arrow labeled LDA. The arrow labeled G_0W_0 indicates the quasi-particle energy that one would obtain by the usual first-order approximation based on a linearization of the self-energy as discussed in equation (2.44). The upper two panels show the imaginary and shifted real parts of the GW self-energy. The zero of the energy axis is set to be the $EsGW_0$ Fermi energy.

from the linearized self-energy of Eq. (2.44) cannot be made. Indeed, the arrow labeled G_0W_0 indicates the quasi-particle energy that one would obtain by using that procedure: clearly, the energy is completely off with respect to the quasi-particle peak in the G_0W_0 spectral function (red curve with diamonds in Fig. 2.8). Moreover, in the non-self-consistent G_0W_0 calculation the satellite is much farther from the quasi-particle peak and the weight transfer from the quasi-particle to the satellite is huge, which cannot be justified with any particular strong correlation effect in sodium. Indeed, the situation changes drastically when self-consistent calculations are performed, as one can see from the blue curves with circles in Fig. 2.8: the satellites get closer to the quasi-particle peak (they are located at a distance ≈ 1.5 times the plasmon energy) and their intensity is reduced compared to the G_0W_0. It has been noted in several places that eigenvalue self-consistency is crucial when one is interested in GW satellites [68, 73–75]; the present example is a striking illustration.

Overall, the two core levels behave similarly, although all features discussed here are more pronounced in the deeper core. The results are summarized in the following table.

Table 2.1: Binding energies of sodium core states

methods states	LDA	G_0W_0	$EscGW_0$	experiment [47]
Na 2s (eV)	-52.5	-57.69	-69.39	-63.7
Na 2p (eV)	-25	-29	-33.79	-30.5

In conclusion, the GWA cannot describe the plasmon satellites in bulk sodium for both valence and core, as also found by many other studies of different systems (see e.g. Refs. [11,73,76]). This suggests to introduce the cumulant expansion approximation (CEA) in the next section. The CEA, inspired by the quasi-boson model, is very promising to describe well the plasmon satellites in a system like bulk sodium as it has been shown in Ref. [9].

2.3   The cumulant expansion approximation

In the previous section, we have seen the performance of the GW spectral functions illustrated by a calculation on bulk sodium. The main problem of the GW approximation is the plasmon satellites induced by the spurious `plasmaron`[24]. As discussed in section 1.1.1, the exponential expression of the exact one-body Green's function of the quasi-boson model Hamiltonian yields the plasmon satellites at exactly the plasmon energy of the system. This suggests us to look for an exponential *ansatz* of the Green's function to cure the plasmaron problem. The cumulant expansion approximation (CEA), which is right following this idea, was proposed by Lars Hedin [31] to study the satellites in the electron gas[25]. Hedin's method was based on the diagrammatic expansion of the self-energy where his approximated one-body Green's function has an exponential expression and its expansion generalizes a series of plasmon satellites. Later Gunnarsson, Meden and Schönhammer [77] and Aryasetiawan, Hedin and Karlsson [9] (their work will be refereed to as the TOC96) proposed their cumulant ideas by identifying the cumulant expansion with the self-energy

---

[24]The discussion of the plasmaron has a very long history. A detail historical review of the plasmaron problem can be found in the thesis of Dr. M. Guzzo (section 6.3 and 6.4) of Ref. [17].

[25]As far as I know, Ref. [31] of Hedin was the first cumulant attempt that is beyond the quasi-boson model Hamiltonian to study the satellites of a realistic many-body system.

expansion of the one-body Green's function. Their ideas are consistent with the one of Hedin in Ref. [31], but they gave more detailed derivations that justify the link between the cumulant expansion approximation and the GW self-energy. The CEA has been applied successfully in the *ab-initio* framework to several metal and semiconductors (see e.g. Refs. [9–12, 78]). In particular, the TOC96 in Ref. [9] was performed in the valence state of bulk sodium, leading to a huge improvement of the spectral function over the GW result, compared to the experimental spectrum.

In this section, I am going to study two different cumulant expansion approximations, namely the TOC96, and the retarded cumulant (RC) that was proposed recently by J. Kas, J. Rehr and Reining in Ref. [19]. In particular, I will study TOC96 in more detail since it has been the most widely used cumulant for the past years and its derivation it the most general.

2.3.1 The TOC96

Since we are mainly interested in the photoemission process, we will focus on the derivation of the electron removal part of the cumulant Green's function. As in the case of the GWA, we still start from the Kohn-Sham local-density approximation of the one-particle Green's function (i.e. $G_0 \to G_{ks}^{LDA}$). In TOC96, the one-particle Green's function for the `hole` ($\tau < 0$) is written as

$$G(\tau) = G_0(\tau)e^{C(\tau)} = i\theta(-\tau)e^{-i\mathcal{E}\tau + C(\tau)}\,, \tag{2.46}$$

where $\tau \equiv t_{12} = (t_1 - t_2)$, $C(\tau)$ is the so-called cumulant function, $G_0(\tau) = i\theta(-\tau)e^{-i\mathcal{E}\tau}$, and $\mathcal{E}$ is the KS-LDA eigenvalue of the corresponding state. Note that the above cumulant *ansatz* is only for the hole Green's function and the ansatz for the electron addition is $G^e(\tau) = -i\theta(\tau)e^{-i\mathcal{E}\tau + C^e(\tau)}$, indicating the decoupling between the electron and hole branches of this approach. Following [9], we can expand the cumulant Green's function in equation (2.46) in powers of the cumulant, thus we have

$$G(\tau) = G_0(\tau)\left(1 + C(\tau) + \frac{1}{2!}(C(\tau))^2 + \cdots\right) \equiv G_0(\tau)\sum_{m=0}^{\infty}\frac{C^m(\tau)}{m!}\,, \tag{2.47}$$

We can do a similar expansion for the Green's function with respect to the self-energy from the Dyson equation (2.36d)

$$G = G_0 + G_0 \Sigma G_0 + G_0 \Sigma G_0 \Sigma G_0 + \cdots, \tag{2.48}$$

where the self-energy is $\Sigma = \Sigma^{GW} - V_{xc}^{LDA}$. The cumulant can be obtained by equating terms of the same order in the above two expansions such that the first order reads

$$G_0 C = G_0 \Sigma G_0 \equiv G^{(1)}. \tag{2.49}$$

The above equation can be written in the Kohn-Sham orbitals $\psi_i(x)$ where G_0 is diagonal, which yields

$$G_{ij}^{(1)}(t_1, t_2) = \int dt_3 t_4 G_{ii}^0(t_1, t_3) \Sigma_{ij}(t_3, t_4) G_{jj}^0(t_4, t_2). \tag{2.50}$$

The self-energy contains exchange and correlation components, as well as minus the Kohn-Sham exchange-correlation potential i.e., $\Sigma(t_3, t_4) = \Sigma_c(t_3, t_4) + \Sigma_x \delta(t_3 - t_4) - V_{xc}^{LDA} \delta(t_3 - t_4)$. Writing these terms explicitly, the diagonal elements of the hole Green's function $\mathcal{G} \equiv G_{ii}^{(1)}$ becomes

$$\mathcal{G}^{(1)}(t_{12}) = -e^{-i\mathcal{E}(t_1 - t_2)} \int_{t_1}^{\infty} dt_3 \int_{-\infty}^{t_2} dt_4 \Sigma_c(t_{34}) e^{i\mathcal{E}(t_3 - t_4)}$$
$$- \left(\Sigma_x t_{12} - V_{xc}^{LDA} t_{12} \right) e^{-i\mathcal{E}(t_1 - t_2)}, \tag{2.51}$$

Note that in the above equation, Σ and V_{xc}^{LDA} are the diagonal elements only. The above equation yields a first order cumulant function for a certain state (see Eq. (2.49)) reading as

$$C(t_{12}) = i \int_{t_1}^{\infty} dt_3 \int_{-\infty}^{t_2} dt_4 \Sigma_c(t_{34}) e^{i\mathcal{E}(t_3 - t_4)} + \left(\Sigma_x - V_{xc}^{LDA} \right) t_{12}. \tag{2.52}$$

For simplicity, we drop the time-independent part of the cumulant function and define its correlation part as

$$C_c(t_{12}) = i \int_{t_1}^{\infty} \mathrm{d}t_3 \int_{-\infty}^{t_2} \mathrm{d}t_4 \Sigma_c(t_{34}) e^{i\mathcal{E}(t_3 - t_4)} \,. \tag{2.53}$$

We further put $t_2 = 0$, $t_1 = t < 0$ and $\tau = t_3 - t_4$ since we are in equilibrium. The correlation part of cumulant C_c becomes

$$\begin{aligned} C_c(t) &= i \int_t^{\infty} \mathrm{d}t' \int_{t'}^{\infty} \mathrm{d}\tau \Sigma_c(\tau) e^{i\mathcal{E}\tau} \\ &= i \int_t^0 \mathrm{d}t' \int_{t'}^{\infty} \mathrm{d}\tau \Sigma_c(\tau) e^{i\mathcal{E}\tau} + i \int_0^{\infty} \mathrm{d}t' \int_{t'}^{\infty} \mathrm{d}\tau \Sigma_c(\tau) e^{i\mathcal{E}\tau} \\ &\equiv C_0^c(t) + C_{\infty}^c(t) \,. \end{aligned} \tag{2.54}$$

In order to evaluate the above integrals, the spectral representation of Σ_c is needed, which reads (see Appendix Eq. (D.2e))

$$\Sigma_c(\omega) = \int_{-\infty}^{\mu} \mathrm{d}\omega' \frac{D(\omega')}{\omega - \omega' - i\eta} + \int_{\mu}^{\infty} \mathrm{d}\omega' \frac{D(\omega')}{\omega - \omega' + i\eta} \,, \tag{2.55}$$

where μ is the chemical potential and $D(\omega)$ is the spectral function of the correlation self-energy Σ_c. Using the Krames-Kronig relation, $D(\omega)$ reads

$$D(\omega) = -\frac{1}{\pi} \operatorname{Im} \Sigma_c(\omega) \operatorname{sgn}(\omega - \mu) \,. \tag{2.56}$$

After a Fourier transform of the spectral representation of $\Sigma_c(\omega)$ (the equations for the Fourier transform are in Appendix Eq. A.1), we have

$$\begin{aligned} \Sigma_c(\tau) &= \frac{1}{2\pi} \int \mathrm{d}\omega e^{-i\omega\tau} \Sigma_c(\omega) \\ &= i\theta(-\tau) e^{\eta\tau} \int_{-\infty}^{\mu} \mathrm{d}\omega' D(\omega') e^{-i\omega'\tau} - i\theta(\tau) e^{-\eta\tau} \int_{\mu}^{\infty} \mathrm{d}\omega' D(\omega') e^{-i\omega'\tau} \,, \end{aligned} \tag{2.57}$$

where we have used the spectral representation of the Heaviside step function (see Appendix Eq. (A.2)). Now we can evaluate the integrals in equation (2.54):

$$
\begin{aligned}
C_0(t) &= i \int_t^0 \mathrm{d}t' \int_{t'}^\infty \mathrm{d}\tau \Sigma_c(\tau) e^{i\mathcal{E}\tau} \\
&= i \int_t^0 \mathrm{d}t' \int_{t'}^\infty \mathrm{d}\tau e^{i\mathcal{E}\tau} \left(i\theta(-\tau) e^{\eta\tau} \int_{-\infty}^\mu \mathrm{d}\omega D(\omega) e^{-i\omega\tau} - i\theta(\tau) e^{-\eta\tau} \int_\mu^\infty \mathrm{d}\omega D(\omega) e^{-i\omega\tau} \right) \\
&= -\int_t^0 \mathrm{d}t' \int_{t'}^0 \mathrm{d}\tau \int_{-\infty}^\mu \mathrm{d}\omega e^{i(\mathcal{E}-\omega-i\eta)\tau} D(\omega) + \int_t^0 \mathrm{d}t' \int_0^\infty \mathrm{d}\tau \int_\mu^\infty \mathrm{d}\omega e^{i(\mathcal{E}-\omega+i\eta)\tau} D(\omega) \\
&= i \int_t^0 \mathrm{d}t' \int_{-\infty}^\mu \mathrm{d}\omega \frac{1 - e^{i(\mathcal{E}-\omega-i\eta)\tau}}{\mathcal{E}-\omega-i\eta} D(\omega) + i \int_t^0 \mathrm{d}t' \int_\mu^\infty \mathrm{d}\omega \frac{D(\omega)}{\mathcal{E}-\omega+i\eta} \\
&= i \int_t^0 \mathrm{d}t' \left(\int_{-\infty}^\mu \mathrm{d}\omega \frac{D(\omega)}{\mathcal{E}-\omega-i\eta} + \int_\mu^\infty \mathrm{d}\omega \frac{D(\omega)}{\mathcal{E}-\omega+i\eta} \right) + \int_{-\infty}^\mu \mathrm{d}\omega \frac{e^{i(\mathcal{E}-\omega-i\eta)t} - 1}{(\mathcal{E}-\omega-i\eta)^2} D(\omega) \\
&= -i\Sigma_c(\mathcal{E})t + \int_{-\infty}^\mu \mathrm{d}\omega \frac{e^{i(\mathcal{E}-\omega-i\eta)t}}{(\mathcal{E}-\omega-i\eta)^2} D(\omega) + \frac{\partial}{\partial\omega'} \int_{-\infty}^\mu \mathrm{d}\omega \frac{D(\omega)}{\omega'-\omega-i\eta}\bigg|_{\omega'=\mathcal{E}} \\
&= -i\Sigma_c(\mathcal{E})t + \int_{-\infty}^\mu \mathrm{d}\omega \frac{e^{i(\mathcal{E}-\omega-i\eta)t}}{(\mathcal{E}-\omega-i\eta)^2} D(\omega) + \frac{\partial\Sigma_c^h(\omega)}{\partial\omega}\bigg|_{\omega=\mathcal{E}}\,,
\end{aligned}
\tag{2.58}
$$

where we have defined the hole part of the correlation self-energy Σ_c^h that reads

$$
\Sigma_c^h(\omega) = \int_{-\infty}^\mu \mathrm{d}\omega' \frac{D(\omega')}{\omega-\omega'-i\eta}\,.
\tag{2.59}
$$

The second integral in equation (2.54) can be evaluated in the same way, leading to

$$
C_\infty(t) = i \int_0^\infty \mathrm{d}t' \int_{t'}^\infty \mathrm{d}\tau \Sigma_c(\tau) e^{i\mathcal{E}\tau} = \frac{\partial\Sigma_c^e(\omega)}{\partial\omega}\bigg|_{\omega=\mathcal{E}}\,,
\tag{2.60}
$$

with the electron part of the correlation self-energy Σ_c^e defined as

$$
\Sigma_c^e(\omega) = \int_\mu^\infty \mathrm{d}\omega' \frac{D(\omega')}{\omega-\omega'+i\eta}\,.
\tag{2.61}
$$

We now add the part due to the time-independent quantities which are Σ_x and V_{xc}^{LDA} in the cumulant function (see Eq. (2.52)). The hole Green's function of TOC96 finally reads

$$
\mathcal{G}^{C96}(\tau) = i\theta(-\tau)e^{-i\mathcal{E}\tau}\exp\left(-i\Sigma(\mathcal{E})\tau + \left.\frac{\partial\Sigma(\omega)}{\partial\omega}\right|_{\omega=\mathcal{E}} + \int_{-\infty}^{\mu} d\omega\frac{e^{i(\mathcal{E}-\omega-i\eta)\tau}D(\omega)}{(\mathcal{E}-\omega-i\eta)^2}\right);
$$

$$
= i\theta(-\tau)e^{-i\mathcal{E}\tau}\exp\left(-i\Sigma(\mathcal{E})\tau + \left.\frac{\partial\Sigma(\omega)}{\partial\omega}\right|_{\omega=\mathcal{E}} + \frac{1}{\pi}\int_{-\infty}^{\mu} d\omega\frac{e^{i(\mathcal{E}-\omega-i\eta)\tau}\,\text{Im}\,\Sigma^h(\omega)}{(\mathcal{E}-\omega-i\eta)^2}\right).
$$

(2.62)

The electron Green's function can be calculated analogously. Now one can understand that the central quantity of the TOC96 is actually the GW self-energy. However, instead of solving the Dyson equation using the GW self-energy, the cumulant function is calculated from a double time integral of the shifted GW self-energy (see Eq. (2.52)). As a result, one can show that the CEA yields the exact Green's function of the quasi-boson Hamiltonian (see Eq. (1.1)) (this will be discussed in Chapter 4).

Now we can give an analysis of each term in the cumulant function. The first term in the exponential $\Sigma(\mathcal{E})$ induces an energy shift with respect to the KS-LDA eigenvalue $\mathcal{E}$ such that the final quasi-particle energy from TOC96 is $\mathcal{E} + \Sigma(\mathcal{E})$, which is essentially the GW quasi-particle energy (see equation (2.42)) whose real and imaginary parts are $\mathcal{E} + \text{Re}\,\Sigma(\mathcal{E})$ and $\text{Im}\,\Sigma(\mathcal{E})$, respectively. In particular, the real part of the QP energy reads

$$
\varepsilon_{QP} = \mathcal{E} + \text{Re}\,\Sigma(\mathcal{E}) = \mathcal{E} - V_{xc}^{LDA} + \text{Re}\,\Sigma^{G_0W_0}(\mathcal{E}) \equiv \mathcal{E} - V_{xc}^{LDA} + \text{Re}\,\Sigma^{EscGW_0}(\varepsilon_{QP}).
$$

(2.63)

The second term gives the normalized quasi-particle weight. The derivative of the imaginary part of self-energy at $\mathcal{E}$ is in general very small, i.e. $\left.\frac{\partial\,\text{Im}\,\Sigma(\omega)}{\partial\omega}\right|_{\omega=\mathcal{E}} \approx 0$. Therefore the QP renormalization factor $\mathbf{Z}$ of TOC96 reads

$$
\mathbf{Z}^{C96} = \exp\left(\left.\frac{\partial\,\text{Re}\,\Sigma(\omega)}{\partial\omega}\right|_{\omega=\mathcal{E}}\right).
$$

(2.64)

Note that the quasi-particle renormalization factor from TOC96 is different from the GWA in equation (2.45). This issue will be discussed in Chapter 4.

The third term yields a series of plasmon satellites. Using the Kramers-Kronig relation (see appendix Eq. (A.3)), supposing $\mathrm{Im}\,\Sigma^h \approx \pi\lambda\delta(\omega - \mathcal{E} + \omega_p)$ where ω_p is the plasmon energy (suppose no dispersion for the moment) and λ is the weight of Σ^h, this term becomes

$$\exp\left(\frac{\lambda}{\omega_p^2}e^{i\omega_p\tau}\right) = \sum_{m=0}^{\infty}\left(\frac{\lambda}{\omega_p^2}\right)^m e^{im\omega_p\tau}\,, \tag{2.65}$$

which generates satellites at ω_p, $2\omega_p$ *etc.*.

The spectral function of sodium valence $3s$ at the Γ point calculated from TOC96 in equation (2.62) is shown in figure 2.9. The black dashed curve is $\mathrm{G_0W_0}$ spectral function reproduced from Ref. [9], which is slightly different from my GW calculation (red curve with diamonds that is the same curve in the lower panel of figure 2.7), especially in the plasmaron satellite region. This is because I have used more k-points in the Brillouin zone than Aryasetiawan *et al.*. My $\mathrm{G_0W_0}$ spectrum is almost identical to the EscGW$_0$ result as shown in figure 2.7. Similar $\mathrm{G_0W_0}$ spectral functions can be also found in Ref. [79], which confirms my $\mathrm{G_0W_0}$ calculation. The cumulant expansion approximation calculated from equation (2.62) is shown by the black solid curve, where the plasmon satellite replica are observed at the energy difference ≈ 6 eV that is the plasmon energy of sodium.

Fig. 2.9 shows that TOC96 can describe the plasmon satellites in sodium, much better than the GWA. What about the constraints I have mentioned in section 1.3? One can proof that TOC96 does not conserve particle number, since[26]

$$\int_{-\infty}^{\infty} \mathrm{d}\omega\, \mathcal{G}^{C96}(\omega) \equiv \int_{-\infty}^{\mu} \mathrm{d}\omega\, \mathcal{G}^{C96}(\omega) < 1\,. \tag{2.66}$$

Another drawback of TOC96 is that it only gives satellites on one side of the quasiparticle peak due to the decoupling of electron and hole branches in its original ansatz (see Eq. (2.46)). Taking equation (2.62) for example, the expansion of the last term only gives satellites below the chemical potential μ. It is valid when the orbital is far from the Fermi level. However, when the orbital is close to the Fermi level where the states are partially

---

[26]This is because the electron self-energy Σ^e in Eq. (2.61) enters the **Z**-factor through Eq. (2.64), which determines the normalization of the spectrum. However, it does not enter in the last term of $\mathcal{G}^{C96}$ in Eq. (2.62) that is responsible for producing the plasmon satellites. Thus the TOC96 conserves the particle number only when $\Sigma^e \approx 0$. This issue will be discussed in detail in Chapter 4.
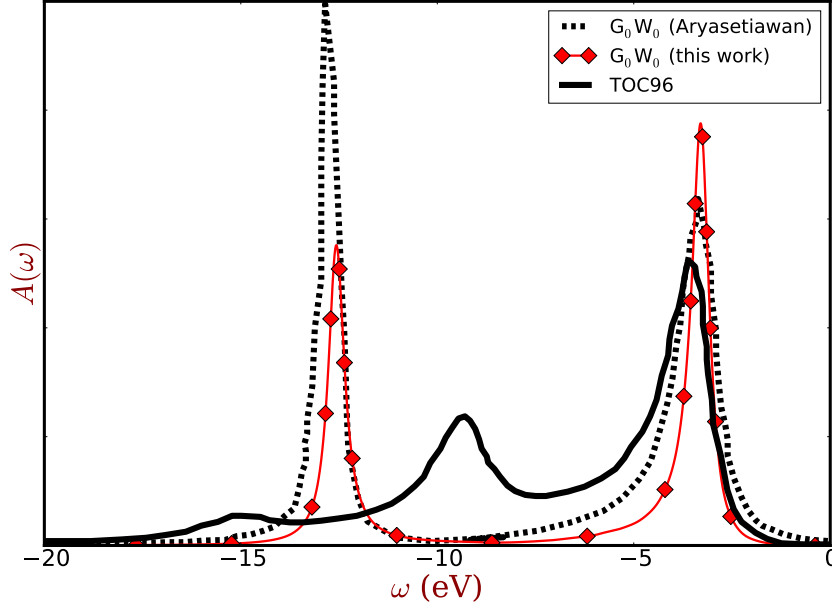
Figure 2.9: Intrinsic spectral function of the sodium valence $3s$ at the Γ point. Black curves are reproduced from Ref. [9]. Dashed and solid curves are G_0W_0 and cumulant spectral functions, respectively. The red curve with diamonds is the G_0W_0 spectral function from my calculation that was also shown in the lower panel of figure 2.7. To have a good comparison, I have shifted the my G_0W_0 spectrum by 0.1 eV such that the QP peak is centered at the same energy as the result of Aryasetiawan *et al.* [9].

occupied, as discussed in section 1.1.1, there should be satellites on the other side of the quasi-particle peak to conserve the total spectrum (i.e. $\int A(\omega)\mathrm{d}\omega = 1$). Actually these two drawbacks are linked because the reason why this cumulant does not conserve particle number is the fact that it is not able to give the correct spectrum on the other side of the quasi-particle induced by the partially occupied states. I will discuss in detail about the performance of the TOC96 in Chapter 4.

2.3.2   The retarded cumulant

An attempt of going beyond the decoupling of electron and hole branches that has been used for TOC96 was proposed by J. Kas, J. Rehr and Reining in 2014 [19]. In Ref. [19] they stated that the reason why the traditional time-ordered cumulants (TOCs) in Refs. [9, 11, 12, 78] have no spectral weight on the right hand side of the QP peak (for electron removal) is

due to the use of the time-ordered Green's function in the cumulant ansatz. Therefore a simple alternative way of going beyond is the use of the retarded counterparts[27]. The relation between the time-ordered and retarded quantities is summarized in Appendix D. The retarded cumulant ansatz of Ref. [19] reads

$$G^{RC}(t) = G_0^R(t)e^{C^R(t)},\qquad(2.67)$$

which is different from the ansatz of TOC96 just in the use of the corresponding retarded quantities. The retarded cumulant function is obtained by solving symbolically the Dyson equation with the retarded quantities

$$G_0^R e^{C^R} = G_0^R \Sigma^R G_0^R.\qquad(2.68)$$

All the derivations are the same as TOC96 but replacing the time-ordered quantities by the retarded counterparts. An illustration of the spectra in the homogeneous electron gas is shown in Fig. 2.10 taken from Ref. [19]. The spectral functions for a range of states k are shown. The black curves are spectra from a G_0W_0 calculation. As discussed before they fail to produce the multiple satellites while both cumulants exhibit multiple satellites representing the coupling to plasmons. In particular, in a very deep state ($k/k_F = 0.0$) the spectral function of the time-ordered cumulant (e.g. TOC96) (green filled curve) is nearly identical with the retarded cumulant (red thick curve). This is consistent with my above analysis about TOC96. When we go to the states that are close to the the Fermi state k_F, the retarded cumulant gives satellites on both sides of the QP peak, however the time-ordered cumulant only has satellites on one side. Especially in the state where $k/k_F = 1.0^+$, the retarded cumulant yields a spectrum that is almost symmetric with respect to the chemical potential. Actually the GWA, although it gives bad satellites, shows similar behavior (satellites on both sides of the QP peak).

---

[27]The difference between the time-ordered and retarded self-energies can be found in Appendix Eq. (D.1). In the time-ordered self-energy, there are different θ functions that determine different time-ordering of $\Sigma^>$ and $\Sigma^<$. As a consequence, part of $\Sigma^>$ will be dropped in the double time integral in Eq. (2.58). If we use Σ^R where both $\Sigma^<$ and $\Sigma^>$ have the same time-ordering, the full self-energy will be integrated on the same footing. The resulting integration of Σ^R can be found in Eq. (3.63).
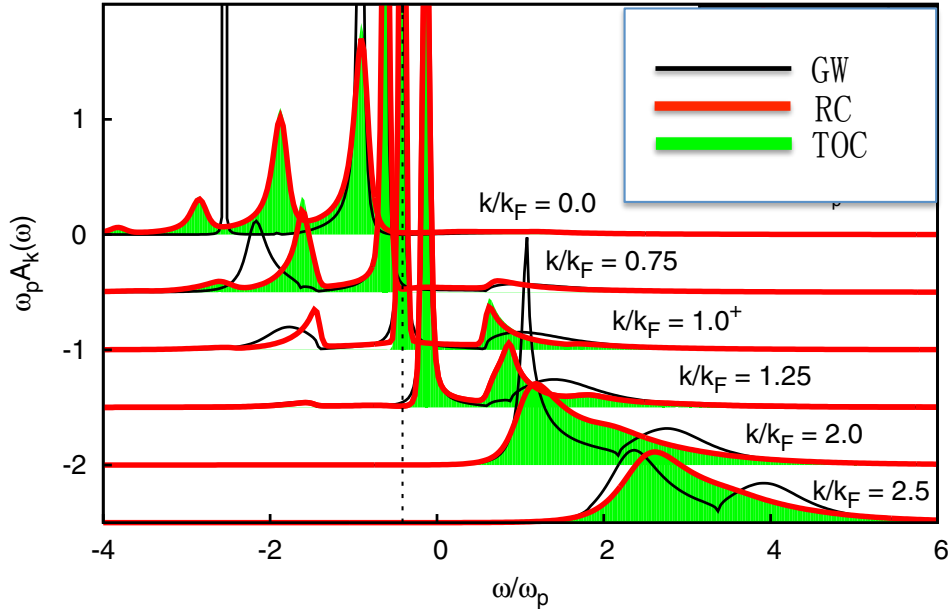
Figure 2.10: The comparison of the spectra calculated from the GWA (G_0W_0), the time-ordered cumulant, and the retarded cumulant in the homogeneous electron gas at zero temperature for $r_s = 4.0$ (which corresponds to the sodium density) in units of the plasmon energy ω/ω_p. The figure is taken from Ref. [19]. The spectral functions $A_k(\omega)$ for a range of states k are shown. The black curves are the GWA results, the thick red curves are the retarded cumulant results and the time-ordered cumulant (TOC) spectra are shown by the green filled curves. The dashed vertical line is set at the chemical potential μ.

Fig. 2.10 is an illustration of the disadvantages of the traditional time-ordered cumulant based on the time-ordered formalism, which yields the decoupling of electron and hole branches. The retarded cumulant seems to be a better method of going beyond the time-ordered cumulant. However, we will see in the following Chapters that, it has some serious drawbacks. A new derivation of this retarded cumulant will be shown in Chapter 3 and a detailed study and discussion will be given in the following Chapters.

2.4   Summary

In this chapter, I have briefly reviewed state-of-the-art theories in electron spectroscopy including the Kohn-Sham density functional theory (KS-DFT), the GW approximation (GW), and the cumulant expansion approximation (CEA). The derivations and links between dif-

ferent methods have been shown. In practice, we start from a Kohn-Sham calculation with the local-density approximation such that the Kohn-Sham eigenvalues and orbitals are obtained. The GW self-energy and Green's function can be calculated with the Kohn-Sham ingredients. The cumulant expansion approximation can be considered as a further step after the GWA because it uses the GW self-energy as its input. Instead of solving the Dyson equation, the cumulant Green's function is calculated from an exponential ansatz.

The spectral functions calculated from different methods are discussed such that the advantages and disadvantages of different approximations are understood. The KS-DFT based on the independent-particle picture with a static local effective potential can only describe the band structure qualitatively and it cannot yield satellites in the spectrum. The GWA based on the quasi-particle picture and a non-local frequency-dependent self-energy, usually improves the band structure with respect to KS-DFT and it yields satellites in the spectrum, but it often fails to describe them correctly. The cumulant expansion approximation, on the other hand, can describe multiple satellites that represent the coupling to plasmon excitations. However, its performance in the valence band region has to be assessed in detail, and as we will see, improvements are needed.

Chapter 3

Unified derivations of the GWA and CEA

In this chapter, I will show unified derivations of the GW approximation and the cumulant expansion approximations including the time-ordered cumulant developed in our group (i.e. the TOC11 from Refs. [11, 20]) and the retarded cumulant that yields the same Green's function as the retarded cumulant from Ref. [19]. The derivations will be shown in this chapter starting from the full functional differential equation of one-body Green's function (also known as the *Kadanoff-Baym equation* [80]), which are different from previous derivations (e.g. Hedin's equations [5]), leading to a more compact formalism for treating the many-body problem. Therefore the proposed derivations can be used for increasingly accurate approximations.

3.1 Linearization

The linearization approximation was proposed by Dr. G. Lani in her PhD thesis [18] and has been published in Ref. [81]. Since all the cumulant expansion approximations can be derived based on the linearization[1], I will briefly explain this process in this section. The `full functional differential equation` (FDE) of the one-particle Green's function has

---

[1]An alternative derivation will be shown in Appendix C where the cumulant expansion approximation can be derived without the linearization.

been derived in Appendix B.2. It reads

$$G(1, 2; \phi) = G_0(1, 2) + \int d3 G_0(1, 3)\phi(3)G(3, 2; \phi) + \int d3 G_0(1, 3)V_H(3; \phi)G(3, 2; \phi)$$
$$+ i \int d34 G_0(1, 3)v_c(3, 4^+)\frac{\delta G(3, 2; \phi)}{\delta \phi(4)}, \tag{3.1}$$

where

$$V_H(3; \phi) = -i \int d4 v_c(3, 4^+)G(4, 4^+; \phi), \tag{3.2}$$

is the Hartree potential in presence of ϕ, G_0 is the non-interacting Green's function, and ϕ is an external time-dependent perturbation.

If one could solve the above FDE, the solution at $\phi = 0$ would be the desired one-particle Green's function G of a many-body system in equilibrium. Note that when the last term is neglected (i.e. G does not change with the variation of ϕ), one retrieves the Hartree approximation for G. Instead, the variation of the Green's function goes beyond the independent-particle picture; it contains the information that excitations are coupled through the last term.

As pointed out in the book by Baym and Kadanoff [80], " there is no known technique to solve functional differential equations like (3.1) in an efficient way." Instead, the equation can be used as a starting point for increasingly accurate approximations.

One of the complications is the fact that the density $\rho(1; \phi) = -iG(1, 1^+; \phi)$ in the Hartree potential in presence of the perturbation ϕ Eq. (3.2) depends on the Green's function such that the third term in Eq. (3.1) is quadratic in G, which makes the whole equation nonlinear. To overcome this problem, we introduce the so-called `linearization approximation` by a Taylor expansion of $V_H(\phi)$ and keep until the linear order term in ϕ:

$$V_H(3; \phi) \approx -i \int d4 v_c(3, 4) \left. G(4, 4^+; \phi)\right|_{\phi=0} - i \int d45 v_c(3, 4^+) \left.\frac{\delta G(4, 4^+; \phi)}{\delta \phi(5)}\right|_{\phi=0} \phi(5), \tag{3.3}$$

where the higher order terms $\mathcal{O}(\phi^2)$ are neglected leading to a linear response of the Hartree potential with respect to the external perturbation.

67

The linearized Hartree potential can be written in two terms:

$$V_H(3; \phi) \equiv V_H^{(0)}(3) + V_H^{(1)}(3; \phi), \tag{3.4}$$

where the first term on the right hand side of the above equation $V_H^{(0)} \equiv v_c \rho$ becomes the Hartree potential in equilibrium (i.e. $\phi = 0$).

The linearization is a reasonable approximation since we are only interested in the solution for vanishing external perturbation ϕ. The first term in the Hartree potential does not depend on ϕ, which suggests to introduce the Hartree Green's function defined as

$$G_H(1,2) \equiv G_0(1,2) + \int d3 G_0(1,3) V_H^{(0)}(3) G_H(3,2). \tag{3.5}$$

Now we want to replace G_0 by G_H in the functional differential equation (3.1). To this end we invert the Dyson equation

$$\int d12 G_0^{-1}(4,1) G_H(1,2) G_H^{-1}(2,5) = \int d12 G_0^{-1}(4,1) G_0(1,2) G_H^{-1}(2,5)$$
$$+ \int d123 G_0^{-1}(4,1) G_0(1,3) V_H^{(0)}(3) G_H(3,2) G_H^{-1}(2,5), \tag{3.6}$$

which yields

$$G_0^{-1}(4,5) = G_H^{-1}(4,5) + V_H^{(0)}(4)\delta(4-5). \tag{3.7}$$

The same trick can be used for the functional differential equation (3.1) (with the linearized V_H in Eq. (3.4)) whose inverse form reads (the arguments have been dropped for simplicity)

$$G^{-1} = G_0^{-1} - (V_H + \phi) - iv_c \frac{\delta G}{\delta \phi} G^{-1}$$
$$= G_H^{-1} - (V_H^{(1)} + \phi) - iv_c \frac{\delta G}{\delta \phi} G^{-1}. \tag{3.8}$$

Now we re-invert the above equation by multiplying with G and G_H on both sides and finally we get the linearized differential equation (LDE) in terms of G_H instead of G_0, which reads

$$
\begin{aligned}
G(1,2;\phi) = {} & G_H(1,2) + i \int \mathrm{d}34 G_H(1,3) v_c(3,4^+) \frac{\delta G(3,2;\phi)}{\delta \phi(4)} \\
& - i \int \mathrm{d}3 G_H(1,3) \left(\int \mathrm{d}45 v_c(3,4^+) \left. \frac{\delta G(4,4^+;\phi)}{\delta \phi(5)} \right|_{\phi=0} + i\delta(3-5) \right) \phi(5) G(3,2;\phi) \,.
\end{aligned}
$$

(3.9)

The term in the large bracket fits the definition of the inverse dielectric function ϵ^{-1} in Eq. (2.25), i.e.

$$
\epsilon^{-1}(3,5) = -i \int \mathrm{d}4 v_c(3,4^+) \left. \frac{\delta G(4,4^+;\phi)}{\delta \phi(5)} \right|_{\phi=0} + \delta(3-5) \,.
$$

(3.10)

With this, the LDE becomes

$$
\begin{aligned}
G(1,2;\phi) = {} & G_H(1,2) + \int \mathrm{d}35 G_H(1,3) \epsilon^{-1}(3,5) \phi(5) G(3,2;\phi) \\
& + i \int \mathrm{d}345 G_H(1,3) \epsilon^{-1}(5,4) v_c(3,4^+) \frac{\delta G(3,2;\phi)}{\delta \int \mathrm{d}6 \epsilon^{-1}(5,6)\phi(6)} \\
= {} & G_H(1,2) + \int \mathrm{d}3 G_H(1,3) \bar{\phi}(3) G(3,2;\phi) + i \int \mathrm{d}34 G_H(1,3) W(3,4^+) \frac{\delta G(3,2;\phi)}{\delta \bar{\phi}(4)} \,,
\end{aligned}
$$

(3.11)

where we have used the definition of the dynamical screened Coulomb interaction W in Eq. (2.30), and the screened external perturbation $\bar{\phi}$ is defined as

$$
\bar{\phi}(1) = \int \mathrm{d}2 \epsilon^{-1}(1,2) \phi(2) \,.
$$

(3.12)

Equation (3.11) is the final linearized differential equation that we are going to use to derive the GW and the cumulant expansion approximations where the dynamically screened Coulomb interaction W is the central quantity. The first term on the right hand side of the linearized differential equation (3.11) represents the propagation of particles in the Hartree potential, the second term describes the propagation in the screened external perturbation,

69

while the last term contains all the complicated `exchange` and `correlation` effects of the system where all the unknown is stored.

3.2 The GW approximation from the linearized differential equation

In section 2.2, I have shown the traditional way of deriving the GW approximation from Hedin's equations by neglecting the three-point vertex correction, i.e. $\tilde{\Gamma} = 1$. Since we have re-derived all the equations from the exact functional differential equation (3.1) and re-formulated the terms, as well as proposed the linearization approximation, the GW approximation can be derived from our linearized differential equation in a more compact way. The reason why we prefer our more compact derivation is because the linearized differential equation (3.11) provides an opportunity to derive further approximations e.g. the GWA and the CEA at the same footing. Moreover, the linearized differential equation provides possibilities to go beyond these present approximations in a way that it is more convenient than dealing with the three-point vertex function in Hedin's equations.

In order to get the GWA, we start from the linearized differential equation which reads

$$
G(1,2;\phi) = G_H(1,2) + \int d3 G_H(1,3)\bar{\phi}(3)G(3,2;\phi) + i \int d34 G_H(1,3)W(3,4^+)\frac{\delta G(3,2;\phi)}{\delta\bar{\phi}(4)}.
$$

(3.13)

The simplest approximation to the above equation is[2]

$$
\left.\frac{\delta G(3,2;\phi)}{\delta\bar{\phi}(4)}\right|_{\phi=0} = \left.\frac{\delta\tilde{G}(3,2;\bar{\phi})}{\delta\bar{\phi}(4)}\right|_{\phi=0} \approx G(3,4)G(4,2).
$$

(3.14)

Like the random phase approximation, the above approximation neglects the interaction between electron and hole. After this approximation, $\phi = 0$ can be taken in the LDE, such

---

[2]Note that the functional of the Green's function on ϕ (i.e., $G[\phi]$) is different from the functional of the Green's function on $\bar{\phi}$ (i.e., $\tilde{G}[\bar{\phi}]$). For the sake of simplicity, I will keep using $G[\phi]$ instead of $\tilde{G}[\bar{\phi}]$ in the following. This is reasonable because we are finally only interested in the Green's function in equilibrium where $\phi = 0$.

that in equilibrium it becomes a Dyson equation that reads

$$G(1,2) = G_H(1,2) + \int \mathrm{d}34 G_H(1,3)\Sigma_{xc}(3,4)G(4,2)\,, \qquad (3.15)$$

where the self-energy is defined as

$$\Sigma_{xc}(1,2) \equiv iG(1,2)W(1,2^+)\,. \qquad (3.16)$$

These two equations (3.15) and (3.16) are equivalent to Hedin's equations (2.34) when the vertex correction is neglected, where the equations leading to the GWA are

$$G(1,2) = G_0(1,2) + \int \mathrm{d}34 G_0(1,3)\Sigma(3,4)G(4,2)\,;$$

$$\Sigma(1,2) = V_H^{(0)}(1)\delta(1,2) + iG(1,2)W(1,2^+)\,.$$

The GW approximation involves hence two approximations: a linearization of the density response (V_H) of the system to the perturbation induced by the electron addition or removal and an approximation of the coupling of excitations, which leads to $\Sigma = iGW$.

Often the GWA is used with two further approximations: first, the Green's function G that appears in Eq. (3.16) is replaced by an independent-particle one, for example a Kohn-Sham Green's function. Second, W is calculated in the RPA. As our derivation shows, these are additional approximations, not indispensable for the GWA. Instead, the derivation suggests that in principle W should be the exact linear response screened Coulomb interaction, which is the time-ordered counterpart of the measurable retarded screened interaction (often called test-charge test-charge interaction instead of the test-charge test-electron one), and that the self-energy should be built with the self-consistent Green's function G. As we will see later, the excitations contained in W directly show up in the satellites. This allows one to confirm that, in agreement with our derivation, W should indeed be the physical screened interaction, and *not* its RPA version.

However, deriving GW from the LDE is not our main purpose, but just to prove that the linearization is a good approximation and the LDE is a good starting point to derive

some approximation beyond the GWA. As I will show in the next section, the cumulant expansion approximation can be also derived from this LDE, yielding a similar Green's function as the TOC96 in Eq. (2.62).

3.3 The TOC11 from the linearized differential equation

In section 2.3 I have introduced the TOC96. In this section, I am going to show the derivation of the TOC11 of Refs. [11,17]. I have re-derived this cumulant and introduced a different derivation in Ref. [20]. But for the sake of compactness, the derivation based on Refs. [11,17] will be shown in this section.

3.3.1 Cumulant from Decoupling approximation

Again we start from the linearized differential equation (3.11). The approximation I am going to use to derive the TOC11 is called the `decoupling approximation`. Following the idea of Ref. [11], I approximately decouple the LDE by supposing that $G(\phi)$ and G_H are diagonal in the same, ϕ-independent, basis (e.g. the Kohn-Sham orbitals). For each diagonal matrix element in such a basis, the LDE becomes

$$\mathcal{G}(t_{12}; \phi) = \mathcal{G}_H(t_{12}) + \mathcal{G}_H(t_{13})\bar{\phi}_{ii}(t_3)\mathcal{G}(t_{32}; \phi) + i\sum_{kl}\mathcal{G}_H(t_{13})W_{kl}^{ii}(t_{34})\frac{\partial\mathcal{G}(t_{32}; \phi)}{\partial\bar{\phi}_{kl}(t_4)}, \quad (3.17)$$

where $\mathcal{G} \equiv G_{ii}$ represents the diagonal elements of the Green's function, the short notation of $t_{12} \equiv (t_1, t_2)$ has been used, and the matrix elements of W is defined as

$$W_{ij}^{kl}(t_{34}) \equiv \int dx_1 x_2\, \varphi_k^*(x_1)\varphi_i(x_2)W_0(x_1, x_2, t_{34})\varphi_j^*(x_2)\varphi_l(x_1)\,. \quad (3.18)$$

Note that I have changed the functional derivative to a partial derivative, since I suppose the basis to be discrete, which corresponds to the calculations in practice. Now if one iterates the above equation for $\mathcal{G}(\phi)$, it turns out that $\mathcal{G}(\phi)$ depends only on the element $\bar{\phi}_{ii}$, i.e. the diagonal part of $\bar{\phi}$. As a consequence, $\dfrac{\partial\mathcal{G}(t_{32}; \phi)}{\partial\bar{\phi}_{kl}}$ is nonzero only when $k = l = i$, which eliminates the sum over k and l in the last term of the above equation. Finally we have a

scalar differential equation that reads

$$\mathcal{G}(t_{12}) = \mathcal{G}_H(t_{12}) + \mathcal{G}_H(t_{13})\bar{\phi}_{ii}(t_3)\mathcal{G}(t_{32}) + i\mathcal{G}_H(t_{13})\mathcal{W}(t_{34})\frac{\partial \mathcal{G}(t_{32})}{\partial \bar{\phi}_{ii}(t_4)}, \qquad (3.19)$$

where

$$\mathcal{W}(t_{12}) = W_{ii}^{ii}(t_{12}) = \int \mathrm{d}x_1 x_2 |\varphi_i(x_1)|^2 |\varphi_i(x_2)|^2 W(x_1, x_2, t_{12}) \qquad (3.20)$$

are the diagonal elements of the screened interaction W. Note that with the decoupling hypothesis that all Green's functions are diagonal automatically, only the diagonal elements of W are needed but without any further approximation on W. The scalar equation (3.19) can be solved exactly. Since it is a first order differential equation, it has more than one solution. Excluding a phase transition, the physical solution is the one that connects to the non-interacting one when $v_c \to 0$ [81]. This solution describes one orbital propagating in the medium given by $\mathcal{W}$ that represents the effects of all other electrons.

For the external potential $\phi = 0$, the solution of equation (3.19) for an occupied state[3] reads

$$\mathcal{G}(t_{12}) = \mathcal{G}_H(t_{12}) \exp\left(-i \int_{t_1}^{t_2} \mathrm{d}t' \int_{t'}^{t_2} \mathrm{d}t'' \, \mathcal{W}(t' - t'')\right), \qquad (3.21)$$

where $\mathcal{G}_H$ contains the effect of the Hartree potential constructed with the ground state density (i.e. at $\phi = 0$) as shown in equation (3.5). The double integral term in the exponential corresponds to the cumulant function $C(\tau)$ in Eq. (2.46). Suppose we are calculating the Green's function of some occupied state, $\mathcal{G}_H(t_{12})$ is non-zero only when $t_1 < t_2$. The time-ordering in the double integral then becomes $t_1 < t' < t'' < t_2$, which means that only the $t' < t''$ part of $\mathcal{W}(t' - t'')$ is included in the cumulant function. This is due to the decoupling approximation we have used in Eq. (3.19) when deriving this cumulant: the electron and hole branches are totally decoupled.

The screened interaction contains two parts, i.e. $W = v_c + W_c$ where the second term represents the correlation part of W that is time-dependent. We can write the correlation part of the screened interaction into its spectral representation (see Appendix (D.2c)) as

---

[3]Strictly speaking, to say one certain state is occupied or unoccupied is not always correct because states can be partially occupied. Throughout this thesis, an occupied state is refereed to as a state below the Fermi level and an unoccupied state is refereed to be a state above the Fermi level.

what we did for Σ_c in Eq. (2.55), which yields

$$\mathcal{W}_c(\omega) = \int_{-\infty}^{0} d\omega' \frac{B(\omega')}{\omega - \omega' - i\eta} + \int_{0}^{\infty} d\omega' \frac{B(\omega')}{\omega - \omega' + i\eta} \equiv \mathcal{W}_c^h(\omega) + \mathcal{W}_c^e(\omega), \qquad (3.22)$$

where[4]

$$B(\omega) = -\frac{1}{\pi} \operatorname{Im} \mathcal{W}(\omega)\operatorname{sgn}(\omega - \mu). \qquad (3.23)$$

Fourier transforming $\mathcal{W}_c(\omega)$ to time domain, we have

$$\mathcal{W}_c(\tau) = i\theta(-\tau)e^{\eta\tau} \int_{-\infty}^{\mu} d\omega' B(\omega')e^{-i\omega'\tau} - i\theta(\tau)e^{-\eta\tau} \int_{\mu}^{\infty} d\omega' B(\omega')e^{-i\omega'\tau}. \qquad (3.24)$$

Due to the time-ordering $t' < t''$, only

$$\mathcal{W}_c^h(\tau) = i\theta(-\tau)e^{\eta\tau} \int_{-\infty}^{\mu} d\omega' B(\omega')e^{-i\omega'\tau}, \qquad (3.25)$$

is included in the cumulant function. Similar to what we did for Σ_c when we derived the TOC96 in section 2.3.1, we can calculate the cumulant function in equation (3.21) by defining $t_2 = 0$, $t_1 \equiv t < 0$ and $\tau \equiv t' - t'' < 0$, yielding

$$C_c(t) = it\mathcal{W}_c^h(\omega = 0) - \left.\frac{\partial \mathcal{W}_c^h(\omega)}{\partial \omega}\right|_{\omega=0} - \frac{1}{\pi} \int_{-\infty}^{\mu} d\omega \frac{\operatorname{Im} \mathcal{W}_c^h(\omega)e^{-i(\omega+i\eta)t}}{(\omega + i\eta)^2}. \qquad (3.26)$$

Plugging the above equation into Eq. (3.21) and putting back the time-independent part of W, the final Green's function from the decoupling approximation reads

$$G(t_{12}) = \mathcal{G}_H(t_{12}) \exp\left(it_{12}\mathcal{W}^h(\omega = 0) - \left.\frac{\partial \mathcal{W}^h(\omega)}{\partial \omega}\right|_{\omega=0} - \frac{1}{\pi} \int_{-\infty}^{\mu} d\omega \frac{\operatorname{Im} \mathcal{W}^h(\omega)e^{-i(\omega+i\eta)t_{12}}}{(\omega + i\eta)^2} \right). \qquad (3.27)$$

The decoupling approximation is a very rough approximation, but it allows us to see the structure of the problem, and the physics that emerges from the exact solution of the linearized equation: since W contains the neutral excitations of the system, expansion of the exponential (i.e. the last term in Eq. (3.27)) creates a series of single, double, and

---

[4]Of course there is no hole or electron part of the screening W itself, but here I define the quantities in a way that is convenient for their later use. Especially this way of definition is consistent with the Green's function and the self-energy.

multiple excitations. As discussed in section 1.1, such an expression is the exact solution of a core electron Hamiltonian [16], where a single fermion is coupled to bosons. Here the bosons are the excitations contained in W, and the fermion is given by G.

The above cumulant Green's function is similar to the Green's function of the TOC96 in Eq. (2.62), but instead of using the GW self-energy, only the screened interaction W is contained in the exponential. In the case of a core level, it is reasonable to divide the system into an isolated level and the rest, which screens the level. But in the case of valence states, no such clear separation exists. However, one can still imagine that one excites a *quasi-particle*, and that excitation of this quasi-particle, in turn, leads to bosonic excitations in the system. However, the quasi-particle is not simply the bare level; it is dressed by the other electrons. In order to improve the description of the quasi-particle, a further GW quasi-particle correction will be introduced in the following paragraphs, leading to the final TOC11.

3.3.2   The GW quasi-particle correction

Eq. (3.27) is not the TOC11 in Ref. [11] yet. Besides the decoupling approximation, the TOC11 also used the GW quasi-particle corrections. In order to get a better description than Eq. (3.27), beyond the decoupling approximation, it is useful to compare to the `GW` approximation, like in the TOC96 where the GW self-energy enters. In the decoupling approximation, the i-th matrix element of the EscGW$_0$ self-energy for $t_1 < t_2$ reads

$$\Sigma_i^{GW,h}(t_{12}) = -\theta(t_2 - t_1)e^{-i\varepsilon_i t_{12}}\mathcal{W}(t_{12}),\qquad(3.28)$$

where ε_i is the quasi-particle energy from a EscGW$_0$ calculation[5].

We can now use Eq. (3.28) to rewrite Eq. (3.21) as

$$\mathcal{G}(t_{12}) = \mathcal{G}_H(t_{12})\exp\left(i\int_{t_1}^{t_2}\mathrm{d}t'\int_{t'}^{t_2}\mathrm{d}t''\,\Sigma_i^{GW,h}(t'-t'')e^{i\varepsilon_i(t'-t'')}\right).\qquad(3.29)$$

---

[5]Note that equation (3.28) is only valid in the decoupling approximation. In general, the GW self-energy contains the sum over all the states, i.e. $\Sigma_{ii} = i\sum_k G_{kk}W_{kk}^{ii}$. Moreover, the GW self-energy is not necessarily the EscGW$_0$ one. The G$_0$W$_0$ self-energy can lead to the same result if we have taken the ε_i properly according to the self-energy. This will be discussed in more detail in section 4.2.

The exponential term in the above equation is similar to equation (2.51) besides the time arguments in the double integral, due to the decoupling approximation. The cumulant Green's function in Eq. (3.27) can now be written in terms of the GW self-energy, leading to

$$\mathcal{G}(t_{12}) = \mathcal{G}^0_{QP}(t_{12}) \exp\left(\left.\frac{\partial \Sigma_i^{GW,h}(\omega)}{\partial \omega}\right|_{\omega=\varepsilon_i}\right) \exp\left(\frac{1}{\pi}\int_{-\infty}^{\mu} d\omega \, \frac{\operatorname{Im}\Sigma_i^{GW,h}(\omega)e^{i(\varepsilon_i-\omega-i\eta)t_{12}}}{(\varepsilon_i-\omega-i\eta)^2}\right),$$

(3.30)

where

$$\mathcal{G}^0_{QP}(t_{12}) = \mathcal{G}_H(t_{12}) \exp\left(-i\Sigma_i^{GW,h}(\varepsilon_i)(t_{12})\right).$$

(3.31)

Within the decoupling approximation, Eq. (3.30) is equivalent to Eq. (3.27). The quasi-particle energy from Eq. (3.30) is the QP energy in $\mathcal{G}^0_{QP}$ which is calculated using only the *hole* part of the GW self-energy as shown in the above equation. It is different from the GW quasi-particle energy where the *whole* GW self-energy is used (see e.g. the QP energy of the TOC96 in Eq. (2.62)).

Up to now, the electron and hole sectors separate: occupied and empty states do not correlate in the decoupling approximation; for example, in Eq. (3.30) only $\Sigma^{GW,h}$ appears. In order to have a better description of the quasi-particle, the full GWA self-energy, and not only its hole part, is used to calculate the quasi-particle shift in the TOC11, which yields

$$\mathcal{G}^{C11}(t_{12}) = \mathcal{G}_{QP}(t_{12}) \exp\left(\left.\frac{\partial \Sigma_i^{GW,h}(\omega)}{\partial \omega}\right|_{\omega=\varepsilon_i}\right) \exp\left(\frac{1}{\pi}\int_{-\infty}^{0} d\omega \, \frac{\operatorname{Im}\Sigma_i^{GW,h}(\omega)e^{i(\varepsilon_i-\omega-i\eta)t_{12}}}{(\varepsilon_i-\omega-i\eta)^2}\right),$$

(3.32)

where $\mathcal{G}_{QP}$ is the Green's function evaluated with GWA quasi-particle energies, which is the same as the TOC96 in equation (2.62). The only difference to the TOC96 is the **Z**-factor that reads

$$\mathbf{Z}^{C11} = \exp\left(\left.\frac{\partial \Sigma_i^{GW,h}(\omega)}{\partial \omega}\right|_{\omega=\varepsilon_i}\right).$$

(3.33)

The **Z**-factor of the TOC11 is important to guarantee conservation of weight of the spectral function, i.e. $\int_{-\infty}^{\infty} A_i(\omega)\mathrm{d}\omega = 1$.

Besides the TOC96, several derivations of this or closely related expressions can be found in the literature. In particular, Langreth [16] has obtained the cumulant Green's function as solution to an electron-boson coupling Hamiltonian (see Eq. (1.1)). In the simplest case of one level and one boson, such a Hamiltonian corresponds to our decoupled LDE (3.19), where $\mathcal{W}$ contains one bosonic excitation. The more complete equation LDE (3.11) couples several fermionic levels and bosonic excitations. With respect to Langreth, our derivation starts from the full many-body Hamiltonian, and not from the already approximate electron-boson coupling model. The solution of the problem is then based on a different mathematical strategy, but of course with similar results, since in both cases the solution is the exact solution to the approximate problem.

Other derivations (see e.g., Refs. [9, 19, 33, 77]) postulate the `GW` self-energy as central ingredient, and either solve the equation of motion from the Green's function approximately [33], or use the cumulant exponential form as ansatz, with the cumulant derived from the constraint that the Dyson equation and the cumulant approach should yield the same result to first order in W [9, 19, 77], as for example for the TOC96.

In our case, the `GW` form of the self-energy appears naturally. The closest derivation to ours is probably the one of Hedin [31] where the diagrammatic expansion of the Green's function is *resummed* thanks to approximations on the recoil effects. As in our derivation, there is no model Hamiltonian, W is the central ingredient, and the `GW` self-energy appears as a result.

A detailed study of the TOC11 in the hole-plasmon coupling model Hamiltonians will be provided in section 4.2. In Chapter 6 I will also show the performance of the TOC11 photoemission spectrum of sodium in the valence and for the core levels by comparing theory and experiment.

3.4 The retarded cumulant

In Section 3.3 I have shown how the TOC11 can be derived from the linearized differential equation (3.11) using the decoupling approximation plus the GW quasi-particle correction. In this section, I am going to start from the LDE again, and introduce an ansatz Green's function that leads to the retarded cumulant Green's function that has been introduced in section 2.3. The LDE (3.11) reads

$$
G(1,2;\phi) = G_H(1,2) + \int d3 G_H(1,3)\phi(3)G(3,2;\phi) + i \int d34 G_H(13)W(3,4^+)\frac{\delta G(3,2;\phi)}{\delta\phi(4)}\,.
$$
(3.34)

For simplicity of the notation, I have used the symbol ϕ to represent the screened external perturbation instead of $\bar{\phi}$ (see footnote 2 in section 3.2.). We can define a new Green's function from the following Dyson equation

$$
G_\phi(1,2) = G_H(1,2) + \int d3 G_H(1,3)\phi(3)G_\phi(3,2)\,,
$$
(3.35)

such that the linearized differential equation (3.34) becomes

$$
G(1,2;\phi) = G_\phi(1,2) + i \int d34 G_\phi(1,3)W(3,4)\frac{\delta G(3,2;\phi)}{\delta\phi(4)}\,.
$$
(3.36)

Note that G_ϕ becomes G_H in equilibrium ($\phi = 0$) and its derivative with respect to ϕ gives

$$
\frac{\delta G_\phi(1,2;\phi)}{\delta\phi(3)} = G_\phi(1,3)G_\phi(3,2)\,.
$$
(3.37)

Note that there is no integration on the repeated index 3 in the above equation (3.37). Now the question is how one can solve equation (3.36) in an efficient way. My strategy is to look for some *ansatz* Green's function that in principle is the exact solution of equation (3.36). Then we can introduce proper approximations to the *ansatz* such that equation (3.36) can be solved in equilibrium using the chosen approximate ansatz.

To be more specifically, we can have a look of the following two *ansatz* Green's functions, for example:

$$G^{A1}(1,2;\phi) = G_\phi(1,2)\exp\left[C(1,2;\phi)\right]; \tag{3.38}$$

$$G^{A2}(1,2;\phi) = \int \mathrm{d}3 G_\phi(1,3)\exp\left[C(3,2;\phi)\right]. \tag{3.39}$$

In principle, both of the above two *ansatz* Green's functions are the exact solution of equation (3.36) because we have the cumulant function C that can be adjusted according to the requirement that $C = \ln\dfrac{\delta G}{\delta G_\phi}$ in Eq. (3.38) or $C = \ln\left(G_\phi^{-1}G\right)$ in Eq. (3.39). However, we could not solve equation (3.36) exactly using these two *ansatz* Green's function directly[6]. One alternative way is that we expand the cumulant function C with respect to the external perturbation ϕ, which requires our cumulant function C to be Taylor expandable with respect to ϕ. We can expect that the expansion can be done when ϕ can be kept relatively small. After expansion, we keep only the zero-order term such that the resulting cumulant function C_0 is ϕ-independent. Thus the approximate ansatz Green's functions are

$$G^{A10}(1,2;\phi) = G_\phi(1,2)\exp\left[C_0(1,2)\right]; \tag{3.40}$$

$$G^{A20}(1,2;\phi) = \int \mathrm{d}3 G_\phi(1,3)\exp\left[C_0(3,2)\right]. \tag{3.41}$$

In the following subsection, I am going to study in detail the second ansatz Green's function (G^{A20}) but not the first one (G^{A10}) because I did not find any promising solution of Eq. (3.36) from the first ansatz. Therefore, the study of the first ansatz is not provided in the thesis.

3.4.1 Ansatz that gives the GWA

In order to see how the ansatz Green's function works, I will take the second ansatz G^{A20} as one example to show how we can get the GW approximation from equation (3.36). Plugging

---

[6]This is because if we could solve Eq. (3.36) using these two ansatzs, this is equivalent to solve the exact many-body problem which is of course if possible. Some approximations must be done.

G^{A20} in Eq. (3.36) and using the property in Eq. (3.37), we have

$$\int d3 G_\phi(1,3) e^{C_0(3,2)} = G_\phi(1,2) + i \int d345 G_\phi(1,3) W(3,4) G_\phi(3,4) G_\phi(45) e^{C_0(5,2)}. \quad (3.42)$$

Now $\phi = 0$ can be taken since the functional derivative with respective to ϕ has already been carried out, leading to

$$\int d3 G_H(1,3) e^{C_0(3,2)} = G_H(1,2) + i \int d345 G_H(1,3) W(3,4) G_H(3,4) G_H(45) e^{C_0(5,2)}. \tag{3.43}$$

The above equation can be simplified by introducing the GW self-energy $\Sigma^{GW}(3,4) = iG_H(3,4) W(3,4)$[7], such that it becomes

$$\int d3 G_H(1,3) e^{C_0(3,2)} = G_H(1,2) + \int d345 G_H(1,3) \Sigma^{GW}(3,4) G_H(45) e^{C_0(5,2)}. \quad (3.44)$$

The above equation is nothing else than the Dyson equation with the GW self-energy[8], which reads

$$G(1,2) = G_H(1,2) + \int d34 G_H(1,3) \Sigma^{GW}(3,4) G(4,2), \quad (3.45)$$

where the knowledge of C_0 in

$$G(1,2) = \int d3 G_H(1,3) e^{C_0(3,2)} \quad (3.46)$$

is not directly needed, although one could of course calculated C_0 from G, the solution of Eq. (3.45).

---

[7]Note that here the GW self-energy is defined in terms of the Hartree Green's function G_H, and the exact screening W instead of the RPA one. Thus the self-energy $\Sigma^{GW}(3,4) = iG_H(3,4) W(3,4)$ corresponds to a one-shot GW self-energy. In practice, the Hartree Green's function will be replaced by the quasi-particle Green's function such that the self-energy becomes the quasi-particle self-consistent GW self-energy.

[8]I have mentioned in section 2.2 that the GW approximation corresponds to neglecting the vertex correction (i.e. $\tilde\Gamma = 1$) in Hedin's equations in Eq. (2.34). Then the one-shot GW self-energy becomes $\Sigma^{GW}(3,4) = iG_H(3,4) W^{RPA}(3,4)$ and the Green's function from the GWA becomes $G(1,2) = G_H(1,2) + i\int d34 G_H(1,3) \Sigma^{GW}(3,4) G(4,2)$ which is similar to Eq. (3.45) but not exactly the same. Because the GW approximation yields the RPA W but in our derivation, W keeps the exact one. We did not put any approximation in W yet. Therefore, strictly speaking our Eq. (3.45) does not really lead to the usual GW approximation but only when we use the RPA W, the solution of Eq. (3.45) retrieves the commonly calculated GW Green's function.

As we can see, the ansatz Green's function in equation (3.41) retrieves the GW approximation. This is good because it proves that our strategy is meaningful: using some proper ansatz Green's function, the solution of the linearized differential equation (3.36) can be as good as the GWA. However, to find the GW approximation is not our final target. The next step is to find some better ansatz that will give us powerful cumulant expansion approximations.

3.4.2 Ansatz that gives a retarded cumulant

Up to now, we have seen how we can use the idea of an *ansatz* Green's function to solve the linearized differential equation approximately and get reasonable results. In this section, I am going to use a new *ansatz* Green's function that combines the previous two *ansatz* Green's functions in Eqs. (3.38) and (3.39). The idea of a combined ansatz is inspired by the fact that we are looking for a quasi-particle dressed by bosons that are summed in an exponential factor. Intuitively, each quasi-particle is given by a diagonal element of a Green's function in a basis, rather than a non-local function in real space. This speaks for Eq. (3.39). On the other side, we have to change the time structure of the ansatz to go beyond the GW approximation, as we have seen in section 3.4.1, and for this Eq. (3.38) is a good candidate. Therefore I make the ansatz reading as:

$$G^{A3}(1, 2; \phi) = \int dx_3 \, G_\phi(x_1, x_3, t_1, t_2) \exp\left[C(x_3, x_2, t_1, t_2; \phi)\right] . \qquad (3.47)$$

Again we will keep only the zero order expansion of the above *ansatz*, such that the final *ansatz* Green's function we are going to study reads

$$\begin{aligned} G(1, 2; \phi) &= \int dx_3 \, G_\phi(x_1, x_3, z_1, z_2) \exp\left[C_0(x_3, x_2, t_1, t_2)\right] \\ &= \int dx_3 \, G_\phi(x_1, x_3, z_1, z_2) \tilde{E}(x_3, x_2, t_1, t_2) , \qquad (3.48) \end{aligned}$$

where we have defined $\tilde{E}(x_3, x_2, t_1, t_2) \equiv \exp\left[C_0(x_3, x_2, t_1, t_2)\right]$. Note that in the linearized differential equation (3.36), the particles are propagating in non-equilibrium due to the presence of the external perturbation ϕ. Therefore all the quantities that are functionals

of ϕ should have the time arguments running on the Keldysh-contour[9]. Here I label the Keldysh-contour time as z and normal time as t as shown in our *ansatz* Green's function in Eq. (3.48). Now we can plug our *ansatz* Green's function Eq. (3.48) into the linearized differential equation (3.36). We first have a look at the differential term in the LDE that reads

$$
\begin{aligned}
\frac{\delta \int \mathrm{d}x_5\, G_\phi(x_3, x_5, z_3, z_2)\tilde{E}(x_5, x_2, t_3, t_2)}{\delta\phi(4)} &= \int \mathrm{d}x_5\, \tilde{E}(x_5, x_2, t_3, t_2)\frac{\delta G_\phi(x_3, x_5, z_3, z_2)}{\delta\phi(4)} \\
&= \int \mathrm{d}x_5\, \tilde{E}(x_5, x_2, t_3, t_2)G_\phi(x_3, x_4, z_3, z_4)G_\phi(x_4, x_5, z_4, z_2) \\
&= G_\phi(3, 4)\int \mathrm{d}x_5\, G_\phi(x_4, x_5, z_4, z_2)\tilde{E}(x_5, x_2, t_3, t_2).
\end{aligned}
\tag{3.49}
$$

We have used relation Eq. (3.37) in the above derivation. With equation (3.49), the LDE in Eq. (3.36) can be written as

$$
\begin{aligned}
&\int \mathrm{d}x_3\, G_\phi(x_1, x_3, z_1, z_2)\tilde{E}(x_3, x_2, t_1, t_2) = G_\phi(1, 2) \\
&+ i\int \mathrm{d}34\, G_\phi(1, 3)W(3, 4)G_\phi(3, 4)\int \mathrm{d}x_5\, G_\phi(x_4, x_5, z_4, z_2)\tilde{E}(x_5, x_2, t_3, t_2).
\end{aligned}
\tag{3.50}
$$

Now we define the GW self-energy in non-equilibrium

$$
\Sigma_\phi(1, 2) = iG_\phi(1, 2)W(1, 2).
\tag{3.51}
$$

Plugging the above Σ_ϕ in Eq. (3.50), we get

$$
\begin{aligned}
&\int \mathrm{d}x_3\, G_\phi(x_1, x_3, z_1, z_2)\tilde{E}(x_3, x_2, t_1, t_2) = G_\phi(1, 2) \\
&+ \int \mathrm{d}34\, G_\phi(1, 3)\Sigma_\phi(34)\int \mathrm{d}x_5\, G_\phi(x_4, x_5, z_4, z_2)\tilde{E}(x_5, x_2, t_3, t_2).
\end{aligned}
\tag{3.52}
$$

In equilibrium Σ_ϕ becomes the GW self-energy $\Sigma_{\phi=0} \equiv \Sigma_{GW} = iG_H W$. Now we can use the Langreth rules [84] in table 3.1 to project the Keldysh-contour time to the real time.

---

[9]The Keldysh formalism is designed for studying quantum mechanical non-equilibrium situations. Before we put the external perturbation to zero ($\phi = 0$), our linearized differential equation is in non-equilibrium such that strictly speaking, we have to use the Keldysh-contour for the quantities that are ϕ-dependent. More information about the non-equilibrium many-body problem can be found for instance in Refs. [82,83].

We decide to calculate the retarded component of our Green's function in equilibrium[10] because from the table 3.1, the retarded component is the simplest one to get from Eq. (3.52).

$c(z_1, z_2) = \int dz\, a(z_1, z)b(z, z_2)$	$c(z_1, z_2) = a(z_1, z_2)b(z_2, z_1)$
$c^> = a^> \cdot b^A + a^R \cdot b^>$	$c^> = a^> b^<$
$c^< = a^< \cdot b^A + a^R \cdot b^<$	$c^< = a^< b^>$
$c^R = a^R \cdot b^R$	$c^R = a^R b^< + a^< b^A$
$c^A = a^A \cdot b^A$	$c^A = a^A b^< + a^< b^R$
$c^T = a^T \cdot b^T - a^< \cdot b^>$	$c^T = a^< b^T + a^R b^<$
$c^{\bar{T}} = a^> \cdot b^< - a^{\bar{T}} b^{\bar{T}}$	$c^{\bar{T}} = a^{\bar{T}} b^< - a^< b^A$

Table 3.1: Identities for the convolution (first column) and product (second column) of two functions in Keldysh space following Langreth rules [84]. Take from Ref. [82]. The superscripts R, A, T, $\bar{T}$ are `retarded`, `advanced`, `time-ordered` and `anti-time-ordered` components, respectively. Note that in the table, the short notations $a \cdot b \equiv \int dt\, a(t_1, t)b(t, t_1)$ and $ab \equiv a(t_1, t_2)b(t_2, t_1)$ are adopted. The GW self-energy is $\Sigma(t_{12}) = iG(t_{12})W(t_{12})$, which is different with the second column so we need to be careful about the order of the time arguments when using these rules.

After using the Langreth rules in table 3.1, we can put the external perturbation to zero ($\phi = 0$). Thus Eq. (3.52) in equilibrium reads (for simplicity, $\Sigma \equiv \Sigma_{\phi=0} \equiv \Sigma_{GW}$ in the following equations)

$$\int dx_3\, G_H^R(x_1, x_3, t_1, t_2)\tilde{E}(x_3, x_2, t_1, t_2) = G_H^R(1, 2)$$

$$+ \int d34\, G_H^R(1, 3)\Sigma^R(34) \int dx_5\, G_H^R(x_4, x_5, t_4, t_2)\tilde{E}(x_5, x_2, t_3, t_2). \qquad (3.53)$$

---

[10]Actually it is not necessary to calculate the retarded component of the GF from Eq. (3.52). We could, in principle calculate any component by projecting the Keldysh time into normal time using the Langreth rules, e.g. the time-ordered Green's function that should induce the same result as the retarded Green's function. In this sense, the conclusion that the retarded cumulant is better than the time-ordered cumulant is not correct. The most important approximations in the time-ordered cumulants (TOC96 and TOC11) are the decoupling between the electron and hole branches.

Suppose now again that we are working on a basis where G_H^R is diagonal. The last term of equation (3.53) becomes

$$\int d34 \int dx_1 x_2 x_5 \varphi_i^*(x_1)\varphi_j(x_2) \sum_k G_{H,kk}^R(t_1,t_3)\varphi_k(x_1)\varphi_k^*(x_3) \sum_{nn'} \Sigma_{nn'}^R(t_3,t_4)\varphi_n(x_3)\varphi_{n'}^*(x_4)$$

$$\times \sum_{k'} G_{H,k'k'}^R(t_4,t_2)\varphi_{k'}(x_4)\varphi_{k'}^*(x_5) \sum_{lm} \tilde{E}_{lm}(t_3,t_2)\varphi_l(x_5)\varphi_m^*(x_2)$$

$$= \int dt_3 t_4 \sum_k G_{H,ii}^R(t_1,t_3)\Sigma_{ik}^R(t_3,t_4)G_{H,kk}^R(t_4,t_2)\tilde{E}_{kj}(t_3,t_2).$$

$$(3.54)$$

Now we can write the whole equation (3.53) in such a basis (suppose for the moment, we are only interested in the diagonal elements). We have

$$G_{H,ii}^R(t_1,t_2)\tilde{E}_{ii}(t_1,t_2) = G_{H,ii}^R(t_1,t_2)$$

$$+ \int dt_3 t_4 \sum_k G_{H,ii}^R(t_1,t_3)\Sigma_{ik}^R(t_3,t_4)G_{H,kk}^R(t_4,t_2)\tilde{E}_{ki}(t_3,t_2). \quad (3.55)$$

We use the approximation that the GW self-energy Σ^R is also diagonal in the basis we have chosen[11]. This yields the final scalar equation that can be solved exactly:

$$\mathcal{G}_H^R(t_{12})\tilde{E}(t_{12}) = \mathcal{G}_H^R(t_{12}) + \int dt_3 t_4 \, \mathcal{G}_H^R(t_{13})\Sigma_{ii}^R(t_{34})\mathcal{G}_H^R(t_{42})\tilde{E}_{ii}(t_{32}), \quad (3.56)$$

where $\mathcal{G} \equiv G_{ii}$ is the diagonal element of the Green's function and $t_{12} \equiv (t_1,t_2)$.

This is the final linearized differential equation of a certain matrix element in a retarded version. Note that in the GW self-energy $\Sigma_{ii}^R = i \sum_k G_{kk}^H W_{kk}^{ii}$ where k runs over all states, so that the interaction of all the states is taken into account. Now we are going to solve the above equation (3.56) as what we did in section 3.3 when we solve Eq. (3.19).

First the retarded Hartree Green's function reads

$$\mathcal{G}_H^R(t_{12}) = -i\theta(t_1 - t_2)e^{-i\varepsilon_i^H(t_1-t_2)}, \quad (3.57)$$

---

[11]In the derivation of the TOC96 in section 2.3 and the TOC11 in section 3.3, we always use the approximation that the GW self-energy is diagonal in the Kohn-Sham orbitals. Here I am using the same approximation. The situation when the self-energy is not diagonal is more complicated and this issue is not provided in this thesis.

where ε_H is the Hartree eigenvalue.

Plugging the above equation (3.57) in Eq. (3.56), we can finally calculate $\tilde{E}$ from

$$\tilde{E}_{ii}(t_{12}) = 1 - i \int_{t_2}^{t_1} \mathrm{d}t_4 \int_{t_4}^{t_1} dt_3 \tilde{\Sigma}_{ii}^R(t_{34}) \tilde{E}_{ii}(t_{32}) \tag{3.58}$$

where $\tilde{\Sigma}_{ii}^R(t_{34}) \equiv \Sigma_{ii}^R(t_{34}) e^{i\varepsilon_i^H(t_3 - t_4)}$, and the time ordering is $t_1 > t_3 > t_4 > t_2$.

As one can check by putting Eq. (3.59) into Eq. (3.58), the solution of the above equation reads

$$\tilde{E}_{ii}(t_{12}) = \exp\left[-i \int_{t_2}^{t_1} \mathrm{d}t_4 \int_{t_4}^{t_1} dt_3 \, \tilde{\Sigma}_{ii}^R(t_{34})\right] . \tag{3.59}$$

Putting the above $\tilde{E}$ in the left hand side of Eq. (3.56), we arrive at the final retarded Green's function, which reads

$$\mathcal{G}^{RC}(t_{12}) = \mathcal{G}_H^R(t_{12}) \exp\left[-i \int_{t_2}^{t_1} \mathrm{d}t_4 \int_{t_4}^{t_1} dt_3 \, \tilde{\Sigma}_{ii}^R(t_{34})\right] . \tag{3.60}$$

This retarded cumulant Green's function is identical to the retarded cumulant in Ref. [19] that has been discussed in section 2.3. Compared to the time-ordered cumulant in Eq. (3.29) which is the TOC11 but without the GW quasi-particle correction (see Eq. (3.29)), the retarded cumulant Green's function $\mathcal{G}^{RC}$ in Eq. (3.60) replaces the single branches of the time-ordered $\mathcal{G}_H$ and Σ^{GW} by their full retarded counterparts. If we had not gone through the Keldysh-contour from Eq. (3.52), but put $\phi = 0$ in Eq. (3.52) to solve it under decoupling approximation, we would have gotten the same cumulant Green's function as equation (3.29) which finally yields the TOC11 with the GW quasi-particle correction.

Similar to the derivation of the TOC96 in section 2.3, the double integral in Eq. (3.60) can be carried out by introducing the spectral representation of the `retarded` self-energy (the subscript ii is dropped for simplicity), which reads (see Appendix (D.2f))

$$\begin{aligned}
\Sigma_c^R(\omega) &= \int \mathrm{d}\omega' \frac{\Gamma(\omega')}{\omega - \omega' + i\eta} \\
&= \int_{-\infty}^{\mu} \mathrm{d}\omega' \frac{\Gamma(\omega')}{\omega - \omega' + i\eta} + \int_{\mu}^{\infty} \mathrm{d}\omega' \frac{\Gamma(\omega')}{\omega - \omega' + i\eta} \equiv \Sigma_c^<(\omega) + \Sigma_c^>(\omega) ,
\end{aligned} \tag{3.61}$$

where

$$\Gamma(\omega) = -\frac{1}{\pi} \operatorname{Im} \Sigma^R_{GW}(\omega) = -\frac{1}{\pi} \left(\operatorname{Im} \Sigma^>_c(\omega) + \operatorname{Im} \Sigma^<_c(\omega) \right). \tag{3.62}$$

Putting $t_2 = 0$ and $t_1 \equiv t > 0$ and $\tau = t_3 - t_4$ in Eq. (3.60), the double integral becomes

$$
\begin{aligned}
- i \int_{t_2}^{t_1} \mathrm{d}t_4 \int_{t_4}^{t_1} \mathrm{d}t_3 \, \tilde{\Sigma}^R(t_{34}) &= - \int_0^t \mathrm{d}t_4 \int_0^{t-t_4} \mathrm{d}\tau \int \mathrm{d}\omega' \, \Gamma(\omega') e^{i(\varepsilon_H - \omega' + i\eta)\tau} \\
&= -i\Sigma^R(\varepsilon_H)t + \left. \frac{\partial \Sigma^R(\omega)}{\partial \omega} \right|_{\omega = \varepsilon_H} - \frac{1}{\pi} \int_{-\infty}^{\mu} \mathrm{d}\omega' \, \frac{\operatorname{Im} \Sigma^<(\omega') e^{i(\varepsilon_H - \omega' + i\eta)t}}{(\varepsilon_H - \omega' + i\eta)^2} \\
&\quad - \frac{1}{\pi} \int_{\mu}^{\infty} \mathrm{d}\omega' \, \frac{\operatorname{Im} \Sigma^>(\omega') e^{i(\varepsilon_H - \omega' + i\eta)t}}{(\varepsilon_H - \omega' + i\eta)^2}.
\end{aligned}
\tag{3.63}
$$

Plugging the above equation in Eq. (3.60), finally the retarded cumulant Green's function reads

$$
\begin{aligned}
G^{RC}(\tau) = -i\theta(\tau) e^{-i\tau\left(\varepsilon_H + \Sigma^R(\varepsilon_H)\right)} &\exp \left(\left. \frac{\partial \Sigma^R(\omega)}{\partial \omega} \right|_{\omega = \varepsilon_H} \right) \\
&\times \exp \left(-\frac{1}{\pi} \int_{-\infty}^{\mu} \mathrm{d}\omega' \, \frac{\operatorname{Im} \Sigma^<(\omega') e^{i(\varepsilon_H - \omega' + i\eta)\tau}}{(\varepsilon_H - \omega' + i\eta)^2} \right) \\
&\times \exp \left(-\frac{1}{\pi} \int_{\mu}^{\infty} \mathrm{d}\omega' \, \frac{\operatorname{Im} \Sigma^>(\omega') e^{i(\varepsilon_H - \omega' + i\eta)\tau}}{(\varepsilon_H - \omega' + i\eta)^2} \right).
\end{aligned}
\tag{3.64}
$$

The first two lines on the right hand side of the above equation lead to the same result as the TOC96 in equation (2.62) (note that $\operatorname{Im} \Sigma^<(\omega) = -\operatorname{Im} \Sigma^h(\omega)$)[12]. Besides the terms (the first two lines of Eq. (3.64)) in the TOC96, the third line of the above equation creates satellites at the opposite side of the quasi-particle peak in the spectrum, with respect to the satellites contained in the TOC96.

In other words, the main difference between the time-ordered cumulants (i.e. the TOC96 and TOC11) and the retarded cumulant is the presence of the last term in Eq. (3.64) which takes into account the interaction between states below and above the Fermi level.

---

[12]The relation between the retarded and time-ordered self-energy can be found in Appendix D, in particular Eqs. (D.2f) and (D.2e).

Therefore if we use the retarded cumulant to calculate core photoemission where $\Sigma^> \approx 0$[13], the retarded cumulant yields the same result as the time-ordered cumulant. However if we calculate valence photoemission spectrum where $\Sigma^> \neq 0$, on one hand the retarded cumulant $\mathbf{Z}$-factor $\exp\left(\left.\dfrac{\partial\Sigma^R(\omega)}{\partial\omega}\right|_{\omega=\varepsilon_H}\right)$ will be the same as the TOC96 but smaller than the TOC11 due to the contribution of $\Sigma^>$, on the other hand, the last term in G^{RC} will induce additional satellites on the other side of the quasi-particle peak, which are absent in the time-ordered cumulant. These satellites restore the conservation of spectral weight that is otherwise guaranteed by using Eq. (3.33).

A detailed study about the retarded cumulant Green's function in model Hamiltonians will be shown in Chapter 4.

3.5 Summary

In this chapter, I have shown a unified derivation of the GW approximation and the cumulant expansion approximations (i.e. the TOC11 and RC) starting from the full functional differential equation of the one-body Green's function. I have proven that all the approximations can be derived from the linearized differential equation where only the linear response of the Hartree potential with respect to the external perturbation has been kept. From the linearized differential equation, a random phase like approximation in $\frac{\delta G}{\delta \phi}$ yields the GW approximation that can be also derived using some proper *ansatz* Green's function. The TOC11 can be obtained from the decoupling approximation which totally decouples different states, neglecting all the interaction between states. In order to have a better description in the quasi-particles, the GW quasi-particle correction has been introduced on top of the decoupling approximation. The retarded cumulant on the other hand, is derived from an ansatz Green's function which is an approximate solution to the linearized differential equation. I have gone through the Keldysh-contour in non-equilibrium and finally projected the linearized differential equation back to the equilibrium when the $\phi = 0$ condition can be fulfilled. The resulting retarded cumulant Green's function has the same expression as

---

[13]The GW self-energy for a core-level quasi-boson model is provided in Eq. (4.33) where Σ only contains the lesser part. On the other hand, the GW self-energy for a two-level model contains both lesser and greater parts as shown in Eq. (4.57).

a previously introduced retarded cumulant that is supposed to be an improvement with respected to the traditional time-ordered cumulant since the decoupling between the electron and hole branches has been eliminated. Indeed, the time-ordered cumulants can also be obtained using the same ansatz, but projecting on time-ordered components and neglecting the coupling between electron and hole branches.

All the derivations I have shown are very compact. The potential of using these derivations to obtain better and better approximation is still to be explored. Latter, we will see that the cumulant expansion approximations including the TOC96, TOC11 and RC, have some drawbacks in the description of the valence photoemission. Therefore, a better approximate Green's function is still needed. In Chapter 5, I will introduce ideas of a constrained retarded cumulant derived from a model. In addition to the derivations I have shown in this chapter, a new derivation which aims at exploring increasingly accurate approximations from our unified derivations will be shown in Appendix C.

Chapter 4

Performance in Model Hamiltonians

In this chapter, I will work on two effective hole-plasmon coupling (HPC) model Hamiltonians which can be solved exactly. I will show a step by step calculation of the exact one-particle Green's function from these two model Hamiltonians such that one can understand more in detail the physical meaning of the Green's function as well as what information we can get from it. Then I will calculate the one-particle Green's function using the approximations I have introduced in previous chapters, i.e. the GW approximation (the G_0W_0 and $EscGW_0$) and different cumulant expansion approximations (TOC96, TOC11 and RC). From the comparison between the approximate and the exact spectral functions of the model Hamiltonians, we can understand more about the performance of different approximations. In particular since most of the calculations are fully analytical, the exact constraints that have been summarized in Chapter 1 will be studied in different approximations. Note that the hole-plasmon coupling model Hamiltonian is an approximate system with respect to the exact many-body system and it is designed for studying the coupling between fermions and plasmons. It can therefore not provide exact answers with respect to the full Hamiltonian, but it simplifies the sophisticated physical phenomena by something we could solve exactly, such that it provides a great deal of insights to improve our understanding of the specific physical phenomena. The aim of this chapter is to answer the following questions

1. What is the difference between the one- and two-level hole-plasmon coupling Hamiltonians? What are they modeling, core or valence photoemission? Why is the hole-plasmon coupling chosen to study photoemission, instead of the electron-plasmon coupling?

2. How can we calculate the exact Green's function of the hole-plasmon coupling Hamiltonians?

3. What is the link between the GWA and the CEA, as well as between different CEAs (TOC96, TOC11 and RC)?

4. What are the performances of the GWA and CEA? Do they fulfill the exact constraints I have mentioned in Chapter 1?

5. Which physics is missing in the various approximations?

4.1   The model Hamiltonians

The physical phenomena we are studying is the coupling between fermions and plasmons. Therefore the model Hamiltonian we will study should be built for describing this specific physical phenomena. As discussed in Chapter 1 the plasmons are collective wave-like oscillations of electrons. They lead to satellites in photoemission spectrum. They have bosonic nature, hence a general fermion-boson coupling model Hamiltonian fits our purpose. It reads

$$\hat{H} = \sum_i \varepsilon_i c_i^\dagger c_i - \sum_{i\neq j} \mathbf{t}_{ij} c_i^\dagger c_j + \omega_p \sum_i a_i^\dagger a_i + g \sum_i c_i^\dagger c_i (a_i^\dagger + a_i). \qquad (4.1)$$

Here $c_i^{(\dagger)}$ and $a_i^{(\dagger)}$ are the annihilation (creation) operators of electrons of energy ε_i and plasmons of energy ω_p, respectively, g is the *on-site* electron-plasmon coupling strength, and $\mathbf{t}$ represents the hopping kinetic energy of electrons. The plasmon dispersion is neglected such that the non-dispersing plasmon (i.e. the Einstein boson) is studied here[1]. The above effective Hamiltonian is an approximation with respect to the full many-body Hamiltonian

---

[1]Plasmon dispersion has been taken into account in the literature e.g., Refs. [30, 34, 85].

in Eq. (2.1). In particular, the electron-electron interaction term in the many-body Hamiltonian is the source of both the third and fourth terms of the above Hamiltonian. In the following we are going to study two simplified versions of this effective Hamiltonian, namely the one- (i.e. $i = 1$ corresponding to core level) and two-level (i.e. $i = 1, 2$ that can model valence states) hole-plasmon coupling Hamiltonian that can be solved exactly.

4.1.1   One-level hole-plasmon coupling Hamiltonian

In section 1.1 I have introduced the quasi-boson model Hamiltonian (see Eq. (1.1)) whose spectral function provides a meaningful description of the hole-plasmon coupling in photoemission. In this section, I am going to study a simplified version of this quasi-boson Hamiltonian that is called the one-level hole-plasmon coupling Hamiltonian (HPC-1). The HPC-1 reads

$$\hat{H} = \varepsilon_0 c^\dagger c + g c c^\dagger (a + a^\dagger) + \omega_p a^\dagger a \,, \tag{4.2}$$

where all the parameters have been introduced in Eq. (4.1). This Hamiltonian can be linked to the decoupled linearized differential equation (3.19) for one orbital and one boson, where the electron is described by a matrix element of $\mathcal{G}$, and the plasmon by $\mathcal{W}$.

The exact spectral function of the above Hamiltonian has been calculated by Langreth [16] (see Eq. (1.5)). Here I am going to show a detailed calculation of the Green's function from this Hamiltonian using the Lehmann representation in Eq. (1.28), which is different from the original method of Langreth in Ref. [16] and closer to the derivations in Ref. [77]. In order to calculate the exact electron removal Green's function, we have to find the eigenenergies and eigenfunctions of the system with and without the one electron. We denote the states of the system as linear combinations of states $|n; m\rangle$ where n and m represent the fermion and plasmon occupations, respectively.

In the initial state, there is one electron in the system such that there is no hole that can couple to plasmons in the HPC-1. The coupling term in Eq. (4.2) does not contribute, leading to the effective Hamiltonian:

$$\hat{H}^{N=1} = \varepsilon_0 c^\dagger c + \omega_p a^\dagger a \,. \tag{4.3}$$

The basis vectors for $N = 1$ are $|1;0\rangle$, $|1;1\rangle$, $\cdots$, $|1;m\rangle$ where m is the plasmon occupation number that can go to infinity. In this basis the Hamiltonian becomes an $(m+1) \times (m+1)$ diagonal matrix. Hence the eigenvalues and eigenfunctions of the one-electron system ($N = 1$) are easily obtained as shown in table 4.1.

Table 4.1: Eigenvalues and coefficients of the eigenvectors of the one-electron system

$E_m^{N=1}$ \ $\left|\Psi_m^{N=1}\right\rangle$	$|1;0\rangle$	$|1;1\rangle$	$|1;2\rangle$	$|1;3\rangle$	$\cdots$	$|1;m\rangle$
ε_0	1	0	0	0	$\cdots$	0
$\varepsilon_0 + \omega_p$	0	1	0	0	$\cdots$	0
$\varepsilon_0 + 2\omega_p$	0	0	1	0	$\cdots$	0
$\varepsilon_0 + 3\omega_p$	0	0	0	1	$\cdots$	0
$\vdots$	$\vdots$	$\vdots$	$\vdots$	$\vdots$	$\ddots$	$\vdots$
$\varepsilon_0 + m\omega_p$	0	0	0	0	$\cdots$	1

The ground state has the lowest energy such that we have

$$E_0^{N=1} = \varepsilon_0 \,; \tag{4.4a}$$

$$\left|\Psi_0^{N=1}\right\rangle = |1;0\rangle \,. \tag{4.4b}$$

After photoemission, a hole is left behind that couples to the plasmons. Therefore the HPC-1 in Eq. (4.2) acting on the final state becomes

$$\hat{H}^{N=0} = g(a + a^\dagger) + \omega_p a^\dagger a \equiv \Delta + \omega_p \tilde{a}^\dagger \tilde{a}. \tag{4.5}$$

Here I have made a linear transformation of the boson operators by introducing an energy shift Δ such that $\hat{H}^{N=0}$ is diagonal in the new basis represented by $|0;\tilde{m}\rangle$ where $\tilde{m}$ is the occupation of the renormalized plasmons, and $\tilde{a}^{(\dagger)} \equiv a^{(\dagger)} + \gamma$. With some simple algebra, one can show that

$$\Delta = -\frac{g^2}{\omega_p} \,; \tag{4.6a}$$

$$\gamma = \frac{g}{\omega_p} \,. \tag{4.6b}$$

Therefore the eigenvalues of $\hat{H}^{N=0}$ are

$$E_{\tilde{m}}^{N=0} = -\frac{g^2}{\omega_p} + \tilde{m}\omega_p \,. \tag{4.7}$$

The new basis $|0;\tilde{m}\rangle$ can be expressed by a linear combination of the old basis $|0;m\rangle$ with coefficients $v_m^{\tilde{m}}$, hence we have

$$|0;\tilde{m}\rangle = v_0^{\tilde{m}} |0;0\rangle + v_1^{\tilde{m}} |0;1\rangle + v_2^{\tilde{m}} |0;2\rangle + \cdots = \sum_{m=0}^{\infty} v_m^{\tilde{m}} |0;m\rangle \,. \tag{4.8}$$

The coefficients $v_m^{\tilde{m}}$ can be calculated using the properties of boson operators[2] , thus we get

$$(v_0^{\tilde{m}})^2 = \frac{1}{\tilde{m}!}\left(\frac{g^2}{\omega_p^2}\right)^{\tilde{m}} e^{-\frac{g^2}{\omega_p^2}} \equiv \frac{1}{\tilde{m}!}\beta^{\tilde{m}} e^{-\beta} \,, \tag{4.9}$$

where $\beta \equiv \frac{g^2}{\omega_p^2}$. The complete eigenvalues and eigenvectors of $\hat{H}^{N=0}$ are shown in table 4.2.

Table 4.2: Eigenvalues and coefficients of the eigenvectors of the zero-electron system

$E_{\tilde{m}}^{N=0}$ $\quad |\Psi_{\tilde{m}}^{N=0}\rangle$	$|0;0\rangle$	$|0;1\rangle$	$|0;2\rangle$	$|0;3\rangle$	$\cdots$	$|0;m\rangle$
$-\frac{g^2}{\omega_p}$	v_0^0	v_1^0	v_2^0	v_3^0	$\cdots$	v_m^0
$-\frac{g^2}{\omega_p} + \omega_p$	v_0^1	v_1^1	v_2^1	v_3^1	$\cdots$	v_m^1
$-\frac{g^2}{\omega_p} + 2\omega_p$	v_0^2	v_1^2	v_2^2	v_3^2	$\cdots$	v_m^2
$-\frac{g^2}{\omega_p} + 3\omega_p$	v_0^3	v_1^3	v_2^3	v_3^3	$\cdots$	v_m^3
$\vdots$	$\vdots$	$\vdots$	$\vdots$	$\vdots$	$\ddots$	$\vdots$
$-\frac{g^2}{\omega_p} + \tilde{m}\omega_p$	$v_0^{\tilde{m}}$	$v_1^{\tilde{m}}$	$v_2^{\tilde{m}}$	$v_3^{\tilde{m}}$	$\cdots$	$v_m^{\tilde{m}}$

Our analytical results shown in Tab. 4.2 can be confirmed by comparing to the eigenvalues and coefficients of the eigenvectors from the exact numerical diagonalization of $\hat{H}^{N=0}$ in the basis $|0;m\rangle$. At the same time, this serves as a test of the numerical solution that will be reached for the two-level hole-plasmon coupling model, which cannot be solved analytically.

---

[2]The properties we have used are $\langle m|m\rangle = 1$, $a|m\rangle = \sqrt{m}|m-1\rangle$, $a^\dagger|m\rangle = \sqrt{m+1}|m+1\rangle$ and $|m\rangle = \frac{1}{\sqrt{m!}}(a^\dagger)^m |0\rangle$.
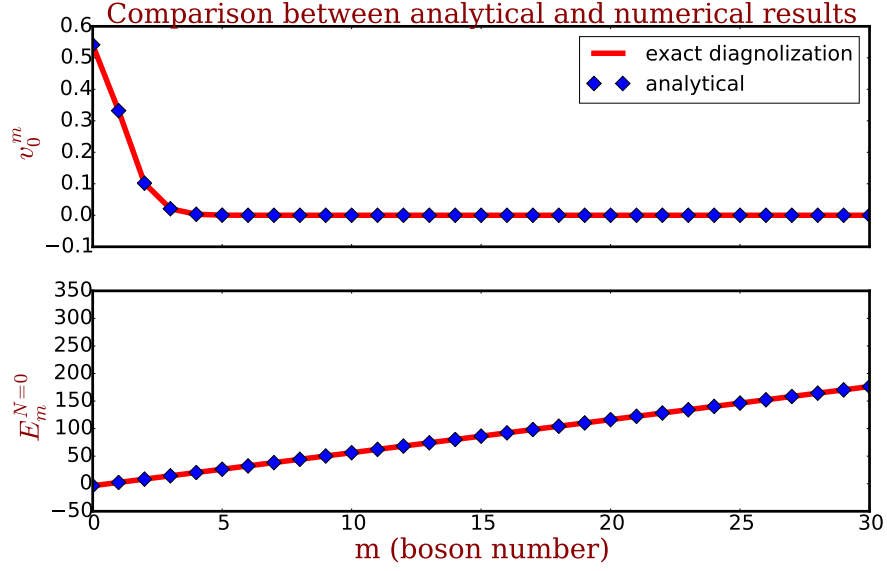
Figure 4.1: The upper and lower panels show the coefficients of the eigenfunctions and the eigenvalues of $\hat{H}^{N=0}$, respectively. Red curves are the dataset from the exact numerical diagonalization of $\hat{H}^{N=0}$ whose matrix elements are shown in Eq. (4.10). Blue diamonds are our analytical results $v_0^{\tilde{m}}$ (upper panel) in Eq. (4.9) (only these coefficients are used to calculate the Green's function in Eq. (4.11)) and $E_m^{N=0}$ (lower panel) in Eq. (4.7), respectively. Note that in the plot I have replaced the symbol $\tilde{m}$ by m, which is equivalent to the original equations.

The matrix elements of $\hat{H}^{N=0}$ are

$$H[m, m] = m\omega_p \,; \tag{4.10a}$$

$$H[m, m+1] = H[m+1, m] = g\sqrt{m+1} \,, \tag{4.10b}$$

and all other matrix elements are zero.

The comparison is shown in Fig. 4.1. All the analytical results (blue diamonds) are sitting on top of the exact numerical results (red curve), which confirms our analytical and numerical calculations.

The one-particle Green's function for electron removal can be calculated using the Lehmann representation Eq. (1.28):

$$G^h(\omega) = \sum_{\tilde{m}=0}^{\infty} \frac{\left[\langle \Psi_{\tilde{m}}^{N=0} | c | \Psi_0^{N=1} \rangle\right]^2}{\omega - (E_0^{N=1} - E_{\tilde{m}}^{N=0}) - i\eta} = \sum_{\tilde{m}=0}^{\infty} \frac{(v_0^{\tilde{m}})^2}{\omega - (\varepsilon_0 + \frac{g^2}{\omega_p} - \tilde{m}\omega_p) - i\eta}$$

$$= \sum_{\tilde{m}=0}^{\infty} \frac{\beta^{\tilde{m}} e^{-\beta}}{\tilde{m}!} \frac{1}{\omega - (\varepsilon_0 + \frac{g^2}{\omega_p} - \tilde{m}\omega_p) - i\eta} . \tag{4.11}$$

All the eigenvalues and eigenvectors can be found in tables 4.1 and 4.2. Note that only $v_0^{\tilde{m}}$ appears because $\langle 0; m | c | 1; 0 \rangle \neq 0$ only if $m = 0$. The spectral function of the above Green's function reads

$$A^h(\omega) = \sum_{m=0}^{\infty} \frac{\beta^m e^{-\beta}}{m!} \delta\left(\omega - \varepsilon_0 - \frac{g^2}{\omega_p} + m\omega_p\right) . \tag{4.12}$$

The electron removal spectral function $A^h(\omega)$ is the same as the one of Langreth in Eq. (1.5) and a detailed discussion has been provided in section 1.1. In particular, this spectral function conserves the particle number and the spectral weight because

$$\int_{-\infty}^{\mu} A^h(\omega) \, \mathrm{d}\omega = \int_{-\infty}^{\infty} A^h(\omega) \, \mathrm{d}\omega = \sum_{m=0}^{\infty} \frac{\beta^m e^{-\beta}}{m!} = 1 . \tag{4.13}$$

Since there is only one orbital in the HPC-1, the constraint of the poles summarized in section 1.3 is meaningless. As I mentioned before, similar to the quasi-boson model the HPC-1 describes a single (core) state coupled to plasmons. Hence there is no interaction between different states[3]. This suggests to introduce a two-level hole-plasmon coupling Hamiltonian to get closer to valence photoemission where the interaction between states is taken into account.

Putting the electron back in the hole-plasmon coupling Hamiltonian

The HPC-1 in Eq. (4.2) can be also used to perform the inverse process, namely to calculate the inverse photoemission spectrum starting from zero electrons. We only consider the

---

[3]This is the reason why the HPC-1 is good for modeling core photoemission. Most often, the core is far from the valence such that the core can be approximate as a decoupled state that couples only to the plasmons.

ground state as starting point. In the initial state there is now one `hole` (zero electrons) in the orbital of energy ε_0, and the hole couples to the plasmons. The ground state eigenenergy and eigenfunction of the zero-electron system are given in Tab. 4.2 as

$$E_0^{N=0} = -\frac{g^2}{\omega_p} \; ; \tag{4.14a}$$

$$\left| \Psi_0^{N=0} \right\rangle = v_0^0 \left| 0;0 \right\rangle + v_1^0 \left| 0;1 \right\rangle + v_2^0 \left| 0;2 \right\rangle + \cdots \equiv \sum_{\tilde{m}=0}^{\infty} v_{\tilde{m}}^0 \left| 0;\tilde{m} \right\rangle \; . \tag{4.14b}$$

The analytic result for the coefficients is

$$(v_{\tilde{m}}^0)^2 = \frac{1}{\tilde{m}!} \beta^{\tilde{m}} e^{-\beta} \; . \tag{4.15}$$

After the inverse photoemission, we have one `electron` in the system hence the coupling term does not contribute. Therefore the eigenenergies and eigenfunctions are

$$E_m^{N=1} = \varepsilon_0 + m\omega_p \; ; \tag{4.16a}$$

$$\left| \Psi_m^{N=1} \right\rangle = \left| 1;m \right\rangle \; . \tag{4.16b}$$

The electron addition Green's function and intrinsic spectral function are

$$G^e(\omega) = \sum_{m=0}^{\infty} \frac{\beta^m e^{-\beta}}{m!} \frac{1}{\omega - (\varepsilon_0 + \frac{g^2}{\omega_p} + m\omega_p) + i\eta} \; ; \tag{4.17a}$$

$$A^e(\omega) = \sum_{m=0}^{\infty} \frac{\beta^m e^{-\beta}}{m!} \delta\left(\omega - \varepsilon_0 - \frac{g^2}{\omega_p} - m\omega_p \right) . \tag{4.17b}$$

The comparison between electron removal and addition spectral functions is shown in Fig. 4.2. Compared to the electron removal spectrum in Eq. (4.12), the electron addition spectrum has the same quasi-particle energy $\varepsilon_0 + \frac{g^2}{\omega_p}$ but the plasmon satellites are on the right hand side of the quasi-particle peak (blue curve in Fig. 4.2). The two spectral functions are symmetric, reflecting the fact that the system can recover after photoemission and inverse photoemission processes. In photoemission, one electron is removed from the system. The quasi-particle energy ε_{QP} tells the energy level this one electron was occupying before emitted. The plasmon satellites induced by the excitation of photoemission appear

97

at an energy lower than ε_{QP} because the energy of the total system (one electron is the ground state, versus the photoelectron plus the system in an excited state) is conserved. The inverse photoemission adds the electron back to its original orbital ε_{QP}, simultaneously the plasmons are excited leading to satellites at an energy higher than ε_{QP}.
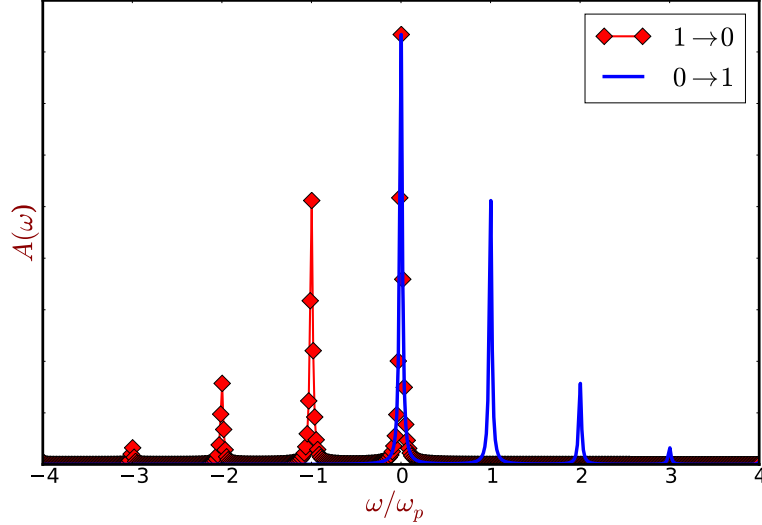

Figure 4.2: The spectral functions of the one-level hole-plasmon coupling Hamiltonian (HPC-1) in Eq. (4.2). The red line with diamonds and blue solid line are electron removal (PES) Eq. (4.12) and addition (IPES) Eq. (4.17b) spectra, respectively. I have put Lorentzian broadening $\eta = 0.1$ in both spectral functions. The quasi-particle energy has been shifted to zero, i.e. $\varepsilon_{QP} = \varepsilon_0 - \frac{g^2}{\omega_p} = 0$.

This is what the exact spectra should be. However, as we will see in the next section (see 4.2) when we use the GWA or CEA to calculate the electron addition and removal spectral functions of the HPC-1, the situation will change. This will explain why I have chosen the hole-plasmon coupling, instead of the electron-plasmon coupling to study the photoemission process.

4.1.2 Two-level hole-plasmon coupling Hamiltonian

As discussed before, the HPC-1 is designed for modeling the core photoemission where the coupling between orbitals can be neglected, but not for the valence photoemission. Here I am going to study a generalized two-level hole-plasmon coupling model Hamiltonian (HPC-

2) that was proposed by Gunnarsson, Meden, and Schönhammer in Ref. [77] to study higher order cumulants in the presence of the orbital interaction. The HPC-2 reads

$$\hat{H} = \varepsilon_0 \sum_{i=1}^{2} c_i^\dagger c_i + \omega_p \sum_{i=1}^{2} a_i^\dagger a_i - \mathbf{t}(c_1^\dagger c_2 + c_2^\dagger c_1) + g \sum_{i=1}^{2} (a_i^\dagger + a_i) c_i c_i^\dagger. \qquad (4.18)$$

Compared to the HPC-1 in Eq. (4.2), we choose to have again one electron in the HPC-2, but now two sites where the one electron can stay. The electron can jump between two sites through the hopping kinetic term labeled as $\mathbf{t}$. The hole-plasmon coupling is on-site as represented by the last term of the above equation, i.e. only when the plasmons and the hole are on the same site, can they couple with strength $g \neq 0$[4]. In order to calculate the Green's function of the HPC-2, it is more convenient to work in `orbital basis` defined as

$$c_\pm^{(\dagger)} = \frac{1}{\sqrt{2}} \left(c_1^{(\dagger)} \pm c_2^{(\dagger)} \right) ; \qquad (4.19a)$$

$$a_\pm^{(\dagger)} = \frac{1}{\sqrt{2}} \left(a_1^{(\dagger)} \pm a_2^{(\dagger)} \right) ; \qquad (4.19b)$$

where the subscripts $\pm$ represent `bonding` and `anti-bonding` orbitals, respectively. In the orbital basis, the HPC-2 Eq. (4.18) can be separated into two Hamiltonians:

$$\hat{H}^+ = \omega_p a_+^\dagger a_+ + \frac{g}{\sqrt{2}} (c_+ c_+^\dagger + c_- c_-^\dagger)(a_+^\dagger + a_+) ; \qquad (4.20a)$$

$$\hat{H}^- = (\varepsilon_0 - \mathbf{t}) c_+^\dagger c_+ + (\varepsilon_0 + \mathbf{t}) c_-^\dagger c_- + \omega_p a_-^\dagger a_- + \frac{g}{\sqrt{2}} (c_+ c_-^\dagger + c_- c_+^\dagger)(a_-^\dagger + a_-). \qquad (4.20b)$$

$\hat{H}^\pm$ are separated according to the boson operators $a_\pm$[5] such that they commute, i.e. $\left[\hat{H}^+, \hat{H}^- \right] = 0$. This separation simplifies the calculation because we can diagonalize these two Hamiltonians separately to have the eigenenergies and eigenfunctions of each Hamiltonian. Then the eigenenergies and eigenfunctions of the total Hamiltonian can be calculated

---

[4]The on-site hole-plasmon coupling reminds some aspects of dynamical mean filed theory (DMFT) [86–88], where couplings are local. Cumulant-like results are found also in that context, e.g. Ref. [89].

[5]In this thesis, I use the subscripts $\pm$ for bonding and anti-bonding orbital distinguished by fermion operators $c_\pm^{(\dagger)}$ and superscript to represent the separation according to boson operators $a_\pm^{(\dagger)}$. For example G_-^+ in Eq. (4.22) represents the anti-bonding orbital Green's function of $\hat{H}^+$ in Eq. (4.20a).

from

$$E = E^+ + E^- \, ; \tag{4.21a}$$

$$|\Psi\rangle = |\Psi^+\rangle |\Psi^-\rangle \, . \tag{4.21b}$$

Here E and $|\Psi\rangle$ are the eigenenergy and eigenfunction of the HPC-2 in Eq. (4.18), $E^{\pm}$ and $|\Psi^{\pm}\rangle$ are eigenergies and eigenfunctions of $\hat{H}^{\pm}$ in Eq. (4.20).

$\hat{H}^+$ in Eq. (4.20a) is nothing else than the HPC-1 in Eq. (4.2) in the case of $\varepsilon_0 = 0$. Consequently, the Green's function is the same as the one in equation (4.11) when $\varepsilon_0 = 0$, which reads

$$G_{\pm}^+(\omega) = \sum_{m_+=0}^{\infty} \frac{\tilde{\beta}_1^{[m_+]} e^{-\tilde{\beta}_1}}{m_+!} \frac{1}{\omega - (\frac{\tilde{g}}{\omega_p} - m_+\omega_p) - i\eta} \, , \tag{4.22}$$

where $\tilde{g} = \frac{g}{\sqrt{2}}$ and $\tilde{\beta}_1 = \frac{g^2}{2\omega_p^2}$. All the eigenenergies and eigenfunctions can be found in Tabs. 4.2 and 4.1 (replace ε_0 and g by 0 and $\tilde{g}$, respectively).

$\hat{H}^-$ in Eq. (4.20b) is more difficult due to the mixed term $(c_+ c_-^\dagger + c_- c_+^\dagger)(a_-^\dagger + a_-)^6$. What we can do is to write $\hat{H}^-$ in a basis reading as $|n_+, n_-; m_+, m_-\rangle$ where $n_{\pm}$ and $m_{\pm}$ are the occupations of electrons and plasmons in each orbital, respectively. Then we diagonalize $\hat{H}^-$ numerically in this basis. I have checked that with increasing number of plasmons in the anti-bonding orbital (i.e. $m_- \to \infty$), the diagonalization converges to the exact result. In the initial state where there is one electron, the matrix elements of $\hat{H}^-$ read

$$H^-[2m_-, 2m_-] = 2m_- w_0 + \varepsilon_0 - \mathbf{t} \, ; \tag{4.23a}$$

$$H^-[2m_- + 1, 2m_- + 1] = (2m_- + 1)\omega_p + \varepsilon_0 + \mathbf{t} \, ; \tag{4.23b}$$

$$H^-[m_-, m_- + 1] = H^{-1}[m_- + 1, m_-] = g\frac{\sqrt{m_- + 1}}{\sqrt{2}} \, ; \tag{4.23c}$$

and all other elements are zero. In practice, the plasmon number $m_-^{max} = 200$ is adopted to have a converged ground state energy. After diagonalization, we only need the ground state energy E_0^- (the lowest eigenenergy) and eigenfunction $|\Psi_0^-\rangle$. The ground state wavefunction

---

[6] As stated by Gerald D. Mahan in his book [2] page 229: "Any terms which permit a direct interaction between the states usually render the Hamiltonian unsolvable, at least exactly."

reads

$$\left| \Psi_0^- \right\rangle = \sum_{m_-=0}^{\infty} v_{[2m_-]} \left| 1, 0; 2m_- \right\rangle + \sum_{m_-=0}^{\infty} v_{[2m_-+1]} \left| 0, 1; 2m_- + 1 \right\rangle . \tag{4.24}$$

Note that the ground state energy E_0^- and the coefficients of the eigenvectors v_m are numerical results. After photoemission, there is no electron in $\hat{H}^-$, hence the problematic term vanishes, leading to

$$\hat{H}^- = \omega_p a^\dagger a , \tag{4.25}$$

whose eigenvalues and eigenfunctions are simply

$$E_{m_-}^{N=0} = m_- \omega_p ; \tag{4.26a}$$

$$\left| \Psi_{m_-}^{N=0} \right\rangle = \left| 0, 0; m_- \right\rangle . \tag{4.26b}$$

The bonding orbital electron removal Green's function can be calculated from

$$
\begin{aligned}
G_+(\omega) &= \sum_{m_-=0}^{\infty} \sum_{m_+=0}^{\infty} \frac{\left(\langle \Psi_0^+ | \, \langle \Psi_0^- | \, c_+^\dagger \, | \Psi_{m_-}^{N=0} \rangle \, | \Psi_{m_+}^{N=0} \rangle \right)^2}{\omega - (E_0^{N=1} - E_{m_+}^{N=0} - E_{m_-}^{N=0}) - i\eta} \\
&= \sum_{m_-=0}^{\infty} \sum_{m_+=0}^{\infty} \frac{\tilde{\beta}_1^{[m_+]} e^{-\tilde{\beta}_1}}{m_+!} \frac{\left(\langle \Psi_0^- | \, c_+^\dagger \, | \Psi_{m_-}^{N=0} \rangle \right)^2}{\omega - (E_0^+ + E_0^- + \frac{\tilde{g}^2}{\omega_p} - m_+\omega_p - E_{m_-}^{N=0}) - i\eta} \\
&= \sum_{m_-=0}^{\infty} \sum_{m_+=0}^{\infty} \frac{\tilde{\beta}_1^{[m_+]} e^{-\tilde{\beta}_1}}{m_+!} \frac{v_{[2m_-]}^2}{\omega - (\frac{\tilde{g}^2}{\omega_p} - m_+\omega_p + E_0^- - 2m_-\omega_p) - i\eta} .
\end{aligned} \tag{4.27}
$$

The anti-boding orbital Green's function can be calculated analogously, leading to

$$G_-(\omega) = \sum_{m_-=0}^{\infty} \sum_{m_+=0}^{\infty} \frac{\tilde{\beta}_1^{[m_+]} e^{-\tilde{\beta}_1}}{m_+!} \frac{v_{[2m_-+1]}^2}{\omega - (\frac{\tilde{g}^2}{\omega_p} - m_+\omega_p + E_0^- - (2m_- + 1)\omega_p) - i\eta} . \tag{4.28}$$

Finally the spectral function of the two-level hole-plasmon coupling Hamiltonian reads

$$A_+(\omega) = \sum_{m_-=0}^{\infty} \sum_{m_+=0}^{\infty} \frac{\tilde{\beta}_1^{[m_+]} e^{-\tilde{\beta}_1} v_{[2m_-]}^2}{m_+!} \delta\left(\omega - E_0^- - \frac{g^2}{2\omega_p} + (m_+ + 2m_-)\omega_p\right); \qquad (4.29a)$$

$$A_-(\omega) = \sum_{m_-=0}^{\infty} \sum_{m_+=0}^{\infty} \frac{\tilde{\beta}_1^{[m_+]} e^{-\tilde{\beta}_1} v_{[2m_-+1]}^2}{m_+!} \delta\left(\omega - E_0^- - \frac{g^2}{2\omega_p} + (m_+ + 2m_- + 1)\omega_p\right). \quad (4.29b)$$

The quasi-particle peak is obtained from A_+ in Eq. (4.29a) for $m_- = m_+ = 0$. The corresponding quasi-particle renormalization factor $\mathbf{Z}$ reads

$$\mathbf{Z} = e^{-\tilde{\beta}_1} v_0^2. \qquad (4.30)$$

Note that we have some parameters (E_0^- and v_m) which are calculated numerically. The situation is different from the exact spectral function of the HPC-1 (see Eq. (4.12)) where the fully analytical result can be obtained. The spectral functions in Eq. (4.29) are shown in Fig. 4.3 where parameters are chosen that correspond to the bulk sodium bottom valence state[7]. Some important properties of the exact spectral function in Eq. (4.29) are summarized below:

1. First, there is an electron removal spectrum in the anti-bonding orbital. It means that the anti-bonding orbital is also partially occupied in the ground state due to the hole-plasmon coupling, i.e. the two orbitals are interacting with each other leading to two partially occupied (or unoccupied) orbitals.

2. Second, we only have one quasi-particle peak in the electron removal spectrum that stays in the bonding orbital matrix element. In the anti-bonding orbital matrix element, we have only satellites but no electron removal quasi-particle, because all the excitations in the anti-bonding orbital are due to interaction. When there is no interaction, there is no spectrum in this orbital. This is consistent with the definition of

---

[7]Throughout the thesis, if not otherwise specified, the bulk sodium bottom valence parameters are corresponding to the bandwidth $2\mathbf{t} = 3.0$ eV, the plasmon energy $\omega_p = 6.0$ eV and the coupling constant $g = 4.5$ eV yielding the exact quasi-particle renormalization factor in Eq. (4.30) $\mathbf{Z} \approx 0.65$. Note that although we have chosen all the parameters corresponding to bulk sodium bottom valence state, it is still a very rough correspondence. However it is sufficient to understand the overall effects on the spectral functions as observed in the intrinsic spectral function of bulk sodium bottom valence state, which is at the Γ point in the Brillouin zone.

the satellites in footnote 3 of Chapter 1. Note that the position of the anti-bonding orbital satellites are the same as the bonding orbital satellites, which is consistent with the `constraint of poles` in the exact Green's function (see the summary 1.3 of Chapter 1) .

3. Conservation of particle number. One can show that $\int_{-\infty}^{\mu} d\omega \left(A_+(\omega) + A_-(\omega) \right) = 1$, therefore the exact spectral function in Eq. (4.29) conserves the particle number. Since we have spectra on both orbitals, we have partial occupation, i.e. $\int_{-\infty}^{\mu} d\omega \, A_{\pm}(\omega) < 1$.
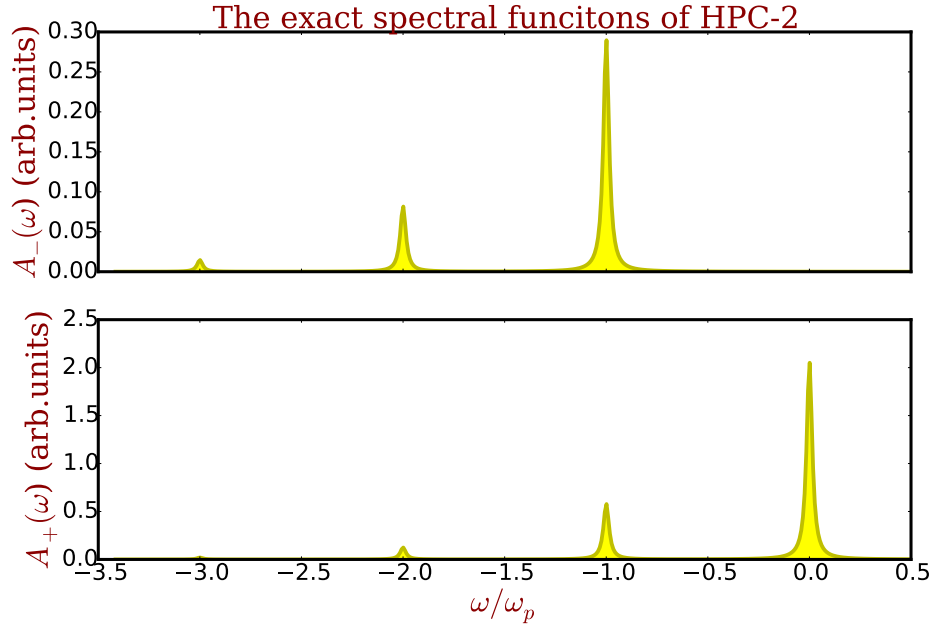

Figure 4.3: The exact spectral functions of the two-level hole-plasmon coupling Hamiltonian (HPC-2) . The parameters in Eq. (4.18) are chosen consistent with the bulk sodium bottom valence state, i.e. the plasmon energy $\omega_p = 6.0$ eV, $\varepsilon_0 = \mathbf{t} = 1.5$ eV yielding a 3 eV bandwidth, as well as the coupling constant $g = 4.5$ eV yielding the exact renormalization factor $\mathbf{Z} = 0.65$. The upper and lower panels show the spectral function of the anti-bonding and bonding orbitals, respectively. The exact QP energy has been shifted to zero, i.e. $E_0^- + \frac{g^2}{2\omega_p} = 0$. I have used $\eta = 0.1$ Lorentzian to broaden both spectral functions. Note the change of scale between the two plots.

4.2 Performance of approximations to spectra in the model Hamiltonians

In the previous section, I have shown how to calculate the Green's function of the one- and two- level hole-plasmon coupling model Hamiltonians and discussed the exact spectral functions of these two model Hamiltonians. In this section, I am going to use the GW approximation and the cumulant expansion approximations including the TOC96, TOC11, and RC to calculate the spectral functions of these two Hamiltonians. From the comparison between the exact and approximate spectral functions, I will discuss the advantages and disadvantages of different approximations.

4.2.1 The one-level hole-plasmon coupling model

I start from the HPC-1 in Eq. (4.2) to calculate the GWA and CEA spectral functions. In particular, I will explain why the hole-plasmon coupling is chosen to study the photoemission spectroscopy, instead of the electron-plasmon coupling at the end of this subsection.

The GWA in HPC-1

I have shown that the GW self-energy is the central quantity for both the GWA and CEA, such that first we have to calculate the GW self-energy of the HPC-1.

The non-interacting electron removal Green's function of the HPC-1 reads

$$G_0(\omega) = \frac{1}{\omega - \varepsilon_0 - i\eta} \, .$$

(4.31)

The plasmon propagator of such an Hamiltonian reads[8]

$$W_0(\omega) = \frac{g^2}{\omega - \omega_p + i\eta} - \frac{g^2}{\omega + \omega_p - i\eta} \, .$$

(4.32)

---

[8]Note that this plasmon propagator corresponds to the exact dynamical screened Coulomb interaction that should appear in the one-level hole-plasmon coupling Hamiltonian as mentioned in the context around the Eq. (1.4). For the consistency of the notation, we still use W_0 but keep in mind that it is not the RPA W here.

As discussed before, the plasmon excitation stems from the poles in the inverse dielectric function ϵ^{-1}, hence it can be seen in the screening $W = \epsilon^{-1}v_c$. This explains why W_0 in Eq. (4.32) has poles at plasmon energy $\pm\omega_p$ with the weight g^2 representing the possibility of the excitation due to couplings to the fermion. The one-shot GW self-energy is the convolution of $G_0(\omega)$ and $W_0(\omega)$, yielding[9]

$$\Sigma^{G_0W_0}(\omega) = iG_0(\omega) * W_0(\omega) = \frac{i}{2\pi}\int \mathrm{d}\omega'\, G_0(\omega')W_0(\omega - \omega')e^{i\eta\omega'}$$

$$= \frac{g^2}{\omega - \varepsilon_0 + \omega_p - i\eta}. \tag{4.33}$$

As a consequence of the convolution, the GW self-energy has its pole at $\varepsilon_0 - \omega_p$, i.e. the pole in G_0 minus the pole in W_0. Since we only have the electron removal part of G_0, the convolution yields one pole in $\Sigma^{G_0W_0}$[10]. The G_0W_0 Green's function can be calculated from the following Dyson equation

$$G^{G_0W_0}(\omega) = \left[G_0(\omega)^{-1} - \Sigma^{G_0W_0}(\omega)\right]^{-1} = \frac{f_1}{\omega - \varepsilon_1 - i\eta} + \frac{f_2}{\omega - \varepsilon_2 - i\eta}. \tag{4.34}$$

We find

$$f_1 = \frac{1}{2}\left(1 + \frac{\omega_p}{\omega_p^2 + 4g^2}\right); \tag{4.35a}$$

$$f_2 = \frac{1}{2}\left(1 - \frac{\omega_p}{\omega_p^2 + 4g^2}\right); \tag{4.35b}$$

$$\varepsilon_1 = \varepsilon_0 - \frac{\omega_p}{2} + \frac{\omega_p}{2}\sqrt{1 + \frac{4g^2}{\omega_p^2}}; \tag{4.35c}$$

$$\varepsilon_2 = \varepsilon_0 - \frac{\omega_p}{2} - \frac{\omega_p}{2}\sqrt{1 + \frac{4g^2}{\omega_p^2}}. \tag{4.35d}$$

---

[9]Note that $e^{i\eta\omega'}$ determines the direction of the contour when we use Cauchy's residue theorem. Since η is positive, ω' must run counter-clockwise through the positive imaginary plane of ω'. The GW self-energy in Eq. (4.33) is a simplified version of $\Sigma_k(\omega) = \sum_{i,s\neq 0} \frac{|V_{k,i}^s|^2}{\omega + \omega_s \mathrm{sgn}(\mu - \varepsilon_\mathrm{i}) - \varepsilon_\mathrm{i}}$ in Ref. [34], where V is defined as the *fluctuation potential*.

[10]This GW self-energy is actually the hole part of the GW self-energy. If the non-interacting Green's function contains both electron and hole parts, it will yield a GW self-energy containing the electron and hole parts as well. This will be seen in the GW self-energy of the HPC-2 later in this section.

Therefore the G_0W_0 electron removal spectral function of the HPC-1 reads

$$A^{G_0W_0}(\omega) = \frac{1}{2}\left(1 + \frac{\omega_p}{\omega_p^2 + 4g^2}\right)\delta\left(\omega - (\varepsilon_0 - \frac{\omega_p}{2} + \frac{\omega_p}{2}\sqrt{1 + \frac{4g^2}{\omega_p^2}})\right)$$
$$+ \frac{1}{2}\left(1 - \frac{\omega_p}{\omega_p^2 + 4g^2}\right)\delta\left(\omega - (\varepsilon_0 - \frac{\omega_p}{2} - \frac{\omega_p}{2}\sqrt{1 + \frac{4g^2}{\omega_p^2}})\right). \qquad (4.36)$$

The above spectral function is shown by the blue dashed curve in Fig. 4.4. It has one quasi-particle peak at ε_1 with weight f_1 and one satellite at ε_2 with weight f_2. Compared to the exact spectral function in equation (4.12), on one hand $A^{G_0W_0}$ does not give the exact quasi-particle energy: it is close to the exact one because $\varepsilon_1 = \varepsilon_0 + \frac{g^2}{\omega_p} + \mathcal{O}(g^4)$[11], which is correct to the second order in g. The QP energy obtained from a linearization in Eq. (2.44) is even worse as illustrated by the black arrow labeled as " linear " in Fig. 4.4. On the other hand, $A^{G_0W_0}$ does not give satellite replica, instead only one satellite appears at energy between the first and second exact satellites. The G_0W_0 spectral function conserves the spectral weight and the particle number because one can show that

$$\int_{-\infty}^{\infty} d\omega\, A^{G_0W_0}(\omega) = 1\,; \qquad (4.37a)$$

$$\int_{-\infty}^{\mu} d\omega A^{G_0W_0}(\omega) = 1\,. \qquad (4.37b)$$

As mentioned before, the constraint of the poles summarized in section 1.3 is meaningless in the HPC-1 since the occupation is either 0 or 1.

One could hope that the self-consistency improves the GWA spectrum in the HPC-1. Therefore we have a look at the $EscGW_0$ spectral function of the HPC-1. Following the idea of Hedin [34], the $EscGW_0$ can be simulated by introducing an energy shift Δ in the non-interacting Green's function, which yields

$$G_0^{Esc}(\omega) = \frac{1}{\omega - \Delta - \varepsilon_0 - i\eta}\,, \qquad (4.38)$$

---

[11]We have used the Taylor series of $\sqrt{1+x} = 1 + \frac{1}{2}x - \frac{1}{8}x^2 + \cdots$.

where

$$\Delta = \mathrm{Re}\,\Sigma^{G_0 W_0}(\varepsilon_0) = \frac{g^2}{\omega_p}\,. \tag{4.39}$$

With this choice, the pole in G_0^{Esc} is $\varepsilon_{QP} = \varepsilon_0 + \frac{g^2}{\omega_p}$ that is the exact quasi-particle energy of the HPC-1 (see Eq. (4.12)). The energy self-consistent G yields the energy self-consistent GW self-energy that reads

$$\Sigma^{Esc}(\omega) = \frac{g^2}{\omega - \Delta - \varepsilon_0 + \omega_p - i\eta}\,. \tag{4.40}$$

Thus the self-consistent GW self-energy contains a pole at the quasi-particle energy minus the plasmon energy. The EscGW$_0$ Green's function can be calculated from

$$G^{EscGW_0} = \left[G_0(\omega)^{-1} - \Sigma^{Esc}(\omega) \right]^{-1}\,. \tag{4.41}$$

The above Dyson equation can be solved analytically like what I did in the G$_0$W$_0$ case (see Eq. (4.34)). The resulting electron removal EscGW$_0$ spectral function reads[12]

$$A^{EscGW_0}(\omega) = \frac{\omega_p^2}{\omega_p^2 + g^2}\delta\left(\omega - \varepsilon_0 - \frac{g^2}{\omega_p}\right) + \frac{g^2}{\omega_p^2 + g^2}\delta(\omega - \varepsilon_0 + \omega_p)\,. \tag{4.42}$$

The above spectral function is shown by blue solid curve with up-triangles in Fig. 4.4. Similar to the G$_0$W$_0$ spectral function, A^{EscGW_0} has two poles: one quasi-particle peak at $\varepsilon_0 + \frac{g^2}{\omega_p}$ that is the same as the exact quasi-particle energy of the HPC-1 (see Eq. (4.12)), and the other peak is the GW plasmaron satellite that has a distance from the QP peak larger than ω_p. The EscGW$_0$ improves the position and the weight of the QP peak, however the satellite replica cannot be obtained.

Also $A^{EscGW_0}(\omega)$ conserves the spectral weight and particle number, since

$$\int_{-\infty}^{\infty} \mathrm{d}\omega\, A^{EscGW_0}(\omega) = \int_{-\infty}^{\mu} \mathrm{d}\omega A^{EscGW_0}(\omega) = 1\,. \tag{4.43}$$

The energy self-consistency corrects the G$_0$W$_0$ QP energy but still cannot give the correct plasmon satellites appearing in the exact spectral function of the HPC-1 (yellow

---

[12]The EscGW$_0$ spectral function in Eq. (4.42) is in agreement with the result in Ref. [34].
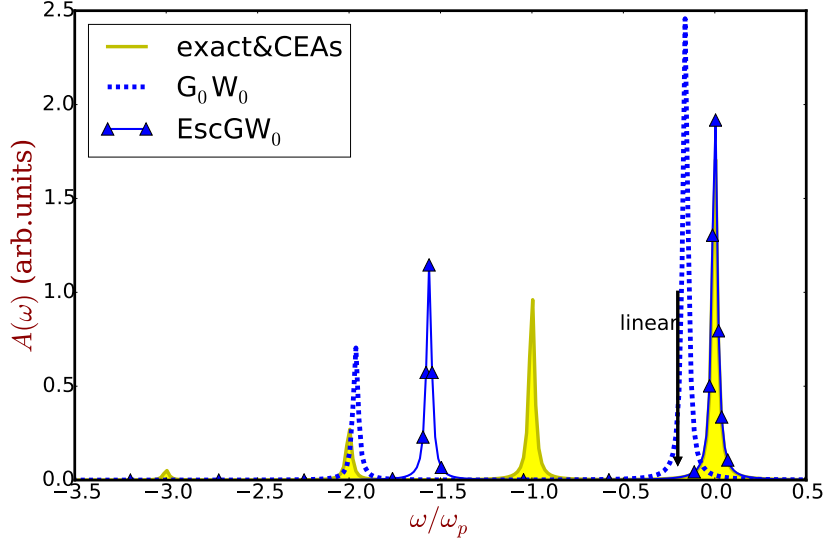
Figure 4.4: The electron removal spectral functions of the one-level hole-plasmon coupling Hamiltonian (HPC-1). The yellow filled curve is the exact spectral function of the model Hamiltonian in equation (4.12). The cumulant expansion approximation yields the exact spectral function of the HPC-1 as shown in equation (4.47). The blue dashed curve is the spectral function calculated from the one-shot GW (G_0W_0) in equation (4.36). The blue solid line with up-triangles represents the spectral function calculated using the energy self-consistent GW in Eq. (4.42). The black arrow labeled " linear " represents the quasi-particle energy from the linearization approximation in Eq. (2.44). The exact quasi-particle energy has been shifted to zero. I have used the Lorentzian broadening $\eta = 0.1$ in all plots. The parameters are corresponding to bulk sodium bottom valence state.

filled plot in Fig. 4.4). This is the well known failure of the GW approximation (the plasmaron)[13] that has been discussed in section 2.2. Besides the position of the peaks, G_0W_0 overestimates the quasi-particle weight. Self-consistency improves a bit but still gives too much weight on the quasi-particle peak compared to the exact spectrum. This can be explained analytically in such a simple model. The GW and exact quasi-particle

---

[13]Note that, only the G_0W_0 and EscGW$_0$ have been studied in this thesis but not the fully self-consistent GW (scGW). In Ref. [90], the authors studied the fully self-consistent GW approximation in a similar electron-boson coupling Hamiltonian and found that the scGW are also able to produce multiple plasmon satellites, although not as well as the cumulant expansion approximations.

renormalization factors are (see Eq. (2.45))

$$\mathbf{Z}^{GW} = \left[1 - \frac{\partial \operatorname{Re} \Sigma^{Esc}(\omega)}{\partial \omega} \bigg|_{\omega = \varepsilon_{QP}} \right]^{-1} = [1 + \beta]^{-1} = \sum_{n=0}^{\infty} (-\beta)^n ; \qquad (4.44a)$$

$$\mathbf{Z}^{exact} = e^{-\beta} = \sum_{n=0}^{\infty} \frac{(-\beta)^n}{n!} . \qquad (4.44b)$$

They are identical to first order in β, consistently with the fact the Σ^{GW} is correct to first order in g^2. As shown in Fig. 4.5, the quasi-particle weights from the $\mathrm{EscGW_0}$ (blue line with down-triangles) are always larger than the exact ones (red line with up-triangles). As we will see later that, this conclusion also holds for the HPC-2.

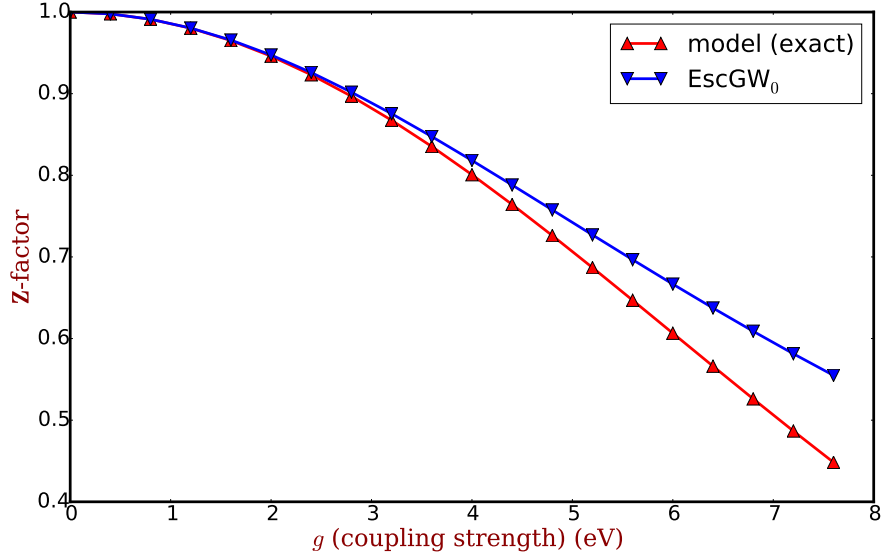Figure 4.5: The quasi-particle renormalization factors: GW (blue line with down-triangles) and exact (red line with up-triangles) in Eq. (4.44) as a function of the coupling constant g. I have used the same parameters as in Fig. 4.4.

The CEA in HPC-1

One can show that in the one-level hole-plasmon coupling Hamiltonian (HPC-1) Eq. (4.2), all the cumulant expansion approximations (TOC96, TOC11 and RC) yield the same result

that is the exact one[14]. In order to calculate the cumulant Green's function as shown in Eqs. (2.62), (3.32) and (3.64), we have to calculate each component of the cumulant function in terms of the GW self-energy. The needed expressions are

$$\operatorname{Re}\Sigma^{G_0W_0}(\varepsilon_0) = \operatorname{Re}\Sigma^{EscGW_0}(\varepsilon_{QP}) = \frac{g^2}{\omega_p}\,; \tag{4.45a}$$

$$\left.\frac{\partial\operatorname{Re}\Sigma^{G_0W_0}(\omega)}{\partial\omega}\right|_{\omega=\varepsilon_0} = \left.\frac{\partial\operatorname{Re}\Sigma^{EscGW_0}(\omega)}{\partial\omega}\right|_{\omega=\varepsilon_{QP}} = -\frac{g^2}{\omega_p^2} = -\beta\,; \tag{4.45b}$$

$$\frac{1}{\pi}\int_{-\infty}^{\mu}d\omega\,\frac{e^{i(\varepsilon_0-\omega-i\eta)\tau}\operatorname{Im}\Sigma^{G_0W_0}(\omega)}{(\varepsilon_0-\omega-i\eta)^2} = \frac{1}{\pi}\int_{-\infty}^{\mu}d\omega\,\frac{e^{i(\varepsilon_{QP}-\omega-i\eta)\tau}\operatorname{Im}\Sigma^{EscGW_0}(\omega)}{(\varepsilon_{QP}-\omega-i\eta)^2} = \beta e^{i\omega_p\tau}\,. \tag{4.45c}$$

Then the cumulant Green's function of the HPC-1 reads (see Eq. (2.62) or (3.30))

$$G^C(\tau) = i\theta(-\tau)e^{-i\varepsilon_{QP}\tau}e^{-\beta}\exp\left(\beta e^{i\omega_p\tau}\right), \tag{4.46}$$

where the QP energy is $\varepsilon_{QP} = \varepsilon_0 + \dfrac{g^2}{\omega_p}$.

The final spectral function from the CEA reads

$$A^C(\omega) = \sum_{m=0}^{\infty}\frac{\beta^m e^{-\beta}}{m!}\delta\left(\omega - \varepsilon_0 - \frac{g^2}{\omega_p} + m\omega_p\right), \tag{4.47}$$

which is the same as the exact spectral function in equation (4.12). Note that Eqs. (4.45) show that the self-consistency in the GW self-energy does not change the cumulant Green's function whereas it is important for the GWA itself. When I derived the retarded cumulant in section 3.4, the self-energy is defined as $\Sigma = iG_H W$ (see Eq. (3.51) when $\phi = 0$) that corresponds to the one-shot Σ, which explains why $\Sigma^{G_0W_0}$ in equation (4.45) gives the good cumulant Green's function. If we use $\Sigma^{EscGW_0} = iG_0^{Esc}W$ where only the energies are updated during iteration, we should replace all non-interacting eigenenergies (ε_0) by the quasi-particle energy in G^{Esc}, i.e. $\varepsilon_{QP} = \varepsilon_0 + \frac{g^2}{\omega_p}$. In such a way, we can use the self-consistent Σ in the cumulant Green's function, which yields the same result as using

---

[14]I have shown that the only difference in different CEAs is the use of the greater part of the self-energy. Since in the HPC-1, the greater part of the self-energy is zero, all CEAs yield the same result.

the one-shot Σ. For this reason, I will always use the one-shot GW self-energy to calculate the cumulant Green's function in the following paragraphs of this section.

The electron addition spectra of the GWA and CEA

In order to calculate the electron addition spectral function, we have to start from the `electron` part of the non-interacting Green's function that reads (the hole part is shown in Eq. (4.31))

$$G_0^e(\omega) = \frac{1}{\omega - \varepsilon_0 + i\eta} \, . \tag{4.48}$$

The plasmon propagator is the same as the one in equation (4.32). The resulting self-energy for electron addition reads

$$\Sigma^e(\omega) = \frac{g^2}{\omega - \varepsilon_0 - \omega_p + i\eta} \, . \tag{4.49}$$

We have seen above that in order to have a better quasi-particle energy from the GWA, we have to use the energy self-consistent GW self-energy thus in the electron addition calculation, I will not calculate the G_0W_0 Green's function but only the energy self-consistent one. Solving the same Dyson equation as (4.41) with the `electron` part of G_0^e and Σ^e, the final EscGW$_0$ spectral function for electron addition reads

$$A_{IPES}^{EscGW_0}(\omega) = \frac{\omega_p^2}{\omega_p^2 + g^2} \delta\left(\omega - \varepsilon_0 + \frac{g^2}{\omega_p}\right) + \frac{g^2}{\omega_p^2 + g^2} \delta(\omega - \varepsilon_0 - \omega_p) \, . \tag{4.50}$$

Similarly we can calculate the cumulant spectral function that reads

$$A_{IPES}^C(\omega) = \sum_{m=0}^{\infty} \frac{\beta^m e^{-\beta}}{m!} \delta\left(\omega - \varepsilon_0 + \frac{g^2}{\omega_p} - m\omega_p\right) . \tag{4.51}$$

Neither the GWA nor CEA gives the correct quasi-particle energy for the inverse photoemission process compared to the exact electron removal spectral function in Eq. (4.17b). This is because the GWA and CEA are doing different processes: the inverse photoemission spectral function of Eq .(4.17b) is the electron addition process from the system with particle number $N = 0$ to $N = 1$. However, what the GWA and CEA are calculating here

are the electron addition process from $N = 1$ to $N = 2$. Since we can only study the one electron in the HPC-1, it is impossible to calculate the electron addition process from $N = 1$ to $N = 2$ because with only one orbital, we can only put one electron.

What we can do is to use the GWA or the CEA to calculate the electron addition process from $N = 0$ to $N = 1$, which will give the correct QP energy when comparing to the exact one. This issue has been discussed in Langreth's article [16] where extra diagrams are needed when calculating the self-energy from the *linked-cluster theorem*. It also explains why when Gunnarsson, Meden, and Schönhammer studied the photoemission of a two-level `electron-plasmon coupling` Hamiltonian, an extra diagram for the self-energy was needed (see Ref. [77]). In order to avoid the extra diagrams of Refs. [16, 77], the hole-plasmon coupling Hamiltonian is adopted to study the photoemission process in this thesis. Analogously, the electron-plasmon coupling Hamiltonian is good for the study of the inverse photoemission process, where again the extra diagrams can be avoided.

4.2.2 The GWA in HPC-2

Above I have shown the performance of the GWA and CEA spectral functions in the HPC-1, in particular all cumulant Green's functions yield the same result that is identical to the exact one. In this section, I will test the performance of these approximations in the two-level hole-plasmon coupling Hamiltonian (HPC-2) in (4.18). The non-interacting Green's function of the HPC-2 in the orbital (bonding and anti-bonding) basis reads

$$G_0(\omega) = \begin{pmatrix} \frac{1}{\omega - (\varepsilon_0 - \mathbf{t}) - i\eta} & 0 \\ 0 & \frac{1}{\omega - (\varepsilon_0 + \mathbf{t}) + i\eta} \end{pmatrix}, \tag{4.52}$$

which is diagonal: the bonding and anti-bonding matrix elements are the upper and lower blocks of the diagonal elements, respectively.

Since in the HPC-2, the coupling between the plasmon and hole are only on-site, the plasmon propagator of such an Hamiltonian diagonalizes in the site basis. This leads to the

only non-zero matrix elements of W_0 are

$$W_{0,ii}^{ii}(\omega) = W_{0,jj}^{jj}(\omega) = \frac{g^2}{\omega - \omega_p + i\eta} - \frac{g^2}{\omega + \omega_p - i\eta} . \qquad (4.53)$$

Transforming the above W_0 in the site basis to the `orbital` basis, we have the matrix elements reading as

$$W_{0,++}^{++}(\omega) = W_{0,++}^{--}(\omega) = W_{0,--}^{++}(\omega) = W_{0,--}^{--}(\omega) = \frac{\tilde{g}^2}{\omega - \omega_p + i\eta} - \frac{\tilde{g}^2}{\omega + \omega_p - i\eta} , \qquad (4.54)$$

where $\tilde{g} = \dfrac{g}{\sqrt{2}}$, and

$$W_{0,ij}^{kl}(\omega) \equiv \int dx_1 x_2\, \varphi_k^*(x_1)\varphi_i(x_1)W_0(x_1, x_2, \omega)\varphi_j^*(x_2)\varphi_l(x_2) , \qquad (4.55)$$

and φ_i represents the single-particle basis function labeled i. All other matrix elements of W_0 are zero.

The $\mathrm{G_0W_0}$ self-energy in the orbital basis is defined as

$$\Sigma_{ij}^{G_0W_0}(\omega) = i \sum_k G_{kk}^0(\omega) * W_{0,kk}^{ij}(\omega) , \qquad (4.56)$$

and it is diagonal in the orbital basis. The diagonal elements are

$$\Sigma_{+}^{G_0W_0}(\omega) = \Sigma_{-}^{G_0W_0}(\omega) = \frac{\tilde{g}^2}{\omega - (\varepsilon_0 - \mathbf{t} - \omega_p) - i\eta} + \frac{\tilde{g}^2}{\omega - (\varepsilon_0 + \mathbf{t} + \omega_p) + i\eta} . \qquad (4.57)$$

How to calculate the energy self-consistent Σ ?

In Eq. (4.40) I have used an energy shift Δ in the self-energy proposed by Hedin in Ref. [34] which yields the exact QP energy of the HPC-1. However, this trick is not so simple in the HPC-2 because we have two orbitals now. As a consequence, we have two self-energies

113

$\Sigma_{\pm}^{G_0 W_0}$ that lead to two energy shifts:

$$\Delta_+ = \operatorname{Re} \Sigma_+^{G_0 W_0}(\varepsilon_0 - t) = \frac{\tilde{g}^2}{\omega_p} - \frac{\tilde{g}^2}{\omega_p + 2\mathbf{t}} \; ; \tag{4.58a}$$

$$\Delta_- = \operatorname{Re} \Sigma_-^{G_0 W_0}(\varepsilon_0 + t) = -\frac{\tilde{g}^2}{\omega_p} + \frac{\tilde{g}^2}{\omega_p + 2\mathbf{t}} \equiv -\Delta_+ \; . \tag{4.58b}$$

The original idea of Hedin is to use Δ_+ in all orbitals, which yields

$$\Sigma_{\pm}^{Hedin}(\omega) = \frac{\tilde{g}^2}{\omega - \Delta_+ - (\varepsilon_0 - \mathbf{t} - \omega_p) - i\eta} + \frac{\tilde{g}^2}{\omega - \Delta_+ - (\varepsilon_0 + \mathbf{t} + \omega_p) + i\eta} \; . \tag{4.59}$$

The energy self-consistent GW self-energy I will use are[15]

$$\Sigma_+^{EscGW_0}(\omega) = \frac{\tilde{g}^2}{\omega - \Delta_+ - (\varepsilon_0 - \mathbf{t} - \omega_p) - i\eta} + \frac{\tilde{g}^2}{\omega - \Delta_+ - (\varepsilon_0 + \mathbf{t} + \omega_p) + i\eta} \; ; \tag{4.60a}$$

$$\Sigma_-^{EscGW_0}(\omega) = \frac{\tilde{g}^2}{\omega - \Delta_- - (\varepsilon_0 - \mathbf{t} - \omega_p) - i\eta} + \frac{\tilde{g}^2}{\omega - \Delta_- - (\varepsilon_0 + \mathbf{t} + \omega_p) + i\eta} \; ; \tag{4.60b}$$

where the bonding orbital self-energy is the same as Σ_+^{Hedin}, but I have used a different shift in the anti-bonding self-energy $\Sigma_-^{EscGW_0}$. The reason why I did not use $\Sigma_{\pm}^{Hedin}$ can be seen from the QP energies calculated using the QP equation (2.42). The GW QP energies of the HPC-2 from the QP equation are

$$\varepsilon_{QP,+}^{GW} = \varepsilon_0 - \mathbf{t} + \operatorname{Re} \Sigma_+^{G_0 W_0}(\varepsilon_0 - \mathbf{t}) = \varepsilon_0 - \mathbf{t} + \Delta_+ \equiv \varepsilon_0 - \mathbf{t} + \Sigma_+^{EscGW_0}(\varepsilon_{QP,+}^{GW}) \; ; \tag{4.61a}$$

$$\varepsilon_{QP,-}^{GW} = \varepsilon_0 + \mathbf{t} + \operatorname{Re} \Sigma_-^{G_0 W_0}(\varepsilon_0 + \mathbf{t}) = \varepsilon_0 + \mathbf{t} + \Delta_- \equiv \varepsilon_0 + \mathbf{t} + \Sigma_-^{EscGW_0}(\varepsilon_{QP,-}^{GW}) \; . \tag{4.61b}$$

The comparison of the QP energies calculated from $\Sigma_{\pm}^{Hedin}$ and $\Sigma_{\pm}^{EscGW_0}$ are shown in Fig. 4.6. The red circles are shifted $\operatorname{Re} \Sigma_{\pm}^{EscGW_0}$ which cross zero at QP energies represented by the black arrows labeled ε_{QP}^{GW} (see Eq. (4.61)) for both orbitals. The blue curves show the shifted $\operatorname{Re} \Sigma_{\pm}^{Hedin}$ that gives the correct QP energy in the bonding orbital but not in the anti-bonding orbital. For this reason, in the following context the energy self-consistent

---

[15]Note that Hedin's trick of introducing an energy shift in the self-energy is equivalent to the exact EscGW$_0$ only in the HPC-1. Whenever there are more than one orbitals (e.g. the bulk sodium), this trick becomes an approximation to the EscGW$_0$. The method I have suggested in Eq. (4.60) will work better than using only one energy shift to all orbitals as shown in Eq. (4.59). This method can be used also in real system calculations. It can be taken as an cheap alternative for the computationally expensive fully iterative EscGW$_0$ calculation.

GW self-energy in Eq. (4.60) is chosen to calculate the EscGW$_0$ Green's function, instead of $\Sigma_\pm^{Hedin}$ in Eq. (4.59).
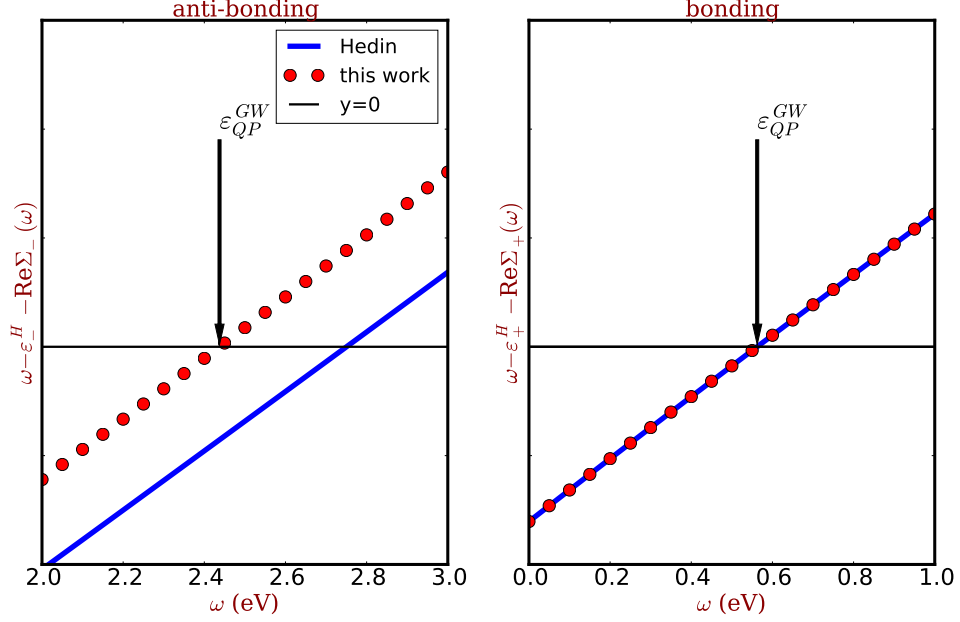

Figure 4.6: The quasi-particle energies calculated from different approximately energy self-consistent self-energies. The shifted real part of $\Sigma_\pm^{Hedin}$ Eq. (4.59) and $\Sigma_\pm^{EscGW_0}$ are shown as blue solid curve and red circles, respectively. Left panel is the anti-bonding results and right panel is the bonding orbital results. The black arrows labeled ε_{QP}^{GW} are the QP energies from the QP equation which are shown in Eq. (4.61). The parameters are chosen consistent with the bulk sodium bottom valence state, i.e. the same as in Fig. 4.3. Note that in Fig. 4.3, the horizontal axis has been defined as ω/ω_p and the bonding orbital QP energy has been shifted to zero. Here the horizontal axis is ω and there is no shift on the QP energy.

The GW Green's function can be calculated from the following Dyson equation and depending on which self-energy we use, the Green's function can be either G$_0$W$_0$ or EscGW$_0$ one:

$$G_\pm(\omega) = \left(G_{\pm,0}^{-1}(\omega) - \Sigma_\pm(\omega) \right)^{-1} . \tag{4.62}$$

The final spectral functions can be calculated from $A = \pi^{-1}|\text{Im}\,G|$. They are shown in Fig. 4.7. The upper and lower panels are spectral functions of anti-bonding and bonding orbitals, respectively.
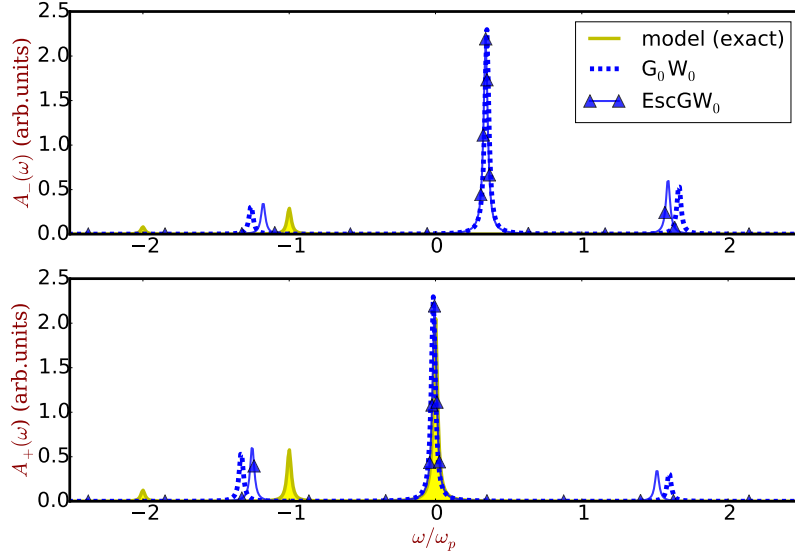
Figure 4.7: The electron removal spectral functions of the two-level hole-plasmon coupling Hamiltonian. I have shifted the exact quasi-particle in Eq. (4.29) to zero and all other plots have the same shifts. The Lorentzian broadening $\eta = 0.1$ is used in all plots. The spectral functions calculated from the G_0W_0 (blue dashed curve), $EscGW_0$ (blue line with up-triangles) are compared with the exact one (yellow filled curve). The upper and lower panels are spectra of anti-bonding and bonding orbitals, respectively. I have chosen the parameters corresponding to bulk sodium bottom valence state, as in Figs. 4.3 and 4.6.

I have mentioned in section 4.1.2 that we can only calculate the electron removal spectral functions from the HPC-2 such that we only have the exact spectrum (yellow filled curve) on the negative part of the horizontal axis (i.e. $\omega/\omega_p < 0$) in Fig. 4.7. From the GW approximation, we can calculate the whole spectra including the electron removal (i.e. particle number from $N = 1$ to $N = 0$) and addition (i.e. particle number from $N = 1$ to $N = 2$). This is why all blue curves have additional spectra on the positive part of the horizontal axis which are absent in the exact spectra in Fig. 4.7. For this reason, we will only compare the spectra on the negative side in Fig. 4.7. This holds for all the following comparisons between approximate and the exact spectral functions of the HPC-2.

We first have a look at the bonding orbital spectral functions as shown in the lower panel of Fig. 4.7. The origin of the GW electron addition spectrum in the bonding orbital (spectrum for $\omega/\omega_p > 0$) is the term $iG_-W_{--}^{++}$ in the self-energy (see Eqs. (4.56) and (4.60)), which conserves the spectral weight, i.e. $\int_{-\infty}^{\infty} A_+(\omega)\,d\omega = 1$. When we only

integrate the spectral function until the chemical potential, it gives the occupation of that orbital $\int_{-\infty}^{\mu} A_+(\omega)\,d\omega = n_b < 1$ (the performance of the occupations from the EscGW$_0$ can be seen from the blue line with down-triangles in Fig. 4.12). Therefore, the GWA (both G$_0$W$_0$ and EscGW$_0$) conserves the spectral weight and gives partial occupation of the bonding orbital in the HPC-2.

One can also show that GW conserves the particle number[16] by considering the additional electron removal spectrum in the anti-bonding orbital (blue curves on the negative horizontal axis of the upper panel), i.e. $\int_{-\infty}^{\mu} (A_+(\omega) + A_-(\omega))\,d\omega = 1$. This is reasonable because the bonding and anti-bonding orbitals are both partially occupied in the GW approximation, so both of them should contribute to the electron removal spectra, although the description of the satellites is not good.

Fig. 4.7 shows that the GWA does not fulfill the constraint of the poles that has been summarized in section 1.3 since both G$_0$W$_0$ and EscGW$_0$ give satellites at different energies in bonding and anti-bonding orbitals.

Overall, GW gives good quasi-particle energies but bad satellites as shown in Fig. 4.8. All the GW satellites appear at the energies where $\omega - \varepsilon_0 + \mathbf{t} - \mathrm{Re}\,\Sigma(\omega) = 0$ instead of close to the peak in $\mathrm{Im}\,\Sigma(\omega)$. Self-consistency improves the position of the quasi-particle and satellites. Besides the position of all the peaks, the GWA overestimates the quasi-particle weight compared to the exact spectral function, which is similar to the conclusion we have found in the HPC-1 (see Eq. (4.44) and Fig. 4.5).

4.2.3   The CEAs in HPC-2

All of the CEAs give the exact Green's function in the HPC-1 but as we will see in this section, the situation is different when we use different cumulant approaches in the HPC-2.

The TOC96

First we have a look at TOC96 in Eq. (2.62). As I have mentioned before, I am going to use the G$_0$W$_0$ self-energy Eq. (4.57) in the calculation of all cumulants such that the

---

[16]In general, the one-shot GW does not necessarily conserve the particle number (see e.g. Ref. [91]). But in this model study, I have put the chemical potential between the electron removal and addition QP energies such that all GW calculations conserve the particle number. This holds at least for the HPC-1 and HPC-2.
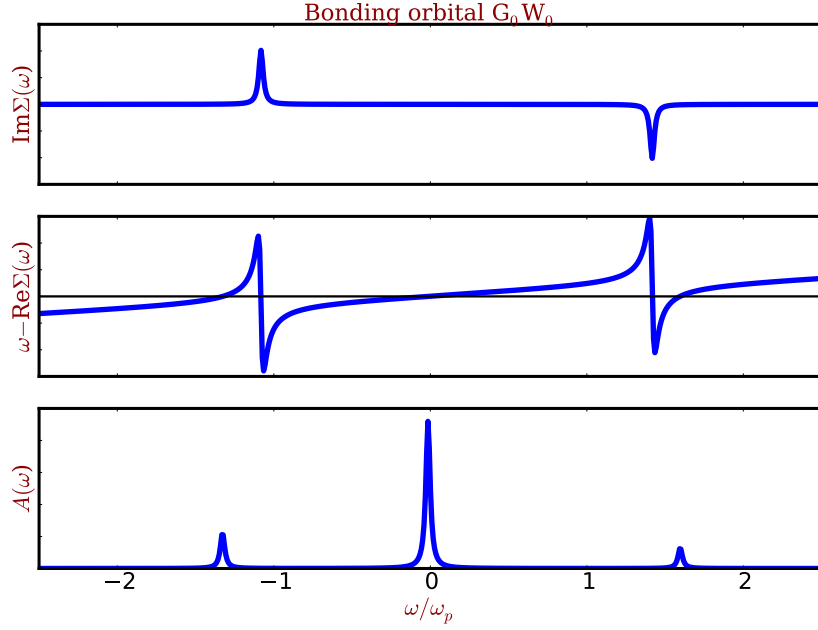
Figure 4.8: Bonding orbital G_0W_0 spectra (lower panel), the corresponding imaginary part (upper panel) and shifted real part (middle panel) of self-energy. The parameters are the same as in Fig. 4.7.

superscript " G_0W_0" in the self-energy is dropped for simplicity. The `hole` and `electron` parts of the self-energy in equation (4.57) are

$$\Sigma_{\pm}^h(\omega) = \mathcal{P}\frac{\tilde{g}^2}{\omega - (\varepsilon_0 - \mathbf{t} - \omega_p)} + i\pi\tilde{g}^2\delta(\omega - \varepsilon_0 + \mathbf{t} + \omega_p)\,; \qquad (4.63a)$$

$$\Sigma_{\pm}^e(\omega) = \mathcal{P}\frac{\tilde{g}^2}{\omega - (\varepsilon_0 + \mathbf{t} + \omega_p)} - i\pi\tilde{g}^2\delta(\omega - \varepsilon_0 - \mathbf{t} - \omega_p)\,. \qquad (4.63b)$$

Plugging the above self-energies in TOC96 Eq. (2.62) and replacing the KS-LDA eigenenergies by the corresponding orbital energies, i.e.

$$\varepsilon_+^H = \mathcal{E}_+ - V_{xc,+}^{LDA} = \varepsilon_0 - \mathbf{t}\,;$$

$$\varepsilon_-^H = \mathcal{E}_- - V_{xc,-}^{LDA} = \varepsilon_0 + \mathbf{t}\,;$$

118

we have the final Green's function of the TOC96, which reads

$$G_+^{C96}(\tau) = i\theta(-\tau)e^{-i\varepsilon_+^{C96}\tau}e^{-\tilde{\beta}_1-\tilde{\beta}_2}\exp\left(\tilde{\beta}_1 e^{i\omega_p\tau}\right) ; \tag{4.65a}$$

$$G_-^{C96}(\tau) = -i\theta(\tau)e^{-i\varepsilon_-^{C96}\tau}e^{-\tilde{\beta}_1-\tilde{\beta}_2}\exp\left(\tilde{\beta}_1 e^{-i\omega_p\tau}\right) ; \tag{4.65b}$$

where I have defined

$$\varepsilon_+^{C96} = \varepsilon_0 - \mathbf{t} + \frac{\tilde{g}^2}{\omega_p} - \frac{\tilde{g}^2}{\omega_p + 2\mathbf{t}} ; \tag{4.66a}$$

$$\varepsilon_-^{C96} = \varepsilon_0 + \mathbf{t} - \frac{\tilde{g}^2}{\omega_p} + \frac{\tilde{g}^2}{\omega_p + 2\mathbf{t}} ; \tag{4.66b}$$

$$\tilde{\beta}_1 = \frac{\tilde{g}^2}{\omega_p^2} ; \tag{4.66c}$$

$$\tilde{\beta}_2 = \frac{\tilde{g}^2}{(\omega_p + 2\mathbf{t})^2} . \tag{4.66d}$$

The quasi-particle energies of the TOC96 are actually the same as the EscGW$_0$ (see Eq. (4.61)) using the self-energies in Eq. (4.60). This can also be seen in Figs. 4.10 and 4.11: the quasi-particle energies of the retarded cumulant are the same as the EscGW$_0$. I will show later that the quasi-particle energies of the TOC96, TOC11 and RC are all identical, which therefore are identical to the EscGW$_0$ quasi-particle energies. This confirms the use of the energy self-consistent self-energy $\Sigma_\pm^{EscGW_0}$ in Eq. (4.60), instead of $\Sigma_\pm^{Hedin}$ in Eq. (4.59). If we had used Σ_-^{Hedin} in the EscGW$_0$ calculation, it would have yielded an anti-bonding quasi-particle energy different from ε_-^{C96}.

The corresponding spectral functions from the TOC96 are

$$A_+^{C96}(\omega) = \sum_{m=0}^{\infty}\frac{\tilde{\beta}_1^m e^{-\tilde{\beta}_1-\tilde{\beta}_2}}{m!}\delta\left(\omega - \varepsilon_+^{C96} + m\omega_p\right) ; \tag{4.67a}$$

$$A_-^{C96}(\omega) = \sum_{m=0}^{\infty}\frac{\tilde{\beta}_1^m e^{-\tilde{\beta}_1-\tilde{\beta}_2}}{m!}\delta\left(\omega - \varepsilon_-^{C96} - m\omega_p\right) ; \tag{4.67b}$$

they are shown as red curves in Fig. 4.9 for small and large coupling cases.

When the coupling is not so strong as shown in the left panel of Fig. 4.9, in the bonding orbital (red curves in the lower panel of that figure), the TOC96 gives a very good electron removal spectrum compared to the exact one, but contrary to the GWA, it does
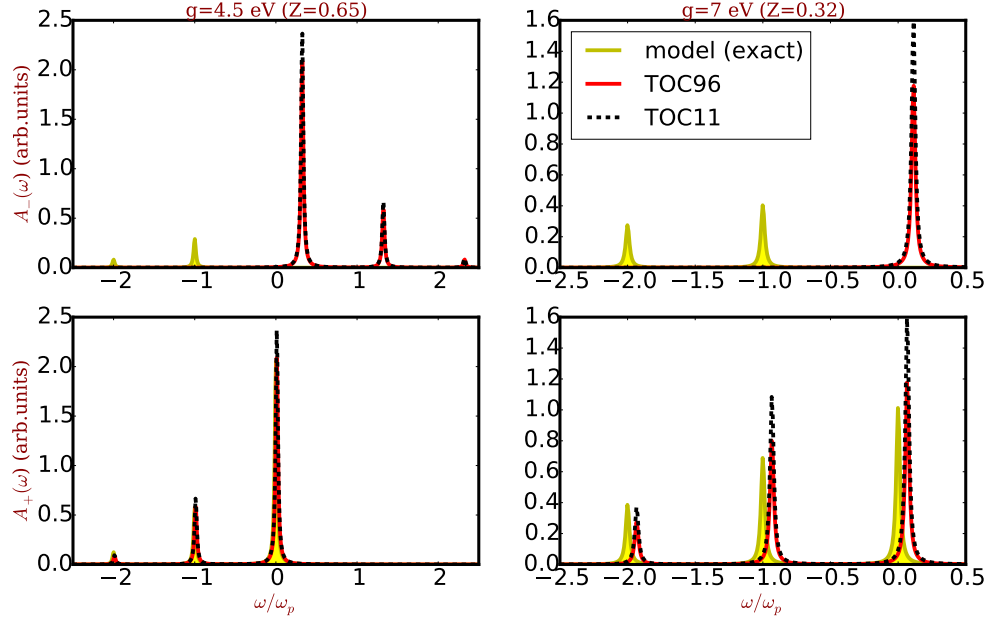
119

Figure 4.9: The spectral functions of the two-level hole-plasmon coupling Hamiltonian. Left panel: the coupling $g = 4.5$ eV that is consistent with bulk sodium bottom valence. Right panel: the coupling $g = 7$ eV that yields the QP renormalization factor $\mathbf{Z} = 0.32$. The horizontal axis of the right panel has been kept until the range of our interest. All other parameters are the same as in Fig. 4.7. Also the horizontal axises of the left and right panels are defined analogously to previous figures. Upper and lower panels are the spectra of the anti-bonding and bonding orbitals, respectively. The Lorentzian broadening $\eta = 0.1$ is used in all plots. The yellow filled curves are the exact spectral functions of the model Hamiltonian in equation (4.29). The red curves are the spectral functions calculated using the TOC96 in equation (4.67). The black dashed curves are the cumulant spectral functions calculated with the TOC11 in (4.70).

not provide any electron addition spectrum in the bonding orbital. This leads to the non-conserved spectral weight because one can show that the total spectral weight calculated from the TOC96 is $\int_{-\infty}^{\infty} \mathrm{d}\omega\, A_+^{C96}(\omega) = \exp\left(-\tilde{\beta}_2\right) < 1.$

In the anti-bonding orbital (upper panel of Fig. 4.9), the TOC96 does not give any electron removal spectrum, which instead appears in the exact spectrum. The only spectrum in this orbital is for electron addition whose weight is not complete since $\int_{-\infty}^{\infty} \mathrm{d}\omega\, A_+^{C96}(\omega) = \exp\left(-\tilde{\beta}_2\right) < 1.$

As a consequence, the total particle number is not conserved because

$$\int_{-\infty}^{\mu} \mathrm{d}\omega \left(A_+^{C96}(\omega) + A_-^{C96}(\omega) \right) = \exp\left(-\tilde{\beta}_2 \right) < 1 \,. \tag{4.68}$$

When the coupling is stronger as shown in the right panel of Fig. 4.9, the bonding orbital spectrum of the TOC96 is still reasonably good compared to the exact one, although all the peaks are shifted to the right with respect to the exact spectrum.

Therefore, TOC96 actually only calculates parts of the photoemission spectra. It does not calculate the anti-bonding orbital electron removal satellites which should have appeared at the same energy as the satellites in the bonding orbital as shown in the exact spectral function (yellow filled curve in the upper panel in Fig. 4.9). The TOC96 gives a partially occupied bonding orbital like the exact one because $n_+^{C96} = \exp\left(-\tilde{\beta}_2 \right) < 1$ as shown by the red curve with down-triangles in Fig. 4.12. In the coupling range that we are interested in, the bonding orbital occupation given by the TOC96 is very good compared to the exact one.

The reason why the TOC96 cannot conserve the particle number or spectral weight has been mentioned in section 2.3. The **Z**-factor of the TOC96 is $\mathbf{Z}^{C96} = \exp\left(-\tilde{\beta}_1 - \tilde{\beta}_2 \right)$, which comes from the *whole* GW self-energy including Σ^h and Σ^e (see Eq. (2.64)). However, only Σ^h enters the cumulant function that determines the satellite weights (i.e. $\tilde{\beta}_1$). In order to conserve both spectral weight and particle number, Σ^e must also enter in the cumulant function such that $e^{-\tilde{\beta}_2} \sum_m \dfrac{\tilde{\beta}_2^m}{m\,!} = 1$ can appear to conserve both spectral weight and particle number.

This is however not completely straightforward. The electron part of the GW self-energy Σ^e should be used properly to calculate the electron removal spectrum, otherwise although the spectral weight and total particle number are conserved, some drawbacks will appear at the same time. We will see this from the performance of the TOC11 and RC later.

The TOC11

The TOC11 in Eq. (3.32) uses the same self-energy as the TOC96 in Eq. (4.63), thus in the HPC-2 the Green's function of TOC11 reads

$$G_+^{C11}(\tau) = i\theta(-\tau)e^{-i\varepsilon_+^{C11}\tau}e^{-\tilde{\beta}_1}\exp\left(\tilde{\beta}_1 e^{i\omega_p\tau}\right);\tag{4.69a}$$

$$G_-^{C11}(\tau) = -i\theta(\tau)e^{-i\varepsilon_-^{C11}\tau}e^{-\tilde{\beta}_1}\exp\left(\tilde{\beta}_1 e^{-i\omega_p\tau}\right).\tag{4.69b}$$

The corresponding spectral functions are (see the black dashed curves in Fig. 4.9)

$$A_+^{C11}(\omega) = \sum_{m=0}^{\infty} \frac{\tilde{\beta}_1^m e^{-\tilde{\beta}_1}}{m!}\delta\left(\omega - \varepsilon_+^{C11} + m\omega_p\right);\tag{4.70a}$$

$$A_-^{C11}(\omega) = \sum_{m=0}^{\infty} \frac{\tilde{\beta}_1^m e^{-\tilde{\beta}_1}}{m!}\delta\left(\omega - \varepsilon_-^{C11} - m\omega_p\right),\tag{4.70b}$$

where $\varepsilon_\pm^{C11} = \varepsilon_\pm^{C96} = \varepsilon_\pm^{EscGW_0}$. Apparently this cumulant conserves the total spectral weight and particle number, since

$$\int_{-\infty}^{\infty} d\omega\, A_\pm^{C11}(\omega) = 1;\tag{4.71a}$$

$$\int_{-\infty}^{\mu} d\omega\left(A_+^{C11}(\omega) + A_-^{C11}(\omega)\right) = 1.\tag{4.71b}$$

However it does not give the correct partial occupation number of the bonding orbital since $\int_{-\infty}^{\mu} d\omega A_+^{C11}(\omega) \equiv 1$.

The TOC11 in Eq. (4.70) is different from the TOC96 in Eq. (4.67) only in the quasiparticle renormalization factor. The **Z**-factor of the TOC11 is $\mathbf{Z}^{C11} = \exp\left(-\tilde{\beta}_1\right)$, which does not contain Σ^e.

The TOC96 starts from a partially occupied ground state to calculate the electron removal spectrum such that the integration of the bonding orbital spectral function gives a good fractional occupation number (see Eq. (4.68) and the red curve with down-triangles in Fig. 4.12). The TOC11 on the other hand, starts from a fully occupied bonding orbital (i.e. $n_+^{C11} = 1$) and empty anti-boding orbital (i.e. $n_-^{C11} = 0$) due to the decoupling approximation. As a consequence, these two orbitals are totally decoupled. The GW QP correction

(see section 3.3.2) only takes into account the contribution of the orbitals interaction in the shift of the quasi-particle energy, but has no effect on the plasmon satellites.

Alternatively speaking, the TOC96 does not calculate the anti-bonding electron removal satellites that appear in the exact spectral function (yellow filled curve in the upper panel of Fig. 4.9). The TOC11, instead, puts the electron removal spectrum that should have appeared in the anti-bonding orbital, in the bonding orbital, which leads to too much weight in the bonding orbital spectral function as shown by the black dashed curves in the lower panel of Fig. 4.9. In such a way, the TOC11 conserves the spectral weight and the total occupation. In this sense the TOC11 can be interpreted to be the sum of the TOC96 and an additional spectrum as follows (for one state, e.g. the bonding orbital):

$$A^{C11}_{+,1} = \sum_{m=0}^{\infty} \frac{\tilde{\beta}_1^m e^{-\tilde{\beta}_1 - \tilde{\beta}_2}}{m!} \delta\big(\omega - \varepsilon_+^{C11} + m\omega_p\big) = A_+^{C96}\,; \tag{4.72a}$$

$$A^{C11}_{+,2} = \frac{1 - e^{-\tilde{\beta}_2}}{e^{-\tilde{\beta}_2}} \sum_{m=0}^{\infty} \frac{\tilde{\beta}_1^m e^{-\tilde{\beta}_1 - \tilde{\beta}_2}}{m!} \delta\big(\omega - \varepsilon_+^{C11} + m\omega_p\big) = \frac{1 - e^{-\tilde{\beta}_2}}{e^{-\tilde{\beta}_2}} A_+^{C96}\,; \tag{4.72b}$$

$$A_+^{C11} = A^{C11}_{+,1} + A^{C11}_{+,2}\,. \tag{4.72c}$$

In chapter 5 we will see that the new proposed constrained retarded cumulant has some similarity at this point. However the interpretation in $A^{C11}_{+,2}$ is different (see Eq. (5.12b)). More details will be discussed there.

It has been shown that both cumulants can give good total photoemission spectra[17] of some systems where the interaction between states below and above the Fermi level is relatively small (see e.g. Refs. [9,11,12,78]). Even in the valence state of bulk sodium where the top valence crosses the Fermi level, both cumulants give relatively good total spectra compared to the experiment [9,20]. However, I have done the calculation of sodium valence and core using the TOC11 in Ref. [20] and found that although the TOC11 improves the spectrum compared to the GWA in both valence and core, the performance in the valence

---

[17]In the case of the HPC-2, the total photoemission spectrum corresponds to the sum of electron removal spectra of both orbitals. In a real system calculation, the total photoemission spectra of one orbital is the sum of the k-resolved spectra of this orbital over all the k points in the full Brillouin zone, i.e. $A_b^{tot} = \sum_k A_{k,b}$ where k and b label the k-point and band, respectively, and the total photoemission spectra is the sum of A_b^{tot} over all the bands.

is worse than in the core. This issue reflects the challenge of the time-ordered cumulant in the description of sodium valence photoemission that will be discussed in Chapter 6.

4.2.4   The RC

In section 3.4, I have derived the retarded cumulant (RC) Green's function as shown in equation (3.60) which is equal to the retarded cumulant proposed by J. Kas, J. Rehr and Reining in Ref. [19]. In this subsection I am going to test the performance of this retarded cumulant Green's function in the two-level hole-plasmon coupling Hamiltonian.

We start from an orbital where $\varepsilon_+^H = \varepsilon_0 - \mathbf{t} < \mu$ that corresponds to the `bonding` orbital in the HPC-2. The retarded Hartree Green's function in the HPC-2 reads

$$G_H^R(t_{12}) = \theta(t_1 - t_2)\big(G_H^>(t_{12}) - G_H^<(t_{12})\big),$$

where

$$G_{H,+}^<(t_{12}) = ie^{-i\varepsilon_+^H(t_1-t_2)};$$

$$G_{H,+}^>(t_{12}) = 0;$$

$$G_{H,-}^<(t_{12}) = 0;$$

$$G_{H,-}^>(t_{12}) = -ie^{-i\varepsilon_-^H(t_1-t_2)}.$$

We have already calculated the one-shot `time-ordered` GW self-energy as shown in equation (4.57). The corresponding `retarded` self-energy is calculated in the Appendix (see Eq. (D.8)). Now we can calculate the components in the retarded cumulant Green's

function (see Eq. (3.64)) as follows

$$\text{Re}\,\Sigma_+^R(\varepsilon_+^H) = \frac{\tilde{g}^2}{\omega_p} - \frac{\tilde{g}^2}{\omega_p + 2\mathbf{t}}\,; \tag{4.73a}$$

$$\frac{\partial\,\text{Re}\,\Sigma_+^R(\omega)}{\partial\omega}\bigg|_{\omega=\varepsilon_+^H} = -\tilde{\beta}_1 - \tilde{\beta}_2\,; \tag{4.73b}$$

$$-\frac{1}{\pi}\int_{-\infty}^{\mu}\mathrm{d}\omega'\,\frac{\text{Im}\,\Sigma_+^<(\omega')e^{i(\varepsilon_+^H - \omega' + i\eta)\tau}}{(\varepsilon_+^H - \omega' + i\eta)^2} = \tilde{\beta}_1 e^{i\omega_p\tau}\,; \tag{4.73c}$$

$$-\frac{1}{\pi}\int_{\mu}^{\infty}\mathrm{d}\omega'\,\frac{\text{Im}\,\Sigma_+^>(\omega')e^{i(\varepsilon_+^H - \omega' + i\eta)\tau}}{(\varepsilon_+^H - \omega' + i\eta)^2} = \tilde{\beta}_2 e^{-i(\omega_p + 2\mathbf{t})\tau}\,. \tag{4.73d}$$

Note that $2\mathbf{t} \equiv \varepsilon_-^H - \varepsilon_+^H$ in the HPC-2. Therefore the final bonding and anti-bonding matrix elements of the retarded cumulant Green's function are

$$G_+^{RC}(\tau) = -i\theta(\tau)e^{-i\varepsilon_+^{RC}\tau}\exp\left(-\tilde{\beta}_1 - \tilde{\beta}_2\right)\exp\left(\tilde{\beta}_1 e^{i\omega_p\tau}\right)\exp\left(\tilde{\beta}_2 e^{-i(\omega_p + 2\mathbf{t})\tau}\right)\,; \tag{4.74a}$$

$$G_-^{RC}(\tau) = -i\theta(\tau)e^{-i\varepsilon_-^{RC}\tau}\exp\left(-\tilde{\beta}_1 - \tilde{\beta}_2\right)\exp\left(\tilde{\beta}_1 e^{-i\omega_p\tau}\right)\exp\left(\tilde{\beta}_2 e^{i(\omega_p + 2\mathbf{t})\tau}\right)\,; \tag{4.74b}$$

where $\varepsilon_\pm^{RC}$ are the bonding and anti-bonding quasi-particle energies from the retarded cumulant which are:

$$\varepsilon_+^{RC} = \varepsilon_0 - \mathbf{t} + \frac{\tilde{g}^2}{\omega_p} - \frac{\tilde{g}^2}{\omega_p + 2\mathbf{t}}\,; \tag{4.75a}$$

$$\varepsilon_-^{RC} = \varepsilon_0 + \mathbf{t} - \frac{\tilde{g}^2}{\omega_p} + \frac{\tilde{g}^2}{\omega_p + 2\mathbf{t}}\,. \tag{4.75b}$$

Thus all the quasi-particle energies from the EscGW$_0$, TOC96, TOC11 and retarded cumulant are identical (see e.g. Eqs. (4.61) and (4.66) as well as Figs. 4.10 and 4.11).

The retarded cumulant spectral functions for these two orbitals are

$$A_+^{RC}(\omega) = \sum_{m_1,m_2=0}^{\infty}\frac{\tilde{\beta}_1^{m_1}\tilde{\beta}_2^{m_2}e^{-\tilde{\beta}_1 - \tilde{\beta}_2}}{m_1!\,m_2!}\delta\left(\omega - \varepsilon_+^{RC} + m_1\omega_p - m_2(\omega_p + 2\mathbf{t})\right)\,; \tag{4.76a}$$

$$A_-^{RC}(\omega) = \sum_{m_1,m_2=0}^{\infty}\frac{\tilde{\beta}_1^{m_2}\tilde{\beta}_2^{m_1}e^{-\tilde{\beta}_1 - \tilde{\beta}_2}}{m_1!\,m_2!}\delta\left(\omega - \varepsilon_-^{RC} - m_2\omega_p + m_1(\omega_p + 2\mathbf{t})\right)\,. \tag{4.76b}$$

The retarded cumulant spectral functions are shown in Fig. 4.10 together with a comparison with the EscGW$_0$ and exact spectral functions using the sodium bottom valence

parameters. The QP energies of the two orbitals calculated from the RC and EscGW$_0$ are exactly at the same energy, which confirms my suggestion about the use of the energy self-consistent GW self-energy[18] in Eq. (4.60). Again we only have the exact removal spectra such that we can only test the electron removal spectral functions calculated from the retarded cumulant.
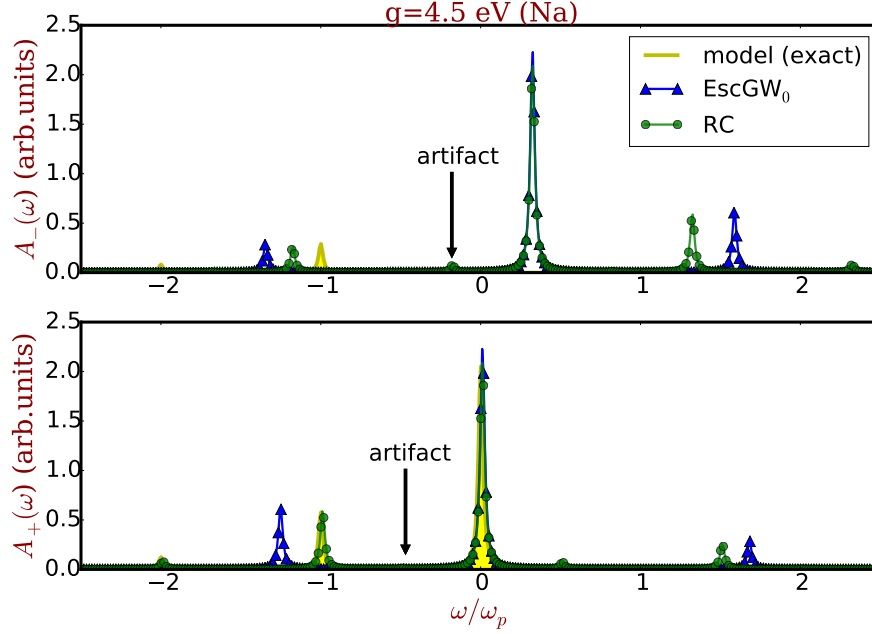

Figure 4.10: The spectral functions of the HPC-2 . All parameters are the same as Fig. 4.9 and Fig. 4.7. Upper panel: the anti-bonding spectrum. Lower panel: the bonding spectrum. The retarded cumulant, and EscGW$_0$ spectral functions are shown by the blue curve with up-triangles and green curve with circles, respectively. The yellow filled curves are the exact spectral functions of the HPC-2. The coupling strength in this figure is $g = 4.5$ eV, leading to $\mathbf{Z} = 0.65$. In Fig. 4.11, the same plots using a larger coupling strength $g = 7.0$ eV yielding $\mathbf{Z} = 0.32$ are shown.

In the bonding orbital (lower panel of Fig. 4.10), the retarded cumulant spectrum (green line with circles) has a very good performance compared to the exact one. It improves the plasmon satellites compared to the GWA. However, the retarded cumulant gives one very small satellite between the QP peak and the first plasmon satellite as shown by the black

---

[18]In principle, the quasi-particle energies from the CEA are identical to the quasi-particle energies of the GWA. The energy self-consistent GW self-energy $\Sigma_{\pm}^{EscGW_0}$ in Eq. (4.60) leads to the same GW quasi-particle energies as the CEA. However $\Sigma_{\pm}^{Hedin}$ in Eq. (4.59) does not yield the same quasi-particle energies as the CEA.

arrow labeled " artifact " in that figure. This spurious structure is not present in the exact spectrum. It stems from the term $(m_1 = m_2 = 1)$ in A_+^{RC} of Eq. (4.76a). This is an artifact induced by the retarded cumulant. The stronger the coupling, the more evident is the artifact as shown in Fig. 4.11 where $g = 7.0$ eV, instead of $g = 4.5$ eV has been used. I will show how one can improve the retarded cumulant by introducing the `constrained retarded cumulant` approach in Chapter 5 such that the artifact will be eliminated.

In the anti-bonding orbital (upper panel of Fig. 4.10), the retarded cumulant spectrum improves the plasmon satellites with respect to the EscGW$_0$ (blue line with up-triangles) because the main satellite of the retarded cumulant is closer to the first satellite of the exact one, and the weight is better. As in the case of the bonding orbital, a spurious peak appears (i.e. $m_1 = m_2 = 1$ in A_-^{RC} of Eq. (4.76b)) between the first main satellite and the QP peak (black arrow labeled " artifact ") of the retarded cumulant spectrum, which can be corrected by the constrained retarded cumulant that will be discussed in Chapter 5.
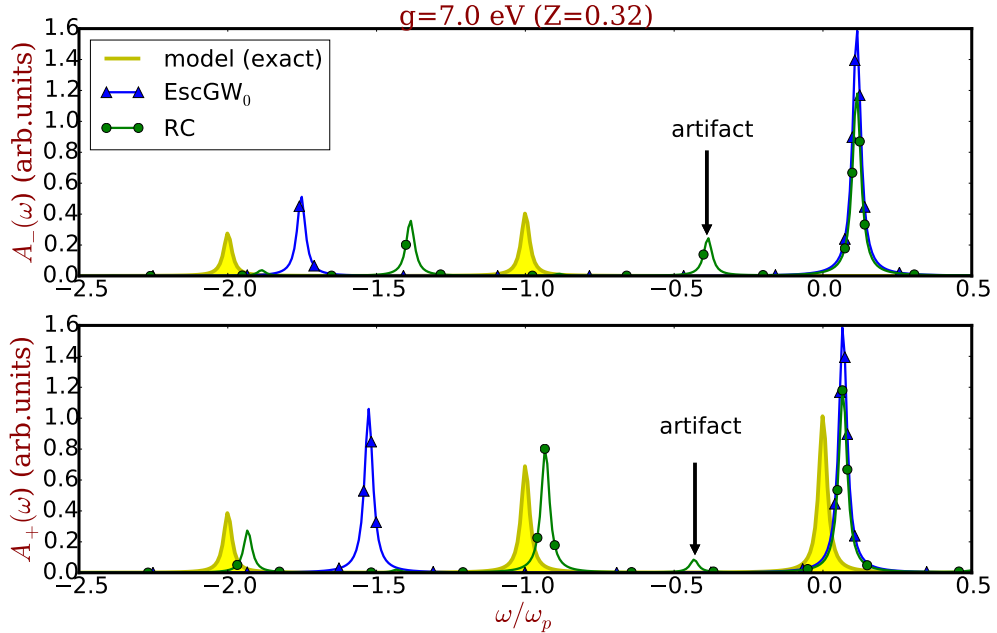

Figure 4.11: The spectral functions of the HPC-2 . All the plots are the same with Fig. 4.10 but with larger coupling strength $g = 7.0$ eV, leading to the QP renormalization factor $\mathbf{Z} \approx 0.32$. Only the electron removal spectrum has been shown.

One can show analytically that the retarded cumulant conserves the total spectral weight because

$$\int_{-\infty}^{\infty} d\omega\, A_{\pm}^{RC}(\omega) = e^{-\tilde{\beta}_1 - \tilde{\beta}_2} \sum_{m_1=0}^{\infty} \sum_{m_2=0}^{\infty} \frac{\tilde{\beta}_1}{m_1!} \frac{\tilde{\beta}_2}{m_2!} = 1\,. \tag{4.77}$$

It is difficult to see analytically whether the retarded cumulant Green's function conserves the total particle number or not, because the term $m_2(\omega_p + 2\mathbf{t})$ in $A_{\pm}(\omega)$ also contributes satellites below the chemical potential μ. But we can see that the retarded cumulant does conserve the particle number from the numerical calculation as shown in Fig. 4.12. All the occupations shown in Fig. 4.12 are calculated by putting the chemical potential μ between the QP energies of bonding and anti-bonding orbitals.
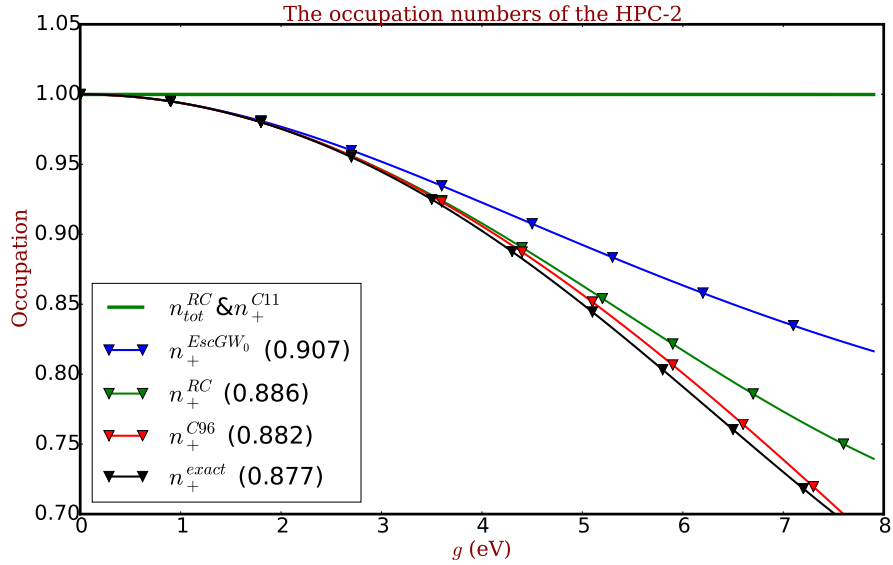

Figure 4.12: Occupation numbers with increasing coupling strength in the HPC-2. The green solid curve is the total occupation number calculated from the retarded cumulant Green's function (Eq. (4.76)), i.e. $\int_{-\infty}^{\mu} \left(A_+^{RC}(\omega) + A_-^{RC}(\omega) \right) d\omega$. As discussed in Eq. (4.71b), the TOC11 has a fully occupied bonding orbital which yields $n_b^{C11} = n_{tot}^{C11} = n_{tot}^{RC} = 1$. The green, blue and red lines with down-triangles are the bonding orbital occupations of the retarded cumulant, EscGW$_0$, and TOC96. The black line with down-triangles shows the exact bonding orbital occupation. The numbers in the legend represent the occupation when $g = 4.5$ eV that is consistent with the sodium bottom valence.

The last question about the retarded cumulant Green's function is: does it fulfill the constraint that poles of G_+ and G_- are the same (see the constraint of poles summarized in section 1.3)? Apparently not, as can be seen in Fig. 4.10: the positions of the anti-bonding satellites are not the same as the positions of bonding orbital satellites.

Therefore, both the TOC11 and RC conserve the spectral weight and particle number in a different way. The TOC11 drops the electron part of the self-energy. The RC uses the whole self-energy (Σ^h and Σ^e) but not in a proper way, leading to some spurious structures and a relatively bad anti-bonding removal spectrum.

4.3 Summary

In this chapter, I have studied the spectral functions calculated from the GWA (the G_0W_0 and EscGW$_0$) and CEA (TOC96, TOC11 and RC) in two hole-plasmon coupling model Hamiltonians. The GW approximation can give good QP energies, but the QP weight is slightly overestimated compared to the exact one. As has been mentioned in section 2.2, The G_0W_0 and EscGW$_0$ can not provide the plasmon satellite replica which appear in the exact spectral functions of the model Hamiltonians. There is only one satellite, due to a plasmaron. The cumulant expansion approximation yields the exact spectral function in the HPC-1 because the electron part of the GW self-energy is zero in such a simple model. This explains why the CEAs can give very good spectral function of systems where the interaction between orbitals is negligible. In the HPC-2 where the GW self-energy contains both electron and hole parts reflecting the interaction between orbitals, none of the CEAs can reproduce the satellites in the exact spectral functions. All CEAs have very good spectral functions in the bonding orbital, but the anti-bonding orbital spectrum is never satisfactory. None of the CEAs fulfills all our exact constraints that haven been summarized in section 1.3:

- The TOC96 does not conserve the spectral weight, nor the particle number. However it gives very good partial occupation of the bonding orbital. Since it does not give any electron removal spectrum in the anti-bonding orbital, the constraint of the poles (see the summaries in section 1.3) is meaningless.

- The TOC11 conserves both the spectral weight and particle number, however it cannot give the correct partial occupation of the bonding orbital. Like the TOC96, it does not give any electron removal spectrum in the anti-bonding orbital. This is because these two cumulant expansion approximations are based on the decoupling between electron removal and addition branches as discussed in sections 2.3 and 3.3.

- The retarded cumulant conserves both the spectral weight and the total particle number. It improves the partial occupation of the bonding orbital with respect to the GWA, although the occupation is worse than the TOC96. Moreover, the retarded cumulant can give some electron removal satellites in the anti-bonding orbital, but they are not in the correction position: they do not fulfill the constraint of the poles (see the summaries in section 1.3). In addition to that, the retarded cumulant induces some spurious satellites that are not present in the exact spectral functions of the HPC-2. The larger the coupling strength, the stronger these artifacts.

These observations will now serve as a motivation and guideline to search for possible improvements on one side (see Chapter 5), and to analyze findings in sodium as a prototypical real system on the other side (see Chapter 6).

Chapter 5

The constrained retarded cumulant Green's function

In Chapter 4 we have seen the performance of the spectral functions from different approximations by comparing to the exact spectral functions of the hole-plasmon coupling model Hamiltonians. The cumulant expansion approximations (CEAs) yield the exact spectral function of the one-level hole-plasmon coupling model (HPC-1), however none of the present CEAs is able to reproduce well enough the exact spectral function of the two-level hole-plasmon coupling model (HPC-2). This means the cumulant expansion approximations are probably still not good enough to describe valence photoemission, where the interaction between the states below and above the Fermi level is not negligible. In order to have a better description of the valence photoemission spectrum, I am going to propose a new cumulant expansion approximation in this chapter that will be referred to as the `constrained retarded cumulant` (CRC). To derive the constrained retarded cumulant, first we have to study in detail the exact Green's function of the HPC-2. In particular an approximate analytical expression of the exact Green's function of the HPC-2 will be shown, from which we can find the link between the analytical Green's function and the retarded cumulant Green's function in the HPC-2. In this way, some proper constraints can be introduced on top of the retarded cumulant, leading to the constrained retarded cumulant Green's function which fulfills these exact constraints. Then I will show a generalized expression of this constrained

retarded cumulant Green's function that could be applied to the calculation of real systems, and predict the effects of the constrained retarded cumulant in valence photoemission.

5.1 An approximate fully analytical Green's function of the HPC-2

Before I propose the constrained retarded cumulant, I will first discuss some insight I have obtained from the two-level hole-plasmon coupling Hamiltonian calculation. In section 4.1.2, I have shown how to calculate the exact Green's function of the HPC-2. However, the exact Green's function (see Eq. (4.29)) is not fully analytical because the diagonalization of $\hat{H}^-$ Eq. (4.20b) is done numerically. The numerical parameters forbid us to see the link between the exact Green's function and the GW self-energy. To get rid of this difficulty, I will first show how I can find an approximate fully analytical expression of the Green's function that is still in better agreement with the exact Green's function of the HPC-2 than all previous methods. This requires a good approximation for both the ground state energy E_0^- and the coefficients of the wavefunction v_m in the exact Green's function (see Eq. (4.29)).

The ground state energy of $\hat{H}^-$ for one electron can be calculated to second order in $\tilde{g}$, which reads[1]

$$E_0^- \approx E_0^{g^2} = \varepsilon_0 - \mathbf{t} - \frac{\tilde{g}^2}{\omega_p + 2\mathbf{t}} . \tag{5.1}$$

This analytical ground state energy yields the quasi-particle energy to second order in $\tilde{g}$ which reads

$$\varepsilon_{QP}^{g^2} = \varepsilon_0 - \mathbf{t} - \frac{\tilde{g}^2}{\omega_p + 2\mathbf{t}} + \frac{\tilde{g}^2}{\omega_p} . \tag{5.2}$$

The above QP energy is the same as the EscGW$_0$ QP energy (see Eq. (4.61)), and hence of all CEAs (see e.g. Eq. (4.75)). The performance of this analytical ground state energy compared to the exact numerical total energy can be seen in Fig. 5.1, where the red curve shows the ground state total energies (E_0^-) from the exact diagonalization of $\hat{H}^-$ and the diamonds show the ground state energies ($E_0^{g^2}$) calculated from Eq. (5.1) with increasing

---

[1]This analytical ground state energy can be calculated by diagonalizing the $\hat{H}^-$ matrix in the basis of $|n_+, n_-; m_+, m_-\rangle$ when $m_-^{max} = 1$.

coupling constant g. The coupling strength has been limited to the range of our interest, in particular $g = 4.5$ eV corresponds to the sodium bottom valence state where the error of our approximation in Eq. (5.1) is about 6% compared to the numerical results. Therefore, in the range of our interest, Eq. (5.1) is a sufficiently good approximation to the exact total energy for our purpose.
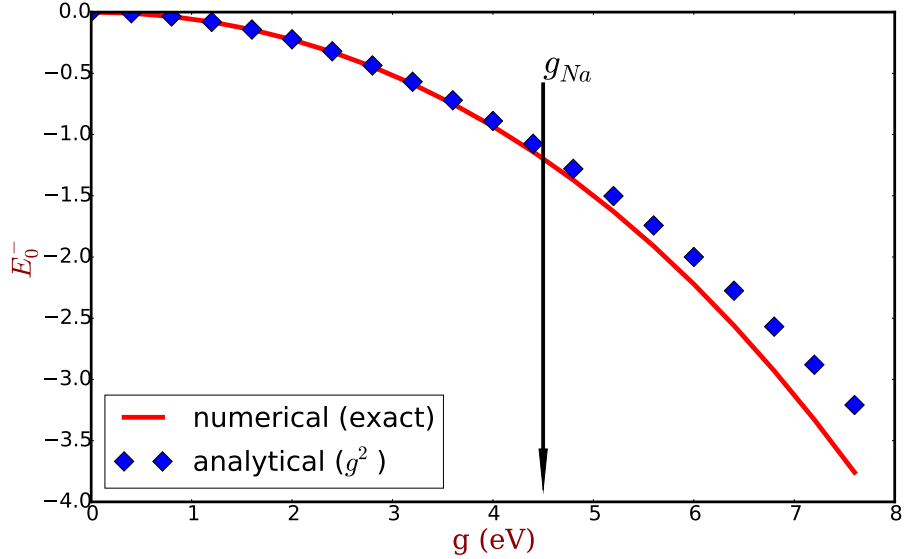

Figure 5.1: The performance of the second order expansion of the ground state energy in equation (5.1). The parameters are corresponding to bulk sodium bottom valence state, i.e. $\varepsilon_0 = \mathbf{t} = 1.5$ eV and $\omega_p = 6$ eV. Red curve is the exact numerical total energy E_0^- and blue diamonds are the total energy calculated from the second order expression in Eq. (5.1). In particular, $g = 4.5$ eV (black arrow labeled "g_{Na}") corresponds to the sodium case where the error of the second order expansion is about 6%. This figure shows that Eq. (5.1) is a sufficiently good approximation to the exact total energy of the HPC-2.

In order to have the fully analytical approximated Green's function, we have to know the analytical expression of the coefficients of the eigenfunctions v_m in equation (4.24). There are conditions to approximate v_m because it affects the occupation. For example if we want to conserve the total particle number, we have to find an approximation that fulfills the following property:

$$\sum_{m=0}^{\infty} v_m^2 = 1 \,. \tag{5.3}$$

There are many Taylor series that can do this job thus the above property is not enough for finding good approximations. Thanks to the fully analytical expression of the retarded cumulant Green's function (see Eq. (4.74)) and its good performance for the weight of the spectra as shown in Fig. 4.10, we can try to use the function that controls the weight of the retarded cumulant spectra to approximate the coefficients of the exact one. This leads to[2]

$$v_m \approx \frac{\tilde{\beta}_2^m}{m!} e^{-\tilde{\beta}_2} , \tag{5.4}$$

where $\tilde{\beta}_2 = \frac{\tilde{g}^2}{(\omega_p + 2\mathbf{t})^2}$. The above approximation conserves the particle number since $e^{-x} \sum_{m=0}^{\infty} \frac{x^m}{m!} = 1$. We can see the performance of this approximation in Fig. 5.2. When we are in a weakly correlated system where the coupling is small (e.g. $g < 3$ eV), our approximated v_m in equation (5.4) is nearly identical to the exact one (the red up- and down-triangle dataset in Fig. 5.2). The data sets corresponding to the bulk sodium bottom valence are shown in blue up- and down-triangles where our approximation is still good ($\sim$ 2% error)[3]. Even in the strong coupling case where $g = \omega_p = 6$ eV as shown in the green dataset, our approximation can be taken as acceptable ($\sim 8\%$ error).

Using these approximate formulas (Eqs. (5.1) and (5.4)), the approximate analytical Green's function reads now[4]

$$G_+(\tau) = \frac{i}{2}\theta(-\tau)e^{-i\varepsilon_+\tau}e^{-\tilde{\beta}_1-\tilde{\beta}_2} \exp\left(\tilde{\beta}_1 e^{i\omega_p\tau}\right) \left[\exp\left(\tilde{\beta}_2 e^{i\omega_p\tau}\right) + \exp\left(-\tilde{\beta}_2 e^{i\omega_p\tau}\right)\right] ; \tag{5.6a}$$

$$G_-(\tau) = \frac{i}{2}\theta(-\tau)e^{-i\varepsilon_+\tau}e^{-\tilde{\beta}_1-\tilde{\beta}_2} \exp\left(\tilde{\beta}_1 e^{i\omega_p\tau}\right) \left[\exp\left(\tilde{\beta}_2 e^{i\omega_p\tau}\right) - \exp\left(-\tilde{\beta}_2 e^{i\omega_p\tau}\right)\right] ; \tag{5.6b}$$

where $\varepsilon_+ = \varepsilon_0 - \mathbf{t} + \frac{\tilde{g}^2}{\omega_p} - \frac{\tilde{g}^2}{\omega_p + 2\mathbf{t}}$ is the bonding quasi-particle energy.

---

[2]Note that the ground state energy is kept until the order g^2, however the approximate coefficients in Eq. (5.4) contain higher order terms in g.

[3]The error is calculated from v_0 that corresponds to the weight of the quasi-particle peak, which has the largest error.

[4]Take Eqs. (5.1) and (5.4) in the exact Green's function shown in Eqs. (4.27) and (4.28). Then Fourier transform the resulting Green's functions from frequency space to time space. I have also used the property of

$$\sum_{m=0}^{\infty} \frac{\tilde{\beta}_2^{2m} e^{-\tilde{\beta}_2}}{2m!} = e^{-\tilde{\beta}_2} \frac{e^{\tilde{\beta}_2} + e^{-\tilde{\beta}_2}}{2} = \frac{1 + e^{-2\tilde{\beta}_2}}{2} ;$$

$$\sum_{m=0}^{\infty} \frac{\tilde{\beta}_2^{2m+1} e^{-\tilde{\beta}_2}}{2m+1!} = e^{-\tilde{\beta}_2} \frac{e^{\tilde{\beta}_2} - e^{-\tilde{\beta}_2}}{2} = \frac{1 - e^{-2\tilde{\beta}_2}}{2} .$$
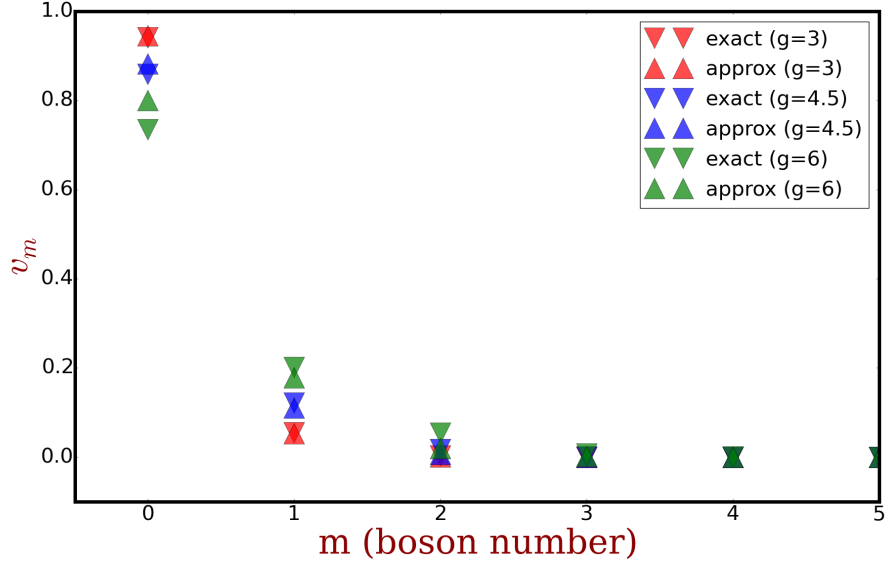
Figure 5.2: The performance of the second order expansion in equation (5.4). I have used the same parameters as Fig. 5.1, i.e. bulk sodium bottom valence state parameters. Up- and down- triangles are the exact (Eq. (4.24)) and approximate coefficients of the ground state wavefunction (Eq. (5.4)), respectively. Red data are the results for $g = 3$ eV. Blue are $g = 4.5$ eV which corresponds to sodium, with an error of about 2% and green are $g = 6$ eV with an error about 8%.

Now we analyze the terms in the square brackets in equation (5.6) such that further approximations can be introduced:

$$\frac{1}{2}\left[\exp\left(\tilde{\beta}_2 e^{i\omega_p\tau}\right) + \exp\left(-\tilde{\beta}_2 e^{i\omega_p\tau}\right)\right] = 1 + \frac{1}{2!}\tilde{\beta}_2^2 e^{i2\omega_p\tau} + \cdots \approx 1\,; \tag{5.7a}$$

$$\frac{1}{2}\left[\exp\left(\tilde{\beta}_2 e^{i\omega_p\tau}\right) - \exp\left(-\tilde{\beta}_2 e^{i\omega_p\tau}\right)\right] = \tilde{\beta}_2 e^{i\omega_p\tau} + \frac{1}{3!}\tilde{\beta}_2^3 e^{i3\omega_p\tau} + \cdots \approx \tilde{\beta}_2 e^{i\omega_p\tau}\,. \tag{5.7b}$$

When $\tilde{\beta}_2 \ll 1$, $\tilde{\beta}_2^m$ ($m > 1$) will be very small[5] so that they can be neglected. Thus the Green's function for $\tilde{\beta}_2 \ll 1$ reads[6]

$$G_+(\tau) = i\theta(-\tau)e^{-i\varepsilon_+\tau}e^{-\tilde{\beta}_1-\tilde{\beta}_2}\exp\left(\tilde{\beta}_1 e^{i\omega_p\tau}\right)\,; \tag{5.8a}$$

$$G_-(\tau) = i\theta(-\tau)\tilde{\beta}_2 e^{-i(\varepsilon_+-\omega_p)\tau}e^{-\tilde{\beta}_1-\tilde{\beta}_2}\exp\left(\tilde{\beta}_1 e^{i\omega_p\tau}\right)\,. \tag{5.8b}$$

---

[5]In the case of sodium bottom valence where $g \approx 4.5$ eV leading to $\tilde{\beta}_2 \approx 0.3$, the higher order term (i.e. $\frac{\tilde{\beta}_2^m}{m!}$ with $m > 1$) can be neglected in a good approximation.

[6]The resulting G_+ in Eq. (5.8a) is identical to the G_+^{C96} in Eq. (4.65a) whose performance is shown by the red curves in the lower panel of Fig. 4.9. It has very good agreement with the exact bonding spectra.

However, the above Green's function does not conserve the particle number anymore because one can show that

$$\int_{-\infty}^{\mu} d\omega \, (G_+(\omega) + G_-(\omega)) = e^{-\tilde{\beta}_2} + \tilde{\beta}_2 e^{-\tilde{\beta}_2} \neq 1 \,. \tag{5.9}$$

In order to conserve the particle number, we have to change the anti-bonding Green's function consistently with the bonding Green's function. This means if we have kept the zero order expansion that yields $n_+ = e^{-\tilde{\beta}_2}$ in the bonding Green's function (see Eq. (5.7a)), we have to keep all the left weights that is $1 - e^{-\tilde{\beta}_2}$ in the anti-bonding Green's function to conserve the particle number, which leads to

$$G_-(\tau) = i\theta(-\tau)e^{-i\varepsilon_+\tau}e^{-\tilde{\beta}_1-\tilde{\beta}_2} \exp\left(\tilde{\beta}_1 e^{i\omega_p\tau}\right) \left[\exp\left(\tilde{\beta}_2 e^{i\omega_p\tau}\right) - 1\right]$$

$$= i\theta(-\tau)e^{-i\varepsilon_+\tau}e^{-\tilde{\beta}_1-\tilde{\beta}_2} \sum_{m=0}^{\infty} \frac{\left[(\tilde{\beta}_1 + \tilde{\beta}_2)^m - \tilde{\beta}_1^m\right]}{m!} e^{im\omega_p\tau} \,. \tag{5.10}$$

Fourier transform of Eqs. (5.8a) and (5.10) yields the final approximated fully analytical Green's function:

$$G_+^{g^2}(\omega) = e^{-\tilde{\beta}_1-\tilde{\beta}_2} \sum_{m=0}^{\infty} \frac{\tilde{\beta}_1^m}{m!} \frac{1}{\omega - (\varepsilon_+ - m\omega_p) - i\eta} \,; \tag{5.11a}$$

$$G_-^{g^2}(\omega) = e^{-\tilde{\beta}_1-\tilde{\beta}_2} \sum_{m=0}^{\infty} \frac{\left[(\tilde{\beta}_1 + \tilde{\beta}_2)^m - \tilde{\beta}_1^m\right]}{m!} \frac{1}{\omega - (\varepsilon_+ - m\omega_p) - i\eta} \,. \tag{5.11b}$$

The corresponding spectral function reads

$$A_+^{g^2}(\omega) = \sum_{m=0}^{\infty} \frac{e^{-\tilde{\beta}_1-\tilde{\beta}_2}\tilde{\beta}_1^m}{m!} \delta(\omega - \varepsilon_+ + m\omega_p) \,; \tag{5.12a}$$

$$A_-^{g^2}(\omega) = e^{-\tilde{\beta}_1-\tilde{\beta}_2} \sum_{m=0}^{\infty} \frac{\left[(\tilde{\beta}_1 + \tilde{\beta}_2)^m - \tilde{\beta}_1^m\right]}{m!} \delta(\omega - \varepsilon_+ + m\omega_p) \,. \tag{5.12b}$$

Note that the bonding spectral function $A_+^{g^2}$ is equivalent to the TOC96 in Eq. (4.67). The anti-bonding electron removal spectral function is the one missing in the TOC96,

137

because the TOC96 can only calculate the electron addition spectral function of the anti-bonding orbital.

The above spectral function conserves the particle number by design:

$$\int_{-\infty}^{\mu} d\omega \left[A_+^{g^2}(\omega) + A_-^{g^2}(\omega) \right] = 1.$$

(5.13)

The bonding orbital occupation is the same as the one from the TOC96 (see Eq. (4.68) and the red line with down-triangles in Fig. 4.12) that is

$$n_+^{g^2} = \int_{-\infty}^{\mu} d\omega \left(A_+^{g^2}(\omega) + A_-^{g^2}(\omega) \right) = \exp\left(-\tilde{\beta}_2 \right) < 1.$$

(5.14)

The good performance of this bonding occupation can be seen from the red curve with down-triangles in Fig. 4.12. Since it conserves the total particle number, the anti-bonding occupation should also be good compared to the exact one. This Green's function has the same quasi-particle energy as the one from the EscGW$_0$ hence all the CEAs, which is very good compared to the exact quasi-particle energy. Moreover, G^{g^2} fulfills the constraint of the poles (see the summary in section 1.3), i.e. the anti-bonding satellites are at the same energies as the bonding satellites.

Finally the performance of the spectral functions in Eq. (5.12) are shown in Fig. 5.3. The purple curve with up-triangles shows the good performance of our approximate spectral functions compared to the model exact one shown by the yellow filled curve in the same figure.

In conclusion, the spectral function A^{g^2} has better performance than all previous approximate spectral functions (i.e. the GWA and CEA) compared to the exact one in the HPC-2. It has the following properties:

1. The ground state energy has been kept until the second order to g in Eq. (5.1).

2. The coefficients of the ground state wavefunction has been approximated using Eq. (5.4).

3. The bonding matrix elements spectral function for electron removal $A_+^{g^2}$ in Eq. (5.12) is identical to the electron removal spectral function of the TOC96 in Eq. (4.67).
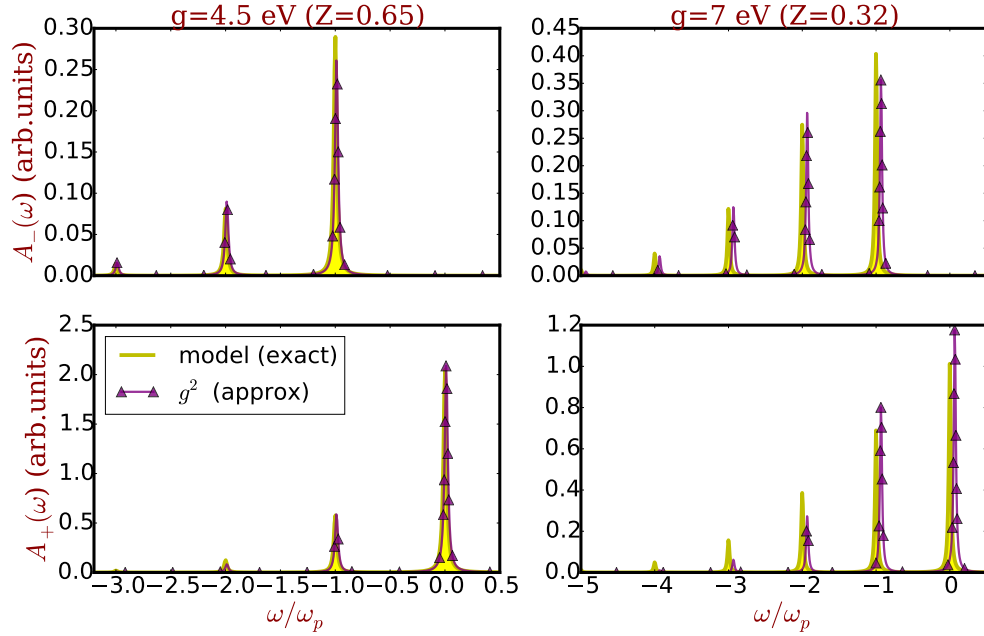
Figure 5.3: The spectral functions of the two-level hole-plasmon coupling Hamiltonian. Left panel: the coupling $g = 4.5$ eV yielding $\mathbf{Z} = 0.65$. Right panel: a stronger coupling $g = 7$ eV yielding $\mathbf{Z} = 0.32$. Yellow filled and purple curves with up-triangles are the exact and approximate (Eq. (5.12)) spectral functions, respectively.

As discussed in section 4.2, this spectral function yields good partial occupation of the bonding orbital compared to the exact one as shown by the red curve with down triangles in Fig. 4.12. However it is not complete because it does not conserve the total particle number, nor the spectral weight. This is corrected by the anti-bonding matrix element of electron removal spectral function $A_-^{g^2}$ in Eq. (5.12).

4. The anti-bonding matrix element $A_-^{g^2}$ in Eq. (5.12) leads to the anti-bonding orbital occupation $n_-^{g^2} = \int_{-\infty}^{\mu} \mathrm{d}\omega A_-^{g^2}(\omega) = 1 - n_+^2$, thus the total particle number is conserved by design. There is no electron removal QP peak in $A_-^{g^2}$ but only satellites because the presence of the anti-bonding orbital electron removal spectrum is only due to interactions: when there is no interaction, there will not be any electron removal spectrum in this orbital.

139

5.2 The constrained retarded cumulant in the HPC-2

The approximate analytical Green's function yields the spectral function in Eq. (5.12) that has a very good performance compared to the exact one. However like the exact spectral function, only the electron removal spectrum has been calculated in Eq. (5.12). In this section, I am going to introduce the so called constrained retarded cumulant, which has the same electron removal part as G^{g^2}. Besides electron removal, it has the corresponding electron addition part to conserve the total spectral weight.

In order to complete the electron removal and addition spectra, we have to first understand why the same orbital (e.g. the bonding orbital) should have both electron removal and addition spectra like what we have seen in the GWA and RC. This is essentially due to the fact of partial occupation of interacting states. I will analyze this issue using a simple two-level system as illustrated in Fig. 5.4.
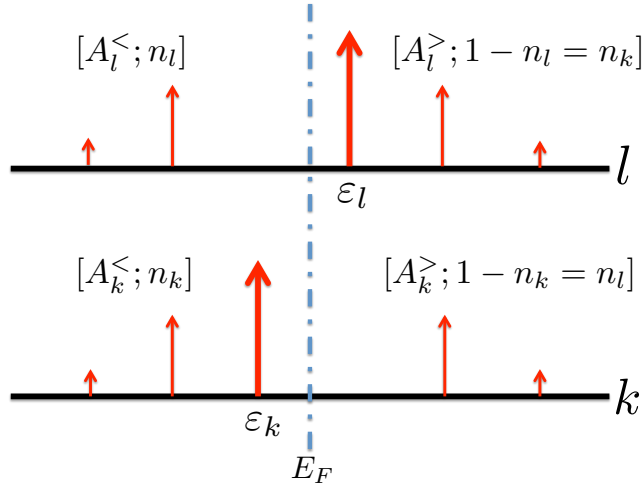

Figure 5.4: Schematic illustration of the spectrum of a two-level system. There are two quasi-particle states in the system: the state k and l are below and above the Fermi level, respectively. The quasi-particle energies of these two states are ε_k and ε_l as represented by the thick red peaks. The thin red peaks represent the satellites.

When a certain quasi-particle state labeled as k is close to the Fermi level (e.g. sodium bottom valence) and its energy $\varepsilon_k < \mu^7$, it can interact with another quasi-particle state

---

[7]I am now talking about the quasi-particle states such that ε_k corresponds to the QP energy of the state k instead of any independent-particle eigenvalues like Hartree or LDA. Thus in the HPC-2, ε_k corresponds to the bonding orbital QP energy $\varepsilon_0 - \mathbf{t} + \frac{\tilde{g}^2}{\omega_p} - \frac{\tilde{g}^2}{\omega_p + 2\mathbf{t}}$, instead of the Hartree eigenvalue $\varepsilon_0 - \mathbf{t}$.

l with energy $\varepsilon_l > \mu$, which is exactly like the interaction between the bonding and anti-bonding orbitals of the HPC-2. Suppose in the simplest case there are only these two states k and l in our system. The direct consequence of the interaction is the partial occupation of both states, which is entirely a correlation effect so that it cannot be seen in any independent-particle picture. When we do photoemission, one electron is removed from our system. It is impossible to tell from which state (k or l) the one electron is removed. The resulting photoemission spectrum of the state k ($A_k^<$)(suppose we can resolve the spectrum of each state) will contain one QP peak at energy ε_k and satellites on the left hand side of the QP peak. The integration of this spectrum until the chemical potential gives the fractional occupation number, i.e. $n_k = \int_{-\infty}^{\mu} A_k^<(\omega) \mathrm{d}\omega < 1$.

The other part of the spectral weight $(1 - n_k)$ is placed in the electron removal spectrum of the partially occupied state l, i.e. $A_l^<$, leading to $n_l = \int_{-\infty}^{\mu} A_l^<(\omega) \mathrm{d}\omega = 1 - n_k < 1$. This spectrum will contain only satellites because the electron removal spectrum is fully induced by the interaction: when there is no interaction, there will not be any electron removal spectrum in the state l. The electron removal satellite energy of the state l should equal the electron removal satellite energy of the state k because no matter from which state the one electron is removed, it always excites all possible excitations of the system. Therefore the Green's functions of these two states G_k and G_l should have the same denominator representing all possible excitations in the system. However the possibility of a certain excitation is determined by the nominator of the Green's function, thus some excitation can have zero weight representing the forbidden excitations. For example, the weight of the bonding QP excitation is zero in the anti-bonding Green's function, which means that there will not be any electron removal QP excitation in the state l. This is right the picture of the exact Green's function of the HPC-2 (see Eq. (4.29)).

Although the HPC-2 cannot provide the electron addition spectrum, we should be able to calculate the electron addition spectrum from the constrained retarded cumulant as what the GW approximation does (see Fig. 4.7) because our theory should be able to calculate the electron removal and addition Green's function on the same footing. In inverse photoemission, one electron is added to the system. The possibility for this electron to be added to the state k is $1 - n_k = n_l$ and to the state l is $1 - n_l = n_k$. The electron addition

spectra of these two states are similar to the electron removal spectra: the electron addition spectrum of the state l ($A_l^>$) has one QP peak at ε_l and plasmon satellites on the right hand side of the QP peak and the electron addition spectrum of the state k ($A_k^>$) has only plasmon satellites at the same energy as the electron satellites of the state k.

In the picture mentioned above, the electron addition spectrum of the bonding orbital should be calculated from the electron addition quasi-particle excitation of the anti-bonding orbital, which yields

$$
\begin{aligned}
G_+^{CRC}(\tau) = {} & - i\theta(\tau)e^{-i\varepsilon_+^{CRC}\tau}e^{-\tilde{\beta}_1-\tilde{\beta}_2}\exp\left(\tilde{\beta}_1 e^{i\omega_p\tau}\right) \\
& - i\theta(\tau)e^{-i\varepsilon_-^{CRC}\tau}e^{-\tilde{\beta}_1-\tilde{\beta}_2}\exp\left(\tilde{\beta}_1 e^{i\omega_p\tau}\right)\left[\exp\left(\tilde{\beta}_2 e^{-i\omega_p\tau}\right)-1\right],
\end{aligned}
\tag{5.15}
$$

where $\varepsilon_\pm^{CRC}$ are the quasi-particle energies from EscGW$_0$ that are the same as all the CEAs. Analogously the constrained retarded cumulant anti-bonding Green's function reads

$$
\begin{aligned}
G_-^{CRC}(\tau) = {} & - i\theta(\tau)e^{-i\varepsilon_-^{CRC}\tau}e^{-\tilde{\beta}_1-\tilde{\beta}_2}\exp\left(\tilde{\beta}_1 e^{-i\omega_p\tau}\right) \\
& - i\theta(\tau)e^{-i\varepsilon_+^{CRC}\tau}e^{-\tilde{\beta}_1-\tilde{\beta}_2}\exp\left(\tilde{\beta}_1 e^{i\omega_p\tau}\right)\left[\exp\left(\tilde{\beta}_2 e^{i\omega_p\tau}\right)-1\right]
\end{aligned}
\tag{5.16}
$$

The corresponding spectral functions are then

$$
A_+^{CRC}(\omega) = \mathbf{Z}_+ \sum_{m=0}^{\infty}\left[\frac{\tilde{\beta}_1^m}{m!}\delta\left(\omega-\varepsilon_+^{CRC}+m\omega_p\right)+\frac{(\tilde{\beta}_1+\tilde{\beta}_2)^m-\tilde{\beta}_1^m}{m!}\delta\left(\omega-\varepsilon_-^{CRC}-m\omega_p\right)\right];
\tag{5.17a}
$$

$$
A_-^{CRC}(\omega) = \mathbf{Z}_- \sum_{m=0}^{\infty}\left[\frac{\tilde{\beta}_1^m}{m!}\delta\left(\omega-\varepsilon_-^{CRC}-m\omega_p\right)+\frac{(\tilde{\beta}_1+\tilde{\beta}_2)^m-\tilde{\beta}_1^m}{m!}\delta\left(\omega-\varepsilon_+^{CRC}+m\omega_p\right)\right].
\tag{5.17b}
$$

The quasi-particle renormalization factor from the CRC is the same as the one from the TOC96 (see Eq. (4.67)) that reads

$$
\mathbf{Z}_\pm = e^{-\tilde{\beta}_1-\tilde{\beta}_2},
\tag{5.18}
$$

which leads to the same occupation of bonding and anti-bonding orbitals as the TOC96 (see Fig. 4.12).

The CRC Green's function fulfills all the exact constraints I have mentioned in the summary of chapter 1, i.e. conservation of both spectral weight and particle number, as well as the fact that the poles of the CRC Green's function are independent on the matrix elements. Moreover, the CRC describes well the partial occupation of two orbitals. The plasmon satellite replica are given with good performance compared to the exact Green's function as shown in Fig. 5.5 for both weak and strong coupling cases. However, the full CRC Green's function can only be obtained in such a simple two-level hole-plasmon coupling model. We will see in the next section, why it is impossible to calculate the constrained retarded cumulant Green's function in Eq. (5.15) in a generalized four-level model.

5.3 Generalization and implementation of the CRC for the calculation of real systems

The constrained retarded cumulant looks perfect in the HPC-2. However, this is not the end of the story yet because real materials are not as simple as a two-level hole-plasmon coupling model Hamiltonian. On one hand, the plasmon is not the simple Einstein boson that does not disperse at all. On the other hand, there are much more states that can interact with each other in real materials. In order to go one step further, we need to see how to get the CRC Green's function in terms of the GW self-energy such that it can be generalized to real system calculations as all other CEAs. Here I take the bonding orbital of the HPC-2 as one example to show how to interpret G_+^{CRC} in equation (5.15) in terms of the GW self-energy Σ (see Eq. (D.8)). The fundamental building blocks of G_+^{CRC} are the
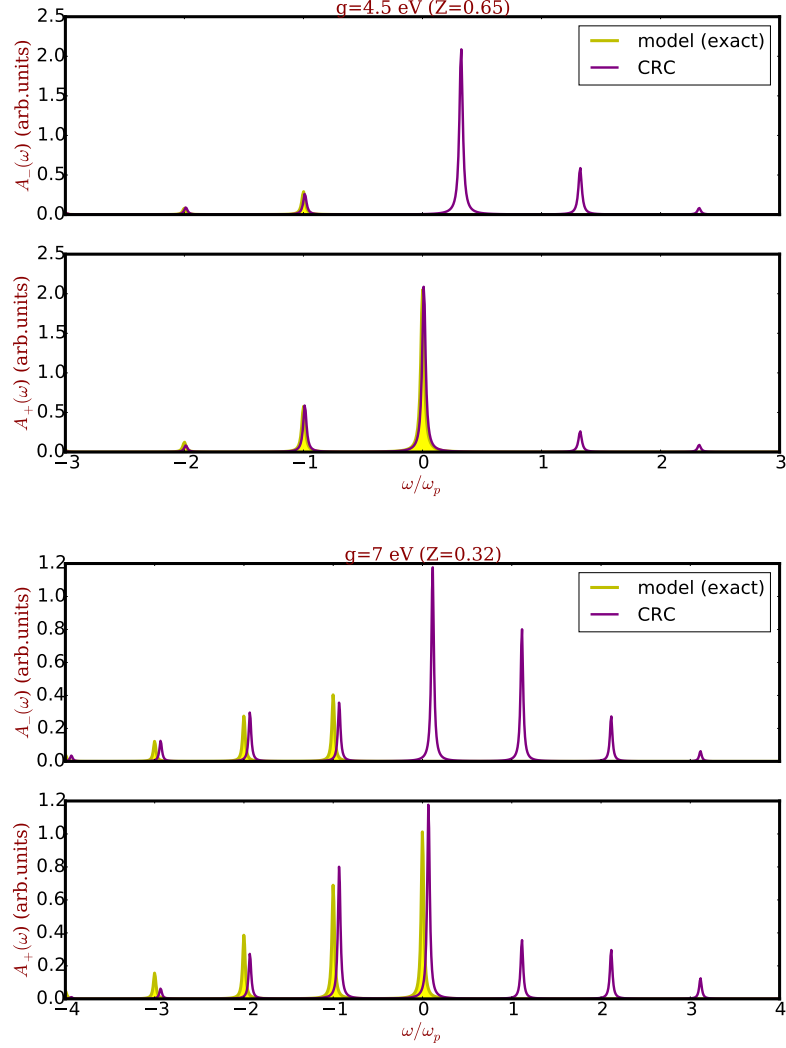
Figure 5.5: The spectral functions of the two-level hole-plasmon coupling Hamiltonian. All parameters are the same as in Fig. 5.3. Upper panel (two figures): the coupling $g = 4.5$ eV yielding $\mathbf{Z} = 0.65$. Lower panel (two figure): a stronger coupling $g = 7$ eV yielding $\mathbf{Z} = 0.32$. Yellow filled and purple curves are the exact and CRC spectral functions (Eq. (5.17)), respectively. The Lorentzian broadening $\eta = 0.1$ eV has been used for all plots.

quasi-particle energies ε_+^{QP} and $\tilde{\beta}_1$ and $\tilde{\beta}_2$ which can be written as

$$\varepsilon_+^{QP} = \mathrm{Re}\,\Sigma_+(\varepsilon_+^H) = \varepsilon_0 - \mathbf{t} + \frac{\tilde{g}^2}{\omega_p} - \frac{\tilde{g}^2}{\omega_p + 2\mathbf{t}} \; ; \tag{5.19a}$$

$$\tilde{\beta}_1 = \left.\frac{\partial\,\mathrm{Re}\,\Sigma_\pm^e(\omega)}{\partial\omega}\right|_{\omega=\varepsilon_+^H} = \left.\frac{\partial\,\mathrm{Re}\,\Sigma_\pm^h(\omega)}{\partial\omega}\right|_{\omega=\varepsilon_-^H} \; ; \tag{5.19b}$$

$$\tilde{\beta}_2 = \left.\frac{\partial\,\mathrm{Re}\,\Sigma_\pm^e(\omega)}{\partial\omega}\right|_{\omega=\varepsilon_+^H} = \left.\frac{\partial\,\mathrm{Re}\,\Sigma_\pm^h(\omega)}{\partial\omega}\right|_{\omega=\varepsilon_-^H} \; . \tag{5.19c}$$

144

5.3.1   A four-level system with dispersionless plasmons

Due to the simplicity of the two-level hole-plasmon coupling model, we cannot distinguish the self-energies of bonding and anti-bonding orbitals because $\Sigma_+ \equiv \Sigma_-$ (see Eq. (4.57)). As a consequence, there are different possible formulas to obtain the same $\tilde{\beta}_1$ and $\tilde{\beta}_2$. In real materials, each state has a different self-energy matrix element. Thus the HPC-2 is not sufficient to generalize our findings. In order to find out the link between the β functions[8] in the CRC Green's function and the GW self-energy, we can have a look at the structure of a more general Σ with four orbitals using the dispersionless plasmon approximation (see a schematic illustration of this four-level system in Fig. 5.6)[9]

$$\Sigma_1(\omega) = \frac{\lambda_1}{\omega - \varepsilon_1 + \omega_1 - i\eta} + \frac{\lambda_{12}}{\omega - \varepsilon_2 + \omega_{12} - i\eta} + \frac{\lambda_{13}}{\omega - \varepsilon_3 - \omega_{13} + i\eta} + \frac{\lambda_{14}}{\omega - \varepsilon_4 - \omega_{14} + i\eta} \,;$$

$$\Sigma_2(\omega) = \frac{\lambda_{12}}{\omega - \varepsilon_1 + \omega_{12} - i\eta} + \frac{\lambda_2}{\omega - \varepsilon_2 + \omega_2 - i\eta} + \frac{\lambda_{23}}{\omega - \varepsilon_3 - \omega_{23} + i\eta} + \frac{\lambda_{24}}{\omega - \varepsilon_4 - \omega_{24} + i\eta} \,;$$

$$\Sigma_3(\omega) = \frac{\lambda_{13}}{\omega - \varepsilon_1 + \omega_{13} - i\eta} + \frac{\lambda_{23}}{\omega - \varepsilon_2 + \omega_{23} - i\eta} + \frac{\lambda_3^2}{\omega - \varepsilon_3 - \omega_3 + i\eta} + \frac{\lambda_{34}}{\omega - \varepsilon_4 - \omega_{34} + i\eta} \,;$$

$$\Sigma_4(\omega) = \frac{\lambda_{14}}{\omega - \varepsilon_1 + \omega_{14} - i\eta} + \frac{\lambda_{24}}{\omega - \varepsilon_2 + \omega_{24} - i\eta} + \frac{\lambda_{34}}{\omega - \varepsilon_3 - \omega_{34} + i\eta} + \frac{\lambda_4}{\omega - \varepsilon_4 - \omega_4 + i\eta} \,;$$

where ε_1, ε_2[10] are below chemical potential μ and ε_3, ε_4 are above μ, $\Sigma_i \equiv \Sigma_{ii}$, each W_{ii}^{jj} has one dispersionless plasmon of energy ω_{ii}^{jj} and weight λ_{ii}^{jj}. Note that since $W_{ii}^{jj} = W_{jj}^{ii}$[11], the short notations of $W_{ii}^{jj} \equiv W_{ij}$ and $W_{ii}^{ii} \equiv W_i$ have been used.

---

[8]The small tilde on top of β has been dropped for simplicity. The function $\tilde{\beta}$ in the CRC Green's function will be refereed to as " the β function " in the following context.

[9]The short notation $\Sigma_i \equiv \Sigma_{ii} = i \sum_k G_{kk} W_{kk}^{ii}$ has been used.

[10]Here ε_i can be considered as the quasi-particle energies, which means the self-energies are calculated from the quasi-particle Green's function. This assumption is not necessary but to be an example, it will be easier to understand.

[11]The screened Coulomb interaction W has the property of $W_{ii}^{jj} = W_{jj}^{ii}$ because the following two equations are equivalent:

$$W_{ii}^{jj}(t_{12}) = \int \mathrm{d}x_1 x_2 \, \varphi_j^*(x_1)\varphi_i(x_2)W(x_1, x_2, t_{12})\varphi_i^*(x_1)\varphi_j(x_2) \,;$$

$$W_{jj}^{ii}(t_{12}) = \int \mathrm{d}x_1 x_2 \, \varphi_i^*(x_1)\varphi_j(x_2)W(x_1, x_2, t_{12})\varphi_j^*(x_1)\varphi_i(x_2) \,;$$

The above self-energies are simplified versions of the Σ in Ref. [34] that reads

$$\Sigma_k = \sum_{i,s\neq 0} \frac{|V_{ki}^s|^2}{\omega - \varepsilon_i + \omega_s \text{sgn}(\mu - \varepsilon_i)} \,, \tag{5.22}$$

where V_{ki}^s is defined as the *fluctuation potential* that plays the same role as our λ: it determines the weight of each plasmon energy ω_s where s labels the dispersion of the plasmon. The four-level self-energy is more general than the two-level one in the sense that each occupied matrix element (e.g., Σ_1) contains two occupied orbitals, instead of only one like the HPC-2 in Eq. (4.57). Therefore, it is closer to a realistic system than the two-level one. Let's take the first orbital labeled as "1" as one example. The imaginary part of the hole self-energy in this orbital reads

$$\frac{1}{\pi} \text{Im} \Sigma_1^h(\omega) = \lambda_1 \delta(\omega - \varepsilon_1 + \omega_1) + \lambda_{12} \delta(\omega - \varepsilon_2 + \omega_{12}) \approx \tilde{\lambda}_1^< \delta\big(\omega - \varepsilon_1 + \tilde{\omega}_1^<\big), \tag{5.23}$$

where the $\tilde{\lambda}$ and $\tilde{\omega}$ are effective strength and plasmon energy, respectively.

The above approximation of the self-energy Eq. (5.23) is consistent with the idea in Ref. [34] (e.g., the section 4.3 in [34])[12].

The β functions of the first orbital thus read[13]

$$\beta_1^< = \left. \frac{\partial \text{Re} \Sigma_1^h(\omega)}{\partial \omega} \right|_{\omega=\varepsilon_1} = \frac{\tilde{\lambda}_1}{\tilde{\omega}_1^2} \,; \tag{5.24a}$$

$$\beta_1^> = \left. \frac{\partial \text{Re} \Sigma_1^e(\omega)}{\partial \omega} \right|_{\omega=\varepsilon_1} = \frac{\lambda_{13}}{(\varepsilon_{13} - \omega_{13})^2} + \frac{\lambda_{14}}{(\varepsilon_{14} - \omega_{14})^2} \,, \tag{5.24b}$$

where $\varepsilon_{ij} \equiv \varepsilon_i - \varepsilon_j$.

---

[12] In section 4.3 of Ref. [34], Hedin discussed the application of the TOC96 in valence photoemission. Two assumptions have been introduced. First the occupation of occupied states are always equal to 1, which makes the TOC96 identical to the TOC11. The second assumption is identical to my Eq. (5.23), which can be seen as an average energy approximation.

[13] For the moment, I did not use the formulation in Eq. (5.23) for the electron part of the self-energy Σ_1^e. A complete idea of a multipole representation of the full self-energy for a real system will be introduced in section 5.3.2.

Now we can calculate the electron removal spectral function of the occupied state with energy ε_1 following the constrained retarded cumulant (see Eq. (5.15)). It reads

$$A_{1,<}^{occ}(\omega) = \mathbf{Z}_1 \sum_{m=0}^{\infty} \frac{(\beta_1^<)^m}{m\,!} \delta(\omega - \varepsilon_1 + m\tilde{\omega}_1)\,, \tag{5.25}$$

where

$$\mathbf{Z}_1 = \exp\left[-\beta_1^< - \beta_1^>\right]. \tag{5.26}$$

This spectral function is exactly the same as the TOC96 for an occupied state (see Eq. (4.67))[14]. The spectral function $A_{1,<}^{occ}$ in Eq. (5.25) is not the complete electron removal spectral function because the QP excitation with energy ε_1 will induce electron removal satellites in the unoccupied orbitals ε_3 and ε_4 to conserve the total particle number. The additional part of the electron removal spectral function induced by the QP excitation of the state ε_1 reads[15]

$$A_{1,<}^{unocc}(\omega) = \mathbf{Z}_1 \sum_{m=0}^{\infty} \frac{[(\beta_1^< + \beta_1^>)^m - (\beta_1^<)^m]}{m\,!} \delta(\omega - \varepsilon_1 + m\tilde{\omega}_1)\,. \tag{5.27}$$

The spectral functions induced by other quasi-particle excitations can be calculated in the same way. An illustration of the constrained retarded cumulant spectral functions are shown in Fig. 5.6. $A_{1,<}^{occ}$ and $A_{2,<}^{occ}$ give the constrained retarded cumulant electron removal spectra of states labeled ε_1 and ε_2, respectively. They are equivalent to the electron removal spectral functions of the same states from the TOC96. $A_{1,<}^{unocc} + A_{2,<}^{unocc}$ equals to the sum of the electron removal spectra of the states labeled ε_3 and ε_4, i.e. $A_{3,<}^{unocc} + A_{4,<}^{unocc}$ represented by the red color in Fig. 5.6. Different from the constrained retarded cumulant in the HPC-2, here the electron removal spectra in the ε_3 and ε_4 (i.e., $A_{3,<}^{unocc}$ or $A_{4,<}^{unocc}$) cannot be distinguished in the constrained retarded cumulant. Actually there is no clear physical meaning of $A_{1,<}^{unocc}$ or $A_{2,<}^{unocc}$ because it does not correspond to the spectrum of any state but only the sum of these two has the physical meaning of total electron removal spectrum

---

[14]The CRC spectral functions $A_{1,<}^{occ}$, $A_{2,<}^{occ}$, $A_{3,>}^{unocc}$, and $A_{4,>}^{unocc}$ in Fig. 5.6 are exactly the same as the one of the TOC96. Instead, the CRC adds the contributions $A_{1,<}^{unocc}$, $A_{2,<}^{unocc}$, $A_{3,>}^{occ}$, and $A_{4,>}^{occ}$ to complete the spectra of the TOC96.

[15]As illustrated in Figs. 5.4 and 5.6, this spectrum is not the electron removal spectrum of the state ε_1, but the contribution of the electron removal spectrum of some unoccupied state.
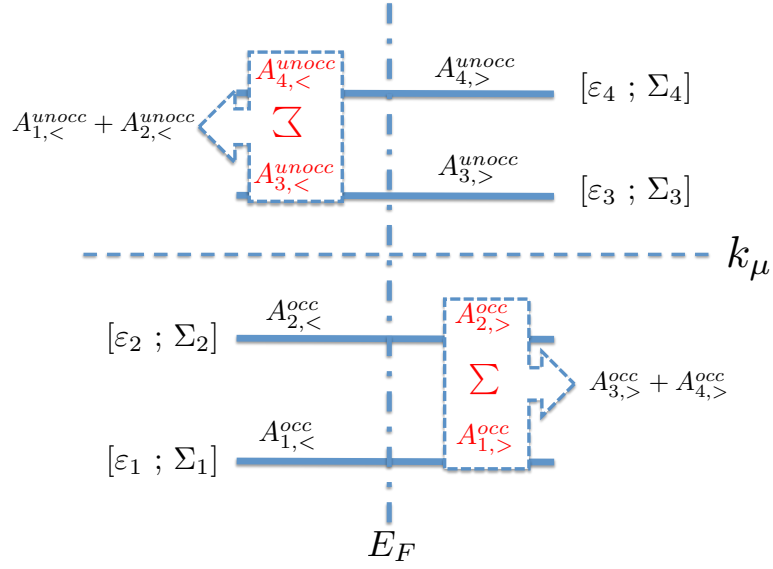
Figure 5.6: A schematic illustration of the four-level system. The states ε_1 and ε_2 are below the chemical potential μ, ε_3 and ε_4 are states above the chemical potential. The self-energy of each state is Σ_i. The electron removal spectral functions of the occupied states (below the chemical potential) are $A_{1,<}^{occ}$ and $A_{2,<}^{occ}$. The electron addition spectral functions of the unoccupied states (above the chemical potential) are $A_{3,>}^{unocc}$ and $A_{4,>}^{unocc}$. The total electron removal spectrum of the unoccupied states are $A_{1,<}^{unocc} + A_{2,<}^{unocc}$, which equals to the sum of electron removal spectrum of each unoccupied state $A_{3,<}^{unocc} + A_{4,<}^{unocc}$, however the individual spectrum of $A_{3(4),<}^{unocc}$ (in red color) cannot be obtained by the constrained retarded cumulant. Analogously the total electron addition spectrum of the occupied states $A_{1,>}^{occ} + A_{2,>}^{occ}$ equals $A_{3,>}^{occ} + A_{4,>}^{occ}$ but the individual spectrum of $A_{1(2),>}^{occ}$ (in red color) is missing.

from all the states above the chemical potential. The effect of these two additional spectra is to conserve the particle number of each state because $\int_{-\infty}^{\mu} \left(A_{1(2),<}^{occ} + A_{1(2),<}^{unocc} \right) \mathrm{d}\omega = 1$.

How about the conservation of spectral weight? Since the electron addition spectrum of the state ε_1 or ε_2 (i.e., $A_{1(2),>}^{occ}$ in Fig. 5.6) cannot be calculated explicitly from the constrained retarded cumulant, the conservation of the spectral weight in each state cannot be studied. However, one can show that the conservation of the particle number leads to the conservation of the total spectral weight, because

$$\int_{-\infty}^{\mu} \left[A_{1,<}^{occ}(\omega) + A_{2,<}^{occ}(\omega) + A_{1,<}^{unocc}(\omega) + A_{2,<}^{unocc}(\omega) \right] \mathrm{d}\omega = 2 \, ; \tag{5.28a}$$

$$\int_{-\infty}^{\mu} \left[A_{1,<}^{occ}(\omega) + A_{2,<}^{occ}(\omega) \right] \mathrm{d}\omega + \int_{\mu}^{\infty} \left[A_{3,<}^{occ}(\omega) + A_{4,<}^{occ}(\omega) \right] \mathrm{d}\omega = 2 \, . \tag{5.28b}$$

The spectral functions in Eqs. (5.25) and (5.27) are the final constrained retarded cumulant spectral functions I am going to use in the real system calculations. In the following, I will show details about the implementation of these formulas into a code[16] for the real system calculations.

5.3.2   Implementation into a computer code

The central quantity of the constrained retarded cumulant is the GW self-energy. In a real system, the self-energy is a matrix when projecting on a certain basis (e.g. the Kohn-Sham or the quasi-particle orbitals). Often, one starts from a Kohn-Sham calculation and assumes the self-energy to be diagonal in the Kohn-Sham orbitals. Each diagonal element $\Sigma_i \equiv \Sigma_{ii}$ corresponds to one state. Suppose we want to calculate a matrix element of the electron removal spectral function in a certain occupied state of energy $\varepsilon_k < \mu$, the corresponding self-energy reads[17] [34]

$$\Sigma_k(\omega) = \sum_i^{occ} \sum_s \frac{\lambda_{i,k,s}^<}{\omega - \varepsilon_i^< + \omega_{i,k,s}^< - i\eta} + \sum_i^{unocc} \sum_s \frac{\lambda_{i,k,s}^>}{\omega - \varepsilon_i^> - \omega_{i,k,s}^> + i\eta}, \qquad (5.29)$$

where the subscript s takes into account the plasmon dispersion, and λ is the weight of the the self-energy. The imaginary part of Σ_k reads

$$\mathrm{Im}\,\Sigma_k(\omega) = \pi \sum_i^{occ} \sum_s \lambda_{i,k,s}^< \delta\left(\omega - \varepsilon_i^< + \omega_{i,k,s}^<\right) - \pi \sum_i^{unocc} \sum_s \lambda_{i,k,s}^> \delta\left(\omega - \varepsilon_i^> - \omega_{i,k,s}^>\right). \quad (5.30)$$

What we are going to use is the imaginary part of $\Sigma_k(\omega + \varepsilon_k)$ which can be written in a multipole representation (see e.g. Refs. [36, 93])

$$\mathrm{Im}\,\Sigma_k(\omega + \varepsilon_k) = \sum_{i=1}^{N^<} \tilde{\lambda}_{i,k}^< \delta(\omega + \tilde{\omega}_{i.k}^<) - \sum_{i=1}^{N^>} \tilde{\lambda}_{i.k}^> \delta(\omega - \tilde{\omega}_{i,k}^>), \qquad (5.31)$$

---

[16]The code used for the CEA calculation is our local code called *the cumulant code* [92]. It was written by Dr. Matteo Guzzo during his thesis for the calculation of the TOC11. During my thesis, I have worked together with Dr. Matteo Guzzo to implement the TOC96 and CRC into this cumulant code.

[17]Now we are talking about one certain occupied state k in a certain band b, thus in practice the state should be labeled (k, b), i.e. $\varepsilon_{k,b}$ or $\Sigma_{k,b}$.

where $N^<$ and $N^>$ are the number of poles to sample the lesser and greater part of Im Σ, respectively. I have defined the sampling frequencies and the corresponding weights as

$$\tilde{\lambda}_{i,k}^{<} = \pi \lambda_{i,k,s}^{<} \, ; \tag{5.32a}$$

$$\tilde{\lambda}_{i,k}^{>} = \pi \lambda_{i,k,s}^{>} \, ; \tag{5.32b}$$

$$\tilde{\omega}_{i,k}^{<} = \varepsilon_k - \varepsilon_i^{<} + \omega_{i,k,s}^{<} \, ; \tag{5.32c}$$

$$\tilde{\omega}_{i,k}^{>} = \varepsilon_i^{>} - \varepsilon_k + \omega_{i,k,s}^{>} \, . \tag{5.32d}$$

Note that all sampling parameters in the above equations are positive. The β functions under the multipole sampling can be calculated from

$$\beta_k^{<} = \sum_{i=1}^{N^<} \frac{\tilde{\lambda}_{i,k}^{<}}{\pi(\tilde{\omega}_{i,k}^{<})^2} \equiv \sum_{i=1}^{N^<} a_{i,k} \, ; \tag{5.33a}$$

$$\beta_k^{>} = \sum_{i=1}^{N^>} \frac{\tilde{\lambda}_{i,k}^{>}}{\pi(\tilde{\omega}_{i,k}^{>})^2} \equiv \sum_{i=1}^{N^>} b_{i,k} \, . \tag{5.33b}$$

The k-matrix element of the electron removal spectrum is

$$
\begin{aligned}
\frac{\pi A_{k,<}^{occ}(\omega)}{\mathbf{Z}_k \Gamma_k} &= \frac{1}{(\omega - \varepsilon_k)^2 + \Gamma_k^2} + \sum_{i=1}^{N^<} \frac{a_{i,k}}{(\omega - \varepsilon_k + \tilde{\omega}_{i,k}^{<})^2 + \Gamma_k^2} \\
&+ \frac{1}{2} \sum_{i \neq j=1}^{N^<} \frac{a_{i,k} a_{j,k}}{(\omega - \varepsilon_k + \tilde{\omega}_{i,k}^{<} + \tilde{\omega}_{j,k}^{<})^2 + \Gamma_k^2} + \frac{1}{2} \sum_{i=1}^{N^<} \frac{a_{i,k}^2}{(\omega - \varepsilon_k + 2\tilde{\omega}_{i,k}^{<})^2 + \Gamma_k^2} \\
&+ \frac{1}{6} \sum_{i=1}^{N^<} \frac{a_{i,k}^3}{(\omega - \varepsilon_k + 3\tilde{\omega}_{i,k}^{<})^2 + \Gamma_k^2} + \frac{1}{2} \sum_{i \neq j=1}^{N^<} \frac{a_{i,k}^2 a_{j,k}}{(\omega - \varepsilon_k + 2\tilde{\omega}_{i,k}^{<} + \tilde{\omega}_{j,k}^{<})^2 + \Gamma_k^2} \\
&+ \frac{1}{6} \sum_{i \neq j \neq l=1}^{N^<} \frac{a_{i,k} a_{j,k} a_{l,k}}{(\omega - \varepsilon_k + \tilde{\omega}_{i,k}^{<} + \tilde{\omega}_{j,k}^{<} + \tilde{\omega}_{l,k}^{<})^2 + \Gamma_k^2} + \cdots .
\end{aligned}
\tag{5.34}
$$

The quasi-particle renormalization factor $\mathbf{Z}_k = \exp\left(-\beta_k^{<} - \beta_k^{>}\right)$, and the quasi-particle inverse lifetime is defined as $\Gamma_k = \text{Im}\,\Sigma(\varepsilon_k)/N^{<}$ [18]. The first line of the above equation (5.34) contains the quasi-particle peak and the first order plasmon satellites. The second line contains the second order satellites and the rest are the third order terms. In principle,

---

[18]In a single pole model, the QP inverse lifetime Γ would obtain the full lifetime broadening. Here we sample the compete imaginary part of Σ including the region that is responsible to the broadening. Therefore we have to reduce Γ accordingly.

all the higher order terms should be calculated, however in practice, our cumulant code calculates until the third order terms as shown in the above equation[19].

The additional electron removal spectrum induced by the electron removal quasi-particle excitation of the occupied state k should have been[20]

$$
\begin{aligned}
\frac{\pi \tilde{A}_{k,<}^{unocc}(\omega)}{\mathbf{Z}_k \Gamma_k} &= \sum_{i=1}^{N^<} \frac{b_{i,k}}{(\omega - \varepsilon_k + \tilde{\omega}_{i,k}^<)^2 + \Gamma_k^2} + \frac{1}{2} \sum_{i \neq j=1}^{N^<} \frac{b_{i,k}^2}{(\omega - \varepsilon_k + \tilde{\omega}_{i,k}^< + \tilde{\omega}_{j,k}^<)^2 + \Gamma_k^2} \\
&+ \frac{1}{2} \sum_{i=1}^{N^<} \frac{(a_{i,k} + b_{i,k})^2 - a_{i,k}^2}{(\omega - \varepsilon_k + 2\tilde{\omega}_{i,k}^<)^2 + \Gamma_k^2} + \frac{1}{6} \sum_{i=1}^{N^<} \frac{(a_{i,k} + b_{i,k})^3 - a_{i,k}^3}{(\omega - \varepsilon_k + 3\tilde{\omega}_{i,k}^<)^2 + \Gamma_k^2} \\
&+ \frac{1}{2} \sum_{i \neq j=1}^{N^<} \frac{\left[(a_{i,k} + b_{i,k})^2 - a_{i,k}^2\right] b_{i,k}}{(\omega - \varepsilon_k + 2\tilde{\omega}_{i,k}^< + \tilde{\omega}_{j,k}^<)^2 + \Gamma_k^2} \\
&+ \frac{1}{6} \sum_{i \neq j \neq l=1}^{N^<} \frac{b_{i,k}^3}{(\omega - \varepsilon_k + \tilde{\omega}_{i,k}^< + \tilde{\omega}_{j,k}^< + \tilde{\omega}_{l,k}^<)^2 + \Gamma_k^2} + \cdots .
\end{aligned} \tag{5.35}
$$

However, there is a serious problem in the above equation, which is the use of b_i. On one hand, the number of poles $N^<$ is not necessarily equal to $N^>$ in Eq. (5.33). As a consequence, we might have less b_i than $\tilde{\omega}_i^<$ which makes the above equation ill-defined. On the other hand, even though we could use the same number of poles for $N^<$ and $N^>$ (i.e. the largest converged number), besides the computation effort we have to handle, how can we find the one-to-one correspondence between b_i and $\tilde{\omega}_i^>$? Note that in equation (5.33), the one-to-one correspondences are between a_i and $\tilde{\omega}_i^<$, b_i and $\tilde{\omega}_i^>$. There is no such relation between b_i and $\tilde{\omega}^<$ and it is impossible to tell how to find this required link. We have to look for some alternatives to implement our constrained retarded cumulant.

The simplest solution to this problem is to assume, first that the number of poles $N^> \equiv N^<$, and second that all b_is are the same[21]. This assumption leads to $b_i = \dfrac{\beta_k^>}{N^<}$ which

---

[19]We have checked the effect of the higher order terms and found that the fourth order terms (that did not appear in Eq. (5.34)) do not have any visible effects in the spectrum. Their contribution to the spectrum are too small but the effort in the computation is very large. Therefore, only up to the third order terms have been kept in our cumulant code. This holds also for the calculation of the TOC96 and TOC11 from our code that will be shown in Chapter 6.

[20]This is in principle, but in practice it is impossible to implement for the reason that will be discussed in the following.

[21]The condition of $N^< = N^>$ can be fulfilled without approximations because in principle, we can always choose the larger number of poles of the two to sample both. i.e., if $N^< > N^<$, we use $N^<$ on both lesser and greater parts of Σ.

is constant. Consequently, $\mathbf{Z}_k = \exp\left(\sum_i^{N^<}(a_i + b_i)\right)$ to keep the correct renormalization. With this approximation, $A_{k,<}^{unocc}$ finally reads

$$
\begin{aligned}
\frac{\pi A_{k,<}^{unocc}(\omega)}{\mathbf{Z}_k \Gamma_k} &= \sum_{i=1}^{N^<} \frac{\beta_k^>/N^<}{(\omega - \varepsilon_k + \tilde{\omega}_{i,k}^<)^2 + \Gamma_k^2} + \frac{1}{2}\sum_{i \neq j=1}^{N^<} \frac{(\beta_k^>/N^<)^2}{(\omega - \varepsilon_k + \tilde{\omega}_{i,k}^< + \tilde{\omega}_{j,k}^<)^2 + \Gamma_k^2} \\
&\quad + \frac{1}{2}\sum_{i=1}^{N^<} \frac{(a_{i,k} + \beta_k^>/N^<)^2 - a_{i,k}^2}{(\omega - \varepsilon_k + 2\tilde{\omega}_{i,k}^<)^2 + \Gamma_k^2} + \frac{1}{6}\sum_{i=1}^{N^<} \frac{(a_{i,k} + \beta_k^>/N^<)^3 - a_{i,k}^3}{(\omega - \varepsilon_k + 3\tilde{\omega}_{i,k}^<)^2 + \Gamma_k^2} \\
&\quad + \frac{1}{2}\sum_{i \neq j=1}^{N^<} \frac{\left[(a_{i,k} + \beta_k^>/N^<)^2 - a_{i,k}^2\right]\beta_k^>/N^<}{(\omega - \varepsilon_k + 2\tilde{\omega}_{i,k}^< + \tilde{\omega}_{j,k}^<)^2 + \Gamma_k^2} \\
&\quad + \frac{1}{6}\sum_{i \neq j \neq l=1}^{N^<} \frac{(\beta_k^>/N^<)^3}{(\omega - \varepsilon_k + \tilde{\omega}_{i,k}^< + \tilde{\omega}_{j,k}^< + \tilde{\omega}_{l,k}^<)^2 + \Gamma_k^2} + \cdots .
\end{aligned}
\tag{5.36}
$$

Each term of $A_{k,<}^{occ}(\omega)$ in Eq. (5.34) generates a term in $A_{k,<}^{unocc}(\omega)$ in the above equation, except the quasi-particle term.

In practice, it is enough to use only one pole to sample the greater part of Σ_k (i.e. $N^> = 1$) because $\tilde{\omega}_i^>$ does not enter in the denominator of $A_{k,<}^{unocc}$. The only parameter from $\Sigma_k^>$ is the total weight $\beta_k^>$ defined in Eq. (5.33). Suppose for the moment we had not introduced any approximation for b_i, then in principle the sampling of individual b_i in Eq. (5.33) depends on the number of poles $N^>$ but the sum $\beta_k^> = \sum_i^{N^>} b_{i,k}$ should be independent of the number of poles. This suggests to use only one pole to sample $\Sigma_k^>$ whose weight is $\beta_k^>$. This simplifies a lot of the computation because almost all the computation time is used in the calculation of $A_{k,<}^{occ}$ in Eq. (5.34). After having $A_{k,<}^{occ}$, the only parameter we need to calculate for $A_{k,<}^{unocc}$ is the weight of the one pole $\beta_k^>$. At the end, the CRC uses almost the same computational time as the TOC11 or TOC96.

One may find a strange phenomena from $A_{k,<}^{unocc}$, namely that all the satellites in the first line in Eq. (5.36) have the same weight which is independent of a_i. This is actually not surprising. It is the consequence of the approximation we have made in equation (5.10) when we try to get the best analytical Green's function of the HPC-2 and at the same time keep the conservation of particle number.

In order to understand the potential effects of the constrained retarded cumulant in the total (i.e. *k-summed*) electron removal spectrum, we can again use the HPC-2 as one example as shown in Fig. 5.7. Actually the HPC-2 can be considered as using the CRC Green's function in Eqs. (5.34) and (5.36) in the case of one pole sampling, i.e. $N^< = N^> = 1$. The total electron removal spectra of the TOC96 (red line with diamonds) and TOC11 (black dashed curve) are the same as their bonding orbital electron removal spectra because they do not give any anti-bonding electron removal spectra. The total electron removal spectrum of the CRC is the sum of the electron removal spectrum of bonding and anti-bonding orbitals in Eq. (5.17).

The TOC11 spectrum has the largest weight on the QP peak because it has the largest $\mathbf{Z}$-factor (see Eq. (4.70)). The TOC96 spectrum has the same QP weight as the CRC, but the satellites have smaller weights than the CRC due to the missing electron removal spectrum in the anti-bonding orbital (i.e. $A_{k,<}^{unocc}$ in Eq. (5.36)). The main effect of the CRC compared to the time-ordered cumulant is the enhancement of the plasmon satellites, which has the best agreement with the exact HPC-2 spectrum (yellow filled curve). Note that this enhancement on the satellite weights becomes larger and larger when we go closer to the Fermi level, because $\beta_k^>$ becomes larger when the state k goes towards to the Fermi level, i.e. $\mu - \varepsilon_k \to 0^+$.

Therefore in a real system calculation where we have much more occupied states, the satellites of the total *k-summed* spectrum calculated using the constrained retarded cumulant should shift towards the quasi-particle peak compared to the satellites calculated using the TOC96 or TOC11. We will see in Chapter 6 whether this is true for the valence photoemission spectrum of sodium.

5.4 Summary

In this chapter, I have first proposed an approximate Green's function of the two-level hole-plasmon coupling Hamiltonian which is fully analytical. Then I have discussed how to obtain the constrained retarded cumulant Green's function in the HPC-2 that fulfills all the exact constraints summarized in Chapter 1 and is inspired by the analytical approximation.
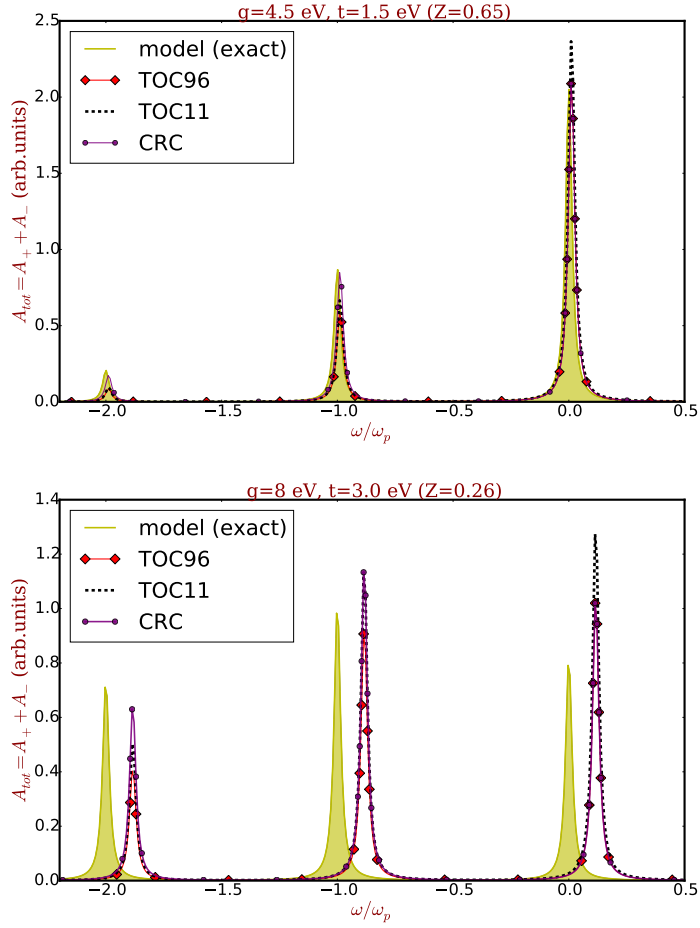
Figure 5.7: The total electron removal spectrum of the HPC-2. Upper panel: parameters are consistent with the sodium bottom valence state. Lower panel: relatively large coupling strength $g = 8$ eV and large bandwidth $\mathbf{t} = 3$ eV instead of 1.5 eV, leading to $\mathbf{Z} = 0.26$. The yellow filled curve is the exact total spectra of the model that come from the sum of the bonding and anti-bonding spectral functions in Eq. 4.29. The red line with diamonds, black dashed and purple line with circles show the total electron removal spectra calculated using the TOC96, TOC11 and CRC, respectively. The Lorentzian broadening $\eta = 0.1$ eV has been used for all plots.

The constrained retarded cumulant Green's function in a generalized four-level system can be written in terms of the GW self-energy such that we can go one step further to extend the constrained retarded cumulant towards calculations for real systems. However, the constrained retarded cumulant cannot provide the individual electron removal spectral functions of the states above the Fermi level, instead only the sum of them can be given. Compared to the previous cumulant expansion approximations (i.e. the TOC96, TOC11

and RC), the constrained retarded cumulant has the following properties in the calculation of the photoemission spectrum:

1. First, $A_{k,<}^{occ}$ ($\varepsilon_k < \mu$) in equation (5.34) is the same as the occupied electron removal spectrum of the TOC96 which gives a very good spectrum of the state k, as well as good partial occupation number. It is different from the TOC11 only in the **Z**-factor, which leads to too much weight on the QP peak in the spectrum of the TOC11. Compared to the spectrum of the retarded cumulant, the spurious satellites have been eliminated, and the constraint of the poles that has been summarized in section 1.3 is fulfilled.

2. The additional contribution to the electron removal spectrum is represented by $A_{k,<}^{unocc}$ in equation (5.36). It does not have a quasi-particle peak but only satellites. $A_{k,<}^{unocc}$ plays the role of adding weights on top of the satellites of $A_{k,<}^{occ}$. The closer the state k to the Fermi level, the larger the added weight will be. As a consequence, in the total *k-summed* photoemission spectrum, the center of the satellites in $A_{k,<}^{occ}$ might shift towards the quasi-particle peak: in the satellite region, the frequencies that are closer to the quasi-particle energy (stemming from the *k-resolved* spectrum of the states k closer to the Fermi level) get more weight than the frequencies farther away (they stem from the *k-resolved* spectrum of the states k farther away from the Fermi level) from the quasi-particle energy. We will see in the next chapter that this is exactly what we would need in order to have a better description of the sodium valence photoemission spectrum, because the TOC11 overestimates the distance between the QP peak and the satellites.

3. Finally, the constrained retarded cumulant would not change anything in the core photoemission emission spectrum of the TOC96, the TOC11 or the RC, because $\beta^>$ of the core self-energy is almost zero. Therefore the spectrum of the constrained retarded cumulant will induce the same core spectra as all other CEAs.

Chapter 6

Cumulant expansion approximation in bulk sodium

In the previous chapter, I have shown the constrained retarded cumulant Green's function and the equations which are implemented in the cumulant code for real system calculations. The effects of the constrained retarded cumulant compared to the traditional time-ordered cumulants (the TOC96 and TOC11) have also been discussed using the HPC-2. In this chapter, I am going to show the calculated photoemission spectrum using the cumulant code by comparing to the experimental photoemission spectrum in bulk sodium, for the valence and the core. In particular the TOC11, TOC96 and the constrained retarded cumulant results are studied in detail using the dynamical screened Coulomb interaction W calculated in the random phase approximation (RPA W).

The RPA W yields some discrepancies between the calculated and experimental spectra. The constrained retarded cumulant improves the spectra with respect to the traditional time-ordered cumulants but is still not good enough. In order to go beyond the random phase approximation and find out the reason why theses disagreements appear, I also provide some analysis using some more advanced calculated W.

Finally the computational details about all the calculations in this thesis are provided such that one can reproduce what has been shown using the same open source codes, i.e. the ABINIT code [43] and the cumulant code [92].

6.1 Sodium photoemission spectrum from the time-ordered cumulant

In section 3.3 I have derived the TOC11 (see Eq. (3.32)). Here I am going to use the TOC11 to calculate the photoemission spectrum of bulk sodium, for the valence and the core, like what I did using the GW approximation in section 2.2.

Like in the case of the constrained retarded cumulant, the implementation of the TOC11 in our cumulant code is also based on the multipole representation of the self-energy as shown in Eq. (5.31). Since the TOC11 does not contain the greater part of the self-energy, only the lesser part needs to be sampled. In the case of bulk sodium, the converged number of poles $N^< = 150$ is adopted in our calculation. The corresponding intrinsic spectral function of a certain occupied state k, i.e. $A_k(\omega) = \pi^{-1} \operatorname{Im} |G_k(\omega)|$ in a multipole representation reads[1]

$$
\begin{aligned}
\frac{\pi A_k(\omega)}{\mathbf{Z}_k \Gamma_k} &= \frac{1}{(\omega - \varepsilon_k)^2 + \Gamma_k^2} + \sum_{i=1}^{N^<} \frac{a_{i,k}}{(\omega - \varepsilon_k + \tilde{\omega}_{i,k}^<)^2 + \Gamma_k^2} \\
&+ \frac{1}{2} \sum_{i \neq j=1}^{N^<} \frac{a_{i,k} a_{j,k}}{(\omega - \varepsilon_k + \tilde{\omega}_{i,k}^< + \tilde{\omega}_{j,k}^<)^2 + \Gamma_k^2} + \frac{1}{2} \sum_{i=1}^{N^<} \frac{a_{i,k}^2}{(\omega - \varepsilon_k + 2\tilde{\omega}_{i,k}^<)^2 + \Gamma_k^2} \\
&+ \frac{1}{6} \sum_{i=1}^{N^<} \frac{a_{i,k}^3}{(\omega - \varepsilon_k + 3\tilde{\omega}_{i,k}^<)^2 + \Gamma_k^2} + \frac{1}{2} \sum_{i \neq j=1}^{N^<} \frac{a_{i,k}^2 a_{j,k}}{(\omega - \varepsilon_k + 2\tilde{\omega}_{i,k}^< + \tilde{\omega}_{j,k}^<)^2 + \Gamma_k^2} \\
&+ \frac{1}{6} \sum_{i \neq j \neq l=1}^{N^<} \frac{a_{i,k} a_{j,k} a_{l,k}}{(\omega - \varepsilon_k + \tilde{\omega}_{i,k}^< + \tilde{\omega}_{j,k}^< + \tilde{\omega}_{l,k}^<)^2 + \Gamma_k^2} + \cdots,
\end{aligned}
\tag{6.1}
$$

where $\mathbf{Z}_k = \exp\left(-\sum_{i=1}^{N^<} a_{i,k}\right)$, $\Gamma_k = \operatorname{Im} \Sigma_k(\varepsilon_k)/N^<$. In our cumulant code, the terms have been calculated up to the third order, hence only the terms appearing in the above equation are calculated.

---

[1] For simplicity, the label of state k contains both labels of band and k-point. In practice $k \to (n, k)$ where n represents the band and k represents the k-point in the Brillouin zone.

6.1.1 The TOC11 in sodium core

We have already discussed the TOC11 spectrum in the hole-plasmon coupling model Hamiltonian and in principle, the cumulant expansion approximations are expected to work best for core levels, provided we use the exact screened Coulomb interaction W. Therefore we start from the sodium core states ($2s$ and $2p$) to test the performance of the TOC11. I have shown the GW spectral functions of sodium core states in section 2.2 using the RPA W, i.e. the dynamically screened Coulomb interaction calculated using the `random phase approximation`. In particular, we have seen the importance of the energy self-consistency on the quasi-particle energies of the sodium core states. To be consistent with the GW approximation, I will first show the TOC11 results using the same $\mathrm{EscGW_0}$ self-energy as the one we have used in the $\mathrm{EscGW_0}$ calculation in section 2.2[2].

Screening from the random phase approximation

The calculated spectral functions of sodium core $2s$ and $2p$ at $k = [0, 0, 0]$ (i.e., the Γ point) using the TOC11 are shown in Fig. 6.1. The TOC11 intrinsic spectrum (red line with up-triangles in the bottom panel) has a QP peak at the same energy as the $\mathrm{EscGW_0}$ but with a smaller weight, which is consistent with our analysis in the hole-plasmon coupling Hamiltonian (see Fig. 4.5). Moreover the TOC11 gives the first plasmon satellite at the energy where $\mathrm{Im}\,\Sigma$ has a peak, reflecting the fact that the TOC11 reproduces the poles in $\mathrm{Im}\,\Sigma$ hence in $\mathrm{Im}\,W$. The satellite replica in the intrinsic spectral function of the TOC11 are almost invisible because the weight of the higher order satellites are too small compared to the QP peak.

The total *k-summed* photoemission spectra of these two core states (for theory and experiment) are shown in Fig. 6.2. The total calculated photocurrent (red curves) satellites are enhanced by including the secondary electron background as well as the extrinsic and interference effects such that the plasmon satellite replica can be observed[3]. The blue

---

[2]In principle, we could also use the $\mathrm{G_0W_0}$ self-energy to calculate the TOC11 Green's function as discussed in section 4.2. The $\mathrm{G_0W_0}$ and $\mathrm{EscGW_0}$ self-energy should give the same CEA result. However, the present cumulant code reads the GW output from the ABINIT code [43] such that it is more convenient to keep the same self-energy in both GW and cumulant calculations.

[3]As discussed in section 1.1, the red curve in Fig. 6.2 has taken into account approximately all the steps in the *three-step* model. More details can been found in Ref. [20].
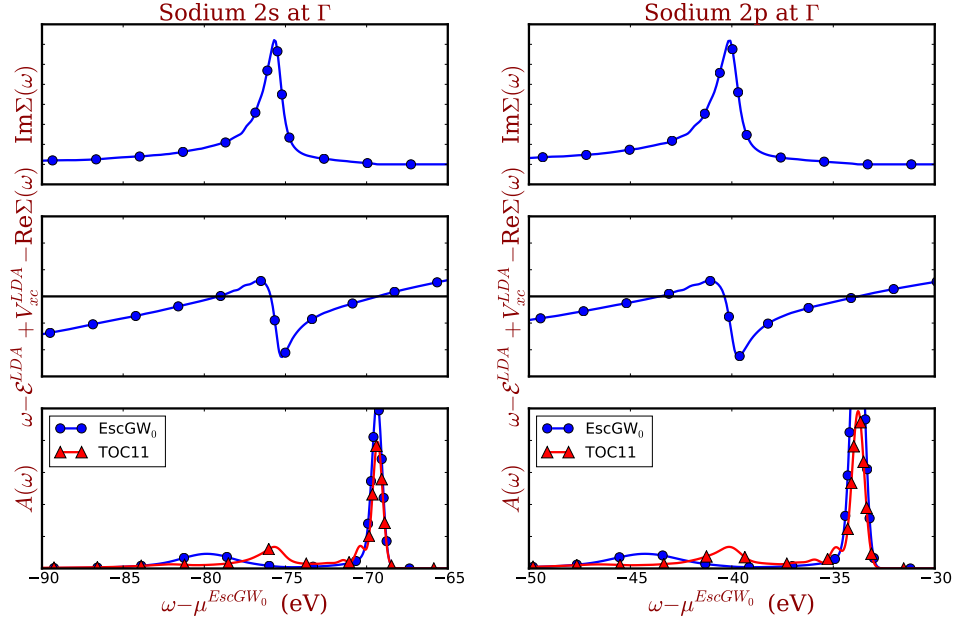
Figure 6.1: Intrinsic spectral functions of sodium $2s$ (left lower panel) and $2p$ (right lower panel) at the Γ point. Blue line with circles and red line with up-triangles are the results of the $EscGW_0$ and TOC11, respectively. The upper panels are the imaginary part of the $EscGW_0$ self-energies of these two core states. The middle panels are the shifted real part of the $EscGW_0$ self-energies that crosses zero at the QP energy. The lower panels show the intrinsic spectral functions where a 0.3 eV Gaussian broadening has been used in both the $EscGW_0$ and TOC11 spectral functions. The zero of the energy axis is set to be the $EsGW_0$ Fermi energy. The shoulders on the left hand side of the TOC11 QP peaks are spurious effects induced by the algorithm of the present multipole sampling, which is discussed in Fig. 6.3.

dashed curve labeled as cumulant is the intrinsic spectrum[4] calculated from the TOC11 and the black line with circles are experimental data reproduced from Ref. [47]. The overall agreement between the calculated photocurrent and experiment is reasonably good. The distance of the satellites from the quasi-particle position is systematically slightly overestimated (larger by ≈ 0.5 eV). Our first hypothesis was that this might be due to the use of the RPA W that overestimates plasmon frequencies in loss or inelastic x-ray scattering spectra, especially with increasing momentum transfer [94, 95]. Since the screening of W

---

[4]The intrinsic spectrum corresponds to the photocurrent of Eq. (1.13) where the dipole matrix element $\hat{\Delta}$ has been calculated corresponding to the photon energy of the experiment.
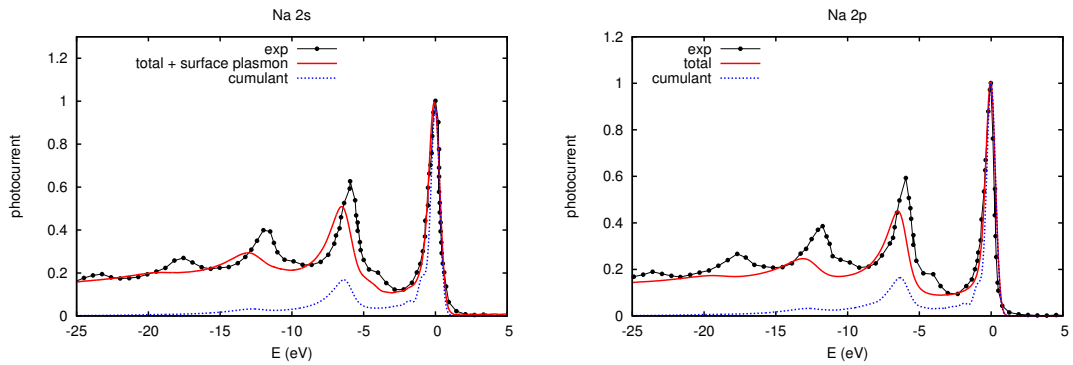
Figure 6.2: Comparison of the experimental photoemission spectrum to the spectrum calculated using the TOC11 + extrinsic + interference approach: Left, Na $2s$; right: Na $2p$. The red solid lines are total calculations, including secondary electron background, black with circles are experimental data [47], and blue dashed are calculated TOC11 intrinsic spectral functions. The total Na $2s$ calculated spectrum also includes an approximation to the surface plasmon contribution. The spectra are angle-integrated. Original experimental data were in arbitrary units: here we have normalized them to the main-peak intensities. The calculated QP energies have been aligned with respect to the experimental QP peaks otherwise the GWA $2s$ level is too deep by about 5 eV, and the $2p$ level by about 3 eV (see table 2.1). The zero of the energy axis is set to be the QP energy of the experiment. Gaussian broadening of 0.3 eV has been used in all calculated spectra. The extrinsic and interference effects have been calculated by my co-author J. Kas and J. Rehr in Ref. [20].

should correspond to the measurable one in order to obtain the correct spectra, this should lead to an error in the satellite positions.

A similar overestimation of the RPA plasmon energy in sodium was also observed in Ref. [94] where the authors showed that the time-dependent local-density approximation (TDLDA) plus the quasi-particle lifetime effects will yield a better description of the dynamical structure factor for sodium when comparing to the experimental result. Later I will show the calculation of W using the TDLDA and discuss the difference in the plasmon energy with respect to the RPA one.

In order to verify the convergence of the multipole sampling, the TOC11 spectra of sodium $2s$ at the Γ point using different numbers of sampling poles ($N^< =1$, 5, 150 and 200) is shown in Fig. 6.3 with the corresponding $\text{Im}\,\Sigma$ (only lesser part is shown). If we use only one pole to sample $\text{Im}\,\Sigma$, we find a larger plasmon satellite energy (≈ 7.6 eV) compared to the distance between the QP energy and the peak in $\text{Im}\,\Sigma$ (i.e. ≈ 6 eV)[5]. When we increase the number of poles to $N = 5$ (green curves), we have more structures in the cumulant spectra but compared to the pole in $\text{Im}\,\Sigma$, apparently 5 poles are still not enough because the satellite in the broadened spectrum (green curve with up-triangles) is not at the position where $\text{Im}\,\Sigma^<$ has a peak. The cumulant spectrum with 150 poles (red curves) gives the first satellite almost at the same position as the pole in $\text{Im}\,\Sigma$, reflecting the fact that convergence of the number of poles to sample $\text{Im}\,\Sigma^<$ has been achieved. The spectrum with 200 poles (black diamonds) is nearly identical to the spectrum using 150 poles, which confirms the convergence of 150 poles. However, there are small shoulders on the left hand side of the QP peak in both spectra of 150 and 200 poles. Those shoulders are induced by the present *equal-area* multipole sampling algorithm and it can be improved by the *equal-space* sampling algorithm[6].

6.1.2 The TOC11 in sodium valence

The TOC11 overestimates the plasmon satellite energy by about 0.5 eV in the sodium core levels. What about the sodium valence where the TOC11 is supposed to be less precise? The traditional time-ordered cumulant (TOC96 and TOC11) faces its challenge in the sodium

---

[5]This is because the one pole will be placed at the center of mass of $\text{Im}\,\Sigma$ that has more weight on the higher energy side than the lower energy side as shown by the blue curve with circles in Fig. 6.3. As a consequence the center of mass of $\text{Im}\,\Sigma$ is shifted towards to the higher energy part with respect to the peak in $\text{Im}\,\Sigma$, leading to a larger distance between the QP and satellites.

[6]The present sampling algorithm is called the *equal-area sampling*. It takes rectangles that have the same area under $\text{Im}\,\Sigma$. The final δ-function represents the area of each rectangle. As a consequence, this sampling method puts more points around the region where $\text{Im}\,\Sigma$ has a peak, but less points in the region where $\text{Im}\,\Sigma$ is very flat (e.g. the region around the QP peak). Therefore although the spectrum is converged to the 150 poles sampling, there are only a few poles at the energies close to the QP peak. These few poles yield the spurious structures as shown on the left hand side of the QP peak in the final broadened spectrum (the red curve with up-triangles in Fig. 6.3). We have changed the sampling algorithm in the cumulant code such that the artificial shoulders in the CEA spectral functions can be eliminated using the so-called *equal-space* sampling. The equal-space sampling distributes the poles with the same density for the whole region of $\text{Im}\,\Sigma$. However, unfortunately there are other issues about the equal-space sampling algorithm left to be studied in detail, so an improved version of the cumulant code is not ready to be shown yet in the present thesis.
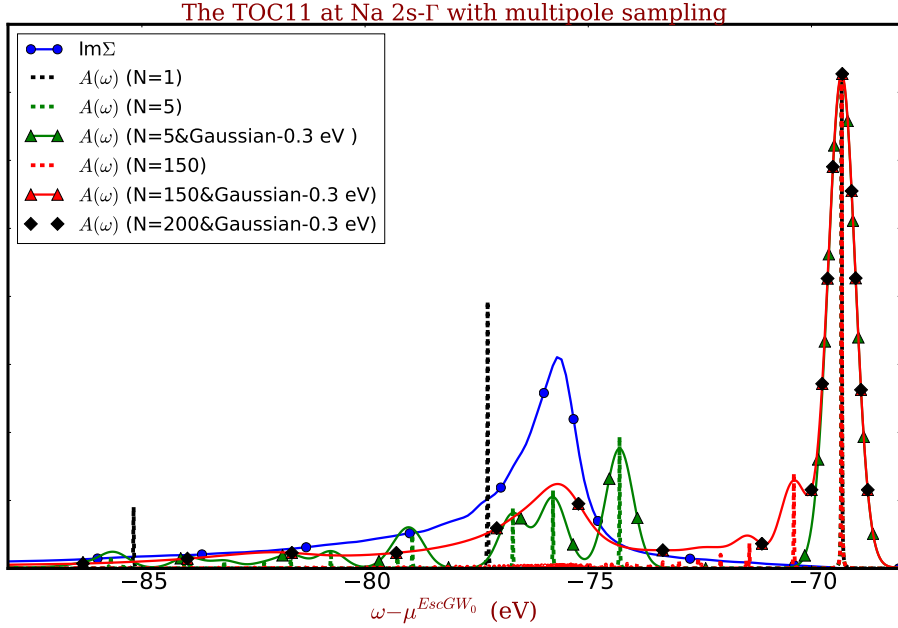
Figure 6.3: Cumulant intrinsic spectra of Na $2s$ Γ point with different number of poles in the sampling of $\mathrm{Im}\,\Sigma$ (only the lesser part is shown). The blue curve with circles is the imaginary part of the self-energy at Γ. The black, green and red dashed curves are the cumulant spectra calculated from 1, 5 and 150 poles of sampling, respectively. The green and red lines with up-triangles are the cumulant spectra with 5 and 150 poles sampling and a 0.3 eV Gaussian broadening. The black diamonds are the spectrum calculated using 200 poles which is on top of the spectrum using 150 poles. The zero of the energy axis is set to be the EsGW_0 Fermi energy.

valence due to the separation of the `electron` and `hole` branches as we have discussed before. The sodium valence band has a strong dispersion and even crosses the Fermi level as shown in the band structure in Fig. 2.1, which reflects the strong interaction between the states below and above the Fermi level in this band. However, it has be shown in Ref. [9] that even in sodium valence, the TOC96 gave a pretty good photoemission spectrum. To verify the performance of the traditional time-ordered cumulant in a situation like sodium valence where the interaction between orbitals is strong, I will show a calculation of the sodium valence using the TOC11. Again I start from the random-phase approximation of the screened Coulomb interaction W.

Screening from the random phase approximation

The TOC11 and EscGW$_0$ intrinsic spectral functions of sodium $3s$ at the Γ point are shown in Fig. 6.4. The EscGW$_0$ spectrum (blue curve with circles) is the same as the one in Fig. 2.6 which is calculated using the RPA W. The red curve with up-triangles and the black curve are the spectral functions calculated using the TOC11 and the TOC96 (see also Fig. 2.9) reproduced from the Ref. [9]. The agreement between the TOC11 and TOC96 is very good, which is consistent with our study in the hole-plasmon coupling model Hamiltonians[7].
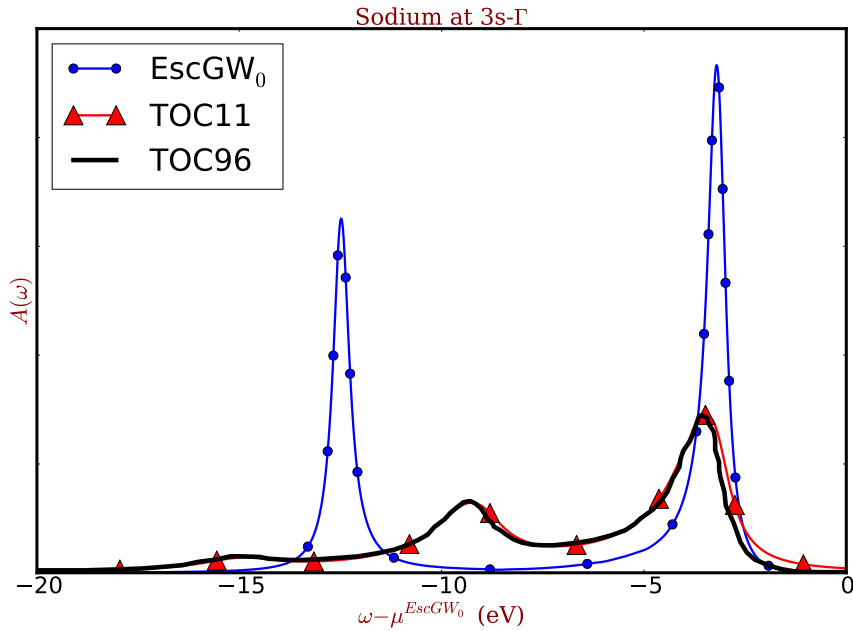

Figure 6.4: Intrinsic spectra of Na $3s$ at the Γ point. The blue curve with circles, red curve with up-triangles and black curve are intrinsic spectra of the EscGW$_0$, TOC11 and TOC96 (reproduced from Ref. [9]), respectively. The zero of the energy axis is set to be the EsGW$_0$ Fermi energy. The is no additional broadening of spectra in this plot. The QP weight of the TOC96 has been aligned according to the QP weight of the TOC11 for good comparison.

The comparison of the experimental photoemission spectrum (black curve with circles reproduced from Ref. [28]) to the spectrum calculated using cumulant+extrinsic+interference

---

[7]Since the spectrum of the TOC96 is reproduced from Ref. [9], I have aligned the weight of the QP peak according to the QP peak of the TOC11 to have a good comparison. But I did not shift the QP energy in Fig. 6.4. The important phenomena in that figure is that the ratio between the weight of the QP peak and satellites are the same between the TOC96 and the TOC11, which is consistent with our analysis in the hole-plasmon coupling model Hamiltonians in section 4.2. Later I will show my own calculation in sodium valence using the TOC11 and TOC96 to confirm this point.

approach (red curve) is shown in Fig. 6.5 where the intrinsic cumulant spectrum is also provided by the blue dashed curve. Similar to the core spectrum as shown in Fig. 6.2, an overestimated plasmon satellite energy is observed as well in the valence band TOC11 calculation and this discrepancy is two-times larger (≈ 1 eV) than for the core states. Besides the error induced by the RPA W, this can be understood by the fact that the traditional time-ordered cumulants have decoupled the electron and hole branches and this separation is better justified in the core than in the valence. The former error is hoped to be corrected by the use of a better W that is close to the measured W, instead of the RPA one, and the latter error might be reduced by the constrained retarded cumulant as discussed in section 5.3.2.

Moreover, the ratio between the QP peak and the satellites in TOC11 is overestimated in both core and valence compared to the experimental spectrum[8]. Similar to the plasmon energy, this discrepancy is also larger in the valence than in the core. The constrained retarded cumulant is designed to enhance the plasmon satellites compared to the traditional time-ordered cumulant. Therefore, we do need the constrained retarded cumulant to have a better description of the sodium valence photoemission spectrum. The calculation of constrained retarded cumulant in sodium valence will be provided in section 6.2.

6.1.3 The TOC96 using RPA screening

We have studied the performance of the TOC11 in sodium valence and core photoemission spectra by comparing to the experiment. Some disagreements between the calculated and experimental spectra have been discussed, in particular the TOC11 overestimates the plasmon satellite energy and the ratio between the weight of the QP and plasmon peaks using

---

[8]The weight ratios between the QP peak and the first satellite in the experiment shown in Figs. 6.2 and 6.5 are about 1/0.6, 1/0.6 and 1/0.9 for sodium $2s$, $2p$ and $3s$, respectively. The calculated TOC11+extrinsic+interference effects spectra show a slightly different weight ratio between the core and the valence: $\approx 1/0.5$ for the core and $\approx 1/0.6$ for the valence, but not enough. The calculated intrinsic spectra in the same figures show the same ratio for all the states, which is about 1/0.2. In this sense, we could think the calculated intrinsic valence spectrum should have a smaller weight ratio than the core spectrum to make the cumulant+extrinsic+interference valence spectrum closer to the experimental one. This is indeed given by the CRC but not the TOCs. However, this is just our rough estimation. The real weight ratio between the QP and satellites are far more complicated due to the extrinsic and interference effects. In addition, even the (intrinsic) **Z**-factor is difficult to deduce from theory and experiment. As can be seen from the right panel of Fig. 1.5 (the weight ratio between QP and satellite links to the momentum distribution), there is some discrepancy even between the quantum Monte-Carlo and experimental results.
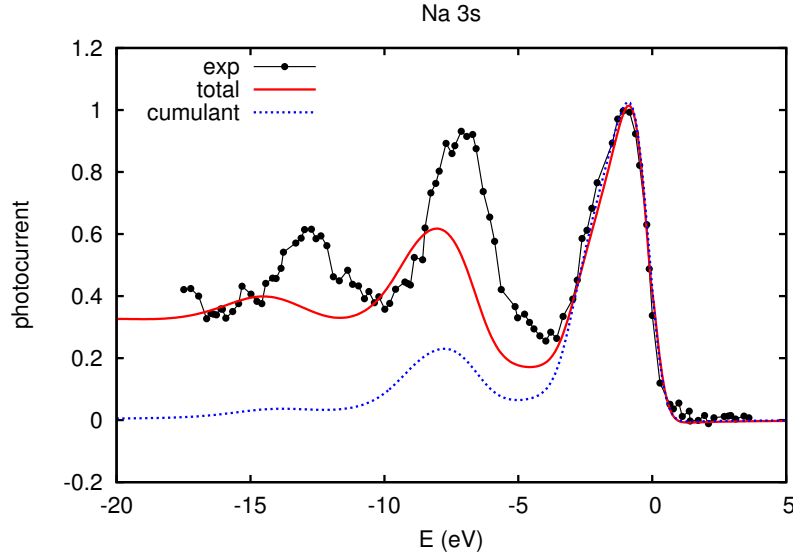
Figure 6.5: Comparison of the experimental photoemission spectrum to the spectrum calculated using the TOC11 + extrinsic + interference approach: valence band. Red solid is total calculation, including a secondary electron background, black with circles is experiment [28], and blue dashed is the intrinsic TOC11 spectral function. The spectra are angle-integrated. Original experimental data were in arbitrary units: here we have normalized them to the main-peak intensities. All the calculated spectra have been Gaussian broadened with 0.3 eV and the QP peak is shifted to the experimental value, otherwise the GWA $3s$ level is too deep by about 0.5 eV.

the RPA W. The discrepancy is larger in the sodium valence than the core. Here I will show the comparison of the spectra calculated using the TOC96 and TOC11 in sodium valence to verify the results we have gotten from the hole-plasmon coupling model Hamiltonian study. Note that we should not expect that the TOC96 improves over the TOC11 spectrum because they are only different in the **Z**-factor.

The sodium valence spectrum at the Γ point is shown in the left panel of Fig. 6.6. As we expected, the TOC96 spectrum (red curve) has smaller weights on all the peaks than the TOC11 spectrum (black curve). However, the difference is very small. If we multiply the spectrum of the TOC11 by $e^{-\beta^>}$ (where $\beta^>$ comes from the sampling of $\Sigma^>$ as shown in Eq. (5.33)), the resulting spectrum (green diamonds) is identical to the TOC96. This verifies our conclusion that the weight ratio between the QP and satellites is indeed the same for the TOC96 and TOC11.
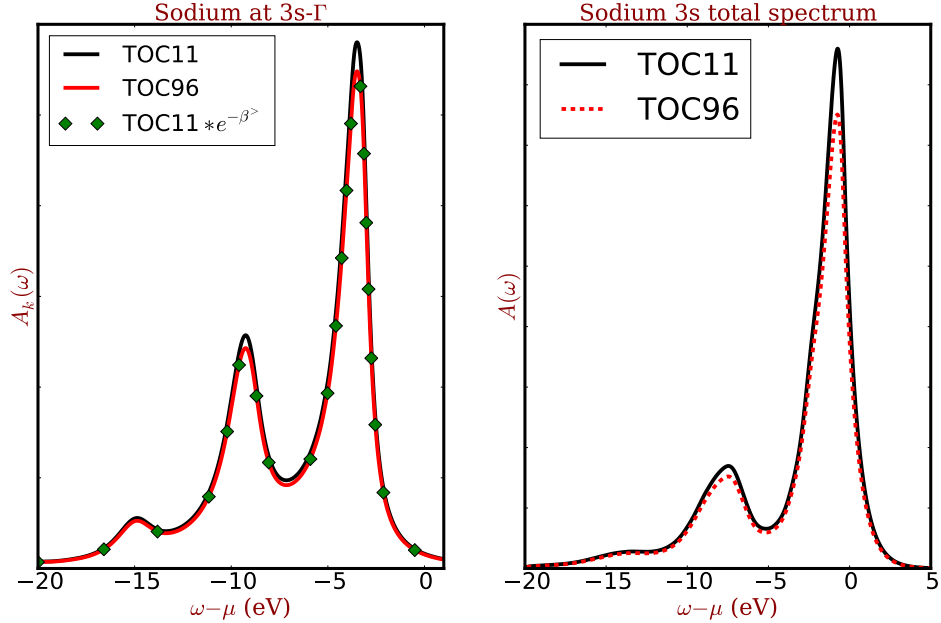
Figure 6.6: Intrinsic spectra of Na $3s$. Left panel: *k-resolved* spectrum at the Γ point. Right panel: total *k-summed* spectrum. The black and red curves (red dashed in the right panel) are the spectra of the TOC11 and TOC96, respectively. The green diamonds in the left panel shows $A^{C11}e^{-\beta^>}$ that is supposed to be the same as A^{C96} from our derivation. Our cumulant code gives indeed what we have expected in sodium valence calculation. The plots in the right panel have Gaussian broadening of 0.3 eV because they are the k-summed total spectra.

The total *k-summed* photoemission spectra are provided in the right panel of Fig. 6.6. A systematic decrease of weights is observed in the TOC96 compared to the TOC11. Therefore, if we had used this TOC96 spectrum to compare to the experimental spectrum in Fig. 6.5, it would for sure yield the same conclusion since we need anyway to align weight of the QP peak for comparison with experiment.

6.2 Sodium valence photoemission spectrum from the constrained retarded cumulant

In the previous section, I have shown the calculated photoemission spectra using the traditional time-ordered cumulants. We do see that the TOC11 and TOC96 spectra become worse when going from sodium core to valence, in particular the overestimation of the plas-

mon satellite energy and weight ratio between the QP and plasmon peaks become larger. I have predicted the effects of the constrained retarded cumulant in valence photoemission in section 5.3.2: we expect some enhancement of the plasmon satellites, and because this enhancement should be larger for the states close to the Fermi level, the plasmon satellites might shift towards to the QP peak. In order to see if the constrained retarded cumulant can indeed correct the discrepancies between the time-ordered cumulants and the experimental spectra, in this section I am going to use the constrained retarded cumulant in Eqs. (5.34) and (5.36) to calculate the sodium valence photoemission spectra and compare to the spectra of the TOC96 and TOC11.
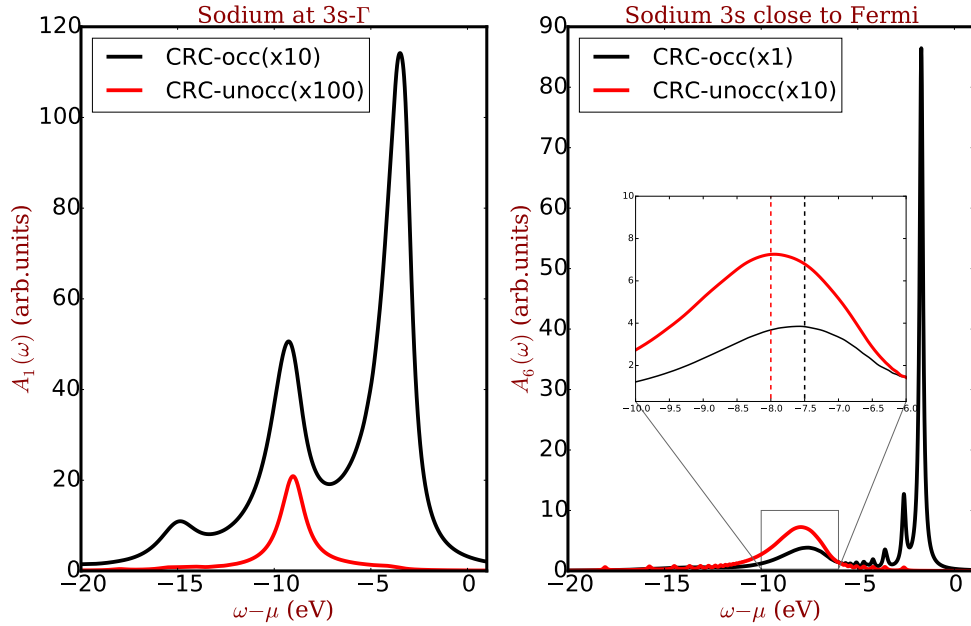
Figure 6.7: Intrinsic *k-resolved* spectra of Na 3*s*. Left panel: $A_{k,<}^{occ}$ in Eq. (5.34) (black curve) and $A_{k,<}^{unocc}$ in Eq. (5.36) where $k_1 = [0,0,0]$, i.e. the Γ point. Right panel: $A_{k,<}^{occ}$ in Eq. (5.34) (black curve) and $A_{k,<}^{unocc}$ in Eq. (5.36) where $k_6 = [0.3125, 0, 0]$, i.e. a state closer to the Fermi than Γ. All the spectra have been scaled (the $\times$ numbers in the legend) in order to have a better comparison. The insert plots in the right panel show the ≈ 0.5 eV discrepancy between the satellites of the $A_{k,<}^{occ}$ and $A_{k,<}^{unocc}$.

We first have a look at the *k-resolved* spectral functions calculated using the CRC in Fig. 6.7. The CRC spectral functions of two k-points are shown in that figure. The left panel is the spectral function at Γ which corresponds to the bottom valence state. The black curve

shows the spectral function $A_{k1,<}^{occ}$ in Eq. (5.34) which is the same as the TOC96. The red curve is the spectral function $A_{k1,<}^{unocc}$ in Eq. (5.36) that is the missing term in the TOC96. It does not have a QP peak but only satellites which are at the same energy as the satellites of $A_{k1,<}^{occ}$. Note that all the spectral functions have been scaled by the numbers shown in the legend. At the Γ-point, the first satellite of $A_{k1,<}^{unocc}$ has a hight ≈ 0.2 in the unit defined in that figure[9].

The right panel shows the same spectra as the left panel in Fig. 6.7, but at $k_6 = [0.3125, 0, 0]$[10] in the Brillouin zone. This is a state close to the Fermi level, as can be seen from its quasi-particle energy. The QP peak is much sharper and stronger than the QP peak at Γ. The small peaks on the left hand side of the QP in $A_{k6,<}^{occ}$ are the spurious structures[11] induced by the *equal-area* sampling algorithm that has been discussed in Fig. 6.3. The first satellite of $A_{k6,<}^{unocc}$ is stronger[12] than the satellite of $A_{k1,<}^{unocc}$ (note the scaling factor). This is consistent with my analysis in section 5.3.2, i.e. the closer the states to the Fermi, the larger the satellite weight in $A_{k,<}^{unocc}$. In order to confirm this point, the imaginary part of the GW self-energy at these two k points is provided in Fig. 6.8. The black curve shows $\text{Im} \Sigma_{k1}$ that has one sharp peak below Fermi and a very weak and broadened peak above Fermi. This leads to a large value of $\beta_{k1}^<$ but small value of $\beta_{k1}^>$ in Eq. (5.33). The satellite weight in $A_{k1,<}^{unocc}$ is determined by the value of $\beta_{k1}^>$. On the other hand, the two peaks in $\text{Im} \Sigma_{k6}$ are more similar, yielding similar $\beta_{k6}^<$ and $\beta_{k6}^>$. This explains why the first satellites of $A_{k6,<}^{occ}$ and $A_{k6,<}^{unocc}$ have much closer weight than the satellites at Γ[13] as shown in the left panel of Fig. 6.7.

Everything seems to be going into the correct direction because the CRC does enhance the plasmon satellites and as what we have expected, the enhancement is stronger when closer to the Fermi. Now it is the time to have a look at the total intrinsic photoemission

---

[9]All the weights can be considered to correspond to $A_{k6,<}^{occ}$ in the left panel of Fig. 6.7 because this is the only one I did not scale.

[10]The k points are defined in terms of the reciprocal space primitive translations (NOT in Cartesian coordinates!).

[11]They should merge to give the total QP broadening as discussed in the footnote 18 in section 5.3.2.

[12]Note that in Fig. 6.7, the weights of different k-points are not taken into account. In practice, there is no equivalent k-point to Γ but there are many equivalent k-points to $k6$. As a consequence, the contribution of A_{k6}^{unocc} to the total k-summed spectra is much larger than A_{k1}^{unocc}.

[13]The ratio of these two satellites equals $\frac{\beta_{k6}^<}{\beta_{k6}^>}$.
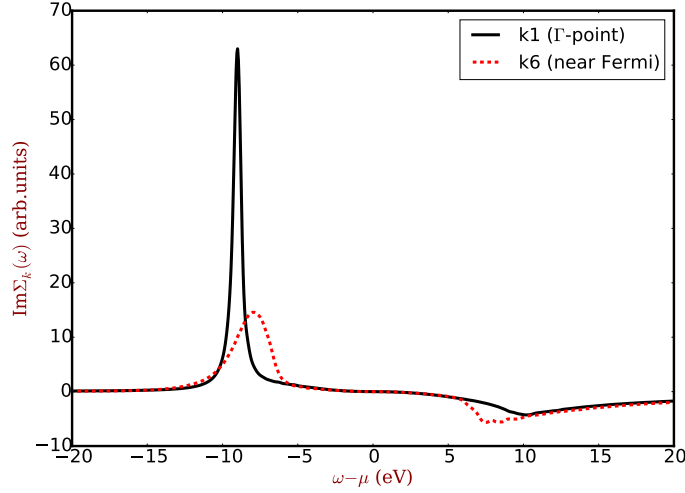
Figure 6.8: The imaginary part of the GW self-energy $\text{Im}\,\Sigma$ at $k_1 = [0, 0, 0]$, i.e. Γ point (black curve) and at $k_6 = [0.3125, 0, 0]$, i.e. a state closer to the Fermi than Γ.

spectra of sodium valence as shown in Fig. 6.9. The black and red dashed curves are the TOC11 and TOC96 spectra, respectively. They have been discussed in Fig. 6.5. The CRC spectrum is shown as purple line with circles. It has the same QP peak as the TOC96 and larger weight on the plasmon satellites, as what we have expected. However, the plasmon satellite peak is centered at almost the same energy as the TOC96 and TOC11. Thus the CRC also overestimates its position by ≈ 1 eV in sodium valence using the RPA-W with respect to the experiment.

What has gone wrong? Why did the result not meet our expectations?

- On one hand, the right panel of Fig. 6.7 (see the insert of that figure) shows that the first satellite in $A_{k6,<}^{unocc}$ is not exactly at the same position as the satellite in $A_{k6,<}^{occ}$. It gives more weight to the left hand side of the satellite. This is not what we want. This discrepancy is ≈ 0.5 eV, which is of the order of magnitude of the value we want to correct in sodium valence using the CRC with respect to the TOC11 or TOC96. This phenomena might come from the approximation I have used when going from $\tilde{A}_{k,<}^{unocc}$ in Eq. (5.35) to $A_{k,<}^{unocc}$ in Eq. (5.36), i.e. the use of an average (constant) $b_i = \beta^>/N^<$.

169
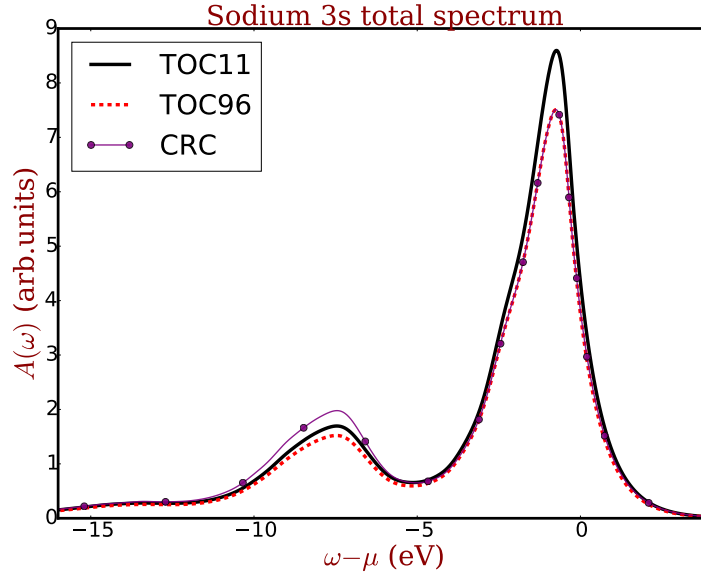
Figure 6.9: Intrinsic total *k-summed* spectra of Na 3*s*. Gaussian broadening of 0.3 eV has been used in all plots. The black, red dashed and purple line with circles are the calculated spectra using the TOC11, TOC96 and CRC, respectively.

- On the other hand, for example, since the QP peak of $A^{occ}_{k6,<}$ in Fig. 6.7 is so strong and sharp, the QP of the total k-summed spectrum might be centered in the QP energy of $A^{occ}_{k6,<}$. However the first satellite of $A^{occ}_{k6,<}$ is relatively small and broadened, hence its contribution to the first satellite of the total spectrum might be also relatively small. The first satellite of the total spectrum might be centered somewhere else. As a consequence, the distance between the QP and the first satellite does not equal the distance in $A^{occ}_{k6,<}$. The promising results of our model study are hence not sufficient to improve the results of a real metal.

In conclusion, the constrained retarded cumulant improves the valence photoemission by enhancing the weight of the plasmon satellites. This effect might be considered to be not so important in the photoemission spectrum, however the correct distribution of the spectral weight is important in the total energies. The study about the total energies will be shown in Chapter 7. However, the overestimation of the distance of the satellite from the QP using the CEA and RPA W is still not solved.

6.3 The screening beyond the random phase approximation

In order to investigate another possible origin of this discrepancy, in this section I will show results using more advanced calculations of W beyond the RPA. The definitions of screened Coulomb interactions using different approximations are provided in Appendix Eq. (C.20). The ideas of this section is as follows:

- First we would like to try a more realistic measurable screening than the RPA one by performing a time-dependent local-density (TDLDA) calculation. I have mentioned in section 6.1 that in Ref. [94], the authors have found that a TDLDA calculation using the test-charge test-charge (TCTC) dielectric function improves the description of the sodium plasmon energy for large wavevector q (mixing transitions that occur between different k points). TDLDA corrected the plasmon energy by about 50% compared to the experimental result. This suggests to first try to calculate the photoemission spectrum using the TCTC dielectric function from a TDLDA calculation.

- Moreover, our derivation in the Appendix C shows that for a systematic improvement of the CEA, one has to use the test-charge test-electron (TCTE) dielectric function. The idea of using the TCTE screened Coulomb interaction has been introduced in section 2.2 when I discussed the physical ingredients in Hedin's equations following Ref. [55].

Therefore, the TCTC and TCTE screening Coulomb interactions will be explored in the following to study the plasmon satellites in sodium. In section 2.2 I have shown that the plasmons stem from the zero of the real part of the dielectric function, i.e. $\epsilon_1(\omega) = 0$. The plasmon energy shows up as a peak in $-\operatorname{Im} \epsilon^{-1}$, and therefore in $\operatorname{Im} W(\omega)$ and in $\operatorname{Im} \Sigma(\omega)$. This suggests to have a detailed study of the imaginary part of the GW self-energy using different screened Coulomb interactions. The $\operatorname{Im} \Sigma(\omega)$ for sodium $2s$ at the Γ point $k = [0, 0, 0]$ in the Brillouin zone is shown in Fig. 6.10.

Since the spectra of the two core states are similar and they almost do not disperse, only the $\operatorname{Im} \Sigma$ of sodium $2s$ at the Γ point is shown in Fig. 6.10. As discussed in section 6.1, the overestimation of the plasmon satellite energy in the sodium core could be mainly
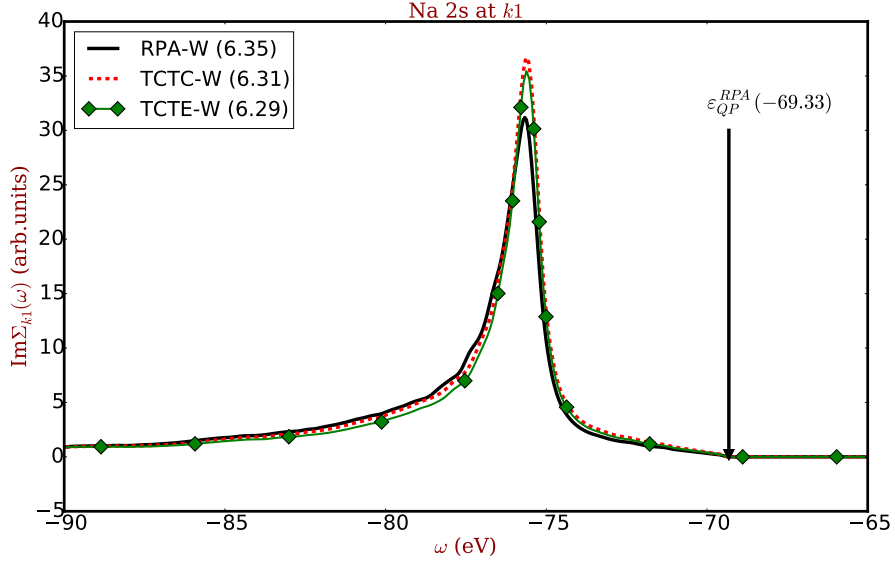
Figure 6.10: The imaginary part of the GW self-energy using the dynamically screened Coulomb interactions in the RPA (black curve) Eq. (C.20a), the TCTC dielectric function (red dashed curve) Eq. (C.20b), and the TCTE dielectric function (green curve with diamonds) Eq. (C.20c). All the plots have been aligned according to the quasi-particle energy calculated using the RPA W as indicated by the black arrow labeled " ε_{QP}^{RPA} ", for good comparison. The real QP energies for the RPA, TCTC, and TCTE are -69.33, -68.74, and -69.82 eV, respectively. The numbers in the legend represent the distance between the QP peak and the peak in Im Σ for different approximations. The experimental distance between the QP and the first satellite of sodium $2s$ in Fig. 6.2 (i.e. from the experiment in Ref. [47]) is ≈ 5.9 eV.

due to the use of the RPA W. The black curve confirms our analysis, because Im Σ using the RPA W shows up as a peak at a distance of 6.35 eV with respect to the QP peak. This distance is about 0.45 eV larger than the distance measured in the experiment in Ref. [47], which is consistent with the conclusion we found in Fig. 6.2. All the cumulant expansion approximations are indeed, reproducing the peak of Im Σ. The results using the TCTC W in Eq. (C.20b) and the TCTE W in Eq. (C.20c) are shown by the red dashed curve and green curve with diamonds, respectively. Both show indeed some improvement with respect to the RPA. However, the effects are small. The largest improvement comes from the TCTE W, consistent with our derivation in Appendix C: it reduces the distance between the QP and the peak in Im Σ by about 0.06 eV for the sodium 2s state, which corresponds to 13% of the error.

The distance between the QP and the peak in $\text{Im}\,\Sigma$ for the sodium valence is shown in Fig. 6.11. Since the sodium valence band has a strong dispersion as shown in the band structure in Fig. 2.1, I have chosen the 8 k-points along the Γ-H path. The three calculated Ws lead to a systematic increase of the distance between the QP and the peak in $\text{Im}\,\Sigma$ when the states get closer to the Fermi level. The RPA gives the largest value for this distance, reflecting its bad performance in the spectrum. The TCTC and TCTE Ws show systematic improvements, but not enough to correct the ≈ 1 eV discrepancy with respect to the experiment.
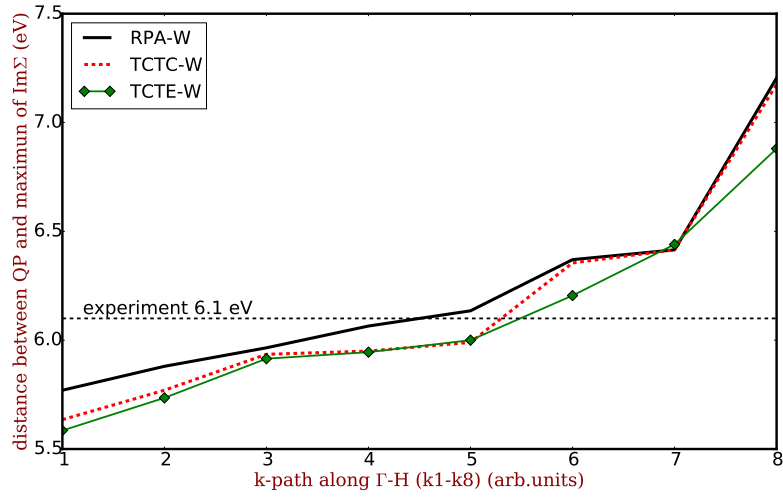
Figure 6.11: The distance between the QP and the peak in $\text{Im}\,\Sigma$ for the sodium valence. The horizontal axis shows the k-points along the Γ-H path (see the sodium band structure in Fig. 2.1) in the first Brillouin zone. As in Fig. 6.10, the black solid curve, red dashed curve, and green line with diamonds are the results using the RPA, TCTC, and TCTE screenings, respectively. The black dashed horizontal curve represents the distance between the QP and first satellite in the experimental spectrum in Ref. [28].

It is disappointing that the TDLDA has such a small effect in $\text{Im}\,\Sigma$ with respect to the RPA. We deduce that the small q vectors dominate in the GW self-energy since the screening W is summed over all the q vectors in the self-energy. The TDLDA kernel $f_{xc}^{LDA} = \dfrac{\delta V_{xc}^{LDA}}{\delta \rho}$ [96] is constant in q, and it is added to the Coulomb interaction $\dfrac{4\pi}{q^2}$ when calculating the dielectric function, i.e. $\epsilon^{-1} = 1 + (v_c + f_{xc})\chi$ [97], such that it has no effect at small q.

The TCTE is better than the RPA or the TCTC results, but since it also uses the same TDLDA kernel f_{xc}^{LDA} the improvement is not sufficient. This suggests that improving the effective TCTE screened Coulomb interaction is important, and one should go beyond TDLDA.

Finally the comparison of the k-summed CRC spectra using the RPA and TCTE Ws is shown in Fig. 6.12. The distance between the QP and satellite using the TCTE screening (green line with diamonds) indeed decreases (the center of mass has shifted towards to the QP peak) compared to the RPA one (black line with circles). However this improvement is not sufficient to correct the discrepancy with respect to the experimental spectrum. As discussed above, we should search for better effective screened interactions including vertex corrections in the future.
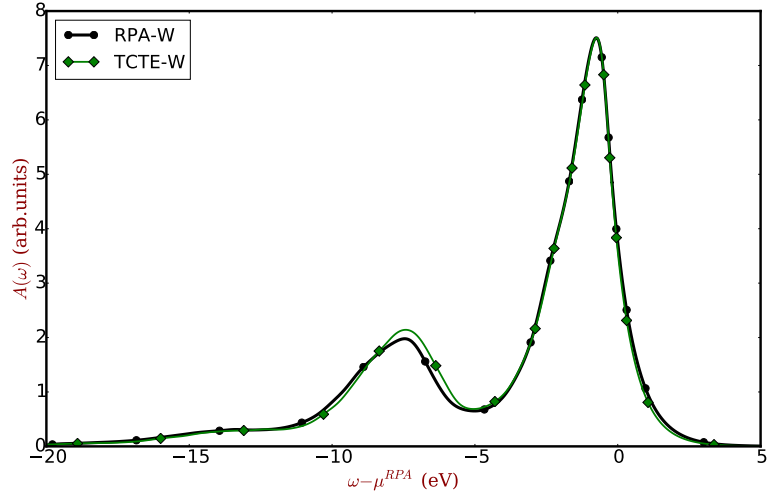
Figure 6.12: The CRC total intrinsic spectra using the RPA (black curve with circles) and TCTE (green curve with diamonds) screening.

6.4   Computational details

The results for the electron removal spectrum of bulk sodium have been obtained with *ab initio* calculations using a plane wave basis and pseudopotentials as implemented in the ABINIT code [43]. Calculations have been performed for the experimental sodium crystal structure at temperature T=5 K [98]. The lattice constant is taken to be 4.225 angstrom. I

have used a sodium Troullier-Martins-type pseudopotential [99] with core and valence states (2s, 2p and 3s) [100]. The Brillouin zone (BZ) of sodium was sampled using a $16\times16\times16$ grid mesh that yields 145 inequivalent k-points in the irreducible Brillouin zone (IBZ), and a smearing temperature of 0.01 Ha was used. This is a fictitious temperature that only serves as a computational trick to speed up the k-point convergence, which explains why I can still use a standard time-ordered formalism for the time-ordered cumulants. I have checked that our results are not biased by the value of the temperature.

The plane-wave cutoff of the LDA ground-state calculation was 200 Hartree. I have used the same RPA screening W_0 for both one shot (G_0W_0) and energy-self-consistent (EscGW$_0$) calculations with 40 bands, 100 plane waves representing the wave functions and the dielectric matrix. Note that the update of the energies can be expected to be the most important contribution to self-consistency in sodium valence because it is close to the homogeneous electron gas. For the core states, we will investigate the effect of updating also wavefunctions in the future. The full frequency dependence of the self-energy was calculated using a contour-deformation technique. We calculated the screening using 100 frequencies on the real axis up to an energy of 25 eV and 10 frequencies on the imaginary axis. The final self-energy converged to 60 bands, 9000 plane waves for both wave functions and the exchange term.

The spectra of the cumulant expansion approximations are calculated using our local *cumulant code*. The cumulant code takes the outputs of the GW calculation from the ABINIT code. In particular, we evaluate Eq. (5.34) for the TOC96, and Eq. (6.1) for the TOC11 using 150 poles in the sampling of ImΣ. The constrained retarded cumulant Green's function in Eqs. (5.34) and (5.36) are evaluated in our cumulant code using 150 poles sampling Im$\Sigma^<$ and 1 pole sampling Im$\Sigma^>$.

6.5 Summary

In this chapter, the photoemission spectra of bulk sodium valence and core from the cumulant expansion approximations, using our local *cumulant code* have been shown, as well as the comparison to the experimental spectra. This simple metal has been extensively

studied, and in particular, it has been shown [9, 79] that the GW approximation does not yield the experimentally observed plasmon satellite series, whereas the cumulant expansion approximation does [9]. However these studies were limited to the valence band, and even there, a more detailed analysis was still missing. Here I provide this analysis, pointing out the role of a spurious plasmaron in the bad performance of the GWA. Moreover, I include the sodium core states ($2s$ and $2p$) in the calculation, thus treating valence and core on the same footing.

The traditional time-ordered cumulants using the random phase approximation of the dynamically screened Coulomb interaction W (RPA W) overestimate the energy of the plasmon satellites, and the weight ratio between the quasi-particle and satellite peaks. The constrained retarded cumulant enhances the weights of satellites in sodium valence such that it improves the valence photoemission with respect to the traditional time-ordered cumulants. However the constrained retarded cumulant gives almost the same overestimation of the energy of satellites when using the RPA W.

In order to find out the origin of the discrepancy between the calculated and experimental spectra, better screened Coulomb interactions W have been studied. In particular the test-charge test-charge (TCTC) and the test-charge test-electron (TCTE) W in the TDLDA are studied. The improvements with respect to the RPA W are systematic, but only about 10-15 % of the error is corrected. Since TDLDA is a quite rough approximation, the systematic improvement is however encouraging further studies concerning effective screened interactions including vertex corrections.

Chapter 7

The total energies

The previous chapters were all dealing with the spectral function (hence the Green's function) because its direct link with the measured photocurrent from photoemission experiment. Besides the photoemission spectrum, the Green's function, however, also provides total energies, as already mentioned in section 1.2.1. It is possible to calculate the ground state total energy from the *Galitskii-Migdal formula* [38] when we have the Green's function of a many-body system. Therefore in this chapter, I am going to study the performance of the total energies in the one- and two-level hole-plasmon coupling Hamiltonians using the approximations I have discussed in this manuscript, i.e. the GW approximation and the cumulant expansion approximation.

Unlike the spectral functions where the position of each peak is important, the total energies depend on the moments (integrals) of the spectral function. Thus a combination of the position of the peaks and the weight distribution is important to describe well the total energies. For this reason, the improvement of the weights of quasi-particle and satellites in the constrained retarded cumulant will play a major role in the total energy calculation.

I will start from the derivation of the *Galitskii-Migdal total energy formula* (GMtot) from the exact electronic many-body Hamiltonian. This allows one to understand that the exact one-body Green's function is indeed able to provide the exact total energy. Then the total energies using the Galitskii-Migdal formula but different Green's functions (model exact, the GWA and the CEA) will be studied. As I will show, there is, however, a fundamental problem with the Galitskii-Migdal formula in our model system. In order to get a

better total energy of the hole-plasmon coupling Hamiltonian, which is an approximation to the exact many-body system, I have derived a new total energy formula that will be refereed to as the *hole-plasmon coupling total energy formula* (HPCtot). In the HPC-2, this new formula, different from the Galitskii-Migdal formula, improves the total energies using the Green's function calculated from the GW approximation or the cumulant expansion approximation.

At the end of this chapter, I will propose an implementation of the hole-plasmon coupling total energy formula using the constrained retarded cumulant Green's function for the calculation of real systems.

7.1 Total energies from the Galitskii-Migdal formula

The Galitskii-Migdal total energy formula [38] is derived from the ground state expectation value of a time-independent electronic many-body Hamiltonian. The Hamiltonian (the same as the equilibrium Hamiltonian in Eq. (B.1)) reads

$$\hat{H} = \int \mathrm{d}x \hat{\psi}^\dagger(x) \hat{h}_0(x) \hat{\psi}(x) + \frac{1}{2} \int \mathrm{d}x_1 x_2 \hat{\psi}^\dagger(x_1) \hat{\psi}^\dagger(x_2) v_c(x_1, x_2) \hat{\psi}(x_2) \hat{\psi}(x_1) = \hat{h} + \hat{v} . \quad (7.1)$$

The total energy of such a Hamiltonian can be calculated from its ground state expectation value, which reads

$$E_0 = \langle \Psi_0 | \hat{H} | \Psi_0 \rangle = \langle \Psi_0 | \hat{h} | \Psi_0 \rangle + \langle \Psi_0 | \hat{v} | \Psi_0 \rangle . \quad (7.2)$$

The ground state expectation value of the single particle part $\hat{h}$ reads

$$\langle \Psi_0 | \hat{h} | \Psi_0 \rangle = \int \mathrm{d}x \, \hat{h}_0(x) \langle \Psi_0 | \hat{\psi}^\dagger(x) \hat{\psi}(x) | \Psi_0 \rangle$$
$$= \int \mathrm{d}x \, \hat{h}_0(x) \lim_{t' \to t} e^{-iE_0(t-t')} \langle \Psi_0 | \hat{\psi}^\dagger(x) e^{-i\hat{H}(t-t')} \hat{\psi}(x) | \Psi_0 \rangle$$
$$= \int \mathrm{d}x \, \hat{h}_0(x) \lim_{t' \to t} \langle \Psi_0 | \hat{\psi}_H^\dagger(xt) \hat{\psi}_H(xt') | \Psi_0 \rangle = \int \mathrm{d}x \, \hat{h}_0(x) \big[-iG(xt, xt^+) \big] . \quad (7.3)$$

We have derived the equation-of-motion of the field operator in the Heisenberg picture in section B.1 (see Eq. (B.9)). It reads

$$i\frac{\partial\hat{\psi}_H(x,t)}{\partial t} = \hat{h}_0(x)\hat{\psi}_H(x,t) + \int \mathrm{d}y\left(\hat{\psi}_H^\dagger(y,t)v_c(y,x)\hat{\psi}_H(y,t)\hat{\psi}_H(x,t)\right). \qquad (7.4)$$

We now multiply by $\hat{\psi}_H^\dagger(x',t')$ on the left hand side of each term in the above equation and calculate the ground state expectation value, which yields

$$\left(i\frac{\partial}{\partial t} - \hat{h}_0(x)\right)\langle\Psi_0|\hat{\psi}_H^\dagger(x',t')\hat{\psi}_H(x,t)|\Psi_0\rangle$$
$$= \int \mathrm{d}y\,\langle\Psi_0|\hat{\psi}_H^\dagger(x',t')\hat{\psi}_H^\dagger(y,t)v_c(y,x)\hat{\psi}_H(y,t)\hat{\psi}_H(x,t)|\Psi_0\rangle . \qquad (7.5)$$

Taking the limit of $x' \to x$ and $t' \to t^+$, and integrating over x, the left hand side of the above equation contains the one-particle Green's function and the right hand side becomes the ground state expectation value of the Coulomb term, thus we have

$$\lim_{t'\to t^+} \int \mathrm{d}x\left(i\frac{\partial}{\partial t} - \hat{h}_0(x)\right)\left[-iG(xt,xt')\right] = 2\langle\Psi_0|\hat{v}|\Psi_0\rangle . \qquad (7.6)$$

Note that only the `hole` part of the one-particle Green's function appears in the above relation due to the specific time ordering, i.e. $t^+ > t$. Taking the above relation back to equation (7.2) and replacing the Coulomb contribution, we have the ground state energy reading as

$$E_0 = \frac{1}{2}\lim_{t'\to t^+} \int \mathrm{d}x\left(i\frac{\partial}{\partial t} - \hat{h}_0(x)\right)\left[-iG(xt,xt')\right] + \int \mathrm{d}x\hat{h}_0(x)\left[-iG(xt,xt^+)\right]$$
$$= -\frac{i}{2}\lim_{t'\to t^+} \int \mathrm{d}x\left(i\frac{\partial}{\partial t} + \hat{h}_0(x)\right)G(xt,xt') . \qquad (7.7)$$

The spectral representation of the `hole` part of the one-particle Green's function reads

$$G^h(x,x,\omega) = \int_{-\infty}^{\mu} \mathrm{d}\omega' \frac{A(x,x,\omega')}{\omega - \omega' - i\eta} . \qquad (7.8)$$

After Fourier transforming the above equation into time space, we have

$$
\begin{aligned}
G^h(x, x, \tau) &= \frac{1}{2\pi} \int d\omega \int_{-\infty}^{\mu} d\omega' \frac{A(x, x, \omega')}{\omega - \omega' - i\eta} e^{-i\omega\tau} \\
&= \frac{1}{2\pi} \int_{-\infty}^{\mu} d\omega' A(x, x, \omega') e^{-i\omega'\tau} \int d\omega \frac{e^{-i\omega''\tau}}{\omega'' - i\eta} \\
&= i\theta(-\tau) \int_{-\infty}^{\mu} d\omega' A(x, x, \omega') e^{-i\omega'\tau} ,
\end{aligned}
\tag{7.9}
$$

where $\tau = t - t^+$, then

$$
\begin{aligned}
E_0 &= \frac{1}{2} \int dx \left(i\frac{\partial}{\partial \tau} + \hat{h}_0(x) \right) \int_{-\infty}^{\mu} d\omega' A(x, x, \omega') e^{-i\omega'\tau} \\
&= \frac{1}{2} \int dx \int_{-\infty}^{\mu} d\omega' \left(\omega' + \hat{h}_0(x) \right) A(x, x, \omega') e^{-i\omega'\tau} \\
&= \frac{1}{2} \int dx \int_{-\infty}^{\mu} d\omega \left(\omega + \hat{h}_0(x) \right) A(x, x, \omega) .
\end{aligned}
\tag{7.10}
$$

Note that the integration over x contains the sum of all space $\boldsymbol{r}$ and spin σ. In `orbital` basis, the Galitskii-Migdal total energy formula reads

$$
E_0^{GM} = \frac{1}{2} \sum_k \int_{-\infty}^{\mu} d\omega \left(\omega + \hat{h}_k^0 \right) A_k(\omega) .
\tag{7.11}
$$

As we can see, the total energy is determined by the occupation numbers $n_k = \int_{-\infty}^{\mu} A_k(\omega) d\omega$ and the first moment[1] $\int_{-\infty}^{\mu} \omega A_k(\omega) d\omega$, where the details of the spectral function do not matter.

Since we will only work on the one electron case in the HPC-1 and HPC-2, we do not need to write the sum over the spin index. But in general, we should also have the sum over spin σ in the above equation[2]. Now we understand why the exact one-body Green's function yields the exact ground state energy of a many-body system from the Galitskii-Migdal formula in Eq. (7.11). This will be important later. In practice, it is impossible to find the exact one-body Green's function, instead, different approximate Green's functions

---

[1]Strictly speaking, the first moment is defined as $\int_{-\infty}^{\infty} \omega A_k(\omega) d\omega$. But for simplicity, we call the first moment of the hole contribution $\int_{-\infty}^{\mu} \omega A_k(\omega) d\omega$ also "simply" the first moment in this thesis.

[2]In a spin-independent system, each state k contains two electrons with spin up and down. Therefore the prefactor $1/2$ in the GMtot Eq. (7.11) will vanish.

(GWA or CEA) have been used in the Galitskii-Migdal formula to study the performance of the total energies. This is exactly what I am going to do in the following paragraphs of this section. However, as I will show at the end of this section, it is not always correct to study the total energies in such a way.

7.1.1 The GMtot in the HPC-1

In Chapter 4, I have already calculated all the spectral functions in the one-level hole-plasmon coupling Hamiltonian (HPC-1) including the exact model spectral function and all the CEAs in Eq. (4.12) (all the CEAs yield the exact spectral function), the G_0W_0 Eq. (4.36) and the EscGW$_0$ Eq. (4.42). Now we can plug these spectral functions into the Galitskii-Migdal formula in Eq. (7.11) to calculate the GMtot.

One can show analytically that all of these three spectral functions lead to the same GMtot, which is the exact ground state energy ε_0 (see Tab. 4.1 in section 4.1)[3], i.e

$$
\begin{aligned}
E_{GMtot}^{model} &= \frac{1}{2} \int_{-\infty}^{\mu} \mathrm{d}\omega \left(\omega + \hat{h}_0(x) \right) A^{model}(\omega) \\
&= \frac{1}{2} \sum_{m=0}^{\infty} \frac{\beta^m e^{-\beta}}{m!} \left(\varepsilon_0 + \frac{g^2}{\omega_p} - m\omega_p \right) + \frac{1}{2}\varepsilon_0 \\
&= \varepsilon_0 + \frac{g^2}{2\omega_p} - \frac{\omega_p}{2} \sum_{m=0}^{\infty} \frac{\beta^m e^{-\beta}}{m!} m \\
&= \varepsilon_0 + \frac{g^2}{2\omega_p} - \frac{\omega_p}{2} \beta \sum_{m=0}^{\infty} \frac{\beta^m e^{-\beta}}{m!} \\
&= \varepsilon_0 \,,
\end{aligned}
$$

and

$$
E_{GMtot}^{GW} = \frac{1}{2} \int_{-\infty}^{\mu} \mathrm{d}\omega \left(\omega + \hat{h}_0(x) \right) A^{GW}(\omega) = \frac{1}{2} \left(\varepsilon_0 + \int_{-\infty}^{\mu} \omega A^{GW}(\omega)\, \mathrm{d}\omega \right) = \varepsilon_0 \,,
$$

where A^{GW} can be the one of G_0W_0 in Eq. (4.36) or the EscGW$_0$ in Eq. (4.42).

---

[3]The chemical potential has been chosen just above the QP energy in each approximation in the HPC-1. In the HPC-2, the chemical potential stays between the QP energies of electron removal and electron addition.

As what we have expected, the GMtot yields the exact total energy using the exact spectral function of the HPC-1. Due to the simplicity of the HPC-1 , both G_0W_0 and $EscGW_0$ give the exact total energy from the Galitskii-Migdal formula as well, although the spectral functions look very different, since their occupation number (for the HPC-1, the occupation number is always 1) and first moment are correct.

7.1.2 The GMtot in the HPC-2

I have analyzed the exact ground state total energy of the HPC-2 in section 4.1.2, which is the lowest eigenenergy E_0^- from the numerical diagonalization of $\hat{H}^-$. In section 5.1 I have also shown an approximated fully analytical ground state energy in the second order of g (i.e. $E_0^{g^2}$) in Eq. (5.1) (see also its performance in Fig. 5.1). Similar to what I have found in the HPC-1, we would expect to get the exact total energy from the Galitskii-Migdal formula when we use the exact spectral functions of the HPC-2 in Eq. (4.29).

The GMtot using the exact spectral function of the HPC-2

Here I plug the exact spectral functions of Eq. (4.29) into the GMtot in Eq. (7.11) and calculate the GMtot separately in two parts namely E_{GMtot1} and E_{GMtot2}:

$$
\begin{aligned}
E_{GMtot1}^{model} &= \int_{-\infty}^{\mu} d\omega \left[\omega A_+^{model}(\omega) + \omega A_-^{model}(\omega) \right] \\
&= \sum_{m_-=0}^{\infty} \sum_{m_+=0}^{\infty} \frac{\tilde{\beta}_1^{[m_+]} e^{-\tilde{\beta}_1} v_{[2m_-]}^2}{m_+!} \left(E_0^- + \frac{g^2}{2\omega_p} - (m_+ + 2m_-)\omega_p \right) \\
&\quad + \sum_{m_-=0}^{\infty} \sum_{m_+=0}^{\infty} \frac{\tilde{\beta}_1^{[m_+]} e^{-\tilde{\beta}_1} v_{[2m_-+1]}^2}{m_+!} \left(E_0^- + \frac{g^2}{2\omega_p} - (m_+ + 2m_- + 1)\omega_p \right) \\
&= E_0^- - \omega_p \sum_{m_-=0}^{\infty} \left(v_{[2m_-]}^2(2m_-) + v_{[2m_-+1]}^2(2m_- + 1) \right); \quad\quad (7.12a) \\
E_{GMtot2}^{model} &= \int_{-\infty}^{\mu} d\omega \left[(\varepsilon_0 - \mathbf{t}) A_+^{model}(\omega) + (\varepsilon_0 + \mathbf{t}) A_-^{model}(\omega) \right] \\
&= \varepsilon_0 - \mathbf{t} \sum_{m_-=0}^{\infty} \sum_{m_+=0}^{\infty} \frac{\tilde{\beta}_1^{[m_+]} e^{-\tilde{\beta}_1} \left(v_{[2m_-]}^2 - v_{[2m_-+1]}^2 \right)}{m_+!} \\
&= \varepsilon_0 - \mathbf{t} \sum_{m_-=0}^{\infty} \left(v_{[2m_-]}^2 - v_{[2m_-+1]}^2 \right). \quad\quad (7.12b)
\end{aligned}
$$

183

The final Galitskii-Migdal total energy using the model exact spectral functions reads

$$E_{GMtot}^{model} = \frac{1}{2}\left(E_{GMtot1}^{model} + E_{GMtot2}^{model}\right).$$

(7.13)

It is difficult to see whether E_{GMtot}^{model} equals E_0^- or not from the above equation due to the numerical parameters. Thus we have to calculate E_{GMtot}^{model} numerically. The comparison with E_0^- is shown in Fig. 7.1. The numerical G_0W_0 and EscGW$_0$ GMtots in the HPC-2 are also shown in the same figure.
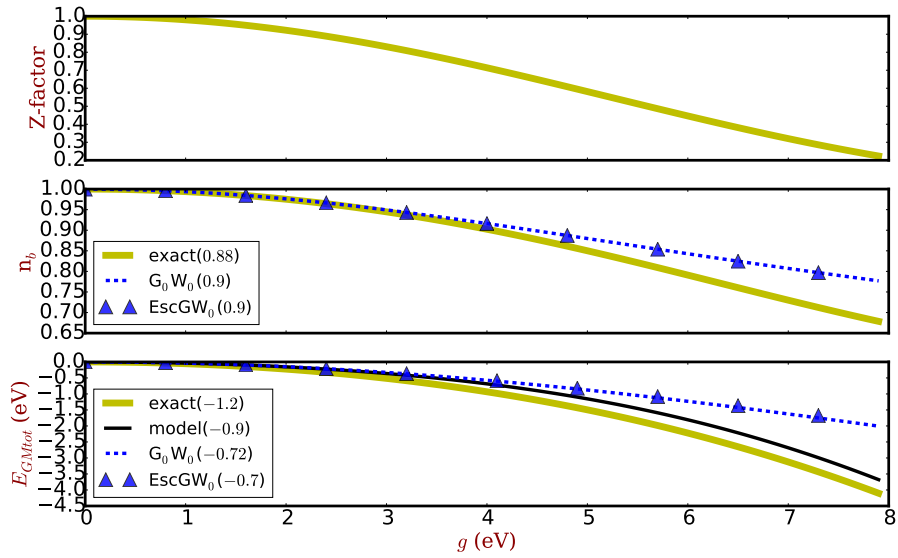
Figure 7.1: Results of Galitskii-Migdal total energies for the HPC-2 as function of coupling strength. Upper panel: the exact QP renormalization factor in Eq. (4.30). Middle panel: the bonding occupation. Lower panel: the Galitskii-Migdal total energies. The numbers in the legend represent the value corresponding to the sodium bottom valence case where $g = 4.5$ eV. The thick yellow curves are the exact results from the HPC-2. The blue dashed and up-triangles are the G_0W_0 and EscGW$_0$ results, respectively. The black curve in the lower panel is the Galitskii-Migdal total energy in Eq. (7.13) that is calculated from the exact model spectral function.

The upper panel of Fig. 7.1 shows the exact **Z**-factor of the HPC-2 in Eq. (4.30). The **Z**-factor decreases from 1 to 0.2 when the coupling increases from 0 to 8 eV. Most often, the systems of our interest have **Z**-factor larger than 0.4 so that the coupling range we are studying in this figure should be enough. The middle panel shows the bonding occupation number where the thick yellow curve represents the exact one, the blue dashed and

up-triangles are the bonding occupation numbers calculated using the G_0W_0 and EscGW$_0$, respectively. They are very similar and both overestimate the bonding occupation. In particular in the case of sodium bottom valence, the overestimation is about 2% (see the numbers in the legend). The lower panel shows the GMtots: the thick yellow curve represents the exact total energy of the HPC-2, i.e. the numerical E_0^-, the black solid curve is the GMtot calculated using the exact spectral function of the HPC-2, i.e E_{GMtot}^{model} in Eq. (7.13), the blue dashed curve and up-triangles are the GMtots calculated using the G_0W_0 and EscGW$_0$ spectral functions. All the GMtots underestimate (absolute value) the total energy of the HPC-2. The exact spectral function leads to better agreement and both GW spectral functions give similar GMtot in the coupling range of interest.

Therefore, the GMtot using the exact spectral function of the HPC-2 does not yield the exact total energy, which is not what we have expected. This means that there is some mismatch between the exact spectral function and the Galitskii-Migdal total energy formula. This issue will be discussed in detail in section 7.2. For now, we continue to study the performance of the GMtots using the CEA spectral functions.

The GMtot using the TOC96 and TOC11 spectral functions

I have calculated all the CEA spectral functions in the HPC-2 in section 4.2. Now I am going to plug the TOC96 (Eq. (4.67)) and TOC11 (Eq. (4.70)) spectral functions into the Galitskii-Migdal formula in Eq. (7.11) to calculate the corresponding Galitskii-Migdal total energies.

Since there is no electron removal spectrum in the TOC96[4] or TOC11, the GMtots from these two spectral functions are

$$E_{GMtot}^{C96} = \frac{1}{2} \int_{-\infty}^{\mu} d\omega \left[(\omega + \varepsilon_0 - \mathbf{t}) A_+^{C96}(\omega) \right] = (\varepsilon_0 - \mathbf{t} - \frac{\tilde{g}^2}{2\omega_p + 4\mathbf{t}}) e^{-\tilde{\beta}_2} ; \qquad (7.14a)$$

$$E_{GMtot}^{C11} = \frac{1}{2} \int_{-\infty}^{\mu} d\omega \left[(\omega + \varepsilon_0 - \mathbf{t}) A_+^{C11}(\omega) \right] = \varepsilon_0 - \mathbf{t} - \frac{\tilde{g}^2}{2\omega_p + 4\mathbf{t}} . \qquad (7.14b)$$

---

[4]In Ref. [101], the Galitskii-Migdal total energies of the TOC96 in a homogeneous electron gas was studied. Since the conservation of the particle number is very important for total energies, in order to conserve the particle number, the author has put the occupation number $n_k = 1$ for all states, which finally yields the TOC96 equivalent to the TOC11. In Ref. [102] the same TOC96 model spectral function was used to study the Galitskii-Migdal total energies of sodium and aluminum, yielding improvements on the lattice constants with respect to the LDA calculation.

The above GMtots are fully analytical, thus we can study their performance by comparing them to the analytical total energy of the HPC-2 (i.e. $E_0^{g^2}$ in Eq. (5.1) and blue dashed curve in Fig. 7.2). We can set the term $\varepsilon_0 - \mathbf{t}$ to zero in the comparison because it appears in all these three GMtots. Then we have $E_{GMtot}^{C96} = \frac{1}{2}e^{-\tilde{\beta}_2}E_0^{g^2}$ and $E_{GMtot}^{C11} = \frac{1}{2}E_0^{g^2}$ such that the absolute values have the relation of $\left|E_0^{g^2}\right| > \left|E_{GMtot}^{C11}\right| > \left|E_{GMtot}^{C96}\right|$. Fig. 5.1 shows that $\left|E_0^{g^2}\right|$ already underestimates the absolute value of the exact total energy $\left|E_0^-\right|$, which implies an even larger underestimation of the $\left|E_{GMtot}^{C11}\right|$ and $\left|E_{GMtot}^{C96}\right|$ as shown by the black diamonds and red circles in Fig. 7.2, respectively. In the same figure, the GMtot using the retarded cumulant spectral functions is calculated numerically as shown in the green up-triangles. It is better than the GMtot using the TOC96 or TOC11 spectral functions, but still by far not good enough when comparing to the exact total energy of the HPC-2.
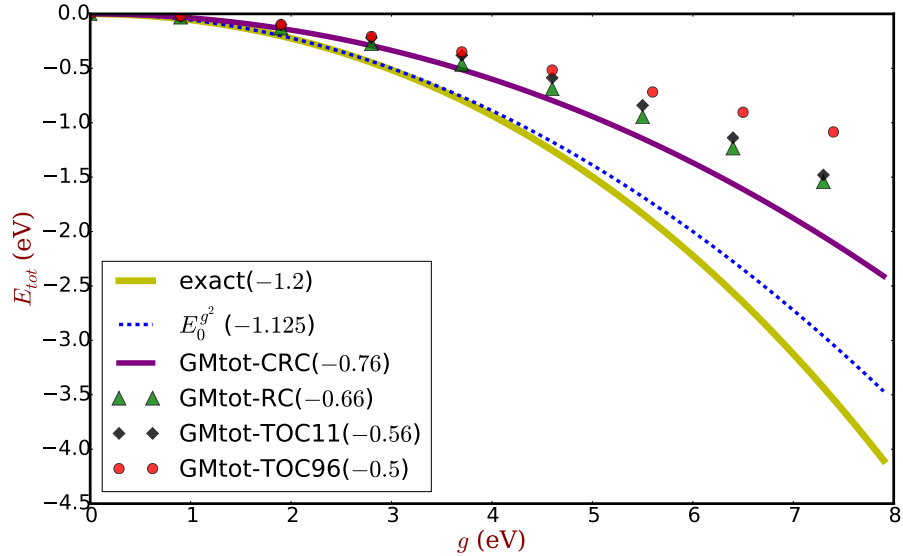
Figure 7.2: The total energies of the HPC-2 in function of the coupling strength. The numbers in the legend correspond to the values in the sodium bottom valence state where $g = 4.5$ eV. The thick yellow curve is the exact total energy of the HPC-2. The blue dashed curve represents the second order ground state energy $E_0^{g^2}$ in Eq. (5.1). The red circles, black diamonds, green up-triangles are the Galitskii-Migdal total energies (GMtots) calculated using the spectral functions of the TOC96 Eq. (7.14a), TOC11 Eq. (7.14b) and RC (numerical integration), respectively. The purple curve is the GMtot calculated using the constrained retarded cumulant spectral functions in Eq. (7.15).

The GMtot using the CRC spectral function

The constrained retarded cumulant spectral function in the HPC-2 has been calculated in Eq. (5.17). Now we plug it into the GMtot in Eq. (7.11), which yields

$$E_{GMtot1}^{CRC} = \int_{-\infty}^{\mu} d\omega \left[\omega A_+^{CRC}(\omega) + \omega A_-^{CRC}(\omega) \right] = \varepsilon_0 - \mathbf{t} - (\omega_p + 2\mathbf{t})\tilde{\beta}_2 - \omega_p\tilde{\beta}_2 ;$$

$$E_{GMtot2}^{CRC} = \int_{-\infty}^{\mu} d\omega \left[(\varepsilon_0 - \mathbf{t}) A_+^{g^2}(\omega) + (\varepsilon_0 + \mathbf{t}) A_-^{g^2}(\omega) \right] = \varepsilon_0 + \mathbf{t} - 2\mathbf{t}e^{-\tilde{\beta}_2} .$$

The final GMtot of CRC reads

$$E_{GMtot}^{CRC} = \frac{1}{2} \left(E_{GMtot1}^{CRC} + E_{GMtot2}^{CRC} \right). \tag{7.15}$$

Its performance is shown in thick purple curve in Fig. 7.2. It gives the best total energy among all the GMtots calculated using approximate spectral functions[5].

However, there are two puzzling facts. First in practice, we are never able to calculate the exact spectral functions. Thus the best total energy we would obtain is the GMtot using CRC, which underestimates absolute value of the exact total energy by about 36.7% in the case of using sodium parameters in the HPC-2. Second, and most importantly, it seems to be impossible that the exact spectral functions do not yield the exact total energy. Is this our limit in the calculation of total energies? If not, how can we do better? Indeed, I will show in the next section that we have to derive a new total energy formula in order to improve the total energies from approximate Green's functions.

7.2 Total energies from hole-plasmon coupling formula

In the previous section, I have shown the derivation of the Galitskii-Migdal formula in Eq. (7.11). However, the exact spectral function of the HPC-2 does not yield the exact total energy E_0^-. This is not what we expected.

---

[5]One can compare the GMtots in the HPC-2 using the sodium bottom valence parameters, i.e. the numbers in the legends of Figs. 7.1 and 7.2. The GMtot using the exact spectral function gives the best performance, the followings are the CRC, GWA, RC, TOC96 and TOC11.

At the beginning, I thought I did something wrong when I calculated the exact Green's function of the HPC-2 in section 4.1. However, I did not find any mistakes in that calculation. This really puzzled me a lot. Finally I understood that the discrepancy does not stem from the spectral function, but from the use of the Galitskii-Migdal formula itself. Therefore, I will show first the derivation of the *hole-plasmon coupling total energy formula* (HPCtot) from the hole-plasmon coupling Hamiltonian.

The general hole-plasmon coupling Hamiltonian with an Einstein boson (without dispersion) reads

$$\hat{H} = \int \mathrm{d}x \hat{\psi}^\dagger(x)\hat{h}_0(x)\hat{\psi}(x) + g\int \mathrm{d}x\hat{\psi}(x)\hat{\psi}^\dagger(x)\left(\hat{\phi}(x) + \hat{\phi}^\dagger(x)\right) + \omega_p\int \mathrm{d}x\hat{\phi}^\dagger(x)\hat{\phi}(x)$$

$$= \hat{h} + \hat{g} + \hat{p}\,, \tag{7.16}$$

where $\hat{\phi}$ is the field operator of the boson (e.g. plasmon), $\hat{h}$ is the one-particle part of the Hamiltonian, $\hat{g}$ and $\hat{p}$ represent the coupling and the plasmon terms, respectively.

We have calculated the commutator of $\hat{h}$ and the fermion field operator $\hat{\psi}(x)$ in equation (B.6). It reads

$$\left[\hat{\psi}(x), \hat{h}\right] = \hat{h}_0(x)\hat{\psi}(x)\,. \tag{7.17}$$

The commutator between $\hat{g}$ and the fermion field operator reads

$$\left[\hat{\psi}(x), \hat{g}\right] = g\int \mathrm{d}x\left[\hat{\psi}(x), \hat{\psi}(x)\hat{\psi}^\dagger(x)\left(\hat{\phi}(x) + \hat{\phi}^\dagger(x)\right)\right]$$

$$= g\int \mathrm{d}x\left[\hat{\psi}(x), \left(\hat{\phi}(x) + \hat{\phi}^\dagger(x)\right)\right]\hat{\psi}(x)\hat{\psi}^\dagger(x) + \left(\hat{\phi}(x) + \hat{\phi}^\dagger(x)\right)\left[\hat{\psi}(x), \hat{\psi}(x)\hat{\psi}^\dagger(x)\right]$$

$$= g\int \mathrm{d}x\left(\hat{\phi}(x) + \hat{\phi}^\dagger(x)\right)\left(\hat{\psi}(x)\hat{\psi}(x)\hat{\psi}^\dagger(x) - \hat{\psi}(x)\hat{\psi}^\dagger(x)\hat{\psi}(x)\right)$$

$$= -g\int \mathrm{d}x\hat{\psi}(x)\left(\hat{\phi}(x) + \hat{\phi}^\dagger(x)\right)\,. \tag{7.18}$$

Therefore we have the final commutator between the hole-plasmon coupling Hamiltonian and the fermion field operator as

$$\left[\hat{\psi}(x), \hat{H}\right] = \hat{h}_0(x)\hat{\psi}(x) - g\int \mathrm{d}x\hat{\psi}(x)\left(\hat{\phi}(x) + \hat{\phi}^\dagger(x)\right)\,. \tag{7.19}$$

The equation-of-motion of the field operator in the Heisenberg picture reads

$$i\frac{\partial \hat{\psi}_H(x,t)}{\partial t} = e^{i\hat{H}t}\left[\hat{\psi}(x), \hat{H}\right]e^{-i\hat{H}t}$$

$$= \hat{h}_0(x)\hat{\psi}(x,t) - g\int \mathrm{d}x\hat{\psi}(x,t)\left(\hat{\phi}(x) + \hat{\phi}^\dagger(x)\right). \tag{7.20}$$

Multiplying by $\hat{\psi}_H^\dagger(x't')$ and taking the ground state expectation value yields

$$\left(i\frac{\partial}{\partial t} - \hat{h}_0(x)\right)\langle\Psi_0|\hat{\psi}_H^\dagger(x't')\hat{\psi}_H(x,t)|\Psi_0\rangle$$

$$= -g\int \mathrm{d}x\,\langle\Psi_0|\hat{\psi}_H^\dagger(x't')\hat{\psi}(x,t)\left(\hat{\phi}(x) + \hat{\phi}^\dagger(x)\right)|\Psi_0\rangle. \tag{7.21}$$

The total energy of the hole-plasmon coupling Hamiltonian can be calculated from

$$E_0^{HPC} = \langle\Psi_0|\hat{h} + \hat{g} + \hat{p}|\Psi_0\rangle$$

$$= \langle\Psi_0|\hat{h}|\Psi_0\rangle - \left(i\frac{\partial}{\partial t} - \hat{h}_0(x)\right)\langle\Psi_0|\hat{\psi}_H^\dagger(x't')\hat{\psi}_H(x,t)|\Psi_0\rangle$$

$$+ \omega_p\int \mathrm{d}x\,\langle\Psi_0|\hat{\phi}^\dagger(x)\hat{\phi}(x)|\Psi_0\rangle$$

$$= -i\frac{\partial}{\partial t}\langle\Psi_0|\hat{\psi}_H^\dagger(x't')\hat{\psi}_H(x,t)|\Psi_0\rangle + \omega_p\int \mathrm{d}x\,\langle\Psi_0|\hat{\phi}^\dagger(x)\hat{\phi}(x)|\Psi_0\rangle$$

$$= \int \mathrm{d}x\int_{-\infty}^{\mu}\mathrm{d}\omega\left(\omega A(x,x,\omega)\right) + E_p, \tag{7.22}$$

where E_p is the ground state plasmon energy $E_p = \omega_p\int \mathrm{d}x\,\langle\Psi_0|\hat{\phi}^\dagger(x)\hat{\phi}(x)|\Psi_0\rangle$ and in the book of Gross, Runge and Heinonen [103] this term is defined as *the energy of zero-point motions*. In `orbital` basis, the HPCtot reads

$$E_0^{HPC} = \sum_k \int_{-\infty}^{\mu}\mathrm{d}\omega\left(\omega A_k(\omega)\right) + E_p. \tag{7.23}$$

The above HPCtot formula is identical to the total energy formula derived for a system of interacting electrons coupled to phonons [104]. Here the role of the phonons is played by the plasmons.

189

Compared to the Galitskii-Migdal formula in Eq. (7.11), there is no term linked to the occupation number but only the first moment, without the factor $1/2^6$. Instead the zero point motion energy of the plasmon E_p is added. In the HPC-1, there is no plasmon at the ground state (see Tab. 4.1) such that the $E_p = 0$ in the HPC-1. In the HPC-2, this term is not zero such that we have to find a way to calculate E_p.
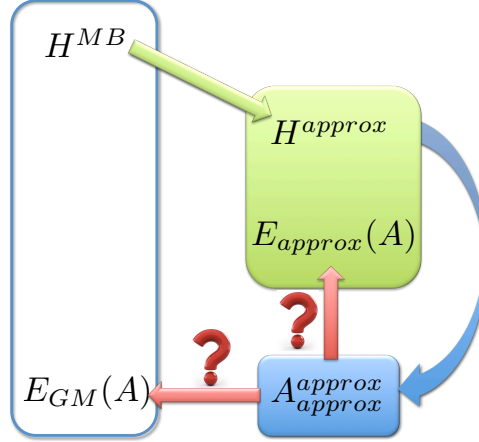

Figure 7.3: Schematic view of the relation between the total energy formulas and the Hamiltonians. The exact total energy formula of the exact many-body Hamiltonian is proven to be the Galitskii-Migdal formula. However, the Galitskii-Migdal formula requires the exact Green's function to reproduce the exact total energy. It is impossible to calculate the exact Green's function of a many-body system. Instead some approximate Hamiltonians (H^{approx}) are introduced (e.g. the hole-plasmon coupling Hamiltonian) which allow us to have the exact Green's functions (of the corresponding approximate Hamiltonians). Consequently, the exact total energy formula of the approximate Hamiltonian H^{approx} may not be the Galitskii-Migdal formula any more, as indicated on the right side. We might have to derive a new total energy formula $E_{approx}[A]$ (i.e. a functional of the spectral function hence the Green's function) corresponding to the approximate Hamiltonian such that the exact spectral function of H^{approx} yields its exact total energy using $E_{approx}[A]$. Since the GW approximation and the cumulant expansion approximation can be considered as some good approximate solution to the approximate hole-plasmon coupling Hamiltonian, the question becomes " *which formula should we use when we have the spectral functions of the GWA or the CEA?* " The direct answer to this question will not be provided in the present thesis, but I will show some studies that reflect the importance of this issue in the following total energy calculations.

---

[6]There should not be the sum over spin in the HPCtot formula. Because we always consider the case of one electron coupled plasmons in the hole-plasmon coupling Hamiltonian.

7.2.1 The HPCtot in the HPC-1

We have seen in section 7.1.1 that in the one-level hole-plasmon coupling Hamiltonian, A^{model} Eq. (4.12), $A^{G_0W_0}$ Eq. (4.36) and A^{EscGW_0} Eq. (4.42) spectral functions yield the exact total energies from the Galitskii-Migdal formula. All the cumulant spectral functions are the same as the exact model spectral function so that they also give the exact total energies from the Galitskii-Migdal formula. Now we have a look what is the total energy calculated from my new formula HPCtot in Eq. (7.23), using different spectral functions. I have analyzed in section 4.1.1 that there is no plasmon in the ground state in the HPC-2, so that the second term E_p in E_0^{HPC} is zero. We only need to calculate the first term. It is easy to show that

$$\int_{-\infty}^{\mu} d\omega \left(\omega A(\omega)\right) = \varepsilon_0 \,, \tag{7.24}$$

is valid for all the spectral functions of the HPC-1, such that we have

$$E_{HPCtot} = \int_{-\infty}^{\mu} d\omega \left(\omega A(\omega)\right) + E_p = \varepsilon_0 \,, \tag{7.25}$$

where $A(\omega)$ can be the exact (hence all the CEAs), as well as the G_0W_0 and EscGW$_0$ in the HPC-1.

Therefore similar to the Galitskii-Migdal formula, the hole-plasmon coupling total energy formula also yields the exact total energies even though we have very different spectral functions from different approximations in the HPC-1.

7.2.2 The HPCtot in the HPC-2

For the model HPC-2, we start from the HPCtot calculated with the exact model spectral function A^{model} in Eq. (4.29). The first part of the HPCtot in Eq. (7.23) is the same as

the first part of the GMtot in Eq. (7.12), thus we have

$$E^{model}_{HPCtot1} = \int_{-\infty}^{\mu} d\omega \left[\omega A^{model}_+(\omega) + \omega A^{model}_-(\omega) \right]$$

$$= E_0^- - \omega_p \sum_{m_-=0}^{\infty} \left(v^2_{[2m_-]}(2m_-) + v^2_{[2m_-+1]}(2m_- + 1) \right). \qquad (7.26)$$

In section 4.1 I have shown that there is no plasmon in the bonding orbital at the ground state (see $\hat{H}^+$ in Eq. (4.20a)). Thus E_p in Eq. (7.23) only contains the ground state expectation value of plasmons in the anti-bonding orbital, which yields

$$E_p = \omega_p \int dx \, \langle \Psi_0 | \hat{\phi}^\dagger(x)\hat{\phi}(x) | \Psi_0 \rangle = \omega_p \sum_{m_-=0}^{\infty} v^2_{[m_-]} \langle 1,0;0,m_- | \left(a^\dagger_- a_- \right) | 1,0;0,m_- \rangle$$

$$= \omega_p \sum_{m_-=0}^{\infty} m_- v^2_{[m_-]} = \omega_p \sum_{m_-=0}^{\infty} \left(v^2_{[2m_-]}(2m_-) + v^2_{[2m_-+1]}(2m_- + 1) \right). \qquad (7.27)$$

Thus E_p in the above equation cancels exactly the second term in Eq. (7.26), which leads to the exact total energy of the HPC-2, i.e.

$$E^{model}_{HPCtot} = E^{model}_{HPCtot1} + E_p = E_0^-. \qquad (7.28)$$

This confirms that indeed, the exact total energy formula of the hole-plasmon coupling Hamiltonian should be the hole-plasmon coupling total energy formula in Eq. (7.23) instead of the Galitskii-Migdal formula in Eq. (7.11). This is what I have analyzed in Fig. 7.3. We have hence found the energy functional for the hole-plasmon coupling Hamiltonian, however it is not only a functional of the spectral function, but it depends on the ground state plasmon energy term E_p.

The physical meaning of E_p is now obvious. $m_- v^2_{[m_-]}$ is the probability of having m_- (the number) plasmons in the anti-bonding orbital component and the sum over m_- gives the total probability of having plasmons in the anti-bonding orbital component. Multiplying by ω_p gives the ground state expectation plasmon energy contribution. Note that the reason why we only have plasmons in the anti-bonding orbital but not in the bonding orbital component is directly linked to the partial occupation. The partial occupation of the two-

level hole-plasmon coupling Hamiltonian stems from the term $(c_+c_-^\dagger + c_-c_+^\dagger)(a_-^\dagger + a_-)$ in $\hat{H}^-$ (see Eq. (4.20b)), such that we will see later that the probability to have plasmons in the anti-bonding orbital component can be approximately calculated from the anti-bonding occupation.

The use of the hole-plasmon coupling total energy formula instead of the Galitskii-Migdal formula in real systems is not obvious. There are many total energies studies using the Galitskii-Migdal formula together with some approximate Green's function (e.g. the GWA or the CEA) (see e.g. Refs. [19, 101, 102, 105]). The final total energy performance is related to the corresponding approximate Green's function. One might wonder whether the approximate Green's function is consistent with the Galitskii-Migdal formula or not. As shown in Fig. 7.3, the Galitskii-Migdal formula is the exact total energy formula of the exact many-body Hamiltonian in Eq. (7.1) that is fully electronic (no boson). However, the hole-plasmon coupling Hamiltonian represents an approximate system with respect to the exact one. It has its own total energy formula that is the hole-plasmon coupling total energy formula in Eq. (7.23). Therefore in order to reproduce the exact total energy of the approximate hole-plasmon coupling Hamiltonian, we have to use the consistent total energy formula which is the hole-plasmon coupling total energy formula, instead of the Galitskii-Migdal formula. The present example (Eqs. (7.13) and (7.28)) is a striking illustration of this point.

This philosophy is quite similar to the use of the cumulant expansion approximation with the GW self-energy versus the use of the Dyson equation with the same GW self-energy[7]. If we have the exact self-energy of a system, the exact one-body Green's function is the solution of the Dyson equation $G = G_0 + G_0 \Sigma G$. However, we are never able to calculate the exact Σ, instead different approximate Σs are used. Consequently, one certain approximate Σ may perform better when used in another formula for calculating the one-body Green's function in order to keep the consistency of approximations. We have seen

---

[7]The Green's function from the cumulant expansion approximation is often referred to as the " GW+cumulant " approach (see e.g. Refs. [12, 78]. In this sense, the Green's function calculated from the GW approximation should be refereed to as the " GW+Dyson equation " approach. The only difference is that the Dyson equation is exact when we have the exact self-energy, but the cumulant functional instead, can be considered as the exact functional of the Green's function, when we have used the GW self-energy in the one-level hole-plasmon coupling Hamiltonian. In the appendix C, I have shown that cumulant-like expressions would be consistent with other self-energies.

that the Green's function calculated using the cumulant expansion approximation fits better with the GW self-energy than the Dyson equation. This is another illustration of the fact that the consistency of approximations is important.

Now the point is that the Green's function calculated from the GW approximation or the cumulant expansion approximation can be considered as a good approximate solution to the approximate hole-plasmon coupling Hamiltonian. The reason is that they are based on the quasi-particle and plasmon picture as mentioned in Chapter 1. This raises one important question, namely " *which total energy formula should we use for the Green's function of the GWA or CEA?* " For the model itself, the answer is obvious, as I will illustrate in the following by comparing the total energies calculated from these two formulas using the same approximated spectral function. The answer for real systems is still unknown, since there may be cancellations between the approximation to the hole-plasmon coupling Hamiltonian and the approximation to the Green's function. This requires further studies.

An approximation to the ground state plasmon energy

In order to propone these studies, in the following we will derive and test an approximation to the HPCtot that might be used in further calculation on real systems. In particular, before we evaluate the HPCtot in Eq. (7.23), we have to find a way to calculate the ground state plasmon energy contribution. In practice, the ground state wavefunction Ψ_0 will be unknown, thus we could not use Eq. (7.27) to calculate E_p. This suggests to use the approximated analytical Green's function of the HPC-2 in Eq. (5.12) again.

The first part of the HPCtot using A^{g^2} reads

$$E^{g^2}_{HPCtot1} = \int_{-\infty}^{\mu} d\omega \left[\omega A^{g^2}_+(\omega) + \omega A^{g^2}_-(\omega) \right] = \varepsilon_0 - \mathbf{t} - (\omega_p + 2\mathbf{t})\tilde{\beta}_2 - \omega_p \tilde{\beta}_2 . \qquad (7.29)$$

Now how could we calculate the ground state plasmon energy $E^{g^2}_p$? Remember that, in section 4.1.2 when we derived the analytical spectral function, we have used the approximation to v_m in Eq. (5.4) that reads

$$v^2_{[m_-]} \approx \frac{e^{-\tilde{\beta}_2} \tilde{\beta}_2^{m_-}}{m_-!} . \qquad (7.30)$$

Using the above approximation, E_p in Eq. (7.27) reads

$$E_p^{g^2} = \omega_p \sum_{m_-=0}^{\infty} m_- v_{[m_-]}^2 = \sum_{m_-=0}^{\infty} \frac{e^{-\tilde{\beta}_2} \tilde{\beta}_2^{m_-}}{m_-!} m_- = \omega_p \tilde{\beta}_2 \,. \qquad (7.31)$$

This leads to the HPCtot calculated using A^{g^2} reading as

$$E_{HPCtot}^{g^2} = E_{HPCtot1}^{g^2} + E_p^{g^2} = \varepsilon_0 - \mathbf{t} - (\omega_p + 2\mathbf{t})\tilde{\beta}_2 \equiv E_0^{g^2} \,. \qquad (7.32)$$

This is consistent with our analysis because the spectral function A^{g^2} starts from the HPC-2 with an approximate ground state energy $E_0^{g^2}$ and now the HPCtot yields the same total energy[8].

Now we have a formula to calculate E_p in Eq. (7.31) where the the only quantities we need are the plasmon energy of the system ω_p (which is supposed to be known, like ε_0 e.g. from an LDA calculation) and $\tilde{\beta}_2$ can be calculated from the electron self-energy (see e.g. Eq. (5.24)), i.e.

$$\tilde{\beta}_2 = \left. \frac{\partial \operatorname{Re} \Sigma_+^e(\omega)}{\partial \omega} \right|_{\omega = \varepsilon_0 - \mathbf{t}} \,. \qquad (7.33)$$

In section 5.1 I have shown that the electron removal constrained retarded cumulant spectral function A^{CRC} in Eq. (5.17) is the same as A^{g^2} such that the HPCtot calculated using the constrained retarded cumulant spectral function is the same as $E_{HPCtot}^{g^2}$ in Eq. (7.32), which has very good agreement with the exact total energy of the HPC-2 (i.e. E_0^-) as shown in Fig. 5.1.

This is not the end of the story yet because the ground-state plasmon energy in Eq. (7.31) is only valid for the constrained retarded cumulant ($A^{CRC} \equiv A^{g^2}$ for electron removal). How about the spectral functions in other cumulant expansion approximations (the TOC96, TOC11 and RC), as well as the GW approximation? The plasmon energy E_p in Eq. (7.31) leads to the same result in all cumulant expansion approximations and the GW approximation, because they all use the same GW self-energy, hence leading to the same $\tilde{\beta}_2$ in Eq. (7.33). Therefore, what we need is an energy functional ($E_p[G]$) which only depends

---

[8]It would not make sense to get better total energies than $E_0^{g^2}$ from the CRC, using some approximate total energy formula. Because the derivation of the CRC starts from the ground state energy $E_0^{g^2}$.

on the Green's function (instead of the self-energy), as the Galitskii-Migdal formula in Eq. (7.11), in order to keep the approximations consistent.

Now we have to find the functional $E_p[G]$ in order to have a consistent hole-plasmon coupling total energy formula. First we have a look how we can link $\tilde{\beta}_2$ in Eq. (7.31) to the Green's function hence the spectral function. I have mentioned before that the ground-state expectation value of plasmons can be linked to the anti-bonding occupation that is nothing else than the integration of the spectral function up to the chemical potential, i.e. $n_- = \int_{-\infty}^{\mu} \mathrm{d}\omega A_-(\omega)$. Now we have a look at the anti-bonding occupation of the constrained retarded cumulant, which reads

$$n_-^{CRC} = \int_{-\infty}^{\mu} \mathrm{d}\omega A_-^{CRC}(\omega) = 1 - e^{-\tilde{\beta}_2} = \sum_{m=1}^{\infty} \frac{-(-\tilde{\beta}_2)^m}{m\,!} \approx \tilde{\beta}_2\,. \tag{7.34}$$

The performance of the above approximation can be seen in Fig. 7.4 where the anti-bonding occupation and plasmon occupation are compared. The blue dataset are the occupations calculated using the constrained retarded cumulant in Eq. (7.34). The diamonds ($\tilde{\beta}_2$) are almost right on top of n_-^{CRC} in the coupling range of interest, which means the plasmon occupation is very close to the electron anti-bonding occupation from the constrained retarded cumulant such that the approximation in Eq. (7.34) is acceptable. However, this approximation becomes worse when we use it in the exact HPC-2 Hamiltonian as shown by the red dataset in Fig. 7.4, especially in the large coupling range: the plasmon occupation can be larger than 0.5 but the electron occupation in the anti-bonding orbital can never cross 0.5, which means no matter how large the coupling, the bonding orbital always has lower energy than the anti-bonding orbital. The bad performance of the approximation in Eq. (7.34) can be explained from the consistency of approximations. The approximation in Eq. (7.34) is based on the constrained retarded cumulant approximation such that it works better in the constrained retarded cumulant Green's function. As we will see later, it also works well for the GW Green's function in the HPC-2.

Therefore the plasmon ground state energy in Eq. (7.31) can be approximated as $E_p^{CRC} = \omega_p n_-^{CRC}$, which leads to the final hole-plasmon coupling total energy functional
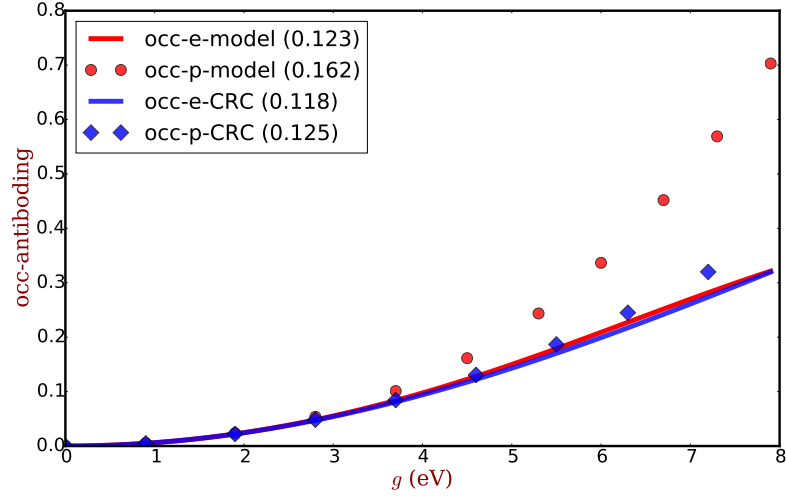
Figure 7.4: Comparison of anti-bonding occupations in HPC-2. The red and blue dataset correspond to the exact occupation of the HPC-2 and the approximate occupation calculated using the constrained retarded cumulant, respectively. The numbers in the legend are the occupation for a set of parameters corresponding to the sodium bottom valence ($g = 4.5$ eV and $\omega_p = 6$ eV). The red curve is the exact anti-bonding occupation of the HPC-2, i.e. $\int_{-\infty}^{\mu} \mathrm{d}\omega A_-(\omega) = \sum_{m}^{\infty} v_{2m+1}^2$ in Eq. (4.29). The red circles are the plasmon occupation from the HPC-2, i.e. $\sum_{m}^{\infty} m v_m^2$ in Eq. (7.27). The blue curve is the anti-bonding occupation from the CRC, i.e. $1 - e^{-\tilde{\beta}_2}$ and the blue diamonds are the plasmon occupation from the CRC, i.e. $\tilde{\beta}_2$.

reading as

$$E_{HPCtot} = \int_{-\infty}^{\mu} \mathrm{d}\omega \left(\omega A_+(\omega) + \omega A_-(\omega) \right) + \omega_p \int_{-\infty}^{\mu} \mathrm{d}\omega A_-(\omega), \qquad (7.35)$$

where only the spectral functions are needed.

The above HPCtot will be used in the following paragraphs to calculate the HPCtot with the spectral functions of the GWA and CEAs.

7.2.3 The HPCtot from the GWA and CEA spectral functions

We have discussed that the traditional time-ordered cumulant does not give any electron removal spectrum in the anti-bonding orbital so that the ground state plasmon energy $E_p = 0$ holds for both the spectral functions of the TOC96 and TOC11. Therefore we only need to calculate the first term in Eq. (7.35) which is already given in Eqs. (7.14a) and (7.14b):

$$E_{HPCtot}^{C96} = \int_{-\infty}^{\mu} \mathrm{d}\omega \left[\omega A_+^{C96}(\omega) \right] = e^{-\tilde{\beta}_2} \left(\varepsilon_0 - \mathbf{t} - \frac{\tilde{g}^2}{\omega_p + 2\mathbf{t}} \right) ; \qquad (7.36)$$

$$E_{HPCtot}^{C11} = \int_{-\infty}^{\mu} \mathrm{d}\omega \left[\omega A_+^{C11}(\omega) \right] = \varepsilon_0 - \mathbf{t} - \frac{\tilde{g}^2}{\omega_p + 2\mathbf{t}} . \qquad (7.37)$$

The HPCtot of the TOC11 $E_{HPCtot}^{C11} = E_0^{g^2}$ (black diamonds in Fig. 7.5) is the same as the HPCtot of the CRC in Eq. (7.32) that has the best performance compared to the exact total energy. The HPCtot of the TOC96 $E_{HPCtot}^{C96} = e^{-\tilde{\beta}_2} E_0^{g^2}$ (red circles in Fig. 7.5) underestimates (absolute value) the exact total energy of the HPC-2. The HPCtot calculated using the GWA and the retarded cumulant spectral functions can be obtained by numerical integration with the chemical potential between the quasi-particle energies of the bonding and anti-bonding orbitals. All the HPCtots in Fig. 7.5 show systematic improvements compared to the GMtots in Figs. 7.1 and 7.2.

We can conclude that in the hole-plasmon coupling Hamiltonian, the hole-plasmon coupling total energy formula works better than the Galitskii-Migdal total energy formula, for the reasons listed below:

1. In the HPC-1, all the spectral functions (the exact one, the GWA and the CEA) give the exact total energy from both HPCtot and GMtot.

2. In the HPC-2, when we use the exact spectral function, only the HPCtot yields the exact total energy as shown in Eq. (7.28). The GMtot using the exact spectral function underestimates (absolute value) the total energy (see black curve in the lower panel of Fig. 7.1). It is the best total energy using the Galitskii-Migdal formula (-0.9 eV using the sodium parameters shown in Fig. 7.1), however compared to all the HPCtots in Fig. 7.5, it is the worst.
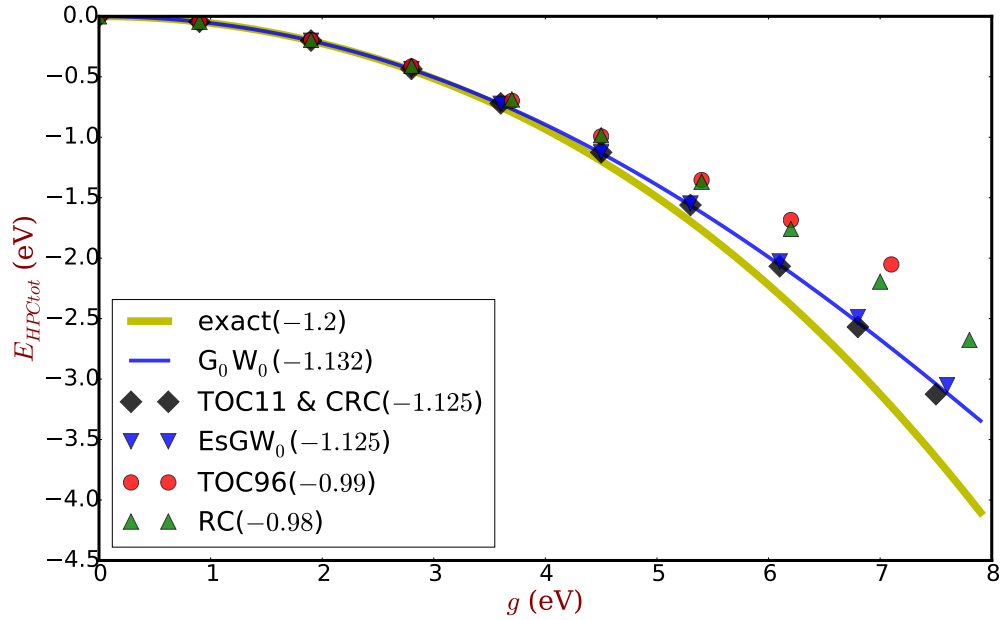
Figure 7.5: The HPCtot calculated from approximate spectral functions. The thick yellow curve is the exact total energy of the HPC-2. The red circles, black diamonds, green up-triangles and blue down-triangles are the HPCtot from the TOC96, TOC11 (hence CRC), RC, and EscGW$_0$, respectively. The blue curve is the G$_0$W$_0$ result and it is very similar to the EscGW$_0$ result. The numbers in the legend are the HPCtot corresponding to the sodium bottom valence where $g = 4.5$ eV and $\omega_p = 6$ eV.

3. In the HPC-2, when we use the GW spectral functions (both G$_0$W$_0$ and EscGW$_0$) the HPCtot (blue dataset in Fig. 7.5) is much better than the GMtot (blue dataset in Fig. 7.1).

4. In the HPC-2, when we use the spectral functions of the CEAs (TOC96, TOC11, RC and CRC), HPCtot is also better than the GMtot. In particular, the TOC11 and CRC gives the best total energy when comparing to the exact total energy of this Hamiltonian[9].

---

[9]The number in the legend in Fig. 7.5 shows that the G$_0$W$_0$ gives the best total energy. However when the coupling strength becomes larger, the total energies given by the CRC and CEA11 are better compared to the exact total energies of the HPC-2. In addition, one should be careful whether the G$_0$W$_0$ spectral function conserves the particle number for real system calculations [91].

7.2.4 Suggestion for real system calculations with HPCtot and CRC Green's function

Since the performance of the HPCtot using the CRC spectral function is so good, in this section I am going to implement this method in real system calculations as what I did for the implementation of the CRC in section 5.3.2.

As mentioned before, one of the disadvantages of the CRC in real system calculations is that it cannot provide explicitly the electron removal spectral functions of the states above the Fermi level. What it can provide is $A_{k,<}^{unocc}$ in Eq. (5.36) where k labels states below the Fermi level. Therefore, there is no one-to-one correspondence between $A_{k,<}^{unocc}$ and the non-interacting part Hamiltonian $\hat{h}_0$. As a consequence, we cannot plug the real system CRC spectral functions Eqs. (5.34) and (5.36) in the Galitskii-Migdal formula in Eq. (7.11). Fortunately the HPCtot formula in Eq. (7.23) does not depend on $\hat{h}_0$, and this makes the implementation of the HPCtot for real system calculations possible.

The first term in the HPCtot is the first moment of the CRC spectral function, which is the same as the first term in the GMtot formula, thus its implementation is straightforward. The difficulty is in the second term E_p that represents the ground-state plasmon energy. We have to find a way to implement the $E_p = \omega_p \tilde{\beta}_2$ in the HPC-2 Eq. (7.31) for real systems. In the implementation of the CRC, each $\tilde{\omega}_{i,k}$ corresponds to one possible plasmon energy of state k and each $\beta_k^>/N$ gives its possibilities. Therefore in real system, the HPCtot formula using the CRC spectral functions can be written as

$$E_{HPCtot}^{CRC} = \sum_{k}^{occ} \left[\int_{-\infty}^{\mu} d\omega \left(A_{k,<}^{occ}(\omega) + A_{k,<}^{unocc}(\omega) \right) + \sum_{i=1}^{N^<} \left(\frac{\beta_k^>}{N^<} \tilde{\omega}_{i,k}^< \right) \right], \qquad (7.38)$$

where k labels the states below the Fermi level in the system, $\tilde{\omega}_i^<$ is the pole from the sampling of $\operatorname{Im}\Sigma_k^<$ defined in Eq. (5.32), and $N^<$ is the number of poles used to sample $\operatorname{Im}\Sigma_k^<$.

Compared to the Galitskii-Migdal formula in Eq. (7.11), our formula does not have the prefactor $1/2$. As I mentioned before, the prefactor $1/2$ will disappear for a spin-independent system in the Galitskii-Migdal formula. Our formula in Eq. (7.38) does not depend on the

spin argument at all because the hole-plasmon coupling Hamiltonian always starts from the ground state with one electron and other electrons are bosonized as plasmons. In this sense, the only difference between the Galitskii-Migdal formula and our newly proposed formula is the second term: in the Galitskii-Migdal form this term is $\sum_{k}^{occ+unocc} \varepsilon_k^0 n_k$ where k runs over all the states and n_k is the occupation of each state; in our new formula Eq. (7.38), it becomes $\sum_{k}^{occ} \sum_{i=1}^{N^<} \left(\frac{\beta_k^>}{N^<} \tilde{\omega}_{i,k}^< \right)$ where k runs over only the occupied states.

This new proposed formula comes out really at the end of my thesis such that we do not have enough time to test its performance for real systems. However, since its similarity to the Galitskii-Migdal formula, it would not be so difficult to at least first test its performance in the homogeneous electron gas. It is difficult to predict the effects of this new formula compared to the present calculations of the Galitskii-Migdal total energies (see e.g. Refs. [19, 101, 102, 105]), because the exchange part of the self-energy is hidden in the orbital energy ε_0 in our model study.

However, our study on the HPCtots (see Fig. 7.5) shows that the HPCtots using the GW spectral functions are very similar to the ones from the CRC spectral functions. This suggests to start from a total energy study using the GW spectral function together with the newly derived HPCtot formula, since the GW approximation has been well developed in many *ab-initio* computation codes. Moreover, the HPCtot from the TOC11 spectral function is the same as the one using the CRC spectral functions as shown in Fig. 7.5. In order to calculate the total energy from the TOC11 we only need to calculate the first moment of the TOC11 spectral functions as shown in Eq. (7.37) due to the consistency of approximations. This is even simpler to realize than GW since in Ref. [19] the TOC11 is already used to study the Galitskii-Migdal total energies in the homogeneous electron gas.

7.3 Summary

In this chapter, the total energies of the one- and two-level hole-plasmon coupling model Hamiltonians are studied in detail using the Galitskii-Migdal and newly derived hole-plasmon coupling total energies formulas. I have also studied the performance of the GW and cumulant expansion approximation in the total energy calculations. In order to have

a better description of the total energy of a system, the consistency of approximations is crucial, because the final total energy will depend on both the energy functional and the approximate Green's function. The Green's function from the cumulant expansion approximation can be considered as a good approximation to the hole-plasmon coupling model Hamiltonian that is an approximate system with respect to the exact many-body Hamiltonian. I have found that the total energy of the model Hamiltonian is much better described with the hole-plasmon coupling total energy formula than with the Galitskii-Migdal formula. In particular, the constrained retarded cumulant gives the best total energy compared to the exact total energy of the two-level hole-plasmon coupling Hamiltonian.

Since the hole-plasmon coupling total energy formula is consistent with the constrained retarded cumulant Green's function, I have proposed an implementation of the this new total energy formula using the constrained retarded cumulant Green's function in real system calculations. Thanks to the similarity between the Galitskii-Migdal and the newly derived hole-plasmon coupling total energy formulas, the realization of this implementation should not be so difficult. Unfortunately, I did not have the time to study the performance of this implementation in any real material before the end of my thesis project. This study will be left after the submission of my thesis. It will be certainly be of great interest to explore to which extent a modified total energy formula might improve results obtained with approximate Green's functions, such as the CEA or the GW ones.

Chapter 8

Conclusion and outlook

8.1 Conclusion

In this manuscript, photoemission spectroscopy has been studied from the theoretical point of view. I have discussed the connection between theory and experiment in the description of photoemission spectra. In particular, I have focused my attention on the correlation effects that appear as satellite structures in photoemission spectra. While the satellites can be induced by different kinds of correlation effects including the coupling of electrons and holes to plasmons (collective oscillation), excitons or interband transitions, or also by more complicated effects such as an excited electron coupled to a bound hole-hole pair, I have restricted my study to the domain of satellites stemming from the coupling of a fermion to neutral excitations, in particular plasmons. Satellites cannot appear in any independent-particle theory, such that a good description of plasmon satellites requires more sophisticated approaches that are able to capture the many-body excitations in condensed matter.

Choices have to be made since the number of theoretical approaches in many-body physics is immense, and this manuscript concentrates on many-body perturbation theory (MBPT) where the one-body Green's function G is the fundamental building block. In particular, the spectral function of the Green's function directly links to the measured photoemission spectrum. For this reason, much of the content in this manuscript focuses on the calculation of the one-body Green's function G that can be obtained approximately from

many state-of-the-art theoretical approaches, e.g. Kohn-Sham density functional theory, the GW approximation and the cumulant expansion approximation *etc.*. In particular, the GW approximation (GWA), due to its success in the calculation of quasi-particle energies, has been the most widely used method in the passed half-century. However, the GWA often fails in the description of satellites. Satellites due to plasmons are indeed found in the GWA, but they are often too far from the quasi-particle energy, and sometimes much too sharp, and in other cases much too weak, as compared to the experiment. The cumulant expansion approximation (CEA) on the other hand, uses the GW self-energy in an alternative way, leading to a better description of the plasmon satellites in the photoemission spectrum. However, the best performance from the present CEAs is found for core levels, whereas more work is needed in the valence band region.

Throughout this manuscript, I have discussed extensively the present GWAs and CEAs, especially their performance for satellites. To be more precise, all the calculations are done using the self-energy calculated in the framework of G_0W_0 and $EscGW_0$. In order to make the complicated approximations more illustrative, I have provided the Green's function calculations using the GWAs and CEAs in two simplified hole-plasmon coupling model Hamiltonians. The advantages and disadvantages of these present approaches have been studied with the help of the exact Green's function from the model Hamiltonians, as well as the exact constraints of the one-body Green's function. None of the approximations is able to provide satisfactory spectra in the two-level hole-plasmon coupling model Hamiltonian that is suppose to model valence photoemission.

In order to go beyond these present approximations, I have provided a unified derivations from the full functional differential equation of the one-body Green's function, which is able to produce all present methods including the GWA, the time-ordered cumulant and the retarded cumulant using proper approximations on the same footing. The potential of this new derivation formalism is not yet fully explored in this manuscript. Much of study is needed to go further and find better approximations from this formalism.

Based on the understanding of the hole-plasmon coupling Hamiltonian and our derivations, I have proposed an advanced CEA that is refereed to as the constrained retarded cumulant. The constrained retarded cumulant together with two traditional time-ordered

cumulants (i.e. TOC96 in Ref. [9] and TOC11 in Ref. [11]) have been implemented in our local cumulant code such that the calculation of real materials can be done. Notably, the computational efforts of the CEAs are negligible compared to the computation of the GWA, since all the parameters of the CEAs can be obtained from a multipole sampling of the GW self-energy after a GW calculation.

Bulk sodium has been chosen as a benchmark to illustrate the GWAs and CEAs in real system calculations beyond the model Hamiltonian studies. In order to go beyond published results, I have calculated the sodium photoemission spectra in both valence and core on the same footing. The importance of the self-consistency of a GW calculation in core states has been emphasized. The traditional time-ordered cumulant faces its challenge in valence photoemission as illustrated from the comparison of calculated and experimental spectra in valence and core. Although the main structures of the spectrum are obtained with reasonably good agreement, the time-ordered cumulant overestimates the energy of the plasmon satellite and the weight ratio between the quasi-particle and satellites in the valence, at least when the random phase approximation of the dynamically screened Coulomb interaction W (RPA W) is used. The constrained retarded cumulant spectrum improves the weight of the satellites but unfortunately, the plasmon energy is still the same as the time-ordered cumulant using the same RPA W. Since our derivation indicates that to first approximation the screening W should correspond to the measurable one in order to obtain the correct spectrum, I had expected that this discrepancy in the plasmon energy should be corrected by using the exact W, instead of the RPA one.

In order to find out the origin of the discrepancy in the energy of the plasmon satellite between the CEA and experimental spectra, studies of W from more advanced approximations than the RPA have been provided. First I have calculated W in the TDLDA. Althought TDLDA improves plasmon spectra at large momentum transfer, the improvement of the plasmon satellites turns out to be negligible. However, a new derivation is shown which indicates that if we start from the Kohn-Sham LDA, the consistent dielectric function in our CEA should be the test charge-test electron (TCTE) one, instead of the measurable test charge-test charge (TCTC) one. The calculated CEA spectrum using the TCTE dielectric function improves the plasmon satellite energy compared to the experi-

mental spectrum, which confirms our analysis about the use of the TCTE instead of the TCTC dielectric function. The improvement is still not large enough, but this might be due to the fact that we have evaluated the TCTE in its simplest approximation, the TDLDA which is known to underestimate the exchange-correlation contribution.

Besides the photoemission spectrum, the one-body Green's function G also provides the total energies because one can show that the ground state expectation value of a certain many-body Hamiltonian can be written as an energy functional of G, i.e. $E[G]$. Once G is obtained, the total energy can be calculated using the proper energy functional $E[G]$. The total energies of the GWAs and CEAs are studied in Chapter 7 using two different energy functionals in the hole-plasmon coupling Hamiltonians. In particular, I start from the most widely used Galitskii-Migdal total energy formula that yields the exact energy of the exact many-body Hamiltonian, and find that the Galitskii-Migdal formula is not the exact functional of the hole-plasmon coupling Hamiltonian: the exact spectral function does not yield the exact total energy using the Galitskii-Migdal formula. This is because the hole-plasmon coupling Hamiltonian is an approximate system with respect to the exact many-body Hamiltonian, consequently the exact total energy functional of the hole-plasmon coupling Hamiltonian becomes the so called hole-plasmon coupling total energy formula whose derivation has been provided in my thesis. This reflects the importance in the consistency of approximations, which is one of the major issues illustrated in this manuscript: *"using the exact functional or not?"*

- One exact relation of the Green's function in MBPT is the Dyson equation $G = G_0 + G_0 \Sigma G$. This means that the exact Σ leads to the exact G. But when Σ has been approximated as Σ^{GW} (i.e. the GWA), should we still use the Dyson equation to calculate G leading to the GW approximation or not? This manuscript has illustrated that G from the cumulant expansion approximation has better performance than the one from the Dyson equation using Σ^{GW}. In particular, the cumulant functional is shown to be the exact one for the core-level quasi-boson model. Although the GW self-energy is an approximation to the real many-body self-energy, it yields the exact

Green's function using the cumulant expansion approximation in the approximate quasi-boson model.

- Similarly, the exact energy functional of the exact many-body Hamiltonian has been shown to be the Galitskii-Migdal formula $E_{GMtot}[G]$. However once some approximate G is plugged in the Galitskii-Migdal formula, the final total energy does not only reflect the performance of the approximate G, but also the energy functional because we have to take into account whether the approximation is consistent or not. The exact total energy functional of the hole-plasmon coupling Hamiltonian is the hole-plasmon coupling total energy formula. The Green's function from the GWA or CEA is an approximate solution of the hole-plasmon coupling such that for the approximate Hamiltonians, the HPCtot is better than the GMtot using these approximate Green's functions.

The total-energy studies in this manuscript show that all HPCtots calculated using the approximate Green's functions have better performance than the GMtots using the same approximate Green's function. In particular the total energy calculated using the constrained retarded cumulant Green's function leads to the best total energy compared to the exact total energy of the hole-plasmon coupling Hamiltonian. Also the EscGW$_0$ shows excellent results when used in the hole-plasmon coupling total energy formula. However, all the total energy studies are still based on the model Hamiltonians in this thesis. Although I have provided an implementation of the hole-plasmon coupling total energy formula in real system calculations, its performance is left to be studied in real materials.

8.2 Future Work

1. The first and the most important future work, from the fundamental theory development point of view, is to apply the derivation of the formalism provided in this manuscript. The potential applications of this formalism to produce increasingly accurate approximations is left to be explored more. In particular, the constrained retarded cumulant proposed in this manuscript is not yet derived from the full functional differential equation of the one-particle Green's function. However, the idea

of the constrained retarded cumulant provides some insight for finding better *ansatz* Green's functions in our derivation formalism, such that we can go further. Therefore, the next step will be to look for an improved ansatz that yields better Green's functions (possibly better than the constrained retarded cumulant) in the description photoemission.

2. The calculated sodium photoemission spectrum is still not good enough compared to the experimental spectrum. This might be cured by improving the description of the dynamically screened Coulomb interaction W using a better test charge-test electron screened Coulomb interaction interaction than the time-dependent local-density approximation.

3. A suggestion for an implementation of the hole-plasmon coupling total energy formula derived in my thesis has been provided for real system calculations, thus in the next step we will test its performance in some real systems, starting from the homogeneous electron gas and sodium.

4. The hole-plasmon coupling Hamiltonian has been used to illustrate the approximate spectral functions and the total energies in my thesis, however, a derivation starting from the exact electronic many-body Hamiltonian and putting into evidence which are the most important approximations in order to arrive at the hole-plasmon coupling model Hamiltonian is still missing. Therefore, we still cannot estimate quantitatively the quality of this approximate hole-plasmon coupling model Hamiltonian compared to real many-body systems. The linearization and decoupling approximations to the equation-of-motion of the one-body Green's function represent the physics of the approximations involved in the Hamiltonian, but for an explicit discussion of the total energy it would be easier to perform the equivalent steps directly on the Hamiltonian. This is left for future work.

Appendix A

Useful formulas

I summarize some useful formulas in this section.

The Fourier transforms used in this thesis are

$$f(\omega) = \int_{-\infty}^{+\infty} \mathrm{d}t\, f(t) e^{i\omega t}\,; \qquad\qquad (A.1a)$$

$$f(t) = \frac{1}{2\pi} \int_{-\infty}^{+\infty} \mathrm{d}\omega\, f(\omega) e^{-i\omega t}\,. \qquad\qquad (A.1b)$$

The differential representations of the Heaviside step function are

$$\theta(\tau) = \lim_{\eta \to 0^+} -\frac{1}{2\pi i} \int_{-\infty}^{+\infty} \mathrm{d}\omega\, \frac{e^{-i\omega\tau}}{\omega + i\eta}\,; \qquad\qquad (A.2a)$$

$$\theta(-\tau) = \lim_{\eta \to 0^+} \frac{1}{2\pi i} \int_{-\infty}^{+\infty} \mathrm{d}\omega\, \frac{e^{-i\omega\tau}}{\omega - i\eta}\,, \qquad\qquad (A.2b)$$

where the infinitesimally small $\eta \to 0^+$ is needed for the convergence of the integral.

The Cauchy principle value is defined as

$$\frac{1}{\omega - \varepsilon \pm i\eta} = \mathcal{P}\frac{1}{\omega - \varepsilon} \mp i\pi\delta(\omega - \varepsilon)\,. \qquad\qquad (A.3)$$

In this thesis we refer to the `conservation of spectral weight` as

$$\int_{-\infty}^{\infty} \mathrm{d}\omega\, A_k(\omega) = 1\,. \qquad\qquad (A.4)$$

where k represents a certain quantum state.

The `conservation of particle number` refers to

$$\int_{-\infty}^{\mu} d\omega \sum_i A_i(\omega) = N \,, \tag{A.5}$$

where the sum runs over all states with one certain spin, and N is the total particle number.

The commutation and anti-commutation rules that will be used in this thesis

$$\left\{ \hat{\psi}(x,t), \hat{\psi}^{\dagger}(x',t) \right\} = \hat{\psi}(x,t)\hat{\psi}^{\dagger}(x',t) + \hat{\psi}^{\dagger}(x',t)\hat{\psi}(x,t) = \delta(x-x') \,; \tag{A.6}$$

$$\left[\hat{\phi}(x,t), \hat{\phi}^{\dagger}(x',t) \right] = \hat{\phi}(x,t)\hat{\phi}^{\dagger}(x',t) - \hat{\phi}^{\dagger}(x',t)\hat{\phi}(x,t) = \delta(x-x') \,, \tag{A.7}$$

where $\hat{\psi}$ and $\hat{\phi}$ are the field operators of the fermions and bosons. The first equation is the `anti-commutation` rule for Fermions and the second equation is the `commutation` rule for bosons. Other useful rules are

$$[A+B, C] = [A, C] + [B, C] \,; \tag{A.8a}$$

$$[A, BC] = [A, B]C + B[A, C] \,; \tag{A.8b}$$

$$[A, BC] = \{A, B\}C - B\{A, C\} \,; \tag{A.8c}$$

$$[AB, C] = A[B, C] + [A, C]B \,; \tag{A.8d}$$

$$[AB, C] = A\{B, C\} - \{A, C\}B \,; \tag{A.8e}$$

$$\{A, BC\} = \{A, B\}C - B[A, C] \,. \tag{A.8f}$$

Appendix B

The equation-of-motion of the one-particle Green's function

The derivation of the equation-of-motion of the one-particle Green's function can be found in many textbooks. Here I recommend the book of Kadanoff and Baym [80], which introduced the equation-of-motion in non-equilibrium, which is often called the Kadanoff-Baym equation.

B.1 In equilibrium

To derive the equation-of-motion of the one-particle Green's function in equilibrium without the external perturbation, we work with the following general Hamiltonian in second quantization:

$$\hat{H} = \int \mathrm{d}x \hat{\psi}^\dagger(x) \hat{h}_0(x) \hat{\psi}(x) + \frac{1}{2} \int \mathrm{d}x_1 x_2 \hat{\psi}^\dagger(x_1) \hat{\psi}^\dagger(x_2) v_c(x_1, x_2) \hat{\psi}(x_2) \hat{\psi}(x_1) \,, \qquad \text{(B.1)}$$

where $\hat{h}_0 = -\frac{\nabla^2}{2} + V_{ext}$ is the non-interacting part of the Hamiltonian[1], and $\hat{\psi}(x)$ is the field operator in the Schrödinger picture.

---

[1]Note that $\hat{h}_0$ and v_c are spin-independent. For simplicity, we put spin arguments also in the spin-independent quantities, but it is understood that this Hamiltonian is equivalent to the initial many-body Hamiltonian we have discussed before in Eq. (2.1).

We have the definition of the one-particle Green's function in equilibrium that reads (see equation (1.14))

$$iG(1,2) \equiv \left\langle \Psi_0 \middle| \mathbb{T}\left[\hat{\psi}_H(1)\hat{\psi}_H^\dagger(2)\right] \middle| \Psi_0 \right\rangle . \tag{B.2}$$

Taking the derivative of G with respect to t_1 (the derivative with respect to t_2 is analogues), we have

$$
\begin{aligned}
\frac{\partial}{\partial t_1}\left(\mathbb{T}\left[\hat{\psi}_H(1)\hat{\psi}_H^\dagger(2)\right]\right) &= \frac{\partial}{\partial t_1}\left(\theta(t_1-t_2)\hat{\psi}_H(1)\hat{\psi}_H^\dagger(2) - \theta(t_2-t_1)\hat{\psi}_H^\dagger(2)\hat{\psi}_H(1)\right) \\
&= \delta(t_1-t_2)\hat{\psi}_H(1)\hat{\psi}_H^\dagger(2) + \delta(t_2-t_1)\hat{\psi}_H^\dagger(2)\hat{\psi}_H(1) \\
&\quad + \theta(t_1-t_2)\frac{\partial\hat{\psi}_H(1)}{\partial t_1}\hat{\psi}_H^\dagger(2) - \theta(t_2-t_1)\hat{\psi}_H^\dagger(2)\frac{\partial\hat{\psi}_H(1)}{\partial t_1} \\
&= \delta(t_1-t_2)\left(\hat{\psi}_H(1)\hat{\psi}_H^\dagger(2) + \hat{\psi}_H^\dagger(2)\hat{\psi}_H(1)\right) + \mathbb{T}\left[\frac{\partial\hat{\psi}_H(1)}{\partial t_1}\hat{\psi}_H^\dagger(2)\right] \\
&= \delta(1-2) + \mathbb{T}\left[\frac{\partial\hat{\psi}_H(1)}{\partial t_1}\hat{\psi}_H^\dagger(2)\right] .
\end{aligned}
\tag{B.3}
$$

Thus to have the equation-of-motion of G, we need to calculate first the equation-of-motion of the field operator in the Heisenberg picture. It reads

$$\frac{\partial\hat{\psi}_H(x',t)}{\partial t} = \left[\hat{\psi}_H(x',t), \hat{H}\right] = e^{i\hat{H}t}\left[\hat{\psi}(x'), \hat{H}\right]e^{-i\hat{H}t} , \tag{B.4}$$

which further requires the commutator of the field operator in the Schrödinger picture and the Hamiltonian. To calculate this commutator, we separate the Hamiltonian (B.1) into the one-particle and two-particle parts as

$$\hat{H} = \hat{h} + \hat{v} , \tag{B.5}$$

and calculate the two parts separately using the commutation properties (A.8). We start from the one-particle part:

$$
\begin{aligned}
\left[\hat{\psi}(x'), \hat{h}\right] &= \int \mathrm{d}x \left[\hat{\psi}_H(x'), \hat{\psi}^\dagger(x)\hat{h}_0(x)\hat{\psi}(x)\right] \\
&= \int \mathrm{d}x \left(\left\{\hat{\psi}(x'), \hat{\psi}^\dagger(x)\right\}\hat{h}_0(x)\hat{\psi}(x) - \hat{\psi}^\dagger\left\{\hat{\psi}(x'), \hat{h}_0(x)\hat{\psi}(x)\right\}\right) \\
&= \int \mathrm{d}x \left(\delta(x - x')\hat{h}_0(x)\hat{\psi}(x) - \hat{\psi}^\dagger\hat{h}_0(x)\left\{\hat{\psi}(x'), \hat{\psi}(x)\right\}\right) \\
&= \hat{h}_0(x')\hat{\psi}(x').
\end{aligned}
\tag{B.6}
$$

The commutation of the field operator and the two-particle part reads

$$
\begin{aligned}
\left[\hat{\psi}(x'), \hat{v}\right] &= \frac{1}{2}\int \mathrm{d}x_1 x_2 \left[\hat{\psi}(x'), \hat{\psi}^\dagger(x_1)\hat{\psi}^\dagger(x_2)v_c(x_1, x_2)\hat{\psi}(x_2)\hat{\psi}(x_1)\right] \\
&= \frac{1}{2}\int \mathrm{d}x_1 x_2 \left(\left\{\hat{\psi}(x'), \hat{\psi}^\dagger(x_1)\right\}\hat{\psi}^\dagger(x_2)v_c(x_1, x_2)\hat{\psi}(x_2)\hat{\psi}(x_1)\right) \\
&\quad - \frac{1}{2}\int \mathrm{d}x_1 x_2 \left(\hat{\psi}^\dagger(x_1)\left\{\hat{\psi}(x'), \hat{\psi}^\dagger(x_2)v_c(x_1, x_2)\hat{\psi}(x_2)\hat{\psi}(x_1)\right\}\right) \\
&= \frac{1}{2}\int \mathrm{d}x_1 x_2 \left(\delta(x' - x_1)\hat{\psi}^\dagger(x_2)v_c(x_1, x_2)\hat{\psi}(x_2)\hat{\psi}(x_1)\right) \\
&\quad - \frac{1}{2}\int \mathrm{d}x_1 x_2 \left(\hat{\psi}^\dagger(x_1)\left\{\hat{\psi}(x'), \hat{\psi}^\dagger(x_2)\right\}v_c(x_1, x_2)\hat{\psi}(x_2)\hat{\psi}(x_1)\right) \\
&\quad + \frac{1}{2}\int \mathrm{d}x_1 x_2 \left(\hat{\psi}^\dagger(x_2)\left[\hat{\psi}(x'), v_c(x_1, x_2)\hat{\psi}(x_2)\hat{\psi}(x_1)\right]\right) \to \equiv 0 \\
&= \frac{1}{2}\int \mathrm{d}x_2 \left(\hat{\psi}^\dagger(x_2)v_c(x', x_2)\hat{\psi}(x_2)\hat{\psi}(x')\right) \\
&\quad - \frac{1}{2}\int \mathrm{d}x_1 \left(\hat{\psi}^\dagger(x_1)v_c(x_1, x')\hat{\psi}(x')\hat{\psi}(x_1)\right) \\
&= \frac{1}{2}\int \mathrm{d}x \left(\hat{\psi}^\dagger(x)v_c(x', x)\hat{\psi}(x)\hat{\psi}(x') - \hat{\psi}^\dagger(x)v_c(x, x')\hat{\psi}(x')\hat{\psi}(x)\right) \\
&= \int \mathrm{d}x \left(\hat{\psi}^\dagger(x)v_c(x', x)\hat{\psi}(x)\hat{\psi}(x')\right).
\end{aligned}
\tag{B.7}
$$

Finally we have

$$
\left[\hat{\psi}(x'), \hat{H}\right] = \hat{h}_0(x')\hat{\psi}(x') + \int \mathrm{d}x \left(\hat{\psi}^\dagger(x)v_c(x', x)\hat{\psi}(x)\hat{\psi}(x')\right),
\tag{B.8}
$$

and the equation-of-motion of the field operator in the Heisenberg picture reads

$$\frac{\partial \hat{\psi}_H(x',t)}{\partial t} = e^{i\hat{H}t}\left[\hat{\psi}(x'), \hat{H}\right]e^{-i\hat{H}t}$$

$$= -i\hat{h}_0(x')\hat{\psi}_H(x',t) - i\int \mathrm{d}x\left(\hat{\psi}_H^\dagger(x,t)v_c(x',x)\hat{\psi}_H(x,t)\hat{\psi}_H(x',t)\right). \quad \text{(B.9)}$$

Putting the above equation back into equation (B.3) we have

$$i\frac{\partial G(1,2)}{\partial t_1} = \delta(1-2) + \left\langle \Psi_0 \left| \mathbb{T}\left[\frac{\partial \hat{\psi}_H(1)}{\partial t_1}\hat{\psi}_H^\dagger(2)\right] \right| \Psi_0 \right\rangle$$

$$= \delta(1-2) - i\hat{h}_0(x_1)\langle\Psi_0|\mathbb{T}\left[\hat{\psi}_H(1)\hat{\psi}_H^\dagger(2)\right]|\Psi_0\rangle$$

$$- i\int \mathrm{d}x_3 v_c(x_1,x_3)\langle\Psi_0|\mathbb{T}\left[\hat{\psi}_H^\dagger(x_3,t_1)\hat{\psi}_H(x_3,t_1)\hat{\psi}_H(x_1,t_1)\hat{\psi}_H^\dagger(x_2,t_2)\right]|\Psi_0\rangle .$$

$$\text{(B.10)}$$

Note that the product $\hat{\psi}_H^\dagger(x_3,t_1)\hat{\psi}_H(x_3,t_1)\hat{\psi}_H(x_1,t_1)$ originates from a single operator, i.e., $\frac{\partial \hat{\psi}(x,t)}{\partial t}$, so that this product must remain together and be regarded as one unit. Hence the only possible time orderings of the above equation are

$$\mathbb{T}\left[\hat{\psi}_H^\dagger(x_3,t_1)\hat{\psi}_H(x_3,t_1)\hat{\psi}_H(x_1,t_1)\hat{\psi}_H^\dagger(x_2,t_2)\right]$$

$$= \hat{\psi}_H^\dagger(x_3,t_1)\hat{\psi}_H(x_3,t_1)\hat{\psi}_H(x_1,t_1)\hat{\psi}_H^\dagger(x_2,t_2) \rightarrow t_1 > t_2; \quad \text{(B.11a)}$$

$$\mathbb{T}\left[\hat{\psi}_H^\dagger(x_3,t_1)\hat{\psi}_H(x_3,t_1)\hat{\psi}_H(x_1,t_1)\hat{\psi}_H^\dagger(x_2,t_2)\right]$$

$$= -\hat{\psi}_H^\dagger(x_2,t_2)\hat{\psi}_H^\dagger(x_3,t_1)\hat{\psi}_H(x_3,t_1)\hat{\psi}_H(x_1,t_1) \rightarrow t_2 > t_1 . \quad \text{(B.11b)}$$

Using the anti-commutation rule $\hat{\psi}_H(x_2,t_1)\hat{\psi}_H(x_1,t_1) = -\hat{\psi}_H(x_1,t_1)\hat{\psi}_H(x_2,t_1)$ that holds for the field operators in the Heisenberg picture of equal times, we can write these four operators as

$$\mathbb{T}\left[\hat{\psi}_H^\dagger(x_3,t_1)\hat{\psi}_H(x_3,t_1)\hat{\psi}_H(x_1,t_1)\hat{\psi}_H^\dagger(x_2,t_2)\right]$$

$$= -\mathbb{T}\left[\hat{\psi}_H(x_1,t_1)\hat{\psi}_H(x_3,t_1)\hat{\psi}_H^\dagger(x_3,t_1)\hat{\psi}_H^\dagger(x_2,t_2)\right],$$

thus we have[2]

$$\langle\Psi_0|\mathbb{T}\Big[\hat{\psi}_H^\dagger(x_3,t_1)\hat{\psi}_H(x_3,t_1)\hat{\psi}_H(x_1,t_1)\hat{\psi}_H^\dagger(x_2,t_2)\Big]|\Psi_0\rangle = G_2(x_1t_1,x_3t_1^+;x_2t_2,x_3t_1^{++})\,,$$

(B.12)

where G_2 is the two-particle Green's function defined as

$$G_2(1,2;3,4) \equiv \frac{1}{(i)^2}\left\langle\Psi_0\Big|\mathbb{T}\Big[\hat{\psi}_H(1)\hat{\psi}_H(2)\hat{\psi}_H^\dagger(4)\hat{\psi}_H^\dagger(3)\Big]\Big|\Psi_0\right\rangle.$$

(B.13)

Putting G_2 into equation (B.10), we finally have the equation-of-motion of the one-particle Green's function as

$$\left(i\frac{\partial}{\partial t_1} - \hat{h}_0(x_1)\right)G(1,2) = \delta(1-2) - i\int dx_3 v_c(x_1,x_3)G_2(x_1t_1,x_3t_1^+;x_2t_2,x_3t_1^{++})$$

$$= \delta(1-2) - i\int d3\, v_c(1,3^+)G_2(1,3^+;2,3^{++})\bigg|_{t_3=t_1}.$$

(B.14)

The equation-of-motion of the one-particle Green's function yields the two-particle Green's function whose equation-of-motion will yield the three-particle Green's function, and so on. For a non-interacting system where $v_c = 0$, we have

$$\left(i\frac{\partial}{\partial t_1} - \hat{h}_0(x_1)\right)G_0(1,2) = \delta(1-2).$$

(B.15)

Its inverse reads

$$G_0^{-1}(1,2) = \left(i\frac{\partial}{\partial t_1} - \hat{h}_0(x_1)\right)\delta(1-2).$$

(B.16)

Hence Eq. (B.14) becomes $G_o^{-1}G = 1 - ivG_2$. Multiplying G_0 yields $G = G_0 - iG_0vG_2$, and finally we have

$$G(1,2) = G_0(1,2) - i\int d34 G_0(1,3)v_c(3,4^+)G_2(3,4^+;2,4^{++}).$$

(B.17)

---

[2]Here we have introduced infinitesimal time differences to guarantee the correct order of all field operators.

B.2   In non-equilibrium

As mentioned above, the equation-of-motion of the one-particle Green's function yields the two-particle Green's function. The equation-of-motion of the two-particle Green's function yields the three-particle Green's function. It is impossible to calculate such an infinite series. In order to truncate this infinite chain and obtain a closed expression, we can use Schwinger's functional derivative approach [54], which introduces a fictitious local external and time-dependent perturbation $\phi(x, t)$ in the initial equilibrium Hamiltonian (B.1) such that we can work with the non-equilibrium Hamiltonian shown below:

$$
\begin{aligned}
\hat{H} = & \int \mathrm{d}x \hat{\psi}^\dagger(x) \hat{h}_0(x) \hat{\psi}(x) + \int \mathrm{d}x \hat{\psi}^\dagger(x) \phi(x, t) \hat{\psi}(x) \\
& + \frac{1}{2} \int \mathrm{d}x_1 x_2 \hat{\psi}^\dagger(x_1) \hat{\psi}^\dagger(x_2) v_c(x_1, x_2) \hat{\psi}(x_2) \hat{\psi}(x_1) \,.
\end{aligned} \tag{B.18}
$$

Note that the above Hamiltonian is time-dependent because of the time-dependent external potential. The corresponding non-equilibrium one-particle Green's function reads

$$
iG(1, 2; \phi) \equiv \frac{\left\langle \Psi_0 \middle| \mathbb{T} \left[\hat{U} \hat{\psi}_H(1) \hat{\psi}_H^\dagger(2) \right] \middle| \Psi_0 \right\rangle}{\left\langle \Psi_0 \middle| \mathbb{T} \left[\hat{U} \right] \middle| \Psi_0 \right\rangle} \,, \tag{B.19}
$$

where the `time-evolution operator` $\hat{U}$ is defined as

$$
\hat{U} \equiv \exp\left(-i \int \mathrm{d}1 \hat{\psi}_H^\dagger(1) \phi(1) \hat{\psi}_H(1) \right) = \exp\left(-i \int \mathrm{d}1 \phi(1) \rho(1) \right), \tag{B.20}
$$

and we have defined the density operator $\hat{\rho}(1) \equiv \hat{\psi}_H^\dagger(1) \hat{\psi}_H(1)$. Working in the `interaction` (Dirac) picture, we have

$$
\left| \hat{\psi}_D(x, t) \right\rangle = \hat{U}(t, t_0) \left| \hat{\psi}_D(x, t_0) \right\rangle \,, \tag{B.21}
$$

where the `time-evolution operator` in the Dirac picture reads

$$
\hat{U}(t, t_0) = \exp\left(-i \int_{t_0}^{t} \mathrm{d}\tau \tilde{\phi}(\tau) \right), \tag{B.22}
$$

and

$$\tilde{\phi}(\tau) = \int \mathrm{d}x \hat{\psi}_D^\dagger(x,\tau)\phi(x,\tau)\hat{\psi}_D(x,\tau)\,. \tag{B.23}$$

The relation between operators in Heisenberg and Dirac pictures is

$$\hat{\psi}_H(x,t) = \hat{U}(t_0,t)\hat{\psi}_D(x,t)\hat{U}(t,t_0)\,, \tag{B.24}$$

where t_0 is the time where one decides the quantities in the two pictures to coincide. The field operator in Dirac picture satisfies

$$i\frac{\partial \hat{\psi}_D(x,t)}{\partial t} = \left[\hat{\psi}_D(x,t), \hat{H}(\phi = 0)\right]\,, \tag{B.25}$$

which is the same as the equilibrium ($\phi = 0$) Heisenberg operator (B.4). Therefore, the one-particle Green's function in non-equilibrium can be written in the Dirac picture as

$$iG(1,2;\phi) = \frac{\left\langle \Psi_0 \left| \mathbb{T}\left[\hat{U}(-\infty,\infty)\hat{\psi}_D(1)\hat{\psi}_D^\dagger(2)\right] \right| \Psi_0 \right\rangle}{\langle \Psi_0 | \hat{U}(-\infty,\infty) | \Psi_0 \rangle}\,. \tag{B.26}$$

We need to take the time derivative of $G(1,2;\phi)$ with respect to t_1 (t_2 is analogous). Note that there is no t_1 dependence in the denominator of equation (B.26). Thus we only need to evaluate the time-ordering in the nominator, where we have for $(-\infty < t_1 < t_2 < \infty)$

$$\begin{aligned}
\mathbb{T}\left[\hat{U}\hat{\psi}_H(1)\hat{\psi}_H^\dagger(2)\right] &= \mathbb{T}\left[\hat{U}(\infty,t_1)\right]\hat{\psi}_D(1)\mathbb{T}\left[\hat{U}(t_1,t_2)\right]\hat{\psi}_D^\dagger(2)\mathbb{T}\left[\hat{U}(t_2,-\infty)\right] \\
&= \mathbb{T}\left[\hat{U}(\infty,t_1)\right]\hat{\psi}_D(1)\mathbb{T}\left[\hat{U}(t_1,-\infty)\right]\hat{\psi}_D^\dagger(2) \\
&= \mathbb{T}\left[\exp\left(i\int_{t_1}^\infty \mathrm{d}2\phi(2)\rho(2)\right)\right]\hat{\psi}_D(1)\mathbb{T}\left[\exp\left(-i\int_{-\infty}^{t_1}\mathrm{d}2\phi(2)\rho(2)\right)\right]\hat{\psi}_D^\dagger(2)\,.
\end{aligned} \tag{B.27}$$

Here the density operator is defined in the Dirac picture $\hat{\rho}_D(1) = \hat{\psi}_D^\dagger(1)\hat{\psi}_D(1)$. One can show that $\rho_D(1) \equiv \rho_H(1)$

$$\begin{aligned}
\rho_H(1) &= \hat{\psi}_H^\dagger(1)\hat{\psi}_H(1) = \hat{U}(t_0,t_1)\hat{\psi}_D^\dagger(1)\hat{\psi}_D(1)\hat{U}(t_1,t_0) \\
&= \rho_D(1)\hat{U}(t_0,t_1)\hat{U}(t_1,t_0) \equiv \rho_D(1)\,.
\end{aligned} \tag{B.28}$$

Note that the two exponentials are function of t_1 so we name them as

$$f_1(t_1) = \exp\left(i \int_{t_1}^{\infty} \mathrm{d}2\phi(2)\rho(2)\right);$$ (B.29)

$$f_2(t_1) = \exp\left(-i \int_{-\infty}^{t_1} \mathrm{d}2\phi(2)\rho(2)\right).$$ (B.30)

Now the derivative with respect to t_1 becomes

$$\frac{\partial f_1(t_1)}{\partial t_1} = \frac{\partial}{\partial t_1}\left(i \int_{t_1}^{\infty} \mathrm{d}2\phi(2)\rho(2)\right) \exp\left(i \int_{t_1}^{\infty} \mathrm{d}2\phi(2)\rho(2)\right)$$

$$= -i \int \mathrm{d}x_2 \phi(x_2, t_1)\rho(x_2 t_1) f_1(t_1);$$ (B.31)

$$\frac{\partial f_2(t_1)}{\partial t_1} = -i \int \mathrm{d}x_2 \phi(x_2, t_1)\rho(x_2 t_1) f_2(t_1).$$ (B.32)

Then the derivative of t_1-dependent part of the Green's function with respect to t_1 becomes

$$\frac{\partial f_1(t_1)}{\partial t_1}\hat{\psi}_D(1)f_2(t_1) + f_1(t_1)\frac{\partial\hat{\psi}_D(1)}{\partial t_1}f_2(t_1) + f_1(t_1)\hat{\psi}_D(1)\frac{\partial f_2(t_1)}{\partial t_1}$$

$$= -i \int \mathrm{d}x_2\phi(x_2,t_1)\rho(x_2 t_1)f_1(t_1)\hat{\psi}_D(1)f_2(t_1)$$

$$- if_1(t_1)\hat{\psi}_D(1)\int \mathrm{d}x_2\phi(x_2,t_1)\rho(x_2 t_1)f_2 + f_1(t_1)\frac{\partial\hat{\psi}_D(1)}{\partial t_1}f_2(t_1)$$

$$= -if_1(t_1)\int \mathrm{d}x_2\phi(x_2,t_1)\left\{\hat{\psi}_D(1),\rho(x_2,t_1)\right\}f_2(t_1) + f_1(t_1)\frac{\partial\hat{\psi}_D(1)}{\partial t_1}f_2(t_1)$$

$$= -if_1(t_1)\int \mathrm{d}x_2\phi(x_2,t_1)\delta(x_1 - x_2)\hat{\psi}_D(1)f_2(t_1) + f_1(t_1)\frac{\partial\hat{\psi}_D(1)}{\partial t_1}f_2(t_1)$$

$$= -if_1(t_1)\phi(1)\hat{\psi}_D(1)f_2(t_1) + f_1(t_1)\frac{\partial\hat{\psi}_D(1)}{\partial t_1}f_2(t_1)$$

$$= -i\mathbb{T}\left[\hat{U}\hat{\psi}_H(1)\right]\phi(1) + \mathbb{T}\left[\frac{\partial\hat{\psi}_H(1)}{\partial t_1}\right].$$ (B.33)

We have used the property in (A.8)

$$\left\{\hat{\psi}_D(1),\rho(x_2,t_1)\right\} = \left\{\hat{\psi}_D(1),\hat{\psi}_D^\dagger(x_2,t_1)\right\}\hat{\psi}_D(x_2,t_1) - \hat{\psi}_D^\dagger(x_2,t_1)\left[\hat{\psi}_D(x_2,t_1),\hat{\psi}_D(1)\right]$$

$$= \delta(x_1 - x_2)\hat{\psi}_D(x_1,t_1).$$ (B.34)

The second term in equation (B.33) has been calculated when we derive the equation-of-motion in equilibrium (see (B.3)), and the equation-of-motion of the field operator in Heisenberg picture has been derived in equation (B.9). Putting back $\hat{\psi}^\dagger(2)$ gives

$$i\frac{\partial G(1,2;\phi)}{\partial t_1} = \frac{\left\langle \Psi_0 \left| \frac{\partial \mathbb{T}\left[\hat{U}\hat{\psi}_H(1)\hat{\psi}_H^\dagger(2)\right]}{\partial t_1} \right| \Psi_0 \right\rangle}{\langle \Psi_0 | \mathbb{T}\left[\hat{U}\right] | \Psi_0 \rangle}$$

$$= G(1,2;\phi)\Big(\phi(1) + \hat{h}_0(x_1)\Big) + \delta(1-2) - i\int dx_3 v_c(x_1,x_3)G_2(x_1 t_1, t_3 t_1; x_2 t_2, x_3 t_1; \phi).$$

(B.35)

Finally, we have the equation-of-motion of the Green's function in non-equilibrium that reads

$$\left(i\frac{\partial}{\partial t_1} - \hat{h}_0(x_1) - \phi(1)\right)G(1,2;\phi) + i\int d3\, v_c(1,3^+)G_2(1,3^+;2,3^{++};\phi)\bigg|_{t_3=t_1} = \delta(1-2).$$

(B.36)

We consider now the change of $G(\phi)$ resulting from an infinitesimal change of the external perturbation ϕ,

$$\phi(3) \to \phi(3) + \delta\phi(3).$$

(B.37)

Then the change of $G(\phi)$ is

$$i\delta G(1,2;\phi) = \delta\frac{\left\langle \Psi_0 \left| \mathbb{T}\left[\hat{U}\hat{\psi}_H(1)\hat{\psi}_H^\dagger(2)\right] \right| \Psi_0 \right\rangle}{\langle \Psi_0 | \mathbb{T}\left[\hat{U}\right] | \Psi_0 \rangle}$$

$$= \frac{\left\langle \Psi_0 \left| \mathbb{T}\left[\delta\hat{U}\hat{\psi}_H(1)\hat{\psi}_H^\dagger(2)\right] \right| \Psi_0 \right\rangle}{\langle \Psi_0 | \mathbb{T}\left[\hat{U}\right] | \Psi_0 \rangle} - \frac{\left\langle \Psi_0 \left| \mathbb{T}\left[\delta\hat{U}\right] \right| \Psi_0 \right\rangle \left\langle \Psi_0 \left| \mathbb{T}\left[\hat{U}\hat{\psi}_H(1)\hat{\psi}_H^\dagger(2)\right] \right| \Psi_0 \right\rangle}{\langle \Psi_0 | \mathbb{T}\left[\hat{U}\right] | \Psi_0 \rangle^2}.$$

(B.38)

The functional derivative of $\hat{U}$ with respect to ϕ reads

$$\frac{\delta\hat{U}}{\delta\phi(3)} = \frac{\delta}{\delta\phi(3)}\exp\left(-i\int d1\phi(1)\hat{\rho}(1)\right) = -i\hat{\rho}(3)\hat{U}.$$

(B.39)

Then we have

$$i\frac{\delta G(1,2;\phi)}{\delta\phi(3)} = -i\frac{\left\langle \Psi_0 \middle| \mathbb{T}\left[\hat{U}\hat{\psi}_H(1)\hat{\psi}_H^\dagger(2)\rho(3)\right] \middle| \Psi_0 \right\rangle}{\langle\Psi_0|\mathbb{T}\left[\hat{U}\right]|\Psi_0\rangle}$$

$$+ i\frac{\left\langle \Psi_0 \middle| \mathbb{T}\left[\hat{U}\rho(3)\right] \middle| \Psi_0 \right\rangle \left\langle \Psi_0 \middle| \mathbb{T}\left[\hat{U}\hat{\psi}_H(1)\hat{\psi}_H^\dagger(2)\right] \middle| \Psi_0 \right\rangle}{\langle\Psi_0|\mathbb{T}\left[\hat{U}\right]|\Psi_0\rangle^2}$$

$$= i\frac{\left\langle \Psi_0 \middle| \mathbb{T}\left[\hat{U}\hat{\psi}_H(1)\hat{\psi}_H(3)\hat{\psi}_H^\dagger(3)\hat{\psi}_H^\dagger(2)\right] \middle| \Psi_0 \right\rangle}{\langle\Psi_0|\mathbb{T}\left[\hat{U}\right]|\Psi_0\rangle}$$

$$- i\frac{\left\langle \Psi_0 \middle| \mathbb{T}\left[\hat{U}\hat{\psi}_H(3)\hat{\psi}_H^\dagger(3^+)\right] \middle| \Psi_0 \right\rangle \left\langle \Psi_0 \middle| \mathbb{T}\left[\hat{U}\hat{\psi}_H(1)\hat{\psi}_H^\dagger(2)\right] \middle| \Psi_0 \right\rangle}{\langle\Psi_0|\mathbb{T}\left[\hat{U}\right]|\Psi_0\rangle^2}$$

$$= i\left(-G_2(1,3;2,3^+;\phi) + G(3,3^+;\phi)G(1,2;\phi)\right), \tag{B.40}$$

which yields

$$G_2(1,3;2,3^+;\phi) = \left(G(3,3^+;\phi) - \frac{\delta}{\delta\phi(3)}\right)G(1,2;\phi). \tag{B.41}$$

Taking the above equation back to equation (B.36), we have

$$\left(i\frac{\partial}{\partial t_1} - \hat{h}_0(x_1) - \phi(1)\right)G(1,2;\phi) + i\int d3v_c(1,3^+)\left(G(3^+,3^{++};\phi) - \frac{\delta}{\delta\phi(3)}\right)G(1,2;\phi)$$

$$= \delta(1-2).$$

When $v_c = 0$, we have the analogue to Eq. (B.15),

$$\left(i\frac{\partial}{\partial t_1} - \hat{h}_0(x_1) - \phi(1)\right)G_0(1,2;\phi) = \delta(1-2). \tag{B.42}$$

Proceeding in a similar way as in the equilibrium case, we obtain

$$G(1,2;\phi) = G_0(1,2) + \int d3G_0(1,3)\phi(3)G(3,2;\phi)$$

$$- i\int d34G_0(1,3)v_c(3,4^+)G(4,4^{++};\phi)G(3,2;\phi)$$

$$+ i\int d34G_0(1,3)v_c(3,4^+)\frac{\delta G(3,2;\phi)}{\delta\phi(4)}. \tag{B.43}$$

This full functional differential equation can be simplified by introducing the Hartree potential in presence of the external perturbation as:

$$
G(1,2;\phi) = G_0(1,2) + \int d3 G_0(1,3)\phi(3)G(3,2;\phi)
$$
$$
\int d3 G_0(1,3)V_H(3;\phi)G(3,2;\phi)
$$
$$
+ i \int d34 G_0(1,3)v_c(3,4^+)\frac{\delta G(3,2;\phi)}{\delta\phi(4)}\,, \tag{B.44}
$$

where

$$
V_H(3;\phi) = -i \int d4 v_c(3,4^+)G(4,4^{++};\phi)\,. \tag{B.45}
$$

Appendix C

New derivations

In this section, I am going to show a new way of treating the full functional differential (FDE) equation (B.44). The FDE reads

$$G(1, 2; \phi) = G_0(1, 2) + G_0(1, \bar{3})\phi(\bar{3})G(\bar{3}, 2; \phi) + G_0(1, \bar{3})V_H(\bar{3}; \phi)G(\bar{3}, 2; \phi)$$
$$+ G_0(1, \bar{3})v_c(\bar{3}, \bar{4}^+)\frac{\delta G(\bar{3}, 2; \phi)}{\delta \phi(\bar{4})}, \tag{C.1}$$

where

$$V_H(3; \phi) = -i \int \mathrm{d}4 v_c(3, 4^+)G(4, 4^{++}; \phi), \tag{C.2}$$

is the Hartree potential in presence of the external perturbation ϕ, and $f(\bar{1})g(\bar{1}) \equiv \int \mathrm{d}1 f(1)g(1)$. Note that the above equation is the exact full functional differential equation (FDE), not the linearized functional differential equation (LDE). We can introduce the Hartree Green's function in presence of ϕ using the following Dyson equation:

$$G_H(1, 2; \phi) = G_0(1, 2) + G_0(1, \bar{3})(\phi(3) + V_H(\bar{3}; \phi))G_H(\bar{3}, 2; \phi), \tag{C.3}$$

such that Eq. (C.1) can be written in terms of $G_H(1, 2; \phi)$, which reads

$$G(1, 2; \phi) = G_H(1, 2; \phi) + iG_H(1, \bar{3}; \phi)v_c(\bar{3}, \bar{4}^+)\frac{\delta G(\bar{3}, 2; \phi)}{\delta \phi(\bar{4})}, \tag{C.4}$$

Now we can introduce an *ansatz* self-energy $\tilde{\Sigma}$ and the corresponding *ansatz* Green's function $\tilde{G}$ from the following Dyson equation

$$\tilde{G}(1,2;\phi) \equiv G_H(1,2;\phi) + G_H(1,\bar{3};\phi)\tilde{\Sigma}(\bar{3},\bar{4};\phi)\tilde{G}(\bar{4},2;\phi)\,;$$

$$= G_0(1,2) + G_0(1,\bar{3})\Big(\phi(\bar{3})\delta(\bar{3},\bar{4}) + V_H(\bar{3};\phi)\delta(\bar{3},\bar{4}) + \tilde{\Sigma}(\bar{3},\bar{4};\phi)\Big)\tilde{G}(\bar{4},2;\phi)\,.$$

$$\text{(C.5)}$$

Note that, if the ansatz self-energy $\tilde{\Sigma}$ was the exact self-energy of the system, the ansatz Green's function $\tilde{G}$ would be the exact Green's function. On the other hand, if $\tilde{\Sigma}$ is some approximate self-energy, $\tilde{G}$ becomes the approximate Green's function corresponding to the self-energy, because $\tilde{G}$ and $\tilde{\Sigma}$ have the one-to-one correspondence defined by the above Dyson equation.

The quantities in the bracket of above equation (C.5) can be re-grouped into a new effective potential $\tilde{\phi}$, which reads

$$\tilde{\phi}(3,4) = \phi(3)\delta(3,4) + V_H(3;\phi)\delta(3,4) + \tilde{\Sigma}(3,4;\phi)\,. \qquad \text{(C.6)}$$

Now we can subtract and add the term $G_H\tilde{\Sigma}G$ in Eq. (C.4), leading to

$$G(1,2;\phi) = G_H(1,2;\phi) + iG_H(1,\bar{3};\phi)v_c(\bar{3},\bar{4}^+)\frac{\delta G(\bar{3},2;\phi)}{\delta\phi(\bar{4})}$$

$$+ G_H(1,\bar{3};\phi)\tilde{\Sigma}(\bar{3},\bar{4};\phi)G(\bar{4},2;\phi) - G_H(1,\bar{3};\phi)\tilde{\Sigma}(\bar{3},\bar{4};\phi)G(\bar{4},2;\phi)$$

$$= \tilde{G}(1,2;\phi) + i\tilde{G}(1,\bar{3};\phi)v_c(\bar{3},\bar{4}^+)\frac{\delta G(\bar{3},2;\phi)}{\delta\phi(\bar{4})} - \tilde{G}(1,\bar{3};\phi)\tilde{\Sigma}(\bar{3},\bar{4};\phi)G(\bar{4},2;\phi)\,.$$

$$\text{(C.7)}$$

We can now use the *chain rule* on the differential term of the above equation, yielding

$$\frac{\delta G(\bar{3},2;\phi)}{\delta\phi(\bar{4})} = \frac{\delta G(\bar{3},2;\phi)}{\delta\tilde{\phi}(\bar{5},\bar{6})}\frac{\delta\tilde{\phi}(\bar{5},\bar{6})}{\delta\phi(\bar{4})}$$

$$= \frac{\delta G(\bar{3},2;\phi)}{\delta\tilde{\phi}(\bar{5},\bar{6})}\left(\delta(4,5,6) - iv_c(\bar{5},\bar{7}^+)\delta(5,6)\frac{\delta G(\bar{7},\bar{7}^+)}{\delta\phi(\bar{4})} + \frac{\delta\tilde{\Sigma}(\bar{5},\bar{6};\phi)}{\delta\phi(\bar{4})}\right)$$

$$= \frac{\delta G(\bar{3},2;\phi)}{\delta\tilde{\phi}(\bar{5},\bar{6})}\left(\delta(4,5,6) + v_c(\bar{5},\bar{7}^+)\delta(5,6)\chi(\bar{7},\bar{4};\phi) + \frac{\delta\tilde{\Sigma}(\bar{5},\bar{6};\phi)}{\delta\phi(\bar{4})}\right)\,. \qquad \text{(C.8)}$$

224

I have used the definition of the `polarizability` in Eq. (2.26) to derive the above equation. Now plugging the above equation back to Eq. (C.7), we get

$$
\begin{aligned}
G(1,2;\phi) &= \tilde{G}(1,2;\phi) - \tilde{G}(1,\bar{3};\phi)\tilde{\Sigma}(\bar{3},\bar{4};\phi)G(\bar{4},2;\phi) \\
&\quad + i\tilde{G}(1,\bar{3};\phi)v_c(\bar{3},\bar{4}^+)\frac{\delta G(\bar{3},2;\phi)}{\delta\tilde{\phi}(\bar{5},\bar{6})}\left(\delta(4,5,6) + v_c(\bar{5},\bar{7}^+)\delta(5,6)\chi(\bar{7},\bar{4};\phi) + \frac{\delta\tilde{\Sigma}(\bar{5},\bar{6};\phi)}{\delta\phi(\bar{4})}\right) \\
&= \tilde{G}(1,2;\phi) - \tilde{G}(1,\bar{3};\phi)\tilde{\Sigma}(\bar{3},\bar{4};\phi)G(\bar{4},2;\phi) \\
&\quad + i\tilde{G}(1,\bar{3};\phi)v_c(\bar{3},\bar{4}^+)\frac{\delta G(\bar{3},2;\phi)}{\delta\tilde{\phi}(\bar{5},\bar{6})}\left(\epsilon^{-1}_{TCTC}(\bar{4},\bar{5};\phi)\delta(5,6) + \frac{\delta\tilde{\Sigma}(\bar{5},\bar{6};\phi)}{\delta\phi(\bar{4})}\right), \quad\quad \text{(C.9)}
\end{aligned}
$$

where the `test-charge test-charge` inverse dielectric function ϵ^{-1}_{TCTC} is defined in Eq. (2.25).

Up to now, we did not introduce any approximation in the FDE. The above equation is just a re-formulation of the FDE such that it is still exact. When the derivative of $\tilde{\Sigma}$ is neglected, and when ϵ^{-1}_{TCTC} is supposed to be independent of ϕ, we are back to the linearization approximation (see the LDE (3.11)).

Start from the Kohn-Sham exchange-correlation potential

Here, I am going to use for the *ansatz* self-energy the Kohn-Sham local exchange–correlation potential, i.e. $\tilde{\Sigma}(1,2) \equiv V_{xc}(1)\delta(1,2)$. Consequently $\tilde{G}(1,2) \equiv G_{ks}(1,2)$. With this choice, Eq. (C.9) becomes

$$
\begin{aligned}
G(1,2;\phi) &= G_{ks}(1,2;\phi) + iG_{ks}(1,\bar{3};\phi)v_c(\bar{3},\bar{4})\frac{\delta G(\bar{3},2;\phi)}{\delta\tilde{\phi}(\bar{5})}\left(\epsilon^{-1}_{TCTE}(\bar{4},\bar{5};\phi) + \frac{\delta V_{xc}(\bar{5};\phi)}{\delta\phi(\bar{4})}\right) \\
&\quad - G_{ks}(1,\bar{3};\phi)V_{xc}(\bar{3};\phi)G(\bar{3},2;\phi). \quad\quad\quad\quad\quad\quad\quad \text{(C.10)}
\end{aligned}
$$

We can now use the chain rule:

$$
\frac{\delta V_{xc}(5;\phi)}{\delta\phi(4)} = \frac{\delta V_{xc}(5;\phi)}{\delta\rho(\bar{6};\phi)}\frac{\delta\rho(\bar{6};\phi)}{\delta\phi(4)} = f_{xc}(5,\bar{6};\phi)\chi(\bar{6},4), \quad\quad\quad \text{(C.11)}
$$

where $f_{xc} = \delta V_{xc}/\delta\rho$ [96] is the TDDFT kernel. Plugging the above equation into Eq. (C.10), we have

$$G(1,2;\phi) = G_{ks}(1,2;\phi) + iG_{ks}(1,\bar{3};\phi)v_c(\bar{3},\bar{4})\frac{\delta G(\bar{3},2;\phi)}{\delta\tilde{\phi}(\bar{5})}\left(\epsilon_{TCTC}^{-1}(\bar{4},\bar{5};\phi) + f_{xc}(\bar{5},\bar{6};\phi)\chi(\bar{6},4)\right)$$

$$- G_{ks}(1,\bar{3};\phi)V_{xc}(\bar{3};\phi)G(\bar{3},2;\phi)$$

$$= G_{ks}(1,2;\phi) + iG_{ks}(1,\bar{3};\phi)v_c(\bar{3},\bar{4})\frac{\delta G(\bar{3},2;\phi)}{\delta\tilde{\phi}(\bar{5})}\epsilon_{TCTE}^{-1}(\bar{4},\bar{5};\phi)$$

$$- G_{ks}(1,\bar{3};\phi)V_{xc}(\bar{3};\phi)G(\bar{3},2;\phi)\,. \tag{C.12}$$

The `test-charge test-electron` inverse dielectric function is defined as $\epsilon_{TCTE}^{-1} = 1 + v_c\chi + f_{xc}\chi$ [97]. Following the idea of section 3.4, now we make an *ansatz* for the Green's function reading

$$G(1,2;\phi) = G_{ks}(1,\bar{3};\phi)\tilde{E}(\bar{3},2)\,. \tag{C.13}$$

Eq. (C.12) becomes

$$G_{ks}(1,\bar{3};\phi)\tilde{E}(\bar{3},2) = G_{ks}(1,2;\phi) - G_{ks}(1,\bar{3};\phi)V_{xc}(\bar{3};\phi)G_{ks}(\bar{3},\bar{6};\phi)\tilde{E}(\bar{6},2)$$

$$+ iG_{ks}(1,\bar{3};\phi)v_c(\bar{3},\bar{4})G_{ks}(\bar{3},\bar{5};\phi)G_{ks}(\bar{5},\bar{6};\phi)\epsilon_{TCTE}^{-1}(\bar{4},\bar{5};\phi)\tilde{E}(\bar{6},2)$$

$$= G_{ks}(1,2;\phi) - G_{ks}(1,\bar{3};\phi)V_{xc}(\bar{3};\phi)G_{ks}(\bar{3},\bar{6};\phi)\tilde{E}(\bar{6},2)$$

$$+ iG_{ks}(1,\bar{3};\phi)G_{ks}(\bar{3},\bar{5};\phi)W^{TCTE}(\bar{3},\bar{5};\phi)G_{ks}(\bar{5},\bar{6};\phi)\tilde{E}(\bar{6},2)\,. \tag{C.14}$$

For arbitrary ϕ there is no solution for $\tilde{E}$, because Eq. (C.13) is an approximation. However, for $\phi = 0$ we obtain

$$G(1,2) = G_{ks}(1,2) + G_{ks}(1,\bar{3})\left(\Sigma^{TCTE}(\bar{3},\bar{5}) - V_{xc}(\bar{3})\delta(3,5)\right)G(\bar{5},2)\,, \tag{C.15}$$

where the `test-charge test-electron` self-energy is defined as

$$\Sigma^{TCTE}(1,2) = iG_{ks}(1,2)W^{TCTE}(1,2) = iG_{ks}(1,2)\epsilon_{TCTE}^{-1}(1,\bar{3})v_c(\bar{3},2)\,, \tag{C.16}$$

following Ref. [97]. The above derivation shows that if we start from the Kohn-Sham local exchange–correlation potential, the screening that appears is $W^{TCTE} = v_c \epsilon_{TCTE}^{-1}$, instead of the test-charge test-charge one.

If the ansatz Green's function in Eq. (C.13) becomes the one that gave the retarded cumulant in Eq. (3.48), i.e.

$$G(1, 2; \phi) = \int \mathrm{d}x_3 \, G_\phi(x_1, x_3, z_1, z_2) \tilde{E}(x_3, x_2, t_1, t_2) , \qquad (C.17)$$

we obtain

$$\mathcal{G}^{RC}(t_{12}) = \mathcal{G}_{ks}^R(t_{12}) e^{it_{12}V_{xc}} \exp\left[-i \int_{t_2}^{t_1} \mathrm{d}t_4 \int_{t_4}^{t_1} \mathrm{d}t_3 \, \tilde{\Sigma}_{ii}^{R,TCTE}(t_{34})\right] . \qquad (C.18)$$

In the same way, Σ^{TCTE} should also appear in the TOC96 and TOC11. This is a very important step: it shows that we should make the self-energy that appears in the cumulant consistent with the starting Green's function. Moreover, it indicates a clear way to obtain better and better approximations. In practice, one should start from the best available self-energy, $\tilde{\Sigma}$ (e.g. V_{xc}, G_0W_0, etc.). Eq. (C.18) or equivalent tells us how to use this self-energy in a cumulant form. If one had guessed the exact self-energy to start with, $\tilde{\Sigma} = \Sigma$ and the correction would be zero, such that there will not be any double counting.

This suggests to first introduce the definitions of two different response functions:

$$\chi^{RPA}(1, 2) = \chi_0(1, 2) + \chi_0(1, \bar{3}) v_c(\bar{3}, \bar{4}) \chi^{RPA}(\bar{4}, 2) ; \qquad (C.19a)$$

$$\chi^{TCTC}(1, 2) = \chi_0(1, 2) + \chi_0(1, \bar{3}) \left[v_c(\bar{3}, \bar{4}) + f_{xc}^{LDA}(\bar{3}, \bar{4})\right] \chi^{TCTC}(\bar{4}, 2) ; \qquad (C.19b)$$

where $\chi_0 \equiv G_{ks}^{LDA} G_{ks}^{LDA}$, and $f_{xc}^{LDA} \equiv \delta V_{xc}^{LDA}/\delta\rho$.

Then the three different approximate screening Ws used in this thesis are defined as

$$W^{RPA}(1, 2) = \left[\delta(1, 3) + v_c(1, \bar{4}) \chi^{RPA}(\bar{4}, 3)\right] v_c(\bar{3}, 2) ; \qquad (C.20a)$$

$$W^{TCTC}(1, 2) = \left[\delta(1, 3) + v_c(1, \bar{4}) \chi^{TCTC}(\bar{4}, 3)\right] v_c(\bar{3}, 2) ; \qquad (C.20b)$$

$$W^{TCTE}(1, 2) = \left[\delta(1, 3) + v_c(1, \bar{4}) \chi^{TCTC}(\bar{4}, 3) + f_{xc}(1, \bar{4}) \chi^{TCTC}(\bar{4}, 3)\right] v_c(\bar{3}, 2) . \qquad (C.20c)$$

Appendix D

The relations between time-ordered and retarded quantities

D.1 General relations

The `time-ordered` and `retarded` quantities used in this thesis are defined as follows:

$$G^T(1,2) = \theta(t_1 - t_2)G^>(1,2) + \theta(t_2 - t_1)G^<(1,2) \equiv G^e(1,2) + G^h(1,2)\,; \quad \text{(D.1a)}$$

$$G^R(1,2) = \theta(t_1 - t_2)\big(G^>(1,2) - G^<(1,2)\big)\,; \quad \text{(D.1b)}$$

$$W_c^T(1,2) = \theta(t_1 - t_2)W^>(1,2) + \theta(t_2 - t_1)W^<(1,2) \equiv W_c^e(1,2) + W_c^h(1,2)\,; \quad \text{(D.1c)}$$

$$W_c^R(1,2) = \theta(t_1 - t_2)\big(W^>(1,2) - W^<(1,2)\big)\,; \quad \text{(D.1d)}$$

$$\Sigma_c^T(1,2) = \theta(t_1 - t_2)\Sigma^>(1,2) + \theta(t_2 - t_1)\Sigma^<(1,2) \equiv \Sigma_c^e(1,2) + \Sigma_c^h(1,2)\,; \quad \text{(D.1e)}$$

$$\Sigma_c^R(1,2) = \theta(t_1 - t_2)\big(\Sigma^>(1,2) - \Sigma^<(1,2)\big)\,. \quad \text{(D.1f)}$$

The subscript c in the screened interaction W and self-energy Σ represent the correlation part because only the correlation part is time-dependent.

In frequency domain, these quantities have their spectral representations defined as:

$$G^T(\omega) = \int_{-\infty}^{\mu} d\omega' \frac{A(\omega')}{\omega - \omega' - i\eta} + \int_{\mu}^{\infty} d\omega' \frac{A(\omega')}{\omega - \omega' + i\eta} \equiv G^h(\omega) + G^e(\omega) \,; \tag{D.2a}$$

$$G^R(\omega) = \int_{-\infty}^{\mu} d\omega' \frac{A(\omega')}{\omega - \omega' + i\eta} + \int_{\mu}^{\infty} d\omega' \frac{A(\omega')}{\omega - \omega' + i\eta} \equiv G^<(\omega) + G^>(\omega) \,; \tag{D.2b}$$

$$W_c^T(\omega) = \int_{-\infty}^{\mu} d\omega' \frac{B(\omega')}{\omega - \omega' - i\eta} + \int_{\mu}^{\infty} d\omega' \frac{B(\omega')}{\omega - \omega' + i\eta} \equiv W_c^h(\omega) + W_c^e(\omega) \,; \tag{D.2c}$$

$$W_c^R(\omega) = \int_{-\infty}^{\mu} d\omega' \frac{B(\omega')}{\omega - \omega' + i\eta} + \int_{\mu}^{\infty} d\omega' \frac{B(\omega')}{\omega - \omega' + i\eta} \equiv W_c^<(\omega) + W_c^>(\omega) \,; \tag{D.2d}$$

$$\Sigma_c^T(\omega) = \int_{-\infty}^{\mu} d\omega' \frac{D(\omega')}{\omega - \omega' - i\eta} + \int_{\mu}^{\infty} d\omega' \frac{D(\omega')}{\omega - \omega' + i\eta} \equiv \Sigma_c^h(\omega) + \Sigma_c^e(\omega) \,; \tag{D.2e}$$

$$\Sigma_c^R(\omega) = \int_{-\infty}^{\mu} d\omega' \frac{D(\omega')}{\omega - \omega' + i\eta} + \int_{\mu}^{\infty} d\omega' \frac{D(\omega')}{\omega - \omega' + i\eta} \equiv \Sigma_c^<(\omega) + \Sigma_c^>(\omega) \,. \tag{D.2f}$$

Note that $\mathrm{Im}\,\Sigma_c^e(\omega) = \mathrm{Im}\,\Sigma_c^>(\omega)$ but $\mathrm{Im}\,\Sigma_c^h(\omega) = -\,\mathrm{Im}\,\Sigma_c^<(\omega)$.

The spectral functions of G, W_c and Σ_c are

$$A(\omega) = -\frac{1}{\pi}\mathrm{Im}G(\omega)\mathrm{sgn}(\omega - \mu)\,, \tag{D.3a}$$

$$B(\omega) = -\frac{1}{\pi}\mathrm{Im}W_c(\omega)\mathrm{sgn}(\omega - \mu)\,, \tag{D.3b}$$

$$D(\omega) = -\frac{1}{\pi}\,\mathrm{Im}\,\Sigma_c(\omega)\mathrm{sgn}(\omega - \mu)\,. \tag{D.3c}$$

D.2 The relations in the HPC-2

The retarded Hartree Green's function of the two-level hole-plasmon coupling Hamiltonian reads

$$G_H^R(t_{12}) = \theta(t_1 - t_2)\big(G_H^>(t_{12}) - G_H^<(t_{12})\big)\,,$$

where

$$G^<_{H,+}(t_{12}) = ie^{-i\varepsilon^H_+(t_1-t_2)} \, ;$$

$$G^>_{H,+}(t_{12}) = 0 \, ;$$

$$G^<_{H,-}(t_{12}) = 0 \, ;$$

$$G^>_{H,-}(t_{12}) = -ie^{-i\varepsilon^H_-(t_1-t_2)} \, .$$

Note that $\varepsilon^H_\pm \equiv \varepsilon_0 \pm \mathbf{t}$ in the two-level model. The plasmon propagator of the two-level model in retarded form reads

$$W^R(t_{12}) = \theta(t_1-t_2)\left(W^>(t_{12}) - W^<(t_{12})\right) \, ; \tag{D.4}$$

$$W^>(t_{12}) = -i\tilde{g}^2 e^{-i\omega_p(t_1-t_2)} \, , \tag{D.5}$$

$$W^<(t_{12}) = -i\tilde{g}^2 e^{i\omega_p(t_1-t_2)} \, . \tag{D.6}$$

The retarded GW self-energy in time domain can be calculated from

$$\begin{aligned}
\Sigma^R(t_{12}) &= \theta(t_1-t_2)\left(\Sigma^>(t_{12}) - \Sigma^<(t_{12})\right), \\
&= i\theta(t_1-t_2)\left(G^>_H(t_{12})W^>(t_{12}) - G^<_H(t_{12})W^<(t_{12})\right), \\
&= -i\tilde{g}^2\theta(t_1-t_2)\left(e^{-i(\omega_p+2\mathbf{t})(t_1-t_2)} + e^{i\omega_p(t_1-t_2)}\right). \tag{D.7}
\end{aligned}$$

Fourier transforming the above self-energy to frequency domain, we have

$$\begin{aligned}
\Sigma^R(\omega) &= \frac{\tilde{g}^2}{2\pi}\int \mathrm{d}\tau \int \mathrm{d}\omega' \frac{e^{-i\omega'\tau}}{\omega'+i\eta}\left(e^{-i(\varepsilon^H_-+\omega_p)\tau} + e^{-i(\varepsilon^H_+-\omega_p)\tau}\right)e^{i\omega\tau}, \\
&= \frac{\tilde{g}^2}{2\pi}\int \mathrm{d}\tau \int \mathrm{d}\omega' \left(\frac{e^{-i(\varepsilon^H_-+\omega_p-\omega+\omega')\tau}}{\omega'+i\eta} + \frac{e^{-i(\varepsilon^H_+-\omega_p-\omega+\omega')\tau}}{\omega'+i\eta}\right), \\
&= \tilde{g}^2 \int \mathrm{d}\omega' \left(\frac{\delta(\varepsilon^H_-+\omega_p-\omega+\omega')}{\omega'+i\eta} + \frac{\delta(\varepsilon^H_+-\omega_p-\omega+\omega')}{\omega'+i\eta}\right), \\
&= \frac{\tilde{g}^2}{\omega-(\varepsilon^H_-+\omega_p)+i\eta} + \frac{\tilde{g}^2}{\omega-(\varepsilon^H_+-\omega_p)+i\eta} = \Sigma^>(\omega) + \Sigma^<(\omega), \tag{D.8}
\end{aligned}$$

230

where I have used

$$\int \mathrm{d}\tau \, e^{\pm i\omega\tau} = 2\pi\delta(\pm\omega) \,, \tag{D.9}$$

$$\delta(-\omega) = \delta(\omega) \,. \tag{D.10}$$

Appendix E

List of publications

- Jianqiang Sky Zhou, J. Kas, Lorenzo Sponza, Igor Reshetnyak, Matteo Guzzo, Christine Giorgetti, Matteo Gatti, Francessco Sottile, J. J. Rehr, and Lucia Reining, *Dynamical effects in electron spectroscopy*, J. Chem. Phys. **143** 184109 (2015).

- Jianqiang Sky Zhou and Lucia Reining, *Dyson equations or cumulants? A unified view on the calculation of spectral functions*, in preparation.

- Jianqiang Sky Zhou and Lucia Reining, *An improved description of the coupling of excitations: the constrained retarded cumulant*, in preparation.

- Jianqiang Sky Zhou and Lucia Reining, *Total energies of the GW and cumulant expansion approximations from a fermion-boson coupling perspective*, in preparation.

- Jianqiang Sky Zhou, Matteo Guzzo, Matteo Gatti, and Lucia Reining, *Plasmon satellites in sodium: beyond the random phase approximation*, in preparation.

Bibliography

[1] A. L. Fetter and J. D. Walecka. *Quantum Theory of Many-particle Systems.* McGraw-Hill, New York, 1971.

[2] Gerald D. Mahan. *Many-Particle Physics.* Plenum, New York, N.Y., 3nd edition, 2000.

[3] E.N. Economou. *Green's Functions in Quantum Physics, 2nd Ed.* Springer-Verlag, Berlin, 1992.

[4] S. Hüfner. *Photoelectron Spectroscopy: Principles and Applications.* Advanced Texts in Physics. Springer, 2003.

[5] Lars Hedin. New method for calculating the one-particle green's function with application to the electron-gas problem. *Phys. Rev.*, 139:A796–A823, Aug 1965.

[6] F Aryasetiawan and O Gunnarsson. The gw method. *Reports on Progress in Physics*, 61(3):237, 1998.

[7] Wilfried G. Aulbur, Lars Jnsson, and John W. Wilkins. Quasiparticle calculations in solids. volume 54 of *Solid State Physics*, pages 1 – 218. Academic Press, 1999.

[8] P. Hohenberg and W. Kohn. Inhomogeneous electron gas. *Phys. Rev.*, 136:B864–B871, Nov 1964.

[9] F. Aryasetiawan, L. Hedin, and K. Karlsson. Multiple plasmon satellites in na and al spectral functions from *Ab Initio* cumulant expansion. *Phys. Rev. Lett.*, 77:2268–2271, Sep 1996.

[10] M Vos, A S Kheifets, E Weigold, S A Canney, B Holm, F Aryasetiawan, and K Karlsson. Determination of the energy-momentum densities of aluminium by electron momentum spectroscopy. *Journal of Physics: Condensed Matter*, 11(18):3645, 1999.

[11] Matteo Guzzo, Giovanna Lani, Francesco Sottile, Pina Romaniello, Matteo Gatti, Joshua J. Kas, John J. Rehr, Mathieu G. Silly, Fausto Sirotti, and Lucia Reining. Valence electron photoemission spectrum of semiconductors: *Ab Initio* description of multiple satellites. *Phys. Rev. Lett.*, 107:166401, Oct 2011.

[12] Johannes Lischner, Derek Vigil-Fowler, and Steven G. Louie. Physical origin of satellites in photoemission of doped graphene: An *Ab Initio gw* plus cumulant study. *Phys. Rev. Lett.*, 110:146801, Apr 2013.

[13] L. Hedin, B.I. Lundqvist, and S. Lundqvist. New structure in the single-particle spectrum of an electron gas. *Solid State Communications*, 5(4):237 – 239, 1967.

[14] B.I. Lundqvist. Single-particle spectrum of the degenerate electron gas. *Physik der kondensierten Materie*, 6(3):193–205, 1967.

[15] Clas Blomberg and Birger Bergersen. Spurious structure from approximations to the dyson equation. *Canadian Journal of Physics*, 50(19):2286–2293, 1972.

[16] D. C. Langreth. Singularities in x-ray spectra of metals. *Phys. Rev. B*, 1:471, 1970.

[17] Matteo Guzzo. *Dynamical correlation in solids: a perspective in photoelectron spectroscopy*. Theses, Ecole Polytechnique X, October 2012. 178 pages.

[18] Giovanna Lani. *Towards a novel approach for the calculation of many-body Green's functions*. Theses, Ecole Polytechnique X, November 2011.

[19] J. J. Kas, J. J. Rehr, and L. Reining. Cumulant expansion of the retarded one-electron green function. *Phys. Rev. B*, 90:085112, Aug 2014.

[20] Jianqiang Sky Zhou, J. J. Kas, Lorenzo Sponza, Igor Reshetnyak, Matteo Guzzo, Christine Giorgetti, Matteo Gatti, Francesco Sottile, J. J. Rehr, and Lucia Reining. Dynamical effects in electron spectroscopy. *The Journal of Chemical Physics*, 143(18), 2015.

[21] Hertz, H. *Ann. Phys.*, 17:983, 1887.

[22] Einstein, A. *Ann. Phys.*, 31:132, 1905.

[23] M. Cardona and L. Ley. *Photoemission in solids: General principles*. Topics in applied physics. Springer-Verlag, 1978.

[24] Andrea Damascelli, Zahid Hussain, and Zhi-Xun Shen. Angle-resolved photoemission studies of the cuprate superconductors. *Rev. Mod. Phys.*, 75:473–541, Apr 2003.

[25] Vladimir N. Strocov, Masaki Kobayashi, Xiaoqiang Wang, Leonid L. Lev, Juraj Krempasky, Victor V. Rogalev, Thorsten Schmitt, Claudia Cancellieri, and Mathilde L. Reinle-Schmitt. Soft-x-ray arpes at the swiss light source: From 3d materials to buried interfaces and impurities. *Synchrotron Radiation News*, 27(2):31–40, 2014.

[26] Saiht. An experimental setup of angle-resolved photoemission spectroscopy — Wikipedia, the free encyclopedia, 2009. [Online; accessed 15 June 2009].

[27] Simo Huotari, J. Aleksi Soininen, Tuomas Pylkkänen, Keijo Hämäläinen, Arezki Issolah, Andrey Titov, Jeremy McMinis, Jeongnim Kim, Ken Esler, David M. Ceperley, Markus Holzmann, and Valerio Olevano. Momentum distribution and renormalization factor in sodium and the electron gas. *Phys. Rev. Lett.*, 105:086403, Aug 2010.

[28] H. Höchst, P. Steiner, and S. Hüfner. Xps investigation of simple metals. *Zeitschrift fr Physik B Condensed Matter*, 30(2):145–154, 1978.

[29] P. NOZIÈRES and C. T. DE DOMINICIS. Singularities in the x-ray absorption and emission of metals. iii. one-body theory exact solution. *Phys. Rev.*, 178:1097–1107, Feb 1969.

[30] P Minnhagen. Aspects on diagrammatic expansion for models related to a homogeneous electron gas. *Journal of Physics C: Solid State Physics*, 8(10):1535, 1975.

[31] Lars Hedin. Effects of recoil on shake-up spectra in metals. *Physica Scripta*, 21(3-4):477, 1980.

[32] F. Bechstedt. Electronic relaxation effects in core level spectra of solids. *physica status solidi (b)*, 112(1):9–49, 1982.

[33] C.-O. Almbladh and L. Hedin. *Handbook on Synchrotron Radiation*, chapter 8. North-Holland, Amsterdam, 1983.

[34] Lars Hedin. On correlation effects in electron spectroscopies and the gw approximation. *Journal of Physics: Condensed Matter*, 11(42):R489, 1999.

[35] C. N. Berglund and W. E. Spicer. Photoemission studies of copper and silver: Theory. *Phys. Rev.*, 136:A1030–A1044, Nov 1964.

[36] M. Guzzo, J.J. Kas, F. Sottile, M.G. Silly, F. Sirotti, J.J. Rehr, and L. Reining. Plasmon satellites in valence-band photoemission spectroscopy. *The European Physical Journal B*, 85(9), 2012.

[37] L. Hedin, J. Michiels, and J. Inglesfield. Transition from the adiabatic to the sudden limit in core-electron photoemission. *Phys. Rev. B*, 58:15565–15582, Dec 1998.

[38] A.B. Migdal V.M. Galitskii. Application of quantum field theory methods to the many body problem. *JETP and ZhETF(Russian original)*, 7:96, July 1958.

[39] M. Born and R. Oppenheimer. *Ann. Phys.*, 84:457, 1927.

[40] R.M. Dreizler and E.K.U. Gross. *Density Functional Theory*. Springer Verlag, Berlin, 1990.

[41] Robert van Leeuwen. Density functional approach to the many-body problem: Key concepts and exact functionals. volume 43 of *Advances in Quantum Chemistry*, pages 25 – 94. Academic Press, 2003.

[42] Klaus Capelle. A bird's-eye view of density-functional theory. *Brazilian Journal of Physics*, 36:1318 – 1343, 12 2006.

[43] X. Gonze, B. Amadon, P.-M. Anglade, J.-M. Beuken, F. Bottin, P. Boulanger, F. Bruneval, D. Caliste, R. Caracas, M. Ct, T. Deutsch, L. Genovese, Ph. Ghosez, M. Giantomassi, S. Goedecker, D.R. Hamann, P. Hermet, F. Jollet, G. Jomard, S. Leroux, M. Mancini, S. Mazevet, M.J.T. Oliveira, G. Onida, Y. Pouillon, T. Rangel, G.-M. Rignanese, D. Sangalli, R. Shaltaf, M. Torrent, M.J. Verstraete, G. Zerah, and J.W. Zwanziger. Abinit: First-principles approach to material and nanosystem properties. *Computer Physics Communications*, 180(12):2582 – 2615, 2009. 40 YEARS OF CPC: A celebratory issue focused on quality software for high performance, grid and novel computing architectures.

[44] W. Kohn and L. J. Sham. Self-consistent equations including exchange and correlation effects. *Phys. Rev.*, 140:A1133–A1138, Nov 1965.

[45] C.-O. Almbladh and U. von Barth. Exact results for the charge and spin densities, exchange-correlation potentials, and density-functional eigenvalues. *Phys. Rev. B*, 31:3231–3244, Mar 1985.

[46] D. M. Ceperley and B. J. Alder. Ground state of the electron gas by a stochastic method. *Phys. Rev. Lett.*, 45:566–569, Aug 1980.

[47] P. Steiner, H. Höchst, and S. Hüfner. Xps investigation of simple metals. *Zeitschrift für Physik B Condensed Matter*, 30(2):129–143, 1978.

[48] In-Whan Lyo and E. W. Plummer. Quasiparticle band structure of na and simple metals. *Phys. Rev. Lett.*, 60:1558–1561, Apr 1988.

[49] M. van Schilfgaarde, Takao Kotani, and S. Faleev. Quasiparticle self-consistent *gw* theory. *Phys. Rev. Lett.*, 96:226402, Jun 2006.

[50] Mois I. Aroyo, Asen Kirov, Cesar Capillas, J. M. Perez-Mato, and Hans Wondratschek. Bilbao Crystallographic Server. II. Representations of crystallographic point groups and space groups. *Acta Crystallographica Section A*, 62(2):115–128, Mar 2006.

[51] Mois I. Aroyo, Danel Orobengoa, Gemma de la Flor, Emre S. Tasci, J. Manuel Perez-Mato, and Hans Wondratschek. Brillouin-zone database on the *Bilbao Crystallographic Server*. *Acta Crystallographica Section A*, 70(2):126–137, Mar 2014.

[52] John P. Perdew, Robert G. Parr, Mel Levy, and Jose L. Balduz. Density-functional theory for fractional particle number: Derivative discontinuities of the energy. *Phys. Rev. Lett.*, 49:1691–1694, Dec 1982.

[53] G. Strinati. Application of the green's functions method to the study of the optical properties of semiconductors. *La Rivista del Nuovo Cimento (1978-1999)*, 11(12):1–86, 2008.

[54] J. Schwinger. *Proceedings of the National Accademy of Science*, 37:452, 1951.

[55] David M. Ceperley Richard M. Martin, Lucia Reining. *Interacting electrons: theory and computational approaches*. Cambridge University Press, 2016.

[56] David Bohm and David Pines. A collective description of electron interactions: Iii. coulomb interactions in a degenerate electron gas. *Phys. Rev.*, 92:609–625, Nov 1953.

[57] Jens Lindhard. *On the properties of a gas of charged particles*. Kbenhavn, E. Munksgaard, 1954.

[58] N.W. Ashcroft and N.D. Mermin. *Solid state physics*. Science: Physics. Saunders College, 1976.

[59] P Minnhagen. Vertex correction calculations for an electron gas. *Journal of Physics C: Solid State Physics*, 7(17):3013, 1974.

[60] G. Stefanucci, Y. Pavlyukh, A.-M. Uimonen, and R. van Leeuwen. Diagrammatic expansion for positive spectral functions beyond *gw*: Application to vertex corrections in the electron gas. *Phys. Rev. B*, 90:115134, Sep 2014.

[61] Stephen L. Adler. Quantum theory of the dielectric constant in real solids. *Phys. Rev.*, 126:413–420, Apr 1962.

[62] Nathan Wiser. Dielectric constant with local field effects included. *Phys. Rev.*, 129:62–69, Jan 1963.

[63] A. G. Marinopoulos, L. Reining, V. Olevano, A. Rubio, T. Pichler, X. Liu, M. Knupfer, and J. Fink. Anisotropy and interplane interactions in the dielectric response of graphite. *Phys. Rev. Lett.*, 89:266406, AUG 12 2002.

[64] R. Hambach, C. Giorgetti, N. Hiraoka, Y. Q. Cai, F. Sottile, A. G. Marinopoulos, F. Bechstedt, and Lucia Reining. Anomalous angular dependence of the dynamic structure factor near bragg reflections: Graphite. *Phys. Rev. Lett.*, 101:266406, Dec 2008.

[65] C. Kramberger, R. Hambach, C. Giorgetti, M. H. Rümmeli, M. Knupfer, J. Fink, B. Büchner, Lucia Reining, E. Einarsson, S. Maruyama, F. Sottile, K. Hannewald, V. Olevano, A. G. Marinopoulos, and T. Pichler. Linear plasmon dispersion in single-wall carbon nanotubes and the collective excitation spectrum of graphene. *Phys. Rev. Lett.*, 100:196803, May 2008.

[66] S. Waidmann, M. Knupfer, B. Arnold, J. Fink, A. Fleszar, and W. Hanke. Local-field effects and anisotropic plasmon dispersion in diamond. *Phys. Rev. B*, 61:10149–10153, Apr 2000.

[67] H. Dröge, A. Fleszar, W. Hanke, M. Sing, M. Knupfer, J. Fink, F. Goschenhofer, C. R. Becker, R. Kargerbauer, and H. P. Steinrück. Complex loss function of cdte. *Phys. Rev. B*, 59:5544–5550, Feb 1999.

[68] Matteo Gatti, Giancarlo Panaccione, and Lucia Reining. Effects of low-energy excitations on spectral properties at higher binding energy: The metal-insulator transition of vo2. *Phys. Rev. Lett.*, 114:116402, Mar 2015.

[69] B. Bergersen, F. W. Kus, and C. Blomberg. Single particle green's function in the electronplasmon approximation. *Canadian Journal of Physics*, 51(1):102–110, 1973.

[70] Hong Jiang, Ricardo I. Gomez-Abal, Patrick Rinke, and Matthias Scheffler. First-principles modeling of localized d states with the gw@LDA + u approach. *Phys. Rev. B*, 82:045108, Jul 2010.

[71] Hong Jiang. Electronic band structures of molybdenum and tungsten dichalcogenides by the gw approach. *The Journal of Physical Chemistry C*, 116(14):7664–7671, 2012.

[72] B. Holm and U. von Barth. Fully self-consistent GW self-energy of the electron gas. *Phys. Rev. B*, 57:2108–2117, Jan 1998.

[73] Matteo Gatti and Matteo Guzzo. Dynamical screening in correlated metals: Spectral properties of srvo$_3$ in the gw approximation and beyond. *Phys. Rev. B*, 87:155147, Apr 2013.

[74] Fabien Bruneval and Matteo Gatti. Quasiparticle self-consistent gw method for the spectral properties of complex materials. In Cristiana Di Valentin, Silvana Botti, and Matteo Cococcioni, editors, *First Principles Approaches to Spectroscopic Properties of Complex Materials*, volume 347 of *Topics in Current Chemistry*, pages 99–135. Springer Berlin Heidelberg, 2014.

[75] T. J. Pollehn, A Schindlmayr, and R. W. Godby. Assessment of the gw approximation using hubbard chains. *J. Phys. Cond. Matter*, 10:1273–1283, FEB 16 1998.

[76] M. Vos, A. S. Kheifets, E. Weigold, and F. Aryasetiawan. Electron correlation effects in the spectral momentum density of graphite. *Phys. Rev. B*, 63:033108, Jan 2001.

[77] O. Gunnarsson, V. Meden, and K. Schönhammer. Corrections to migdal's theorem for spectral functions: A cumulant treatment of the time-dependent green's function. *Phys. Rev. B*, 50:10462–10473, Oct 1994.

[78] Fabio Caruso, Henry Lambert, and Feliciano Giustino. Band structures of plasmonic polarons. *Phys. Rev. Lett.*, 114:146404, Apr 2015.

[79] Marco Cazzaniga. *gw* and beyond approaches to quasiparticle properties in metals. *Phys. Rev. B*, 86:035120, Jul 2012.

[80] Leo F Kadanoff. *Quantum statistical mechanics green's function methods in equilibrium and nonequilibrium problems*. Frontiers in physics. Benjamin-Cummings publ. comp, London Amsterdam Don Mills [etc...], 1962.

[81] G. Lani, P. Romaniello, and L. Reining. Approximations for many-body green's functions: insights from the fundamental equations. *New J. Phys.*, 14, JAN 25 2012.

[82] Gianluca Stefanucci and Robert van Leeuwen. *Nonequilibrium Many-Body Theory of Quantum Systems: A Modern Introduction*. Cambridge University Press, 1 edition, April 2013.

[83] Jørgen Rammer. *Quantum Field Theory of Non-Equilibrium States*. Cambridge Univ., Cambridge, 2007.

[84] D. C. Langreth. Linear and nonlinear response theory with application. In J. T. Devreese and V. E. van Doren, editors, *Linear and Nonlinear Electron Transport in Solids*, pages 3–32. Plenum Press, New York, 1976.

[85] B. I. Lundqvist. Single-particle spectrum of the degenerate electron gas. *Physik der kondensierten Materie*, 6(3):206–217.

[86] Antoine Georges and Gabriel Kotliar. Hubbard model in infinite dimensions. *Phys. Rev. B*, 45:6479–6483, Mar 1992.

[87] M. Jarrell. Hubbard model in infinite dimensions: A quantum monte carlo study. *Phys. Rev. Lett.*, 69:168–171, Jul 1992.

[88] Antoine Georges, Gabriel Kotliar, Werner Krauth, and Marcelo J. Rozenberg. Dynamical mean-field theory of strongly correlated fermion systems and the limit of infinite dimensions. *Rev. Mod. Phys.*, 68:13–125, Jan 1996.

[89] Michele Casula, Alexey Rubtsov, and Silke Biermann. Dynamical screening effects in correlated materials: Plasmon satellites and spectral weight transfers from a green's function ansatz to extended dynamical mean field theory. *Phys. Rev. B*, 85:035115, Jan 2012.

[90] H. Ness, L. K. Dash, M. Stankovski, and R. W. Godby. *gw* approximations and vertex corrections on the keldysh time-loop contour: Application for model systems at equilibrium. *Phys. Rev. B*, 84:195114, Nov 2011.

[91] Arno Schindlmayr. Violation of particle number conservation in the GW approximation. *Phys. Rev. B*, 56:3528–3531, Aug 1997.

[92] Matteo Guzzo. Sf repository. `https://github.com/teoguso/SF_public_2016`, 2016.

[93] J. J. Kas, A. P. Sorini, M. P. Prange, L. W. Cambell, J. A. Soininen, and J. J. Rehr. Many-pole model of inelastic losses in x-ray absorption spectra. *Phys. Rev. B*, 76:195116, Nov 2007.

[94] Marco Cazzaniga, Hans-Christian Weissker, Simo Huotari, Tuomas Pylkkänen, Paolo Salvestrini, Giulio Monaco, Giovanni Onida, and Lucia Reining. Dynamical response function in sodium and aluminum from time-dependent density-functional theory. *Phys. Rev. B*, 84:075109, Aug 2011.

[95] Simo Huotari, Marco Cazzaniga, Hans-Christian Weissker, Tuomas Pylkkänen, Harald Müller, Lucia Reining, Giovanni Onida, and Giulio Monaco. Dynamical response function in sodium studied by inelastic x-ray scattering spectroscopy. *Phys. Rev. B*, 84:075108, Aug 2011.

[96] Francesco Sottile, Valerio Olevano, and Lucia Reining. Parameter-free calculation of response functions in time-dependent density-functional theory. *Phys. Rev. Lett.*, 91:056402, Jul 2003.

[97] R. Del Sole, Lucia Reining, and R. W. Godby. $GW\Gamma$ approximation for electron self-energies in semiconductors and insulators. *Phys. Rev. B*, 49:8024–8028, Mar 1994.

[98] R.W.G. Wyckoff. *Crystal structures*, volume 1. Interscience Publishers, New York, second edition, 1963.

[99] N. Troullier and José Luís Martins. Efficient pseudopotentials for plane-wave calculations. *Phys. Rev. B*, 43:1993–2006, Jan 1991.

[100] Matteo Gatti, Ilya V. Tokatly, and Angel Rubio. Sodium: A charge-transfer insulator at high pressures. *Phys. Rev. Lett.*, 104:216404, May 2010.

[101] B. Holm and F. Aryasetiawan. Total energy from the galitskii-migdal formula using realistic spectral functions. *Phys. Rev. B*, 62:4858–4865, Aug 2000.

[102] Takashi Miyake, Ferdi Aryasetiawan, Hiori Kino, and Kiyoyuki Terakura. Total energy from the many-body perturbation approach with a model spectral function: An application to simple metals. *Phys. Rev. B*, 64:233109, Nov 2001.

[103] E.K.U. Gross, E. Runge, and O. Heinonen. *Many-Particle Theory,*. Taylor & Francis, 1991.

[104] Niko Skkinen, Yang Peng, Heiko Appel, and Robert van Leeuwen. Many-body greens function theory for electron-phonon interactions: Ground state properties of the holstein dimer. *The Journal of Chemical Physics*, 143(23), 2015.

[105] Bengt Holm. Total energies from GW calculations. *Phys. Rev. Lett.*, 83:788–791, Jul 1999.

Titre : Théory de la spectroscopie électronique au-delà de l'état de l'art

Mots clés : spectroscopie théorique, la fonction de Green, couplage fermion-plasmon, cumulants

Résumé : Le sujet de cette thèse se place dans le cadre de la spectroscopie théorique. En particulier, je propose une nouvelle dérivation *ab-initio* pour trouver des approximations pour la fonction de Green à un corps. Cette approche conduit à une meilleure description du couplage fermion-plasmon dans le cadre de la théorie des perturbations à plusieurs corps, qui peut être utilisée pour étudier la spectroscopie de photoémission directe et inverse. En spectroscopie de photoémission, un échantillon est irradié par des photons et des électrons sont émis. A partir de la différence d'énergie du photon incident et des d'électrons sortant, un grand nombre d'informations sur les propriétés de l'échantillon peut être obtenu. Dans le cadre de cette thèse, on peut imaginer que, premièrement, la photoémission crée un trou dans l'échantillon, ce qui provoque la relaxation de tous les électrons restants. En raison de l'interaction attractive entre les trous et les électrons, les électrons se déplacent vers les trous et créent des "quasi-particules". L'interaction effective entre les quasi-particules est l'interaction de Coulomb écrantée dynamiquement, au lieu de l'interaction de Coulomb nue. Par conséquent, la structure de bandes observée est celle de quasi-particules, qui diffère du résultat en particules indépendantes. Deuxièmement, lorsque le trou se propage dans l'échantillon les électrons restants peuvent présenter des oscillations collectives : réponse de la densité à la perturbation. Ce sont des excitations neutres avec une nature approximativement bosonique. Le couplage du trou avec les excitations neutres conduit à des structures supplémentaires dans le spectre de photoémission, appelées satellites. Cela réduit le poids des quasi-particules qui est maintenant fractionnée. Le plus souvent, les satellites dominants sont dus à des plasmons, des oscillations collectives à longue portée. Cela montre que pour avoir une bonne description de la spectroscopie de photoémission, nous devrions étudier la propagation de particules, ainsi que l'interaction entre les particules et les plasmons ou d'autres excitations. La fonction de Green donne l'amplitude de probabilité de particules se propageant d'un point à un autre. Sa partie imaginaire donne la funtion spectrale qui a un lien direct vers le spectre mesuré dans une expérience de photoémission. Les dérivations et approximations proposées dans cette thèse donnent une nouvelle façon de calculer la fonction de Green, ce qui améliore la description de la spectroscopie de photoémission. En outre, cela permet d'accéder d'autres grandeurs qui peuvent être obtenues à partir de la fonction de Green à un corps, en particulier les énergies totales.

Title: Theory of electron spectroscopy beyond the state-of-the-art

Keywords: theoretical spectroscopy, Green's function, fermion-plasmon coupling, cumulants

Abstract: The topic of this thesis is situated in the framework of theoretical spectroscopy. In particular, I propose a new *ab-initio* derivation to find approximations for the one-body Green's function (GF). This approach leads to an improved description of fermion-plasmon coupling in the framework of many-body perturbation theory (MBPT), which can be used to study direct and inverse photoemission spectroscopy. In photoemission, a sample is irradiated by photons and electrons are emitted. From the energy difference of the incoming photon and outgoing electron, a great deal of information on the properties of the sample can be obtained. In this thesis one can imagine that first, the photoemission creates a hole in the sample, which causes all remaining electrons to relax. Due to the attractive interaction between electron and hole, the electrons move toward the holes and dress them to create "quasi-particles". The effective interaction between quasi-particles is the dynamically screened Coulomb interaction instead of the bare one. Second, when the hole propagates in the sample the remaining electrons can show collective oscillations, the density response to the perturbation. These are neutral excitations with approximately bosonic nature. The coupling of the hole to the neutral excitations leads to additional structures in the photoemission spectrum, called satellites. Most often, the dominant satellites are due to plasmons, collective long-range oscillations. This overview shows that in order to have a good description of photoemission, we should study the propagation of particles, as well as the interaction between particles and plasmons or other excitations. The Green's function gives the probability amplitude of particles propagating from one point to another. Its imaginary part yields the spectral function that has a direct link to the spectrum measured in a photoemission experiment. The derivations and approximations proposed in this thesis give a new way to calculate the Green's function, which improves the description of photoemission. Moreover, it gives access to other quantities that can be obtained from the Green's function, in particular total energies.